

**PL-TR-97-2028**

# **CRUSTAL WAVEGUIDE EFFECTS ON REGIONAL PHASES IN CHINA AND SOUTHEAST ASIA**

**Thorne Lay  
Guangwei Fan  
Arthur Rodgers**

**University of California/Santa Cruz  
Earth Sciences Department & Institute of Tectonics  
Earth & Marine Sciences Building  
Santa Cruz, CA 95064**

**10 March 1997**

**Scientific Report No. 1**

**19970707 082**

**Approved for public release; distribution unlimited**



**DEPARTMENT OF ENERGY  
Office of Non-Proliferation  
and National Security  
WASHINGTON, DC 20585**



**PHILLIPS LABORATORY  
Directorate of Geophysics  
AIR FORCE MATERIEL COMMAND  
HANSCOM AFB, MA 01732-3010**


**DTIC QUALITY INSPECTED 3**


SPONSORED BY  
Department of Energy  
Office of Non-Proliferation and National Security

MONITORED BY  
Phillips Laboratory  
CONTRACT No. F19628-95-K-0014

The views and conclusions contained in this document are those of the authors and should not be interpreted as representing the official policies, either express or implied, of the Air Force or U.S. Government.

This technical report has been reviewed and is approved for publication.

  
JAMES F. LEWKOWICZ  
Alternate Contract Manager  
Earth Sciences Division

  
JAMES F. LEWKOWICZ  
Director  
Earth Sciences Division

This report has been reviewed by the ESD Public Affairs Office (PA) and is releasable to the National Technical Information Service (NTIS).

Qualified requestors may obtain copies from the Defense Technical Information Center. All others should apply to the National Technical Information Service.

If your address has changed, or you wish to be removed from the mailing list, or if the addressee is no longer employed by your organization, please notify PL/IM, 29 Randolph Road, Hanscom AFB, MA 01731-3010. This will assist us in maintaining a current mailing list.

Do not return copies of this report unless contractual obligations or notices on a specific document requires that it be returned.

# REPORT DOCUMENTATION PAGE

Form Approved  
OMB No. 0704-0188

Public reporting burden for this collection of information is estimated to average 1 hour per response, including the time for reviewing instructions, searching existing data sources, gathering and maintaining the data needed, and completing and reviewing the collection of information. Send comments regarding this burden estimate or any other aspect of this collection of information, including suggestions for reducing this burden, to Washington Headquarters Services, Directorate for Information Operations and Reports, 1215 Jefferson Davis Highway, Suite 1204, Arlington, VA 22202-4302, and to the Office of Management and Budget, Paperwork Reduction Project (0704-0188), Washington, DC 20503.

1. AGENCY USE ONLY (Leave blank)		2. REPORT DATE 10 March 1997	3. REPORT TYPE AND DATES COVERED Scientific Report No. 1	
4. TITLE AND SUBTITLE  Crustal Waveguide Effects on Regional Phases in China and Southeast Asia			5. FUNDING NUMBERS  F19628-95-K-0014 PE 69120H PR DENN TA GM WU AA	
6. AUTHOR(S) Thorne Lay Guangwei Fan Arthur Rodgers				
7. PERFORMING ORGANIZATION NAME(S) AND ADDRESS(ES)  Earth Sciences Department and Institute of Tectonics University of California, Santa Cruz Earth and Marine Sciences Building Santa Cruz, CA 95064			8. PERFORMING ORGANIZATION REPORT NUMBER	
9. SPONSORING/MONITORING AGENCY NAME(S) AND ADDRESS(ES)  Phillips Laboratory 29 Randolph Rd. Hanscom AFB, MA 01731-3010  Contract Manager: Delaine Reiter/G PE			10. SPONSORING/MONITORING AGENCY REPORT NUMBER  PL-TR- 97-2028	
11. SUPPLEMENTARY NOTES  This research was sponsored by the Department of Energy, Office of Non-Proliferation and National Security, Washington, DC 20585				
12a. DISTRIBUTION / AVAILABILITY STATEMENT  Approval for public release: distribution unlimited			12b. DISTRIBUTION CODE	
13. ABSTRACT (Maximum 200 words)  This research program is addressing the issue of reducing scatter in regional phase discriminant measures associated with waveguide irregularity. We seek to empirically reduce discriminant measure variance, using along-path measures obtained from data bases for surface topography, crustal thickness, and sedimentary layer thickness. Several path-specific measures are found to have significant correlations with regional discriminant measurements, both before and after correction for propagation distance, for events in China and the Middle East. For station WMQ, in western China, variance reductions two to three times as large as those for distance corrections alone can be achieved by simple empirical models obtained by multiple-regression analysis. We are applying multiple-regression analysis for several path properties to all CDSN stations and all broadband stations in the Middle East under this contract. This report presents two preprints: the first addresses variance reduction of discriminant measures at station WMQ, demonstrating the new methodology, and the second is a technical study comparing discriminant measurement procedures applied to data for the Middle East. An appendix documents the full set of empirical relations found for our data for WMQ.				
14. SUBJECT TERMS  Regional seismic discriminants, regional phases, crustal propagation, nuclear discrimination			15. NUMBER OF PAGES 172	
			16. PRICE CODE	
17. SECURITY CLASSIFICATION OF REPORT Unclassified	18. SECURITY CLASSIFICATION OF THIS PAGE Unclassified	19. SECURITY CLASSIFICATION OF ABSTRACT Unclassified	20. LIMITATION OF ABSTRACT SAR	

## Table of Contents

<b>PREFACE</b>	v
<b>STATISTICAL ANALYSIS OF IRREGULAR WAVEGUIDE INFLUENCES ON REGIONAL SEISMIC DISCRIMINANTS IN CHINA</b>	1
Introduction	3
Data	7
Path Effects for Regional Discriminants	17
Multivariate Regression	28
Discussion and Conclusions	41
References	44
<b>COMPARISON OF REGIONAL PHASE AMPLITUDE RATIO MEASUREMENT TECHNIQUES</b>	47
Introduction	48
Regional Earthquake Data at ABKT	49
Time Domain Measurements - Methodology	52
Time Domain Measurements - Results	54
Frequency Domain Measurements - Methodology	54
Comparing Time and Frequency Domain Measurements	58
Discussion	62
References	63
<b>APPENDIX: WMQ DISCRIMINANT MEASURES AND PATH DEPENDENCE</b>	65

DTIC QUALITY INSPECTED 3

## Preface

This research is directed at improving the performance of regional seismic discriminants by developing new approaches for reducing the scatter in discriminant measures imparted by path-specific waveguide heterogeneity. Conventional procedures for regionalization of discriminant measures involve determining empirical distance-dependence of discriminants for regions that have relatively uniform propagation characteristics, with no blockage of phases. Such approaches essentially assume that the best propagation corrections that can be applied are those for a single, regionally averaged empirical distance trend. While this is a useful and necessary step, there is significant residual variance in all regional discriminants after distance correction, and this scatter intrinsically limits the performance of the discriminants, particularly at low frequencies.

Our previous work has demonstrated that consideration of individual path properties allows further empirical reduction of discriminant measure variance, using along-path measures obtained from data bases for surface topography, crustal thickness, and sedimentary layer thickness. Several path-specific measures are found to have significant correlations with regional discriminant measurements, both before and after correction for propagation distance, for events in China and the Middle East. For station WMQ, in western China, variance reductions two to three times as large as those for distance corrections alone can be achieved by simple empirical models obtained by multiple-regression analysis. We are applying multiple-regression analysis for several path properties to all CDSN stations and all broadband stations in the Middle East under this contract. This report presents two preprints: the first addresses variance reduction of discriminant measures at station WMQ, demonstrating the new methodology, and the second is a technical study comparing discriminant measurement procedures applied to data for the Middle East. An appendix documents the full set of empirical relations found for our data for WMQ.

**Statistical Analysis of Irregular Waveguide Influences on Regional Seismic  
Discriminants in China**

by

Guangwei Fan and Thorne Lay

Institute of Tectonics

Department of Earth Sciences

University of California, Santa Cruz

Santa Cruz, CA 95064

submitted to *Bulletin of the Seismological Society of America*

March 10, 1997

## ABSTRACT

Short-period regional phases play an important role in identifying low magnitude seismic events in the context of monitoring the Comprehensive Test Ban Treaty. Amplitude ratios of regional phases comprised mainly of P wave energy ( $P_n$ ,  $P_g$ ) to those comprised mainly of S wave energy ( $S_n$ ,  $L_g$ ) effectively discriminate between explosions and earthquakes in many regions, particularly at frequencies higher than 3 Hz. At lower frequencies, discrimination is usually poor due to large scatter that causes overlapping of event populations. Scatter in regional discriminant measures such as  $P_g/L_g$  ratios is caused by both source and propagation effects, and reducing the scatter imparted by the latter is essential to improving the discriminant performance when events do not share identical paths. Regional phases experience distance-dependent amplitude variations due to effects such as critical angle amplification, geometric spreading, and attenuation. Discriminant measures are usually corrected for empirically determined distance trends for a given region, but large scatter persists after such corrections. This study seeks to develop more sophisticated empirical corrections for path properties in order to further reduce the scatter in regional discriminant measures caused by propagation effects. Broadband seismic waveforms recorded at station WMQ, in western China, demonstrate that regional phase ratios such as  $P_n/L_g$ ,  $P_g/L_g$ ,  $P_n/S_n$ ,  $P_g/S_n$ , and  $S_n/L_g$ , all show significant distance dependence for frequencies less than 6 Hz. However, variations in crustal structure cause additional path-specific amplitude fluctuations that are not accounted for by regionally averaged distance corrections. Blockage of  $L_g$  phases on paths traversing the margins of the Tibetan Plateau is one such effect. Regression analysis demonstrates that regional discriminants measured at WMQ display significant correlations with path-specific properties such as mean elevation, topographic roughness, basement depth and crustal thickness. Multiple regressions using optimal combinations of parameters yield corrections that reduce variance in  $P_g/L_g$  measurements for frequencies less than 3 Hz by a factor of two or more relative to standard distance corrections. This should systematically enhance the performance of the  $P_g/L_g$  discriminant at low frequencies. The method presented here can be used for all regions and all short-period regional discriminants. It is likely that the extraordinary crustal heterogeneity in western China represents an extreme case of path dependent effects.

## INTRODUCTION

Seismic monitoring of the Comprehensive Test Ban Treaty (CTBT) requires high confidence identification of sources of seismic signals. For events larger than about magnitude 4.0, teleseismic signals usually suffice to identify the source (or at least allow ruling it out as a possible nuclear explosion) based on event location, source depth, or waveform characteristics such as P wave polarity or  $m_b/M_s$  ratios. Events with lower magnitudes usually do not produce adequate teleseismic signal amplitudes for reliable source identification, particularly at longer periods, so there is great interest in exploiting the larger amplitude short-period signals recorded at regional distances less than 1500 km from the source. Seismic waves at regional distances tend to be complicated as a result of multiple reflections and phase conversions within the crustal and lithospheric waveguide, particularly in the short period range ( $< 1$  sec) for which high signal-to-noise ratios are observed. The primary strategies for source identification with regional signals involve characterizing frequency dependence of either particular phases (e.g. high frequency/low frequency amplitudes of Pg or Lg) or of the overall source radiation (e.g.  $M_L/M_o$  ratios), or characterizing the relative amounts of S and P energy released by the source (e.g. Pg/Lg ratios). The latter approach is particularly promising as it can exploit relatively narrow band, high frequency observations which have good signal-to-noise properties, and the P/S ratios reflect source radiation effects that directly distinguish earthquakes from explosions.

There are four major regional phases that are commonly considered for regional P/S measurements: Pn and Sn, which are head waves and lithospheric guided waves that propagate primarily in the upper mantle lid just below the Moho boundary, and Pg and Lg, which involve direct P or S crustal arrivals as well as an extended coda of internal crustal reflections and reverberations. Pn/Lg, Pg/Lg, Pn/Sn, and Pg/Sn ratios have all been considered for explosion discrimination, with one ratio or another usually being favored from region to region depending on local crustal properties that influence energy partitioning in the waveguide (some regions excite very weak Pn or Sn arrivals, while in



other areas these may be stronger than Pg or Lg). Experience has shown that these P/S ratios tend to give poor discrimination between explosion and earthquake signals for frequencies near 1 Hz when standard distance corrections are applied, but as the frequency increases the separation of explosion and earthquake populations improves rapidly, often proving quite diagnostic for frequencies above 3 to 5 Hz (e.g. Walter *et al.*, 1995; Taylor, 1996; Hartse *et al.*, 1996). Regional P/S type ratios have significant scatter for both earthquake and explosion populations even on a common path (e.g. Walter *et al.*, 1995), which indicates that source effects such as depth, focal mechanism, stress drop, and proximity to the water table do influence the measures. This scatter is difficult to reduce other than by averaging multiple observations for a given event, which can reduce effects such as those caused by radiation patterns. However, the scatter in regional phase ratios is significantly greater when diverse propagation paths are considered together. This is the typical case for CTBT monitoring situations, in which sparse numbers of stations record events spread over large areas at regional distances. Accounting for propagation effects on regional discriminant measurements is necessary if the scatter is to be reduced to the level of intrinsic source variability, which is the best we can hope for. Low false-alarm identification of outlier signals that may represent violations of the CTBT requires tightly defined discriminant populations for observations on many different paths.

Efforts to understand wave propagation effects on regional phases involve a wide variety of observational and theoretical studies, but we are still far from having good predictive capabilities for most regional signals. This is because the crustal and lithospheric waveguide is very complex with multiple scales of heterogeneity. Our most detailed crustal models are still very simple and poorly constrained, and many areas of CTBT monitoring concern having totally unknown crustal structures, and high frequency wave propagation in the three-dimensional heterogeneous crust is poorly understood and cannot be accurately modeled at present for useful propagation distances. As a result, deterministic approaches to calibrating regional discriminants and correcting observations for propagation effects are

very limited, mainly being restricted to source modeling of longer period energy ( $>3$  sec) in very well-studied regions and for quantifying effects such as phase blockage by waveguide disruptions.

Most efforts to develop regional discriminants rely on empirical approaches for reducing propagation effects, following the basic strategy that has long been used for seismic magnitudes. This involves determining empirical curves of amplitude observations as a function of epicentral distance, which are used to equalize individual phase amplitudes or amplitude ratios to a common distance, "correcting" for propagation effects. Typically, the distance corrections are determined for a well-defined region, recognizing that crustal variations strongly affect the amplitudes of regional phases. Amplitude-distance or amplitude ratio-distance relationships defined for a given region in this fashion implicitly assume that propagation effects (or differential propagation effects in the case of ratios) can be characterized by a single function of path length alone. This is the same as asserting that the crust throughout the region is laterally uniform, such that all paths have the same behavior as long as their path length is the same. Unfortunately, for regional phases (unlike teleseismic magnitudes) this is a poor assumption in almost all regions of the world, especially in tectonically active areas where natural seismicity presents great challenges for CTBT monitoring.

There is certainly value in determining a regionally averaged distance dependence for a given discriminant measure. Differential geometric spreading, attenuation and average crustal waveguide effects on seismic energy partitioning can be accounted for to first order. This assertion is borne out by practice: almost all discriminant measures exhibit some empirical distance dependence, at least in lower frequency bands. However, it is clearly desirable to account for more realistic propagation effects by considering specific path properties, which cause fluctuations about the average pattern manifested in regional distance corrections. Lacking deterministic capabilities for this, and because the problem does not reduce to a simple station correction type of procedure as for teleseismic

magnitudes, we pursue empirical approaches that have been motivated by many previous studies that document the importance of specific path properties.

For example, it has been demonstrated that laterally heterogeneous velocity structure, and changes in crustal discontinuities and crustal thickness affect regional phases (e.g. Kennett, 1986, 1989; Zhang *et al.*, 1994). Blockage of Lg phases by segments of oceanic crust as short as 100 to 200 km is one classic example (e.g. Press and Ewing, 1952; Zhang and Lay, 1995). Lg blockage has also been noted in continental areas with large changes in crustal thickness, as for the Tibetan Plateau (Ruzaikin *et al.*, 1977; Ni and Barazangi, 1983; McNamara *et al.*, 1996) and near the Alpine Mountains (Campillo *et al.*, 1993). Sn phases are strongly attenuated in localized areas of the northern Tibetan Plateau (Ni and Barazangi, 1983) and in the northwesternmost Iranian and Turkish Plateaus and between the Black Sea and Caspian Sea (Kadinsky-Cade *et al.*, 1981; Rodgers *et al.*, 1996). Structure on the Moho has been found to affect Pn phases in Scandinavia (Kvaerna and Doornbos, 1991). Topographic characteristics are sometimes correlated with regional phase behavior as well (Baumgardt, 1990; Zhang and Lay, 1994; Zhang *et al.*, 1996), as are sedimentary structures (Baumgardt and Der, 1994; Zhang *et al.*, 1994). While it is possible in practice to identify regions of phase blockage and to apply alternate discrimination procedures that are not biased by such effects in those areas, the many studies mentioned above establish that waveguide irregularities are expected to be ubiquitous and resulting fluctuations in discriminant measures will exist in every region. Even effects such as blockage may be cumulative effects, with a continuum of behavior that can not be readily regionalized. Empirically reducing the effects seems to be the best approach, much as is done for standard distance corrections.

In this study, we pursue the empirical calibration approach suggested by Zhang and Lay (1994) and Zhang *et al.* (1994, 1996). These studies used the available data bases on crustal properties in different regions to develop path-specific parameters which are tested for correlation with regional phase amplitude ratios. The most reliable parameters that can

be determined for any path are those involving surface topography, for which highly precise models are available. Crude models of crustal thickness and sedimentary layer thickness are also available for most of Eurasia. These models are used parametrically as surrogates for the complex propagation effects produced by the heterogeneous waveguide. Ratios of regional phases recorded at station WMQ, in western China, are analyzed for regionally-averaged distance effects as well as path-specific effects parameterized by measures of surface topography, sedimentary layer thickness and crustal thickness. Both point-wise properties (e.g., maximum or minimum crustal thickness on each path) and path-integrated properties (e.g., mean altitude, mean crustal thickness) are considered. Our goal is to reduce scatter in frequency dependent P/S type seismic discriminants by performing multiple regressions to establish empirical models for propagation corrections. Results are presented for Pg/Lg observations. The models are not unique, and they do not reveal the causal physics controlling the regional phases, but the same statements are true of empirical distance corrections (which are based on, at most, very simplified models of geometric spreading and attenuation that are usually not even consistent with our gross knowledge of Earth layering and regional phase propagation). Significant variance reductions can be achieved with plausible combinations of waveguide parameters, enabling improved discriminant performance at lower frequencies. Such procedures can be readily incorporated into CTBT monitoring operations. The empirical relations that are obtained also provide a starting point for quantitative modeling efforts that can be pursued to quantify the underlying wave propagation effects.

## DATA

Western China is a region with very diffuse seismicity (Figure 1), sparse seismic instrumentation, acute crustal heterogeneity, and prior nuclear testing experience. Thus, it is a region of interest for CTBT monitoring, and many of the practical issues about

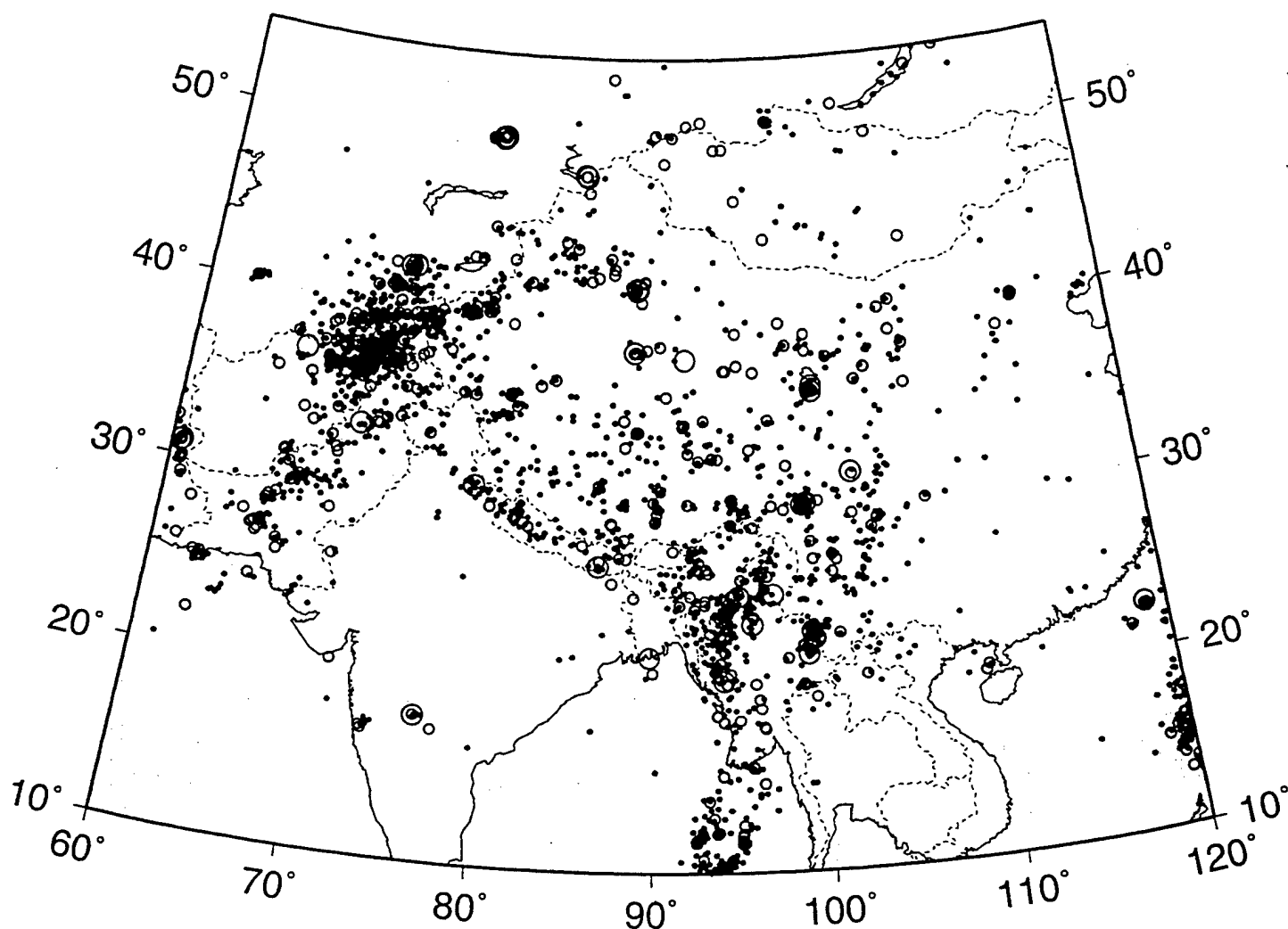


Figure 1. Seismicity in western China and its vicinity. The map shows the epicentral locations for earthquakes from 1988 to 1995 from the PDE catalogue. The small dots represent epicenters of earthquakes with magnitudes  $4.0 \leq m_b < 5.0$ ; the small open circles are epicenters of earthquakes with magnitudes of  $5.0 \leq m_b < 6.0$ ; and large open circles are epicenters for earthquakes with magnitudes of  $6.0 \leq m_b$ .

calibration of regional discriminants are relevant to this region. We analyze 87 earthquakes with magnitudes of  $4.5 \leq m_b \leq 6.1$  that occurred between 1988 and 1995 in western China and its vicinity. These events were all recorded on the broadband vertical component at station WMQ, with the path coverage being shown in Figure 2. Figure 3 shows a few example seismograms, indicating the great variability in broadband waveform complexity on the different paths. To avoid ambiguity in regional phase recognition at very close distances, only events with epicentral distances greater than 240 km are used, with the most distant observations being 2100 km from the station. The events are all large enough to have Harvard centroid moment tensor (CMT) focal mechanisms, and they have fairly well determined locations as a result of numerous teleseismic detections. For events prior to 1994 we use locations given by the International Seismological Centre (ISC) bulletins, and for events after 1994 we use locations from the USGS Preliminary Determination of Epicenters (PDE) catalog. Only events with focal depths less than 50 km are used in this study, but there are relatively large uncertainties in source depth due to the sparse regional station coverage and the complex crustal and upper mantle structure in the region.

Following Walter *et al.* (1995) and Hartse *et al.* (1996), measurements of regional seismic phases are made for all ground motions in specific windows. The  $P_n$  window begins at the onset of the signal (all events are at distances beyond the crossover distance) and ends at the start of the  $P_g$  window. The  $P_g$  and  $S_n$  windows are between group velocities of 6.2 to 5.2 km/sec and 4.8 to 4.0 km/sec, respectively. The  $L_g$  window extends from a group velocity of 3.6 km/sec to a group velocity of 3.0 km/sec. We carefully checked the validity of these windows for capturing the primary energy in each signal. For each phase, the vertical component broadband records (approximately proportional to ground velocity) were windowed and band pass filtered into four frequency bands: 0.75 to 1.5 Hz, 1.5 to 3.0 Hz, 3.0 to 6.0 Hz, and 6.0 to 9.0 Hz, using Butterworth filters. We did not deconvolve the instrument response, as we consider only ratios of phases in the same frequency band, which explicitly cancels the instrument effect.

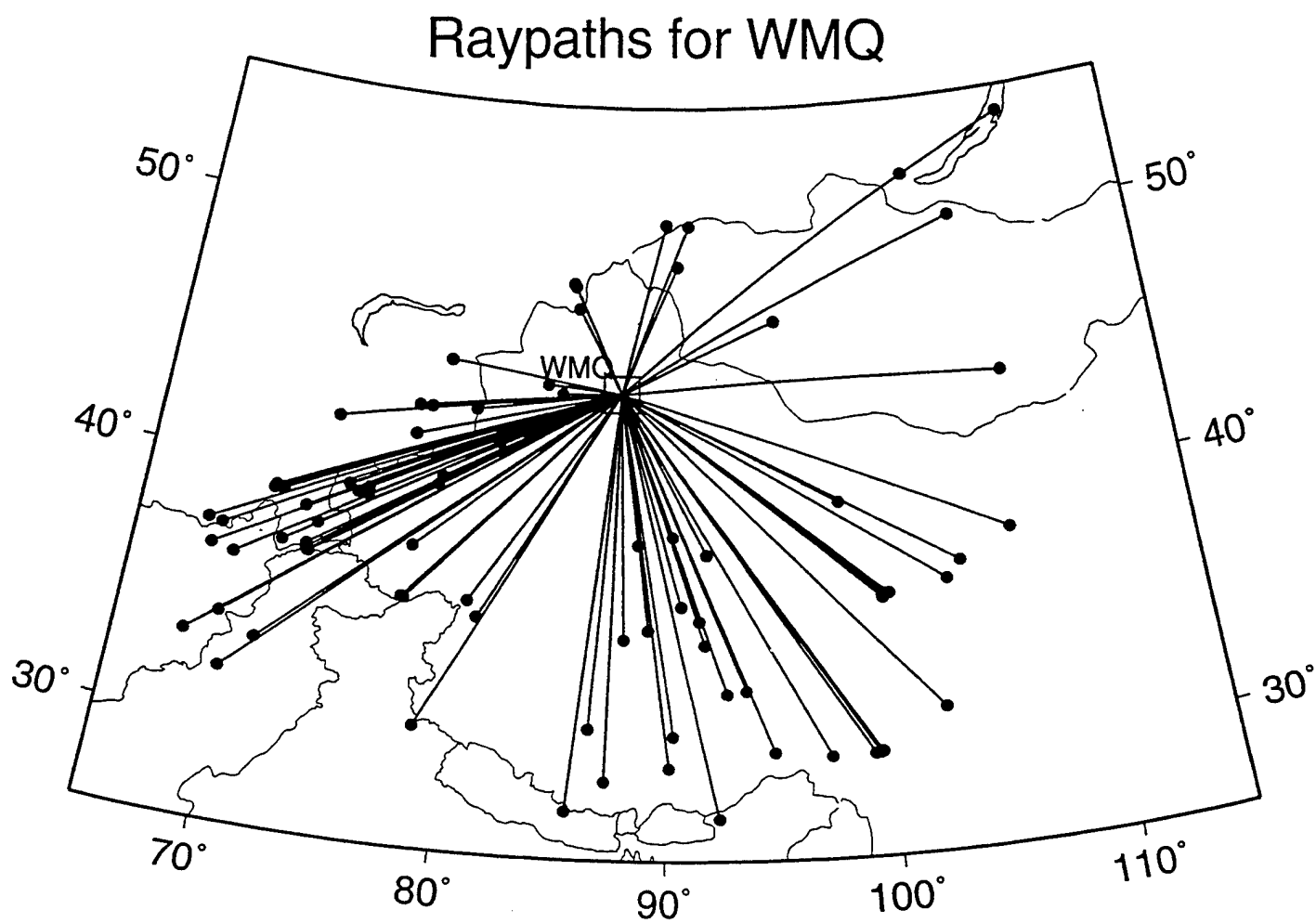


Figure 2. Ray paths from the epicenters of the 87 selected events to the station WMQ in western China.

## Seismic Waveforms Recorded at WMQ

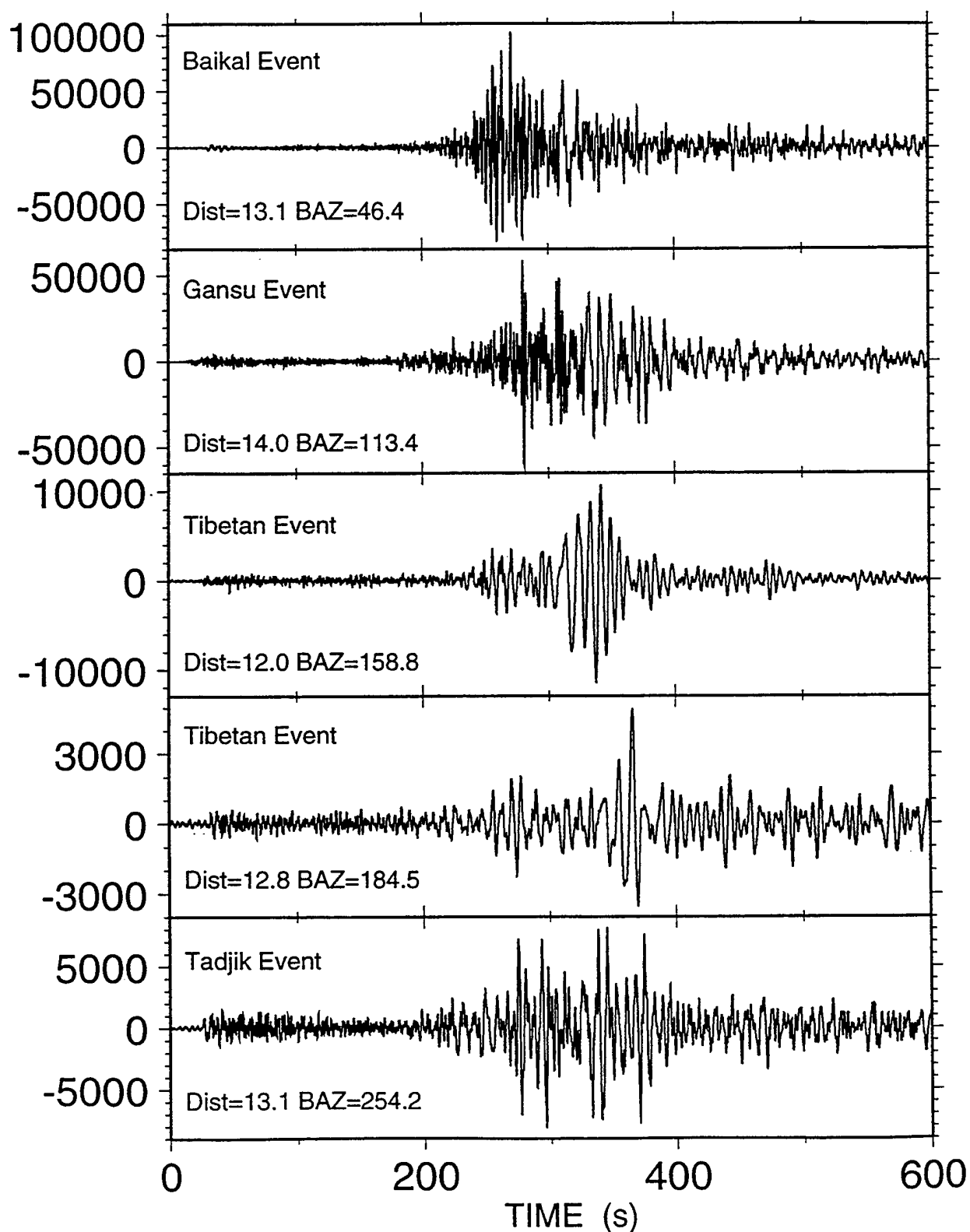


Figure 3. Examples of broadband vertical component seismograms recorded at station WMQ for events in different source regions. The epicentral distance from WMQ is given by Dist, and BAZ indicates the azimuth from the station toward the event.



Previous studies have demonstrated that rms measures of regional phases like Lg have remarkable stability due to the averaging of multiple arrivals (Ringdal *et al.* 1992; Gupta *et al.*, 1992), so we compute rms amplitudes of each phase in the corresponding filtered group velocity windows. Rodgers *et al.* (1997) have considered the various regional phase measurement procedures, and while they recommend frequency domain spectral averaging, the results of time domain measures of velocity traces are not significantly different than for most other commonly used measures (rms ground displacements, spectral averages, etc.). Noise levels are computed using rms measures of the filtered seismograms in the 10 sec window preceding the manually picked first arrival time. Events with Pn signal-to-noise ratios greater than two are considered to be acceptable, given that Pn is usually the weakest regional phase in these data, except when Lg blockage occurs. For most of the events, the signal-to-noise ratios are between 10 to 100.

The ray paths connecting the earthquakes and WMQ sample a large area in the vicinity of western China, including some of the most dramatic topographic features in the world such as the Tibetan Plateau, and the Tien Shan, Pamir and Hindu Kush Mountains. Many ray paths project along or across the mountain belts or the margins of the Tibetan Plateau. Topography in this region is illustrated in Figure 4. The topographic relief data are from the GLOBE (Global Land One-km Base Elevation) project with a spatial resolution of 30 arc-second (one-km). This database was developed by the U.S. Defense Mapping Agency (DMA) and made available by the National Geophysical Data Center (NGDC) of NOAA. The lowest elevation is -152 m near the Turfan Basin (42.6°N, 89.3°E). The highest elevation occurs in the Himalayas, where many mountain peaks are well above 8000 m in altitude. Surface topography is the most precisely known attribute of the regional crustal structure, thus using it as a guide to wave propagation influences is clearly desirable. The general notion is that topography reflects the tectonic character of the crust, with rough topography in active regions with disrupted crust, high topography in areas of tectonically thickened crust, laterally variable topography in areas of rapidly

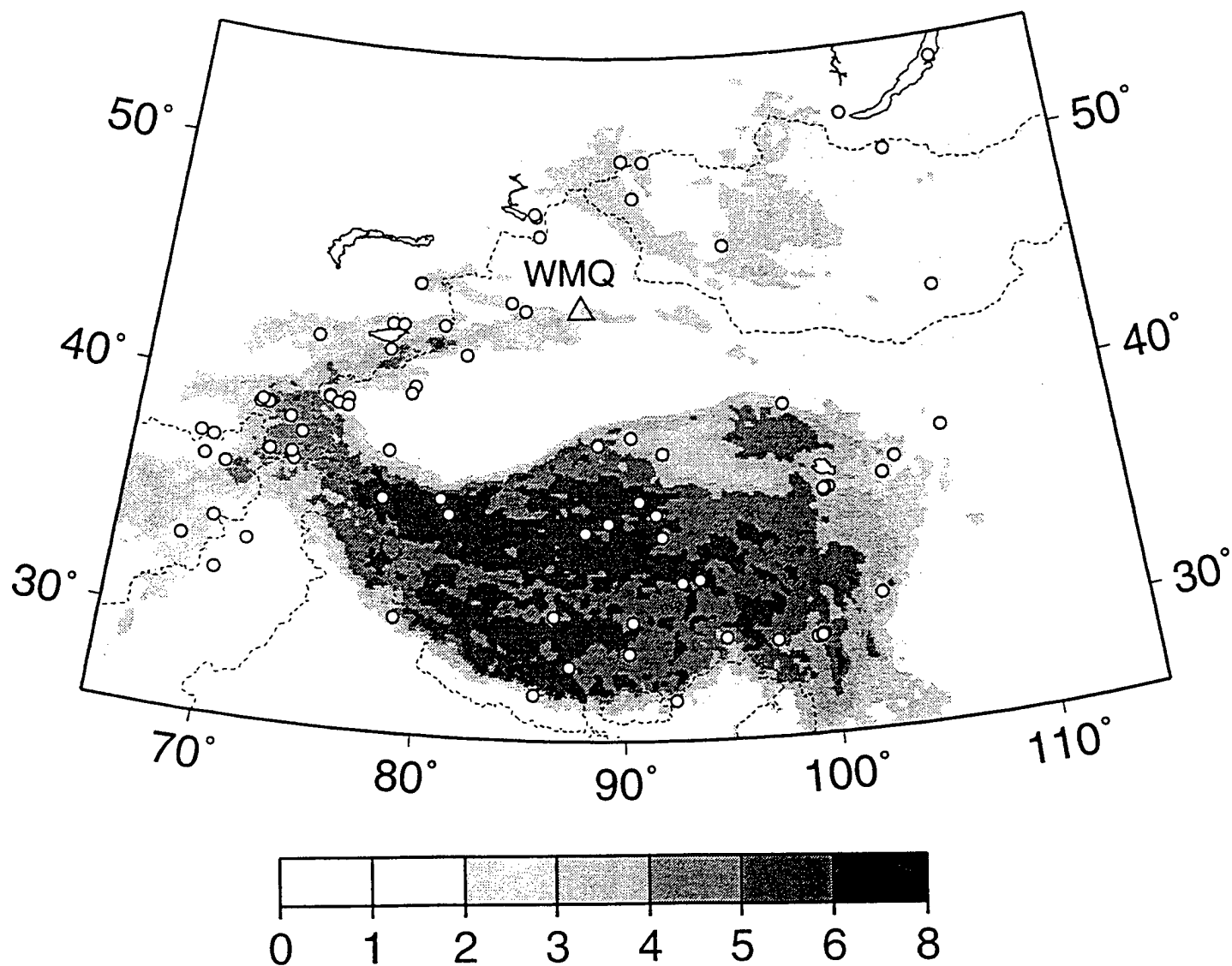


Figure 4. Topography in the study area decimated from a data base with 1 km resolution. The white circles represent the epicenters of the events used in this study.

changing crust and mantle structure, and so on. Given variable degree of isostatic compensation and smoothing effects of sedimentation, topography cannot be expected to reflect all crustal structure variations, but it is clearly a starting point.

Much less is known about the internal crustal structure of the Eurasian crust, but low resolution models of crustal thickness (Moho depth), as shown in Figure 5, and sediment thickness, as shown in Figure 6, are available from the database compiled by Cornell University. These data were digitized from maps compiled by Kunin and Sheyk-Zade (1983) and Kunin (1987) based on deep seismic sounding (DSS) profiles and gridded on a 10 km grid (Fielding *et al.*, 1992). There is no question that the accuracy is limited, but the maps were derived independently from surface topography, and when averaged along any given raypath they probably provide first order average path properties that are not greatly in error. There is much less confidence in any point-wise property or local gradient in the properties in these models, and we keep this in mind when using these characterizations of the waveguide.

Profiles of topography, Moho depth, and sedimentary layer thickness along each great circle path from event epicenter to station WMQ were extracted using software from Wessel and Smith (1991). In order to reduce these functions to measures that can be correlated with regional phase amplitude ratios, we must compute summary parameters. For topography, which is very precisely known, we computer four path-specific parameters: mean elevation, rms roughness (variance) of topography, rms slope of topography from point to point along the path, and topographic skewness, or the third moment of topography, which characterizes the degree of asymmetry of topography around its mean value (Bennett and Mattsson, 1989; Zhang and Lay, 1994). We also calculate minimum, maximum, and mean crustal thickness, and maximum and mean sediment thickness along each path. The minimum and maximum measures are local values, and hence subject to much greater uncertainties than the path-averaged mean values, but local extremes may be responsible for important effects such as blockage of phases. Other

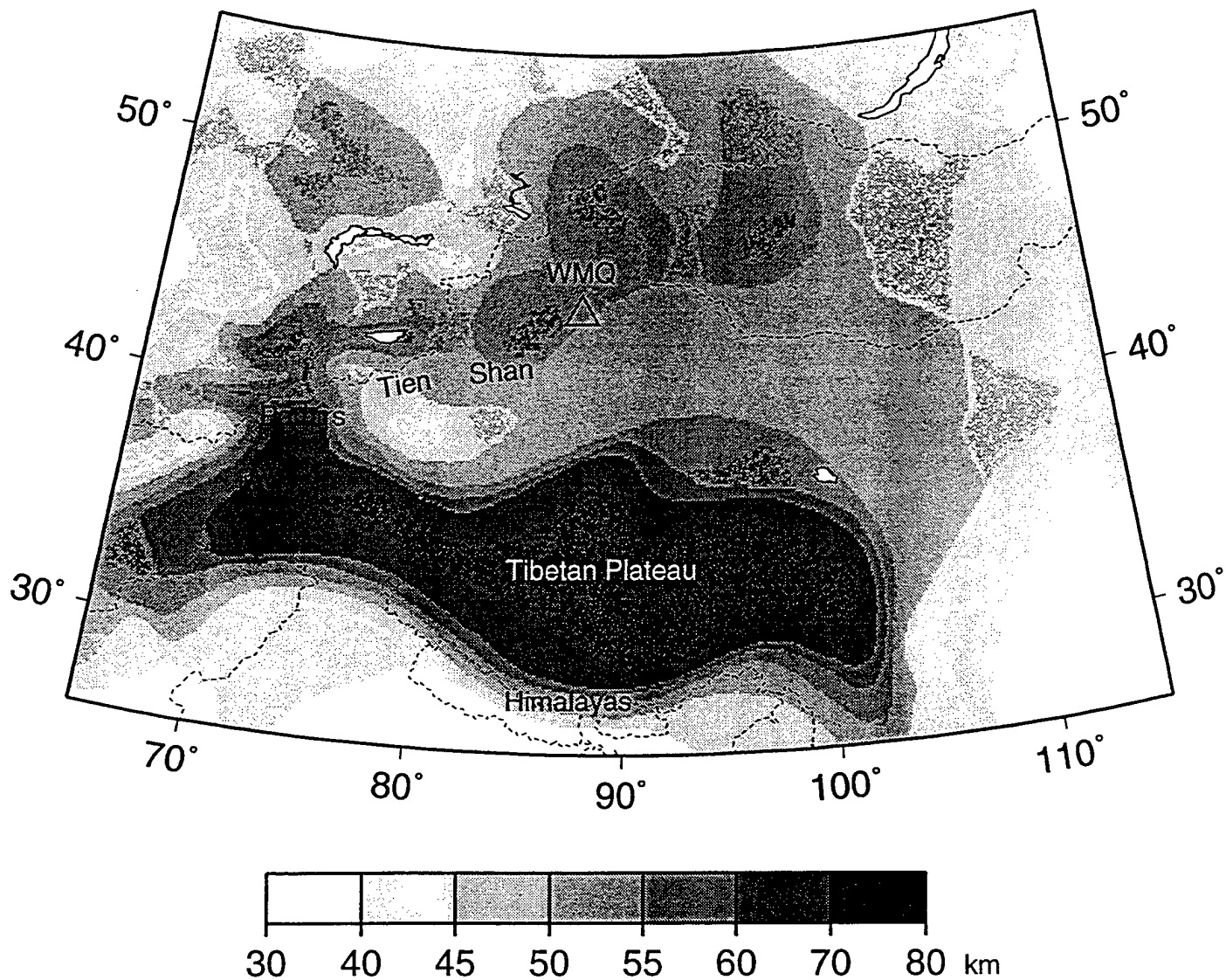


Figure 5. Depth to the Moho discontinuity in the study area. HK, Hindu Kush.

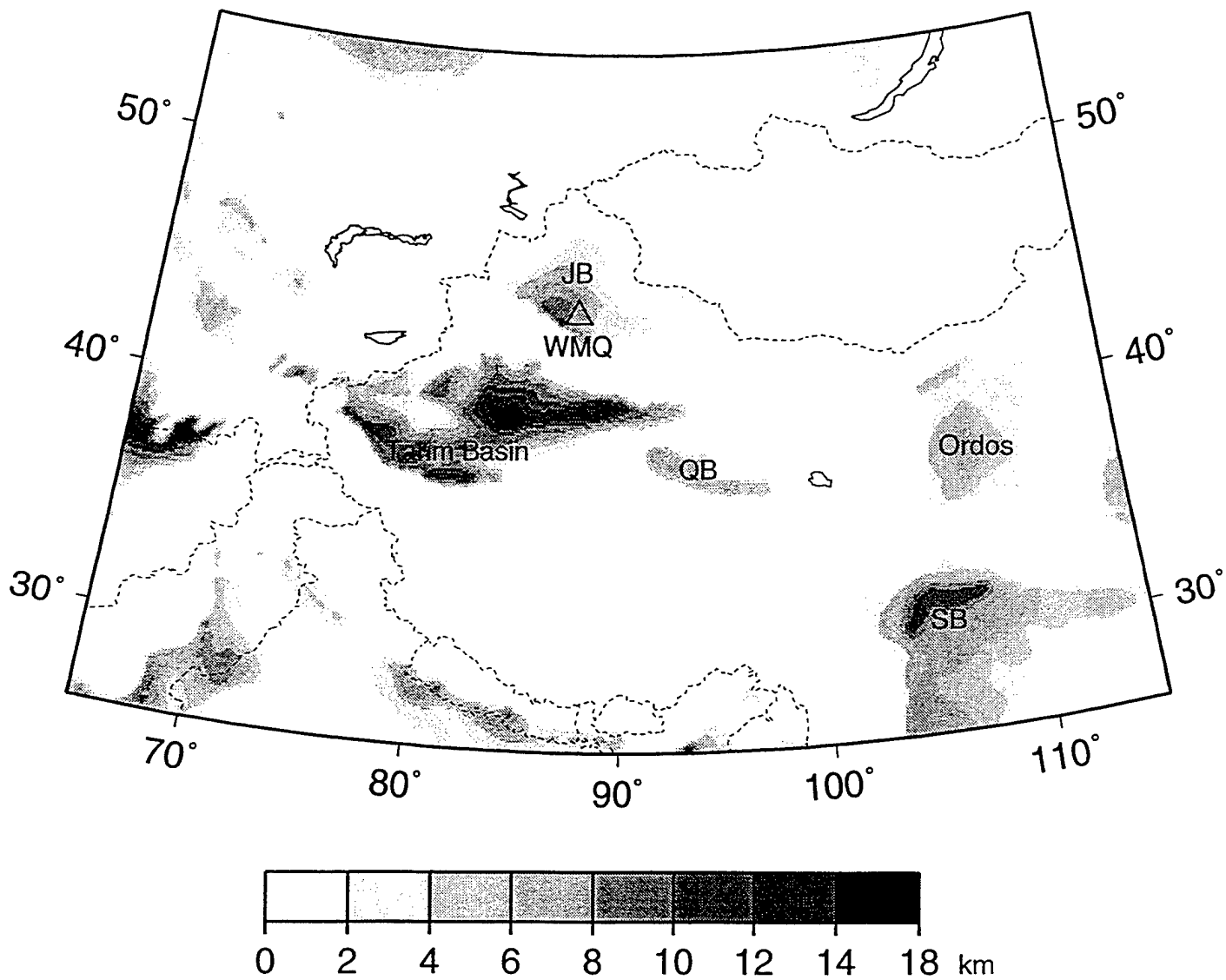


Figure 6. Sedimentary layer thickness in the study area. QB, the Qaidam Basin; JB, the Junggar Basin; SB, the Sichuan Basin.

databases could be considered, such as path averages through tomographic models derived from surface waves or attenuation models, but at present these are all even less reliable for western China than the gross crustal models, so we restrict our attention to the measures listed above.

## PATH EFFECTS FOR REGIONAL DISCRIMINANTS

We have systematically analyzed the path effects on all  $P_n/L_g$ ,  $P_g/L_g$ ,  $P_n/S_n$ ,  $P_g/S_n$ , and  $S_n/L_g$  ratios measured in different frequency bands for the 87 events recorded at WMQ. The first effect to be considered is simple propagation path length. The relative amplitudes of regional phases experience a general distance-dependent variation caused by differential attenuation and geometric spreading (Kennett, 1989; McCormack et al., 1995; Zhang et al., 1996). This distance dependence is expected to be very complex, if one uses regional phase calculations for a simple crustal model, but such calculations are usually poor approximations to actual data, which have many extra arrivals caused by scattering and complex crustal layering. In practice it is found that the regional phase signals, especially when measured as rms values over a group velocity window which contains multiple arrivals, usually have overall amplitude patterns that can be pretty well represented by a power law ( $\Delta^\gamma$ ) form (Sereno, 1991) or an exponential form ( $e^{\gamma\Delta}$ ) (Baumgardt and Der, 1994). Zhang and Lay (1996) proposed a slightly different exponential form for characterizing distance dependence of phase ratios,  $R(\Delta)=10^{\gamma\Delta}$ , which is adopted here. There is not a great deal of difference in these parameterizations, and similar results are obtained even if the corrections are based on  $\log(\Delta)$  rather than  $\Delta$ , as in some studies. It is important to note that even if the crust were laterally uniform, these simple distance expressions are not strictly correct, as the nature of most regional phases is that their amplitudes experience complex variations with distance due to critical angle effects (for example, multiple SmS arrivals in Lg phases can produce a 'bursty' pattern with distance).

Nonetheless, simple amplitude-distance parameterizations like these are the norm and they work very well, as shown below. Given our limited understanding of crustal structure in most regions, using these simple forms is defensible, albeit limited to a very gross characterization of propagation effects.

Linear regressions for all of the regional phase ratios measured at WMQ show clear distance dependence. Apparently, when the rms amplitude averaging of each phase window is performed, the progressively accumulating relative attenuation and geometric spreading effects prove to be primary factors controlling regional phase energy ratios. The highest correlations with propagation distance (up to 0.87) are found for  $\text{Log}(P_n/S_n)$ , with the frequency dependent measures being shown in Figure 7. This is likely due to the fact that both  $P_n$  and  $S_n$  phases mainly propagate within the upper mantle lid beneath the Moho, and relative attenuation and geometric spreading differences associated with varying P and S velocity gradients in the lid produce smoothly accumulating effects with distance traveled. The slopes of the linear regressions and the linear correlation coefficients diminish with increasing frequency, as proves true for all amplitude ratios.  $\text{Log}(P_n/L_g)$  ratios also have strong correlations with distance for frequencies up to 3 Hz ( $>0.80$ ; Figure A3a). Other amplitude ratios of  $P_g/L_g$ ,  $P_g/S_n$ , and  $S_n/L_g$  also display significant distance dependence with the correlation coefficients ranging between 0.4 to 0.7 in the three passbands below 6 Hz (see Appendix Figures A2a, A4a and A6a).

While the amplitude ratios of various regional phases show strong correlations with path length, independent relationships are also found with topographic parameters and other waveguide characteristics. For the various topographic parameters considered, mean path elevation and average surface roughness along each path have the most systematic correlations, as has been observed in other regions (Zhang and Lay, 1994; Zhang et al., 1994, 1996). The correlations for the 5 frequency dependent amplitude ratio measurements with these parameters, without correction for path length, are shown in Figures A2b, A2d, A3b, A3d, A4b, A4d, A5b, A5d, A6b and A6d. In every case the linear correlation

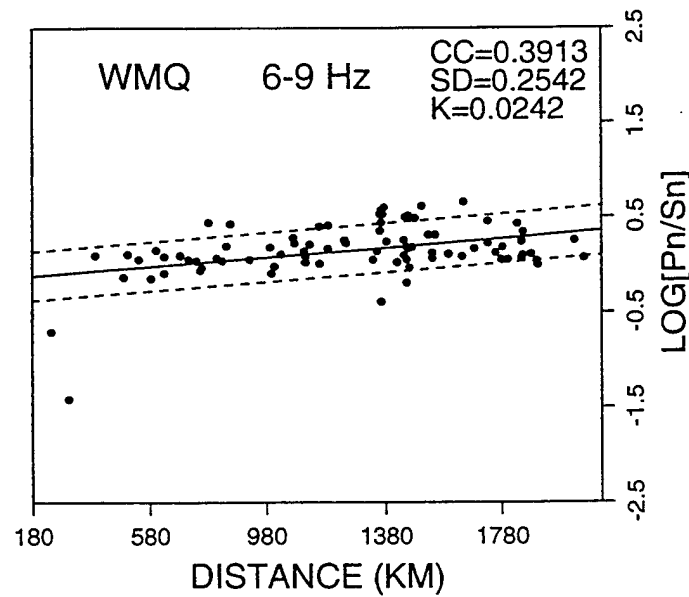
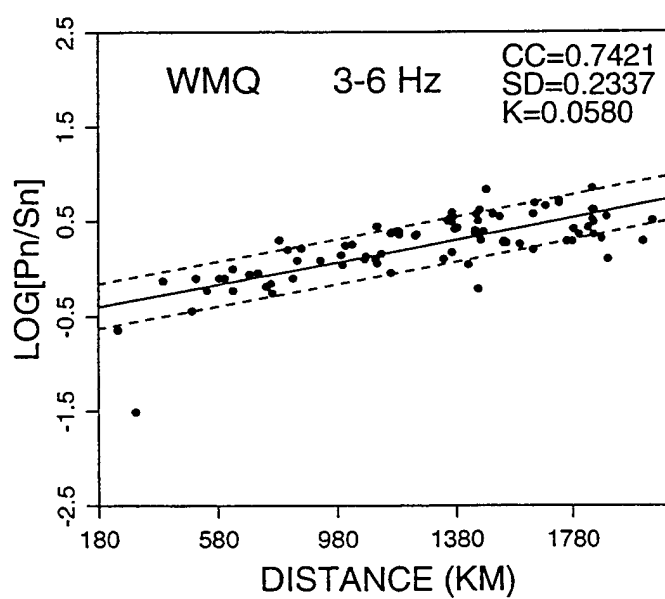
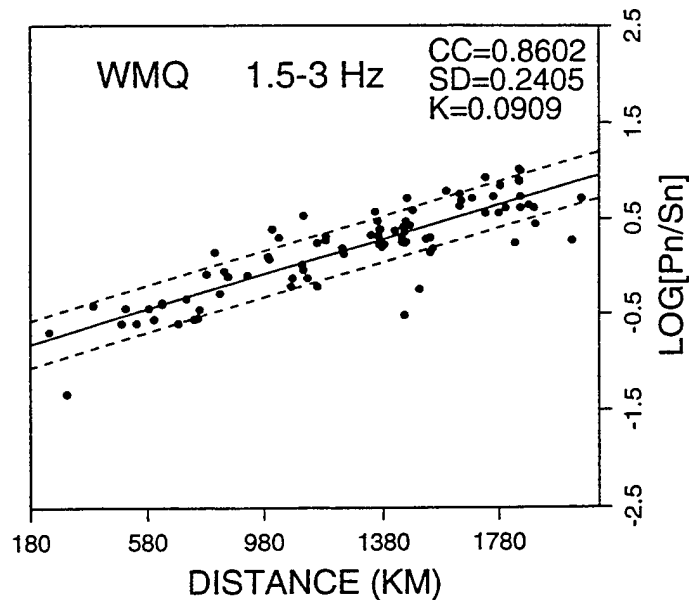
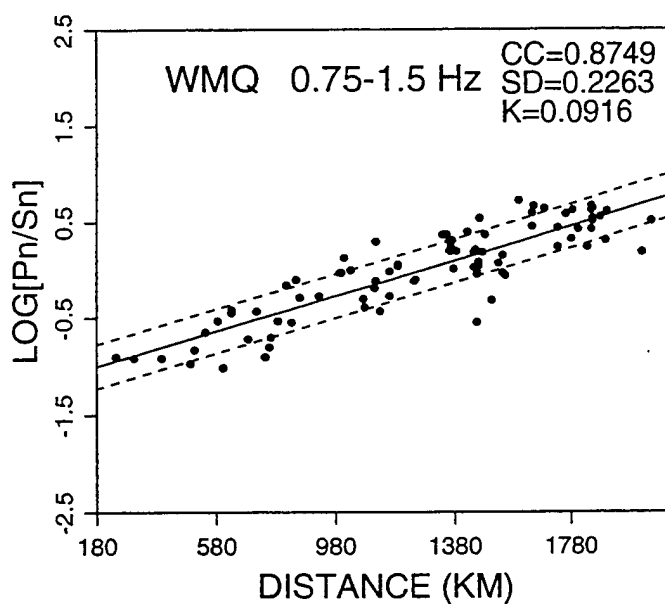


Figure 7.  $\text{Log}(P_n/S_n)$  as a function of distance from the station in various frequency bands. CC, linear correlation coefficients; SD, standard deviation of the linear regression; K, slope of the regression line. The dotted lines indicate  $\pm 1$  standard deviation about the regression line.



coefficients are larger than 0.5 for frequency bands 0.75-1.5 Hz and 1.5-3 Hz, and below 0.5 for higher frequencies. In fact, for all ratios other than those involving Pn, the linear correlation coefficients with mean path elevation and surface roughness are larger than those with path length for the two lower frequency bands. The path-averaged rms slope of topography shows little correlation (linear correlation coefficients less than 0.2) with the logarithmic amplitude ratios in all cases (Figures A2j, A3j, A4j, A5j, A6j), unlike the results for the Russian platform reported in Zhang and Lay (1994). A much larger range of rms slope variations is spanned by our data (from 20 to 220 m per km) in contrast to the small range (2 to 20 m per km) in the study of Zhang and Lay (1994), so their result appears to be an isolated case. The fourth topography parameter, skewness, shows moderate negative correlations (linear correlation coefficients of -0.33 to -0.56) with the regional phase amplitude ratios for frequencies below 3 Hz (Figures A2h, A3h, A4h, A5h and A6h).

Zhang et al. (1996) found that in the western U.S., the strongest single-parameter empirical correlations were found for the product of mean elevation times path length or mean roughness time path length, indicative of a cumulative effect on the amplitude ratios. This is also true of the WMQ observations, with the linear correlation coefficients being systematically higher for frequencies lower than 3 Hz for Pg/Lg (Figures A2f, A2g) Pn/Lg (Figures A3f, A3g), Pg/Sn (Figures A4f, A4g), and Sn/Lg (Figure A6f, A6g). One exception is for  $\text{Log}(P_n/S_n)$ , for which the parameter distance times roughness does not improve the correlations relative to distance alone. This suggests that topographic roughness has little affect on the Moho head waves, as might be expected. For the two lower frequency bands of Pg/Lg measurements the linear correlation coefficients are higher than 0.79 for path parameters based on the products of distance and mean elevation or distance and surface roughness. This can be compared to distance correlations of 0.56 to 0.66 to infer that there are significant variance reductions to be achieved by including additional path information. The most dramatic correlations are for Pn/Lg measurements

with these same products of distance times mean elevation or roughness, with linear correlation coefficients greater than 0.88, although for  $P_n/L_g$  the distance trends alone are very strong (linear correlations larger than 0.8).

Proceeding to additional path characteristics, we anticipate that crustal thickness may be an important parameter because it provides a direct measure of the overall shape of the waveguide in which the regional seismic energy is partitioned. The WMQ data are valuable for assessing this given the large variations in crustal thickness in the region (Figure 5). Seismic reflection and refraction studies have demonstrated that crustal thickness in the Tibetan Plateau is about 65 to 75 km (Hirn et al., 1984), making it one of the thickest crustal areas in the world.  $L_g$  waves are apparently highly attenuated due to a low  $L_g$   $Q$  value within the Tibetan Plateau and blocked at its northern and southern boundaries because of changes in crustal thickness across the margin (McNamara *et al.*, 1996). We find that correlations of  $\text{Log}(P_g/L_g)$  with mean (Figure 8) and maximum (Figure A2o) crustal thickness are higher than those with distance or topography for the 0.75-1.5 Hz band, and comparable for the 1.5-3 Hz band. The correlations are very low for higher frequencies. To a large extent, the low frequency trends reflect the partial and complete blockage of  $L_g$  phases traversing the margin of the Tibetan Plateau, which is also partly responsible for the trends with topography (note the strong correlations between Figures 4 and 5). This is consistent with modeling efforts that used ray diagrams and topography in central Asia, including Tibet, to demonstrate that  $P_g$  and  $L_g$  propagation are affected by changes in the crustal thickness (Kennett, 1989; Bostock and Kennett, 1990). The correlations appear to be stronger at lower frequencies because low frequency  $L_g$  has more predictable effects than the strongly scattered high frequency energy (e.g., Shih *et al.*, 1994). The correlation coefficients for  $\text{Log}(P_g/S_n)$  and mean crustal thickness (Figure A4l) are slightly higher than those with distance (Figure Ana), but slightly lower than those with mean elevation. Correlations of mean or maximum crustal thickness with  $P_n/L_g$ ,  $P_n/S_n$ , and  $S_n/L_g$  are comparable to, or lower than those with topography and, in general,

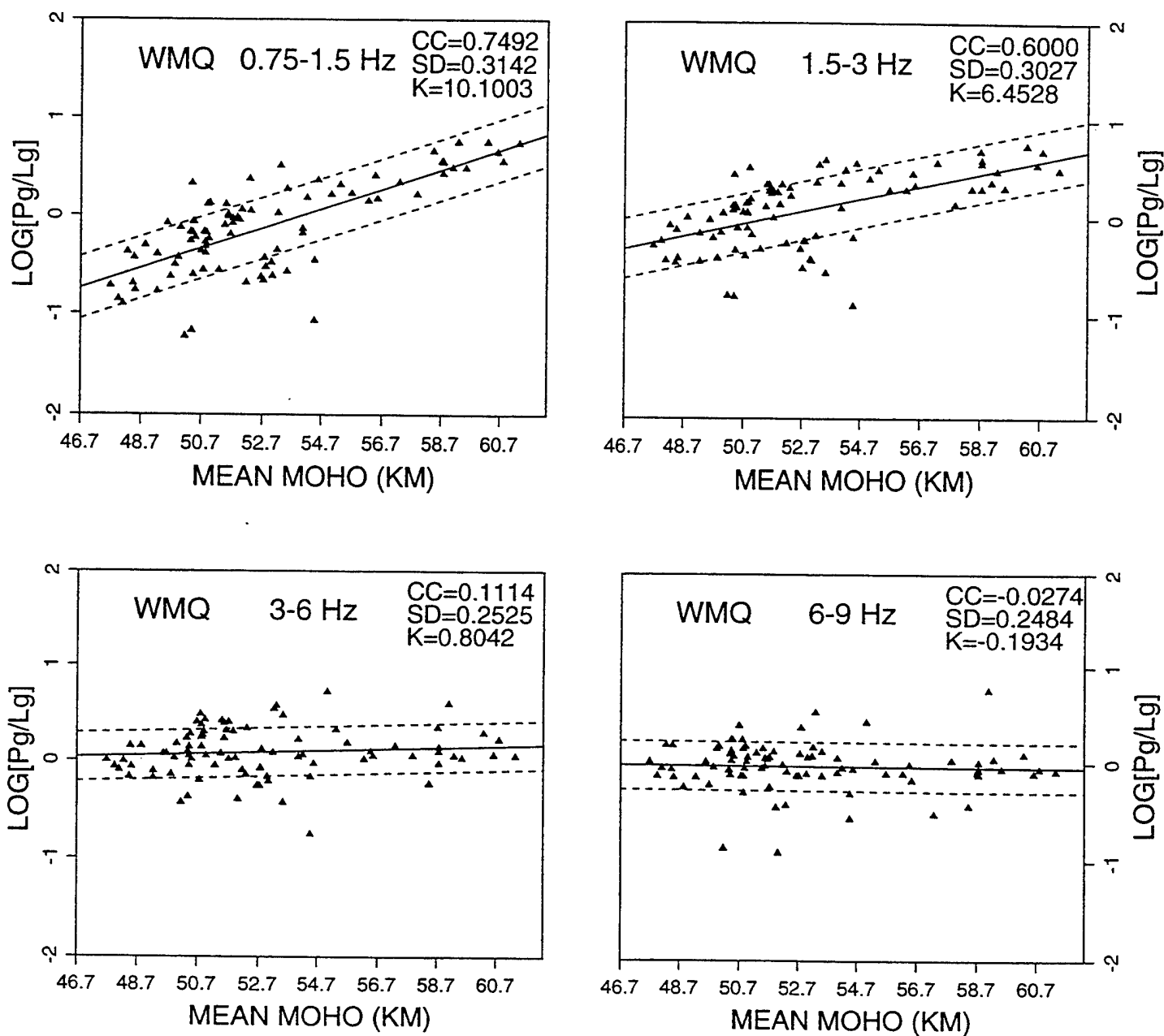


Figure 8.  $\text{Log}(P_g/L_g)$  as a function of mean crustal thickness in various frequency bands. CC, linear correlation coefficient; SD, standard deviation of the linear regression; K, slope of the regression line. The dotted lines indicate  $\pm 1$  standard deviation about the regression line.

weaker than those with distance (Figures A3l, A3o, A5l, A5o, A6l, A6o). In every case we found weak correlations ( $<0.45$ ) with minimum crustal thickness on the path (Figures A2n, A3n, A4n, A5n, A6n) so this is not a very effective parameter for characterizing regional phase amplitude variations in this region.

Sedimentary structures may cause blockage of Lg by capturing energy or by scattering it out of the waveguide (e.g. Baumgardt and Der, 1994; Zhang *et al.*, 1994), and some of our paths do traverse areas of thick sediments in the Tarim Basin, the Junggar Basin, the Sichuan Basin, the Qaidam Basin, and Ordos (Figure 6), so we anticipated significant correlations with parameterizations of sediment thickness. However, the data display relatively weak correlations (absolute values  $< 0.38$ ) with path-averaged sediment thickness (Figures A2p, A3p, A4p, A5p, A6p), and only slightly stronger correlations (absolute values  $< 0.41$ ) with maximum sediment thickness on each path (Figures A2r, A3r, A4r, A5r, A6r). Ratios involving Lg tend to have the highest correlations, and those are in the lower frequency ranges. The localized nature of the sedimentary structures in the region, which thus affect only subsets of raypaths may preclude any general trends from emerging on a regional basis, and the low correlations do not indicate that sedimentary structures are not important on a case by case basis.

These linear regressions suggest that important waveguide parameters include mean crustal thickness, mean elevation and/or rms roughness. However, these parametric measures are not independent, and in fact, they all exhibit significant correlations with distance that must be allowed for before any physical interpretation or optimal path correction strategy can be advanced. This is also true when combinations of parameters are made, such as using the product path length times average elevation, which gives particularly high correlations.

Figure 9a illustrates the collinearity of some of the waveguide properties with propagation distance for our data set. Particularly strong linear correlations are found between mean elevation and distance and between surface roughness and distance. Given

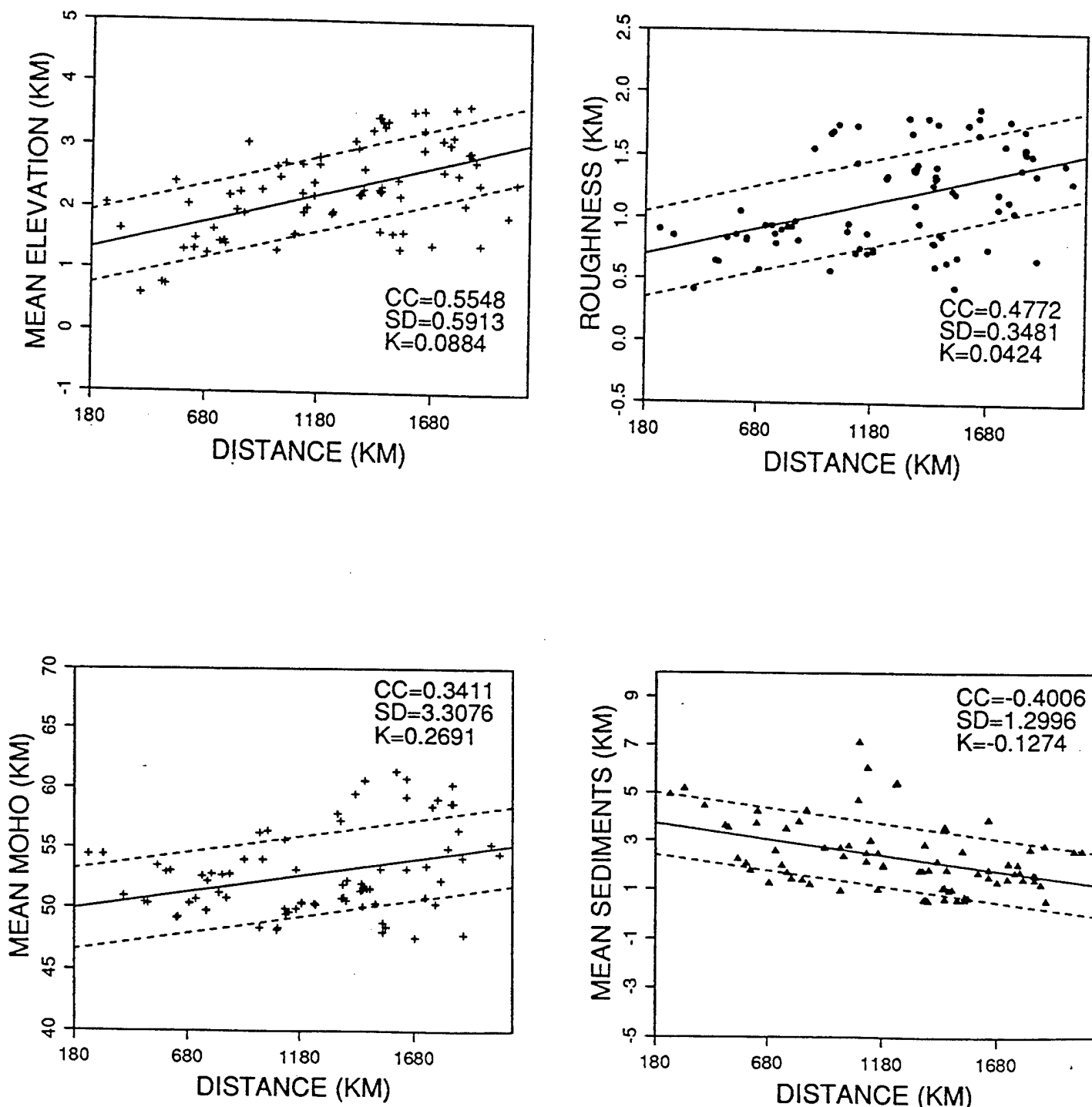


Figure 9. a) Path specific values of mean elevation, rms topographic roughness, mean crustal thickness, and mean sediment thickness as functions of propagation distance from WMQ. CC, linear correlation coefficient; SD, standard deviation of the linear regression; K, slope of the regression line. The dotted lines indicate  $\pm 1$  standard deviation about the regression line. b) Correlations between mean elevation and rms topographic roughness with mean crustal thickness (top) and rms topographic roughness and rms surface slope with mean path elevation (bottom). CC, linear correlation coefficient; SD, standard deviation of the linear regression; K, slope of the regression line. The dotted lines indicate  $\pm 1$  standard deviation about the regression line.

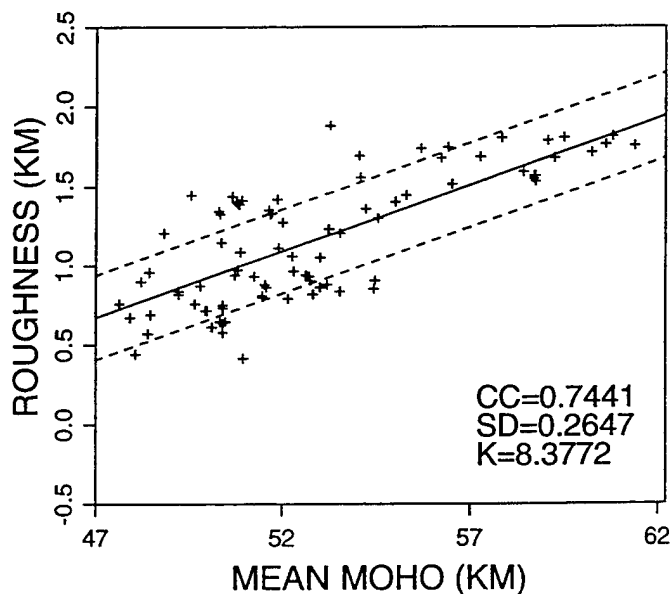
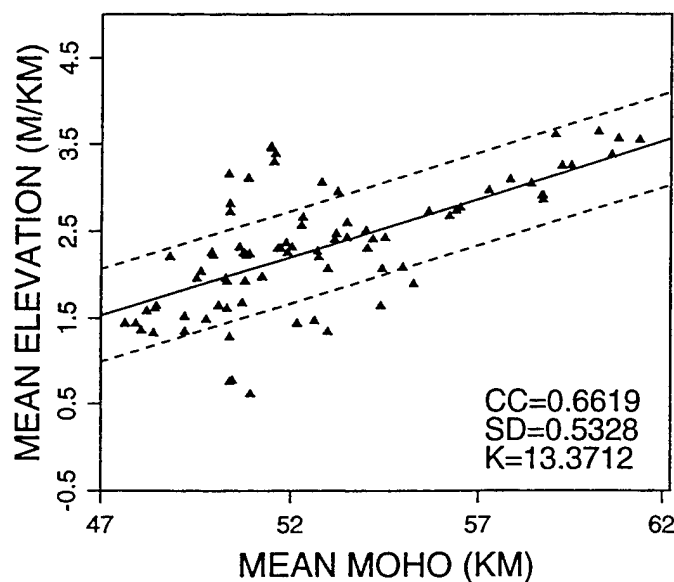
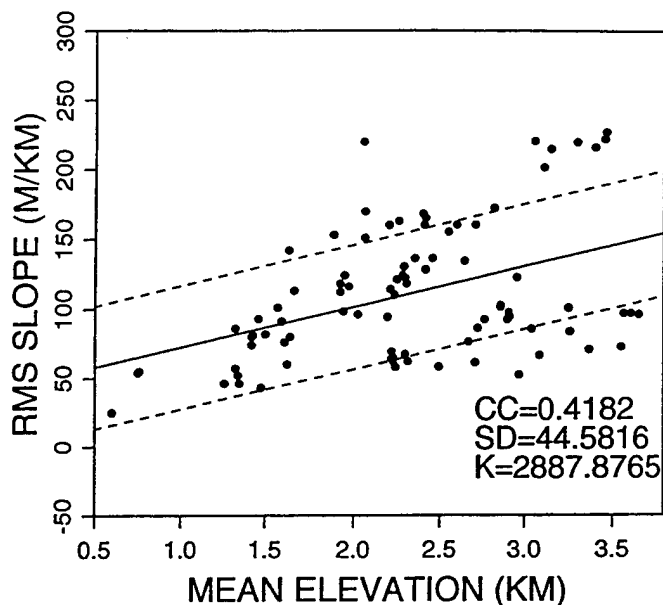
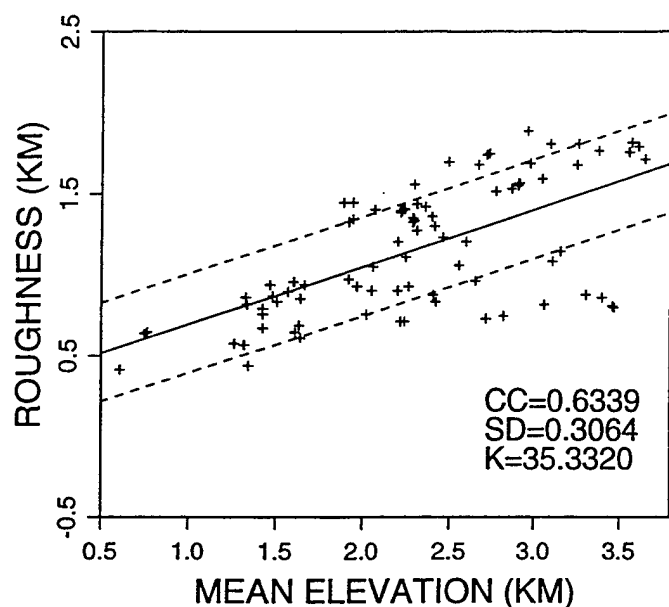


Figure 9. a) Path specific values of mean elevation, rms topographic roughness, mean crustal thickness, and mean sediment thickness as functions of propagation distance from WMQ. CC, linear correlation coefficient; SD, standard deviation of the linear regression; K, slope of the regression line. The dotted lines indicate  $\pm 1$  standard deviation about the regression line. b) Correlations between mean elevation and rms topographic roughness with mean crustal thickness (top) and rms topographic roughness and rms surface slope with mean path elevation (bottom). CC, linear correlation coefficient; SD, standard deviation of the linear regression; K, slope of the regression line. The dotted lines indicate  $\pm 1$  standard deviation about the regression line.

the common procedure of correcting discriminants for distance, the issue that arises is whether or not there is any value in correcting for more than distance. Significant correlations also exist between various parameters of waveguide structure. For example, correlations between mean crustal thickness and mean elevation or rms roughness are particularly strong, as shown in Figure 9b. This reflects isostatic compensation of the crust, as do surface roughness and slope correlations with mean elevation (Figure 9b). Previous studies have detected similar correlations between parameters (e.g. Zhang and Lay, 1994; Zhang *et al.*, 1994), which makes it difficult to isolate the physical effects controlling regional phase energy partitioning.

However, it is straightforward to test whether or not there is correlation with a given parameter after correcting for the effects of other parameters. We did this for all waveguide parameters, after correcting the various frequency dependent logarithmic amplitude ratios for the best linear dependence on distance. The "corrected" data thus correspond to those values that are typically entered into a discriminant procedure. If any of the variance in the residuals can be reduced by correction for additional parameters we would expect to see the discriminant performance improve. We find that the process of correcting for distance systematically reduces the correlations with other parameters (except in a few cases where very little correlation initially existed, such as for  $P_g/L_g$  dependence on mean sediment thickness), typically lowering the correlation coefficients by about 0.1 to 0.3. Figure 10 shows the regression for distance-corrected  $\text{Log}(P_g/L_g)$  measurements with mean crustal thickness. While the correlations are reduced in all frequency bands relative to the raw data correlations in Figure 8, significant correlation remains in the two lower frequency bands, and this can be exploited to further reduce the scatter in the data in an objective fashion. The Appendix includes results for distance correction of all five ratios, for mean elevation (Figures A2c, A3c, A4c, A5c, A6c), roughness (Figures A2e, A3e, A4e, A5e, A6e), skewness (Figures A2i, A3i, A4i, A5i, A6i), slope (Figures A2k, A3k, A4k, A5k, A6k), crustal thickness (Figures A2m, A3m, A4m, A5m, A6m), and

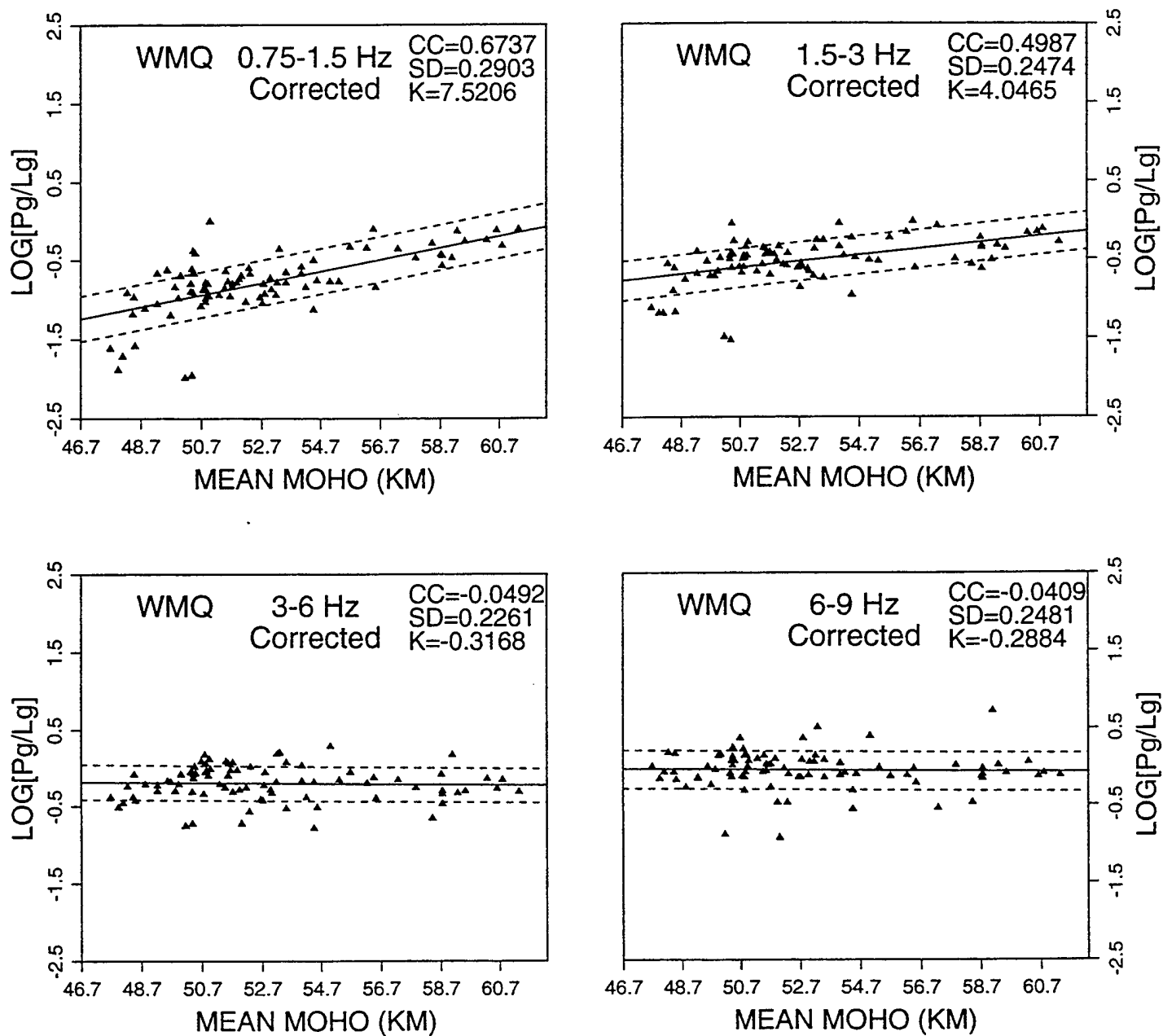


Figure 10.  $\text{Log}(P_g/L_g)$  as a function of mean crustal thickness after distance correction in various frequency bands. CC, linear correlation coefficient; SD, standard deviation of the linear regression; K, slope of the regression line. The dotted lines indicate  $\pm 1$  standard deviation about the regression line.



mean sediment thickness (Figures A2q, A3q, A4q, A5q, A6q). While covariance among the path properties still precludes identifying the controlling parameters, the two low frequency bands indicate empirical dependence (absolute value of linear correlations  $> 0.3$ , with most  $> 0.4$  and up to 0.67) on mean elevation, surface roughness, and crustal thickness, and weaker dependence (absolute value of linear correlations  $> 0.2$ ) on skewness (except for Pg/Sn and Sn/Lg), and mean sediment thickness (only for Pg/Lg and Sn/Lg).

These observations make a solid case for the potential value of empirical correction for path-specific properties beyond simple path length. In order to develop a model which explicitly accounts for (or at least allows for) collinearity of the various path parameters, we use multivariate regression analysis. Keeping in mind that our objective is to obtain a stable procedure for reducing variance in the observations, we do not need to uniquely isolate the causal effects between collinear parameters, as long as their trade-off is incorporated into the model.

## MULTIVARIATE REGRESSION

Multivariate regression allows the determination of the best set of predictor variables from a set of parametric path properties giving an empirical model minimizing the variance in the data. An initial list of variables is defined, based on the preceding separate correlation analysis, then an optimal combination is determined. Variables with such strong collinearity with the other parameters that they fail to contribute significantly to the variance reduction are excluded from the ensuing statistical analysis to minimize the model complexity. For example, maximum and minimum crustal thickness and maximum sediment thickness are not used in the multivariate regression analysis because they provide very redundant information about the shape of the Moho discontinuity and basement structure to simple (and more reliable) path-averaged values. Surface topographic slope is

excluded because it almost never had correlations with the data. We retain five parameters to characterize the path properties:  $x(1)$ , path length;  $x(2)$ , mean altitude;  $x(3)$ , rms roughness;  $x(4)$ , mean crustal thickness; and  $x(5)$ , mean sediment thickness. We construct a model in which these five parameters are initially assumed to influence a given frequency dependent regional phase ratio,  $Y$ , such as  $\text{Log}(P_g/L_g)$ , in the form

$$Y_i = \beta_0 + \beta_1 x_{i1} + \beta_2 x_{i2} + \beta_3 x_{i3} + \beta_4 x_{i4} + \beta_5 x_{i5} + e_i \quad i = 1, 2, \dots, n, \quad (1)$$

where  $Y_i$  is the  $i$ -th observation that is assumed to be a linear combination of the  $x_{i1}, x_{i2}, \dots, x_{i5}$  predictor variables with linear coefficients  $\beta_0, \beta_1, \beta_2, \dots, \beta_5$ ,  $e_i$  is the random error associated with measurement of  $Y_i$ , and  $n$  is the number of observed values. We do not always consider all 5 parameters, and if  $k$  is the number of independent variables considered, the model has  $m = k+1$  unknown parameters ( $m$  varies up to 6). The estimates of  $\beta_j$  that we obtain are indicated by  $b_j$ .

It is desirable to follow an objective procedure for limiting the number of independent parameters while still achieving near optimal variance reduction in the fit to the data. A variable selection technique commonly in use is the stepwise regression procedure, which has two possible versions; forward selection and backward elimination. In our regression model, the path parameters certainly have multicollinearity, which is mainly a problem for uniquely isolating the importance of each parameter. However, this is not all that critical in this case, for we are not attempting to extract a deterministic model for the medium. For example, when normal distance corrections are determined there is no attempt to find a model that predicts them, and the same collinearity with other path parameters ensures that this would be nonunique. Empirical path corrections need not be based on absolute models, and hence we can proceed to find a purely empirical model which gives favorable variance reduction even if some parameters are redundant or trade-off in their contributions to the fit.

To avoid some drawbacks that result from multicollinearity when applying the stepwise regression technique, we did not use backward elimination as did Zhang *et al.* (1994). Instead, we compute all possible linear regressions for our combination of 5 path parameters and then select a preferred set of best parameters for each data type based on statistical properties of the solutions. We use two common criteria: (1) the mean square error (MSE) criterion, and (2) the  $C_p$ -statistic criterion. The MSE is the residual variance:

$$MSE = \frac{SSE}{n - m} = \frac{\sum_{i=1}^n (y_i - \hat{y}_i)^2}{n - m} \quad (2)$$

where SSE represents the sum of squared residuals,  $y_i$  are observed values, and  $\hat{y}_i$  are predicted values for the model. The MSE criterion minimizes the variance, taking into account the number of parameters in the model ( $m$ ), but it does not assess the resolution or contribution of each parameter. Mallows'  $C_p$ -statistic criterion is given by:

$$C_p = \frac{SSE_p}{S_k^2} - (n - 2p) \quad (3)$$

where  $SSE_p$  is the sum of squared errors for the model obtained for a subset of  $p$  variables out of a total of  $k$  predictor variables being considered; and  $S_k^2 = MSE(x_1, x_2, \dots, x_k)$  is the estimation variance based on all  $k$  predictor variables. After all possible regression combinations are determined,  $C_p$  is computed for each case, and regressions that have  $C_p$  values close to  $p$  (i.e. low values) are the most desirable.

Table 1 lists the model coefficients found for all possible regressions for  $\text{Log}(P_g/L_g)$  data in the frequency band of 0.75 to 1.5 Hz. Table 2 gives goodness of fit criteria for all possible regressions for the same data set. Table 2 indicates that there are two models that stand out; the models with parameters  $(x_1, x_2, x_4, x_5)$  or  $(x_1, x_2, x_3, x_4, x_5)$ . Both models have high multiple coefficient of determination ( $R^2$ ), small residual variances, and small  $C_p$  values. Further analysis indicates that the second model containing all five waveguide parameters is not particularly appealing because the estimate of the regression

TABLE 1. Estimated regression coefficients for 0.75-1.5 Hz Log(P<sub>g</sub>/L<sub>g</sub>) data observed at WMQ

Predictor variables	b <sub>0</sub>	b <sub>1</sub>	b <sub>2</sub>	b <sub>3</sub>	b <sub>4</sub>	b <sub>5</sub>
-	-0.114					
x <sub>1</sub> (Distance)	-0.881	0.000596				
x <sub>2</sub> (mH)	-1.218		0.476			
x <sub>3</sub> (Roughness)	-1.161			0.895		
x <sub>4</sub> (mMoho)	-5.458				0.101	
x <sub>5</sub> (mSed.)	-0.086					-0.0123
x <sub>1</sub> , x <sub>2</sub>	-1.339	0.000254	0.387			
x <sub>1</sub> , x <sub>3</sub>	-1.345	0.000281		0.744		
x <sub>1</sub> , x <sub>4</sub>	-5.090	0.000367			0.0851	
x <sub>1</sub> , x <sub>5</sub>	-1.174	0.000692				0.0748
x <sub>2</sub> , x <sub>3</sub>	-1.425		0.267	0.592		
x <sub>2</sub> , x <sub>4</sub>	-4.234		0.257		0.666	
x <sub>2</sub> , x <sub>5</sub>	-1.500		0.524			0.0742
x <sub>3</sub> , x <sub>4</sub>	-3.796			0.510	0.0583	
x <sub>3</sub> , x <sub>5</sub>	-1.143			0.894		-0.00754
x <sub>4</sub> , x <sub>5</sub>	-5.607				0.103	0.0268
x <sub>1</sub> , x <sub>2</sub> , x <sub>3</sub>	-1.490	0.000165	0.223	0.553		
x <sub>1</sub> , x <sub>2</sub> , x <sub>4</sub>	-4.438	0.000274	0.157		0.0682	
x <sub>1</sub> , x <sub>2</sub> , x <sub>5</sub>	-1.774	0.000356	0.419			0.102
x <sub>1</sub> , x <sub>3</sub> , x <sub>4</sub>	-4.038	0.000290		0.346	0.0595	
x <sub>1</sub> , x <sub>3</sub> , x <sub>5</sub>	-1.461	0.000336		0.717		0.0338
x <sub>1</sub> , x <sub>4</sub> , x <sub>5</sub>	-5.430	0.000467			0.0857	0.0791
x <sub>2</sub> , x <sub>3</sub> , x <sub>4</sub>	-3.209		0.202	0.395	0.0409	
x <sub>2</sub> , x <sub>3</sub> , x <sub>5</sub>	-1.567		0.311	0.544		0.0419
x <sub>2</sub> , x <sub>4</sub> , x <sub>5</sub>	-4.341		0.0308		0.0637	0.0628
x <sub>3</sub> , x <sub>4</sub> , x <sub>5</sub>	-3.902			0.500	0.0600	0.0132
x <sub>1</sub> , x <sub>2</sub> , x <sub>3</sub> , x <sub>4</sub>	-3.590	0.000218	0.134	0.311	0.0477	
x <sub>1</sub> , x <sub>2</sub> , x <sub>3</sub> , x <sub>5</sub>	-1.746	0.000246	0.271	0.459		0.0659
x <sub>1</sub> , x <sub>2</sub> , x <sub>4</sub> , x <sub>5</sub>	-4.658	0.000346	0.197		0.0645	0.0907
x <sub>1</sub> , x <sub>3</sub> , x <sub>4</sub> , x <sub>5</sub>	-4.646	0.000395		0.237	0.0680	0.0646
x <sub>2</sub> , x <sub>3</sub> , x <sub>4</sub> , x <sub>5</sub>	-3.451		0.249	0.332	0.0428	0.0468
x <sub>1</sub> , x <sub>2</sub> , x <sub>3</sub> , x <sub>4</sub> , x <sub>5</sub>	-4.185	0.000324	0.180	0.164	0.0541	0.0796

TABLE 2. Goodness of fit criteria for regressions for 0.75-1.5 Hz Log(P<sub>g</sub>/L<sub>g</sub>) data WMQ

Predictor Variables	R <sup>2</sup>	SSE	VARIANCE	C <sub>p</sub>
-		19.129	0.226	-
x1 (Distance)	0.314	13.114	0.154	147.070
x2 (mH)	0.508	9.414	0.111	82.158
x3 (Roughness)	0.559	8.444	0.099	65.140
x4 (mMoho)	0.561	8.393	0.099	64.246
x5 (mSed.)	0.001	19.103	0.225	252.140
x1, x2	0.547	8.658	0.103	70.895
x1, x3	0.613	7.412	0.088	49.035
x1, x4	0.667	6.376	0.076	30.860
x1, x5	0.357	12.309	0.147	134.947
x2, x3	0.654	6.620	0.079	35.140
x2, x4	0.645	6.794	0.081	38.193
x2, x5	0.552	8.573	0.102	69.404
x3, x4	0.642	6.847	0.082	39.123
x3, x5	0.559	8.435	0.100	66.982
x4, x5	0.568	8.273	0.098	64.140
x1, x2, x3	0.670	6.313	0.076	31.754
x1, x2, x4	0.691	5.914	0.071	24.754
x1, x2, x5	0.623	7.205	0.087	47.404
x1, x3, x4	0.699	5.753	0.069	21.930
x1, x3, x5	0.621	7.256	0.087	48.298
x1, x4, x5	0.714	5.477	0.066	17.088
x2, x3, x4	0.689	5.940	0.072	25.211
x2, x3, x5	0.667	6.370	0.077	32.754
x2, x4, x5	0.676	6.197	0.075	29.719
x3, x4, x5	0.644	6.819	0.082	40.632
x1, x2, x3, x4	0.717	5.422	0.066	18.123
x1, x2, x3, x5	0.698	5.769	0.070	24.211
x1, x2, x4, x5	0.751	4.763	0.058	6.579
x1, x3, x4, x5	0.727	5.214	0.064	14.474
x2, x3, x4, x5	0.706	5.630	0.069	21.772
x1, x2, x3, x4, x5	0.757	4.644	0.057	6.474

coefficient for the  $x(3)$  term has a standard deviation which is quite large ( $0.164 \pm 0.113$ ), and the partial F-statistic for this coefficient  $F(\beta_j = 0)$  value is 2.10, smaller than 2.77, the 10% right-tail point of  $F(0.90, 1, 81)$ , indicating that we cannot reject at the 90% confidence level the null hypothesis that  $\beta_3 = 0$ . In contrast, the four-parameter model has satisfactory accuracy in the estimates of all model coefficients and passed an F-test of the overall regression model, for whether at least one of the coefficients is zero. Table 3 lists the model parameters for this case. All partial  $F(\beta_j = 0)$  values are greater than 6.96, the 1% right-tail point of  $F(0.99, 1, 82)$ , thus the model passed all partial F-tests, indicating that the null hypothesis that  $\beta_j = 0$  can be rejected with 99% confidence. In addition, all t-statistics are substantially greater than rejection points at 99.9% confidence level, indicating the  $\beta_j$  is nonzero and the four model parameters are related to the amplitude ratio being considered. If we perform a formal stepwise backward elimination we obtain the same model. Thus, a model which includes the four path parameters, distance, mean altitude, mean crustal thickness, and mean sediment thickness, is preferred. This model explains 75.1% of the total variation in the 87 amplitude  $\text{Log}(P_g/L_g)$  measurements for the frequency band 0.75 to 1.5 Hz.

The primary objective here is to reduce the scatter in the data, and it is helpful to visualize the reduction that occurs for various parameter combinations. Figure 11 displays the scatter in the raw and corrected data for various models obtained by multiple regression. The observations are plotted as a function of magnitude, and ideally there should be no magnitude dependence (none is observed) and as little range of observations as possible (so that an outlying explosion signal could be detected). Noting the large scatter in the raw measurements, it is clear that for this low frequency band, effective source discrimination will be very problematic without path corrections. Standard distance correction gives a significant, 31% variance reduction, but this is actually smaller than that achieved by correcting for just mean path elevation (50% variance reduction), or mean crustal thickness (65% reduction). The added value of multiple parameter regressions is also apparent, with

Table 3. The best set of predictor variables for 0.75-1.5 Hz Pg/Lg data at WMQ

Variable	Estimated $b_j$	Standard Deviation	$F(\beta_j=0)$	$t(\beta_j=0)$
x( 1 )	0.000364	0.0000733	24.7	4.97
x( 2 )	0.197	0.0562	12.3	3.51
x( 4 )	0.0645	0.00996	42.0	6.48
x( 5 )	0.0907	0.0204	19.8	4.45
Intercept	-4.658			

$$R^2 = 0.751 \quad R_a^2 = 0.739$$

The Total Sum of Square (SST) = 19.129

The Error Sum of Square (SSE) = 4.763

The Error Mean Square (MSE) = 0.058

Standard Deviation = 0.241

Number of Observation= 87  $F(4, 82) = 61.834$

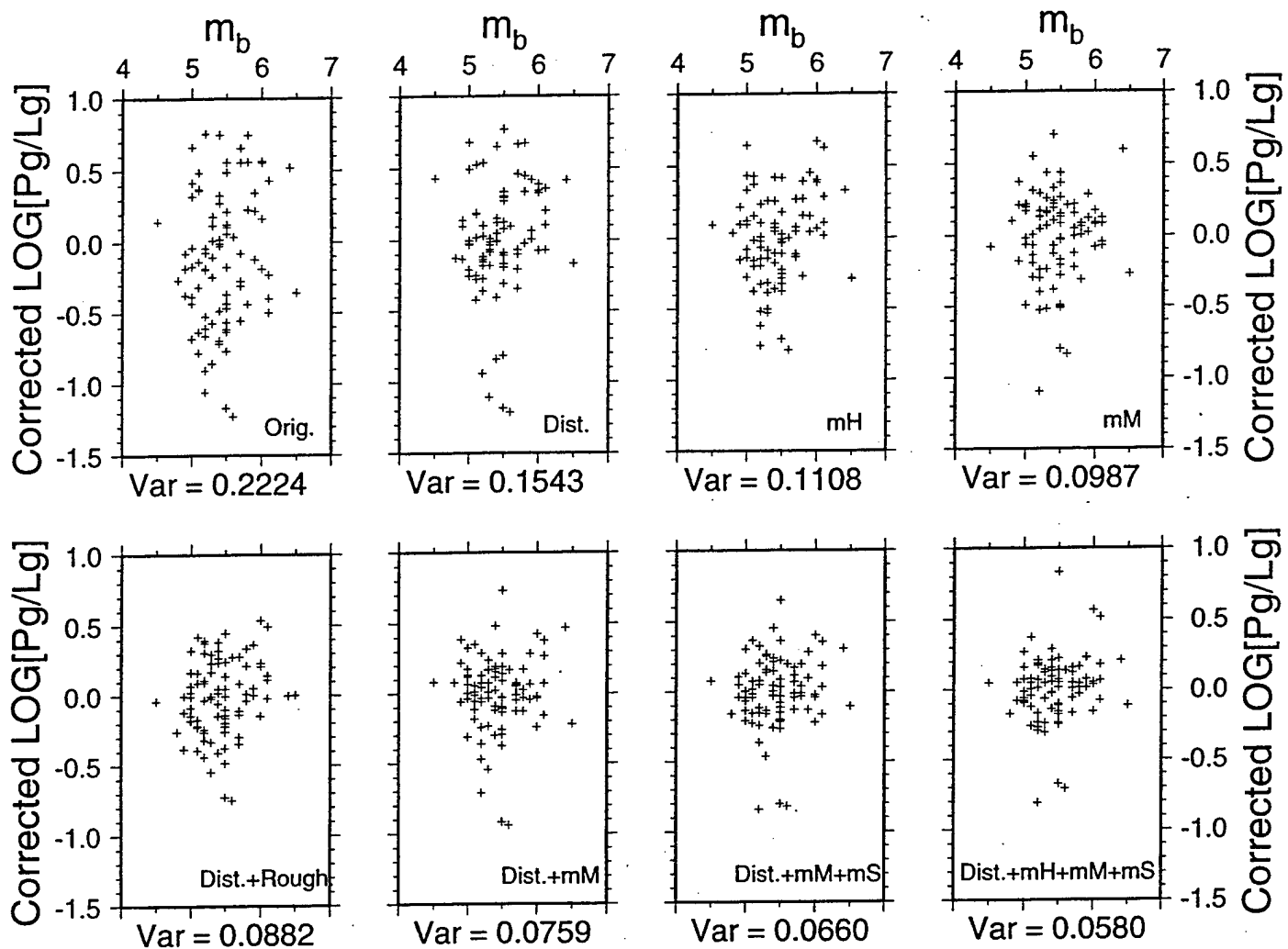


Figure 11.  $\text{Log}(P_g/L_g)$  measurements in the frequency band of 0.75 to 1.5 Hz as a function of event magnitude with various level of propagation correction. Orig., observed data; Dist., corrected for path length; mH, corrected for mean altitude on each path; mM, corrected for mean crustal thickness on each path; Dist.+Rough., corrected for a two-parameter model involving distance and rms roughness; Dist.+mM, corrected for a two-parameter model involving distance and mean crustal thickness; Dist.+mM+mS, corrected for a three parameter model involving distance, mean crustal thickness, and mean sediment thickness; Dist.+mH+mM+mS, corrected for a four parameter model involving distance, mean altitude, mean crustal thickness, and mean sediment thickness. In each case the variance of the observations is indicated below the plot by Var.



two parameter models doubling the variance reduction relative to simple distance corrections, while the preferred four parameter model gives 74% variance reduction, more than twice that of the standard distance correction. Figure 12 portrays the same results as histograms of observations, corrected for various models. The initial data distribution evolves toward an increasingly symmetric, normal distribution with decreasing standard deviation as the model complexity increases.

Qualitatively similar results are found for the lowest frequency band for other phase ratios, as well as for frequencies from 1.5 to 3.0 Hz. The results of multiple regressions for the Pg/Lg observations in the 1.5 to 3.0 Hz band are summarized in Table 4, and the details of the best model are given in Table 5 (results for other phase pairs will be presented in a separate paper). Similar to the lower frequency band, distance correction alone reduces the variance by 42%, while mean path elevation and mean roughness provide better variance reduction on their own. A 4-parameter model involving distance, mean elevation, surface roughness and mean sedimentary layer thickness provides the best overall variance reduction (70%), with all coefficients passing the partial  $F(\beta_j = 0)$  and  $t$ -tests (Table 5). While the overall variance reduction from the additional path parameters is reduced somewhat in this band relative to the lowest frequency band (as expected, given the decreasing correlations observed as frequency increases in Figures 7, 8 and 10), the improvement relative to distance correction alone is still significant. The residual variance of the observations for this model is 74% of that for the best fitting model in the 0.75-1.5 Hz band.

Higher frequency ( $>3$  Hz) observations exhibit weaker dependence on path properties for all of the phase ratios, but path correction procedures can still reduce the scatter, improving discrimination. The results of multiple regressions for the Pg/Lg observations in the 3.0-6.0 Hz band are shown in Table 6. In this case, distance is the best single parameter for correction, giving a 20% variance reduction, but a multiple-regression model involving distance, mean elevation, mean roughness, and mean crustal

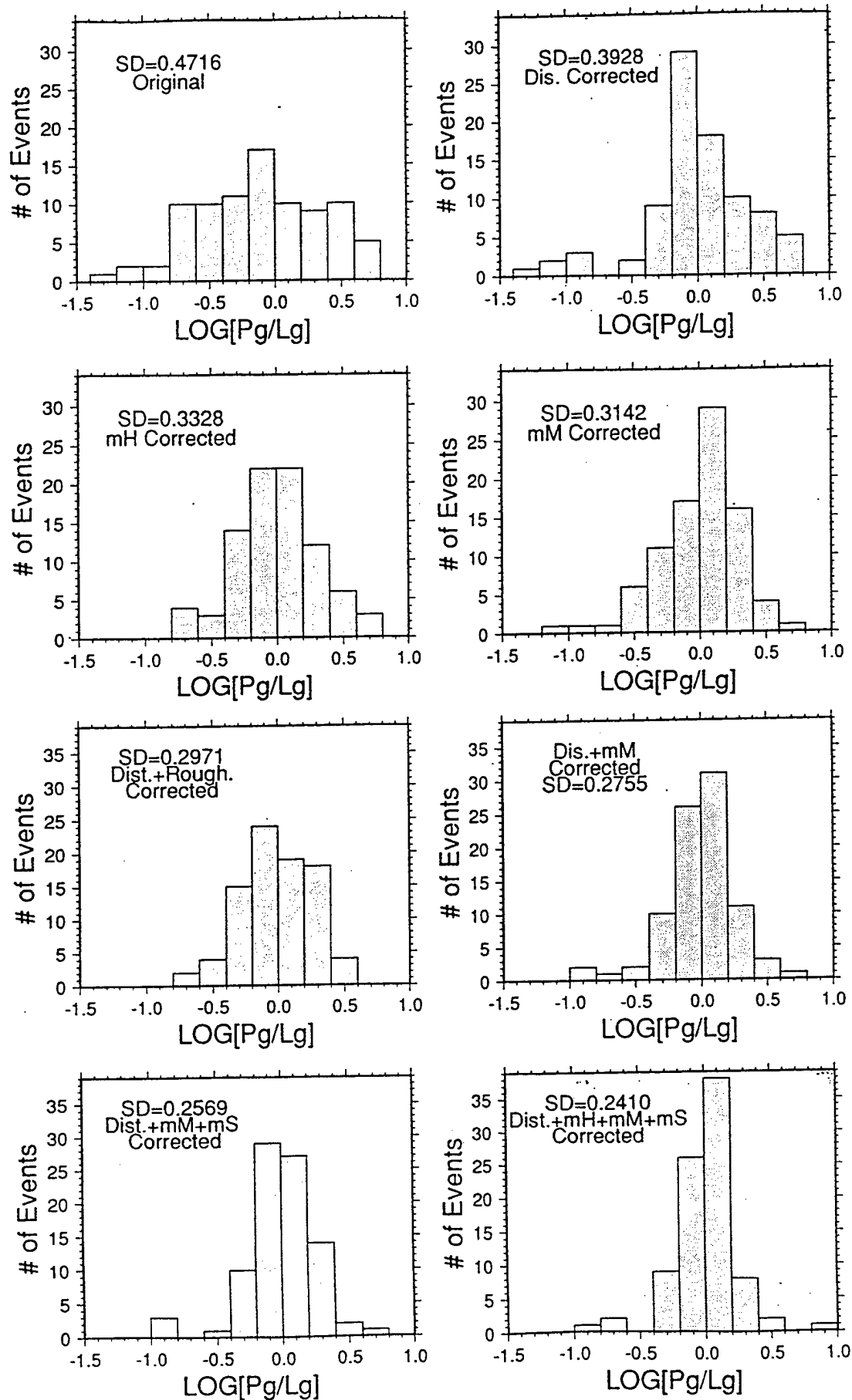


Figure 12. Histograms showing sample distributions of raw and corrected  $\text{Log}(\text{Pg}/\text{Lg})$  measurements for the same models as in Figure 11. The standard deviation of each population is given by SD.

TABLE 4. Goodness of fit criteria for regressions for 1.5-3.0 Hz Log(Pg/Lg) data at WMQ.

Predictor Variables	R <sup>2</sup>	SSE	Variance	C <sub>p</sub>
-		12.171	0.1415	
x <sub>1</sub> (Distance)	0.431	6.928	0.0815	77.742
x <sub>2</sub> (mH)	0.477	6.360	0.0748	65.563
x <sub>3</sub> (Roughness)	0.528	5.747	0.0676	50.341
x <sub>4</sub> (mMoho)	0.360	7.789	0.0916	98.719
x <sub>5</sub> (mSed.)	0.006	12.094	0.1423	197.603
x <sub>1</sub> , x <sub>2</sub>	0.585	5.050	0.0601	36.169
x <sub>1</sub> , x <sub>3</sub>	0.652	4.236	0.0504	17.283
x <sub>1</sub> , x <sub>4</sub>	0.591	4.979	0.0593	34.522
x <sub>1</sub> , x <sub>5</sub>	0.471	6.438	0.0766	68.374
x <sub>2</sub> , x <sub>3</sub>	0.617	4.667	0.0556	27.283
x <sub>2</sub> , x <sub>4</sub>	0.514	5.919	0.0705	56.332
x <sub>2</sub> , x <sub>5</sub>	0.502	6.059	0.0721	59.580
x <sub>3</sub> , x <sub>4</sub>	0.536	5.651	0.0673	50.114
x <sub>3</sub> , x <sub>5</sub>	0.532	5.695	0.0678	51.135
x <sub>4</sub> , x <sub>5</sub>	0.360	7.787	0.0927	99.673
x <sub>1</sub> , x <sub>2</sub> , x <sub>3</sub>	0.684	3.842	0.0463	10.142
x <sub>1</sub> , x <sub>2</sub> , x <sub>4</sub>	0.627	4.542	0.0547	26.383
x <sub>1</sub> , x <sub>2</sub> , x <sub>5</sub>	0.652	4.237	0.0510	19.306
x <sub>1</sub> , x <sub>3</sub> , x <sub>4</sub>	0.661	4.121	0.0496	16.615
x <sub>1</sub> , x <sub>3</sub> , x <sub>5</sub>	0.662	4.109	0.0495	16.336
x <sub>1</sub> , x <sub>4</sub> , x <sub>5</sub>	0.634	4.451	0.0536	24.271
x <sub>2</sub> , x <sub>3</sub> , x <sub>4</sub>	0.617	4.661	0.0562	29.143
x <sub>2</sub> , x <sub>3</sub> , x <sub>5</sub>	0.620	4.620	0.0557	28.193
x <sub>2</sub> , x <sub>4</sub> , x <sub>5</sub>	0.533	5.679	0.0684	52.763
x <sub>3</sub> , x <sub>4</sub> , x <sub>5</sub>	0.538	5.623	0.0677	51.464
x <sub>1</sub> , x <sub>2</sub> , x <sub>3</sub> , x <sub>4</sub>	0.685	3.833	0.0467	11.933
x <sub>1</sub> , x <sub>2</sub> , x <sub>3</sub> , x <sub>5</sub>	0.711	3.520	0.0429	4.671
x <sub>1</sub> , x <sub>2</sub> , x <sub>4</sub> , x <sub>5</sub>	0.685	3.838	0.0467	12.049
x <sub>1</sub> , x <sub>3</sub> , x <sub>4</sub> , x <sub>5</sub>	0.678	3.915	0.0477	13.835
x <sub>2</sub> , x <sub>3</sub> , x <sub>4</sub> , x <sub>5</sub>	0.621	4.616	0.0563	30.100
x <sub>1</sub> , x <sub>2</sub> , x <sub>3</sub> , x <sub>4</sub> , x <sub>5</sub>	0.713	3.489	0.0431	5.951

Table 5. The best set of predictor variables for 1.5-3.0 Hz Log(Pg/Lg) data at WMQ.

Variable	$b_j$	Standard Deviation	$F(b_j=0)$	$t(b_j=0)$
x( 1 )	0.000333	0.0000658	25.6	5.06
x( 2 )	0.171	0.0461	13.7	3.70
x( 3 )	0.324	0.0794	16.7	4.09
x( 5 )	0.0507	0.0185	7.49	2.74
Intercept	-1.226			

$$R^2 = 0.711 \quad R_a^2 = 0.697$$

The Total Sum of Square (SST)= 12.171

The Error Sum of Square (SSE)= 3.520

The Error Mean Square (MSE)= 0.043

Standard Deviation= 0.207

Number of Observation= 87  $F(4, 82) = 50.375$

TABLE 6. Goodness of fit criteria for regressions for 3.0-6.0 Hz Log(Pg/Lg) data at WMQ.

Predictor Variables	R <sup>2</sup>	SSE	Variance	C <sub>p</sub>
-		5.489	0.0638	
x <sub>1</sub> (Distance)	0.207	4.354	0.0512	20.667
x <sub>2</sub> (mH)	0.162	4.601	0.0541	26.548
x <sub>3</sub> (Roughness)	0.168	4.568	0.0537	25.762
x <sub>4</sub> (mMoho)	0.012	5.420	0.0638	46.048
x <sub>5</sub> (mSed.)	0.011	5.430	0.0639	46.286
x <sub>1</sub> , x <sub>2</sub>	0.239	4.176	0.0497	18.428
x <sub>1</sub> , x <sub>3</sub>	0.255	4.090	0.0487	16.381
x <sub>1</sub> , x <sub>4</sub>	0.209	4.342	0.0517	22.381
x <sub>1</sub> , x <sub>5</sub>	0.214	4.313	0.0513	21.690
x <sub>2</sub> , x <sub>3</sub>	0.202	4.382	0.0522	23.333
x <sub>2</sub> , x <sub>4</sub>	0.204	4.367	0.0520	22.976
x <sub>2</sub> , x <sub>5</sub>	0.163	4.596	0.0547	28.428
x <sub>3</sub> , x <sub>4</sub>	0.252	4.108	0.0489	16.810
x <sub>3</sub> , x <sub>5</sub>	0.177	4.517	0.0538	26.548
x <sub>4</sub> , x <sub>5</sub>	0.020	5.378	0.0640	47.048
x <sub>1</sub> , x <sub>2</sub> , x <sub>3</sub>	0.261	4.055	0.0489	17.548
x <sub>1</sub> , x <sub>2</sub> , x <sub>4</sub>	0.277	3.967	0.0478	15.452
x <sub>1</sub> , x <sub>2</sub> , x <sub>5</sub>	0.252	4.107	0.0495	18.786
x <sub>1</sub> , x <sub>3</sub> , x <sub>4</sub>	0.335	3.652	0.0440	7.952
x <sub>1</sub> , x <sub>3</sub> , x <sub>5</sub>	0.256	4.082	0.0492	18.190
x <sub>1</sub> , x <sub>4</sub> , x <sub>5</sub>	0.216	4.302	0.0518	23.429
x <sub>2</sub> , x <sub>3</sub> , x <sub>4</sub>	0.349	3.571	0.0430	6.024
x <sub>2</sub> , x <sub>3</sub> , x <sub>5</sub>	0.202	4.379	0.0528	25.262
x <sub>2</sub> , x <sub>4</sub> , x <sub>5</sub>	0.207	4.354	0.0525	24.667
x <sub>3</sub> , x <sub>4</sub> , x <sub>5</sub>	0.277	3.968	0.0478	15.476
x <sub>1</sub> , x <sub>2</sub> , x <sub>3</sub> , x <sub>4</sub>	0.380	3.402	0.0415	4.000
x <sub>1</sub> , x <sub>2</sub> , x <sub>3</sub> , x <sub>5</sub>	0.266	4.031	0.0492	18.976
x <sub>1</sub> , x <sub>2</sub> , x <sub>4</sub> , x <sub>5</sub>	0.294	3.876	0.0473	15.286
x <sub>1</sub> , x <sub>3</sub> , x <sub>4</sub> , x <sub>5</sub>	0.335	3.647	0.0445	9.833
x <sub>2</sub> , x <sub>3</sub> , x <sub>4</sub> , x <sub>5</sub>	0.352	3.559	0.0434	7.738
x <sub>1</sub> , x <sub>2</sub> , x <sub>3</sub> , x <sub>4</sub> , x <sub>5</sub>	0.380	3.400	0.0420	5.952

thickness provides a 35% variance reduction, with all coefficients being statistically significant at a 99% confidence level. It is particularly notable that the residual variance for the preferred 4-parameter model is essentially identical to that for the preferred 4-parameter model for the 1.5-3 Hz band. This indicates that we are indeed achieving the optimal reduction of variance in the lower frequency band, and discrimination may be equally good across the passband for this data set. Comparable results are found for the other ratios (to be presented elsewhere). The 6-9 Hz band displays very little dependence on path parameters, and we do not show results for that case as we believe that our signal-to-noise ratios are marginal. It may be, however, that when data sets for more localized source regions are considered both distance and other effects may be significant at high frequency. Alternatively, in some regions, no corrections may be warranted, depending on the nature of the regional propagation. Our recommendation is that every station/region be treated on a case by case basis, with multiple regression analysis be explored in each case and the resulting used when the model reduces the variance favorably. Modeling efforts need to be undertaken to place the empirical correlations on a sound physical basis.

## DISCUSSION AND CONCLUSIONS

While the reduction in variance associated with the multiple regression analysis for Pg/Lg phases recorded at WMQ is very encouraging, it must be emphasized that the corresponding model is empirical, is unlikely to generalize because of the extreme path complexity in the region, and is only useful for the frequency bands lower than 3 Hz. The empirical nature of the model is not very troubling, as the same can be said for all standard distance-correction procedures, although they are often motivated by quantitative wavefield behavior in one-dimensional models. The other path attributes considered explicitly require three-dimensional modeling which has not been performed extensively, but the general tendencies are consistent with past empirical and two-dimensional modeling efforts. The

fact that the path complexity around WMQ is very acute, particularly for partial and total blockage of  $L_g$  phases from events in the Tibetan Plateau, is a realistic fact of life for CTBT monitoring. We often will have only a few stations in tectonically complex regions and must have procedures that allow for great path complexity. However, we do expect that different waveguide parameters may emerge as most important in regions of less crustal heterogeneity, and in some cases standard correction for path length may be all that is warranted. The lack of strong path (or distance) dependence of the higher frequency ratios is interesting, as it has commonly been found that discrimination is poor at low frequencies and improves above 3 Hz. Improving the performance at low frequencies is thus highly desirable, and factor of 2 to 3 reductions in the scatter of discriminant measures for an earthquake population should help directly. Again, this is particularly important for tectonically active areas, where strong attenuation may constrain the observed bandwidth of regional phases to lower frequencies.

All of the regional phase amplitude ratios considered;  $P_n/L_g$ ,  $P_g/L_g$ ,  $P_n/S_n$ ,  $P_g/S_n$ , and  $S_n/L_g$ , exhibit frequency dependent variations with propagation distance, and correction for this effect is necessary for discrimination. However, as we have shown, the uncorrected data sometimes correlate better with specific path waveguide properties than they do with distance. This leaves open the issue of what are the controlling effects on regional phases, with factors that are probably important being geometric spreading, attenuation, scattering, sedimentary basins, changes in Moho depth, rough surface topography, and internal crustal structure. There is a need for extensive modeling of realistic (3-dimensional) crustal waveguides with structure at a wide variety of scale lengths, if we are to fully understand the nature of these regional phases.

The WMQ data exhibit significant  $L_g$  blockage, and much of the value of correction for path-specific wave guide properties stems from effects of the Tibetan Plateau. Current discriminant calibration procedures are not well defined, but appear to either screen data based on defined regions of phase blockage (hoping that some other discriminant can be

applied in those regions), or to develop separate distance relations in regionalized areas that have baseline shifts in their regional phase energy partitioning. The systematic relationships observed in this study between distance-corrected regional discriminants and parameters of the wave guide structure suggests that blockage effects involve a continuum of effects rather than bimodal behavior. A regional discriminant calibration strategy that invokes multivariate regression analysis of several path properties such as mean crustal thickness and mean altitude allows all data at a given station in a complex region to be calibrated uniformly, without appealing to separate, possibly poorly constrained, distance corrections for discrete subregions. This can readily be implemented in a CTBT monitoring system. The extent to which it provides high confidence discrimination needs to be further tested, but the basic strategy appears promising.

#### ACKNOWLEDGMENTS

We thank Drs. S. Taylor and H. Hartse of the Los Alamos National Laboratory for providing access to their data for WMQ prior to publication. We thank Dr. Tian-run Zhang for discussions and for providing some of his software. This research was supported by Phillips Laboratory Contract No. F19628-95-K-0014, and by IGPP-LANL UCRP grant #609. This is the contribution #320, the Institute of Tectonics, University of California, Santa Cruz.



## References

- Baumgardt, D. R. (1990). Investigation of teleseismic Lg blockage and scattering using regional arrays, *Bull. Seism. Soc. Am.*, **80**, 2261-2281.
- Baumgardt, D. R., and Z. Der (1994). Investigation of the transportability of the P/S ratio discriminant to different tectonic regions, *Sci. Report 1, PL-TR-94-2299*, ENSCO, Inc., Springfield, Virginia, ADA292944.
- Bennett, J. M. and L. Mattsson (1989). *Introduction to surface roughness and scattering*. Optical Society of America, Washington, D.C.
- Bostock, M. G. and B. L. N. Kennett (1990). The effects of 3-D structure on Lg propagation pattern, *Geophys. J. Int.* **101**, 355-365.
- Campillo, M., B. Feignier, M. Bouchon, and N. Bethoux (1993). Attenuation of crustal waves across the Alpine range, *J. Geophys. Res.*, **98**, 1987-1996.
- Fielding, E. J., B. L. Isacks, and M. Barazangi (1992). A geological and geophysical information system for Eurasia, *Tech. Report 2, F29601-91-K-DB08*, Phillips Lab., Hanscom Air Force Base, Mass.
- Gupta, I. N., W. W. Chan, and R. A. Wagner (1992). A comparison of regional phase from underground nuclear explosions at East Kazakh and Nevada test sites, *Bull. Seism. Soc. Am.* **82**, 352-382.
- Hartse, H. E., S. R. Taylor, W. S. Phillips, and G. E. Randall (1996). A preliminary study of regional seismic discrimination in central Asia with emphasis on western China, *Bull. Seism. Soc. Am.*, in press.
- Hirn, A., A. Nercessian, M. Sapin, G. Jobert, Z. Xu, E. Gao, D. Lu, and J. Teng (1984). Lhasa block and bordering suture--a continuation of a 500-km Moho traverse through Tibet, *Nature*, **307**, 25-27.
- Kadinsky-Cade, K., M. Barazangi, J. Oliver, and B. Isacks (1981). Lateral variations of high-frequency seismic wave propagation at regional distances across the Turkish and Iranian Plateau, *J. Geophys. Res.*, **86**, 9377-9396.

- Kennett, B. L. N. (1986). Lg waves and structural boundaries, *Bull. Seism. Soc. Am.* **76**, 1133-1141.
- Kennett, B. L. N. (1989). On the nature of regional seismic phases - I. Phase representations for P<sub>n</sub>, P<sub>g</sub>, S<sub>n</sub>, L<sub>g</sub>, *Geophys. J.*, **98**, 447-456.
- Kennett, B. L. N. (1993). The distance dependence of regional phase discriminants, *Bull. Seism. Soc. Am.* **83**, 1155-1166.
- Kunin, N. Y. (1987). Distribution of sedimentary basins of Eurasia and the volume of the Earth's sedimentosphere, *Int. Geol. Rev.*, **22**, 1257-1264.
- Kunin, N. Y., and E. R. Sheykh-Zade (1983). New data on lateral inhomogeneities in the upper mantle under western Eurasia, *Dokl. Akad. Nauk. USSR*. **273**, 1087-1091.
- Kvaerna, T. and D. J. Doornbos (1991). Scattering of regional P<sub>n</sub> by Hoho topography, *Geophys. Res. Lett.*, **18**, 1273-1276.
- McCormack, D. A., K. F. Priestley, and H. J. Patton (1995). Distance effects on regional discriminants along a seismic profile in northwest Nevada: NPE and nuclear results, submitted to *Bull. Seism. Soc. Am.*
- McNamara, D. E., T. J. Owens, and W. R. Walter (1996). Propagation characteristics of L<sub>g</sub> across the Tibetan plateau, *Bull. Seism. Soc. Am.*, **86**, 457-469.
- Ni, J., and M. Barazangi (1983). High-frequency seismic wave propagation beneath the Indian Shield, Himalayan Arc, Tibetan Plateau and surrounding regions: high uppermost mantle velocities and efficient S<sub>n</sub> propagation beneath Tibet, *Geophys. J. R. astr. Soc.* **72**, 665-689.
- Press, F., and M. Ewing (1952). Two slow surface waves across North America, *Bull. Seism. Soc. Am.*, **42**, 219-228.
- Ringdal, F., P. D. Marshall, and R. W. Alewine (1992). Seismic yield determination of Soviet underground nuclear explosions at the Shagan River test site, *Geophys. J. Int.* **109**, 65-77.

- Rodgers, A. J., J. F. Ni, and T. M. Hearn (1996). Propagation characteristics of short period  $S_n$  and  $L_g$  in the Middle East, submitted to *Bull. Seism. Soc. Am.*
- Rodgers, A. J., T. Lay, W. R. Walter, and K. M. Mayeda (1997). A comparison of regional phase amplitude ratio measurement techniques, *Bull. Seism. Soc. Am.*, submitted.
- Ruzaikin, A. I., I. L. Nersesov, V. I. Khalturin, and P. Molnar (1977). Propagation of  $L_g$  and lateral variations in crustal structure in Asia, *J. Geophys. Res.*, **82**, 307-316.
- Sereno, T. J. (1991). Simulation of the detection and location capability of regional seismic networks in the Soviet Union, *Final Report*, SAIC-91/1061, San Diego, California.
- Shih, X. R., K. -Y. Chun, and T. Zhu (1994). Attenuation of 1-6 s  $L_g$  waves in Eurasia, *J. Geophys. Res.*, **99**, 23,859-23,874.
- Taylor, S. R. (1996). Analysis of high-frequency  $P_n/L_g$  ratios from NTS explosions and western U.S. earthquakes, *Bull. Seism. Soc. Am.* **86**, 1042-1053.
- Walter, W. R., K. M. Mayeda, and H. Patton (1995). Phase and spectral ratio discrimination between NTS earthquakes and explosions. Part I: Empirical observations, *Bull. Seism. Soc. Am.* **85**, 1050-1067.
- Wessel, P., and W.H.F. Smith (1991). Free software helps map and display data, *EOS* **72**, 441-445.
- Zhang, T.-R., and T. Lay (1994). Analysis of short-period regional phase path effects associated with topography in Eurasia, *Bull. Seism. Soc. Am.* **84**, 119-132.
- Zhang, T.-R., and T. Lay (1995). Why the  $L_g$  phase does not traverse oceanic crust, *Bull. Seism. Soc. Am.* **85**, 1665-1678.
- Zhang, T.-R., S. Schwartz, and T. Lay (1994). Multivariate analysis of waveguide effects on short-period regional wave propagation in Eurasia and its application in seismic discrimination, *J. Geophys. Res.*, **99**, 21,929-21,945.

# Comparison of Regional Phase Amplitude Ratio Measurement Techniques

Arthur J. Rodgers<sup>1</sup>, Thorne Lay<sup>2</sup>, William R. Walter<sup>1</sup> and Kevin M. Mayeda<sup>1</sup>

<sup>1</sup> *Earth Sciences Division,  
Lawrence Livermore National Laboratory, Livermore, California, USA*

<sup>2</sup> *Earth Sciences Department and Institute of Tectonics,  
University of California, Santa Cruz, USA*

Manuscript in preparation for *BSSA*, March 12, 1997

## Abstract

Regional phase amplitude ratio measurements are useful for discriminating earthquakes from explosions and will be essential for seismic monitoring of a Comprehensive Test Ban Treaty (CTBT). However, such measurements have been made in various ways, complicating comparison of different studies. We evaluate several regional phase amplitude ratio measurement procedures. Amplitude measurements are made on both original velocity-proportional broadband seismograms and instrument-deconvolved displacement seismograms in the time and frequency domains. Pn/Lg and Pg/Lg ratios are measured on vertical component waveforms for regional earthquakes observed at the Global Seismic Network (GSN) station ABKT (Alibek, Turkmenistan). Time domain amplitude measurements are made for narrow band filtered waveforms using signal energy measures given by the absolute mean, rms, and envelope mean, and peak measures given by the absolute maximum and envelope maximum. Frequency domain measurements are made by computing the log-mean amplitude within a narrow band from the broadband spectrum of each windowed phase.

Time domain amplitude ratios for raw velocity and instrument deconvolved displacement seismograms are very similar (linear correlations  $\geq 0.97$ ), indicating that the instrument response does not affect the time domain measurements for the broadband GSN data. Time domain amplitude ratios made using the energy or peak measures are well correlated among themselves (linear correlations  $\geq 0.97$ ). However, the energy and peak measures are slightly less well correlated with each other (linear correlations

between 0.87-0.99). For the time domain measures, the correlations generally degrade and the scatter increases for the higher frequency bands. Time and frequency domain measurements are well correlated for the lowest frequency band (0.75-1.5 Hz). However, as the frequency band increases, the correlation decreases and the slope deviates from 1.0. Time domain amplitude ratios (for both Pn/Lg and Pg/Lg) are consistently larger than the frequency domain amplitude ratios. Investigation of the frequency spectra of broadband and narrow band filtered phases revealed that significant energy from outside the pass band, particularly from lower frequencies, possibly biases the time domain measurements. For the highest frequency pass band (6.0-9.0 Hz), deconvolution of the instrument response causes differences between the broadband and filtered spectra. Better agreement between time and frequency domain measurements is found when linear-averaging of the spectrum is used. These observations suggest that log averaged frequency domain measurements are favorable over time domain measurements because: 1) frequency domain measurements offer complete control of which frequencies are used; and 2) log-averaging of the spectra does not over-weight spectral amplitudes associated with lower frequencies within the pass band. Furthermore, spectral measurements are computationally more efficient and convenient for automation than time domain measurements.

## Introduction

Regional broadband seismic data have proven to be effective for discriminating explosions from natural earthquakes. Discrimination at regional distance is especially critical for smaller events ( $m_b \leq 4.5$ ) as these events may not be detected and discriminated teleseismically (Blandford, 1981; Pomeroy et al., 1982). Amplitude and spectral ratios of regional phases, particularly Pn, Pg and Lg, have been shown to separate explosion and earthquake populations in many cases (e.g. Taylor et al., 1988; Walter et al., 1995; Hartse et al., 1996). Complicating the situation, however, are path effects. Regional variations in geologic, tectonic and topographic structure lead to great variability in regional phase amplitudes. Furthermore, recordings of regional events can be noisy due to poor signal excitation and attenuation, especially at high frequencies and distances greater than several hundred kilometers. Nonetheless, measurements of regional phase amplitude ratios can provide a valuable tool for identifying small seismic events under the Comprehensive Test Ban Treaty (CTBT) provided that variations in earthquake generated regional phases are determined for each monitoring station and region. Efforts are under way to map variations in regional phase amplitude

ratios and to understand the path effects in support of CTBT monitoring.

Complicating comparison of various results, however, is the fact that regional phase amplitude measurements have been made in a number of ways, including techniques operating in either the time or frequency domain. Time domain measures have been made on filtered and windowed phases such as peak amplitudes, rms amplitudes and envelope measures (e.g. Nuttli, 1980; Zhang and Lay, 1994; Hartse, et al., 1996). Alternatively, frequency domain measures have been used (e.g. Taylor et al., 1989; Walter et al., 1995). Also, time domain measurements can be made on raw velocity or instrument deconvolved displacement seismograms. Thus, it is important to know if results obtained from different measurement methodologies agree or not and, if they do not, to understand why.

In this study we investigated the process of making regional phase amplitude ratio measurements. Pn/Lg and Pg/Lg amplitude ratios were computed using both time and frequency domain methods on raw velocity and instrument deconvolved displacement seismograms. Results were compared and the cause of differences in the measurements were investigated.

### **Regional Earthquake Data at ABKT**

The data used in this study were recorded at the Global Seismic Network (GSN) station ABKT in Alibek, Turkmenistan. This station has a Streckeisen STS-2 broadband seismometer with flat velocity response from approximately 0.01-10 Hz (sample rate = 20/sec). We collected waveform data recorded at ABKT for earthquakes in the region reported by the National Earthquake Information Service-Preliminary Determination of Epicenters (NEIS-PDE) for the years 1994 and 1995. Reported depths were less than 50 km and body-wave magnitudes,  $m_b$ , were greater than or equal to 4.0. The events, paths and region studied are shown in Figure 1.

All waveform data were previewed and a Pn arrival was picked. Noisy data were discarded. For this study only the vertical component was considered. The instrument response was removed and the data were integrated to displacement. Regional phases were isolated with group velocity windows: Pn 8.0 to 6.2 km/sec; Pg 6.2 to 5.0 km/sec; and Lg 3.6 to 3.0 km/sec. In order to reduce possible biases due to poor event locations and timing errors, all group velocity windows were shifted such that Pn arrives at 7.9 km/sec. Noise was sampled in a 35 sec window ending 5 sec before the Pn arrival. Figure 2 shows an example of the phase windowing.

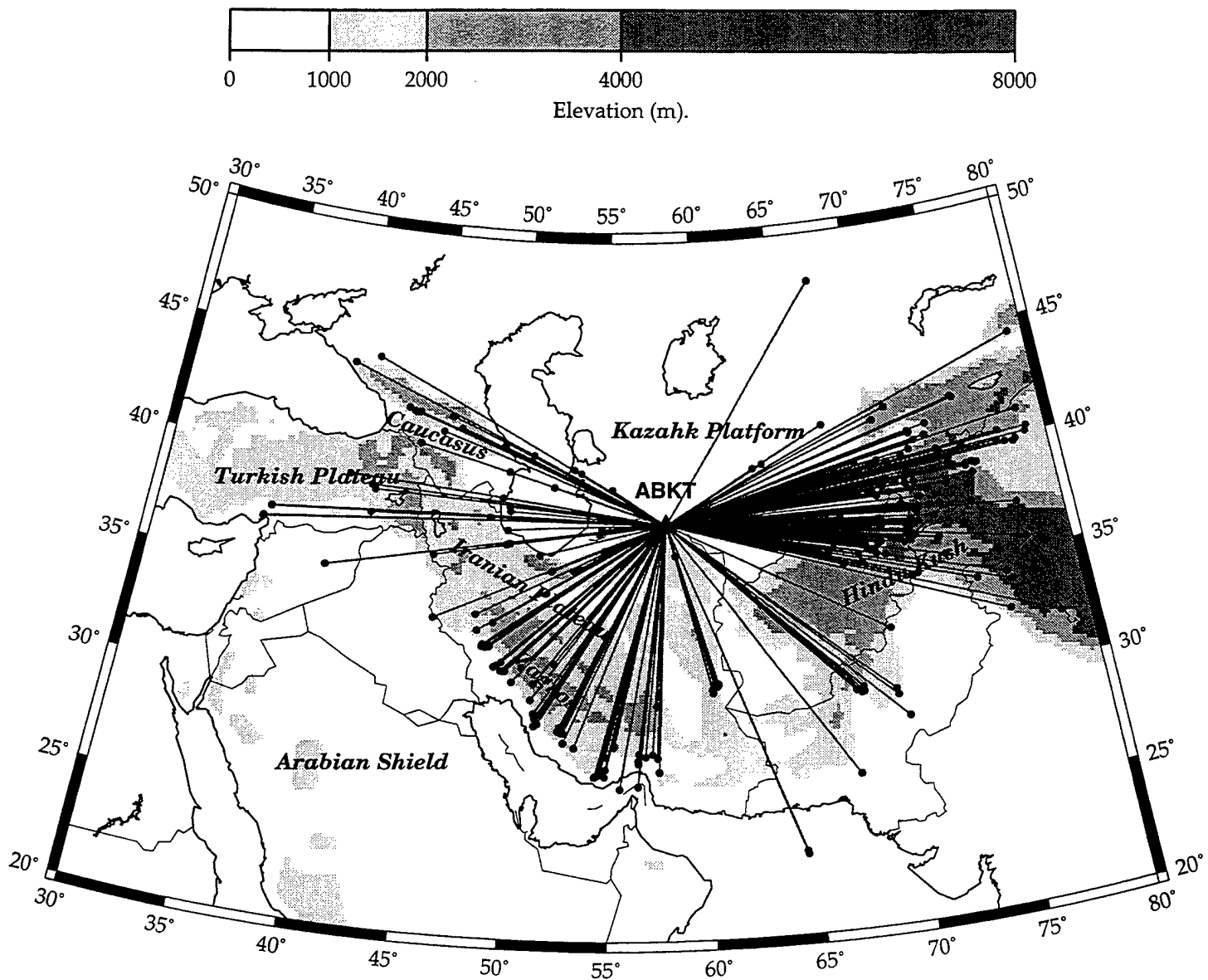


**Figure 1.** Map of events (circles) and paths recorded at GSN station ABKT (triangle). Topographic relief is indicated by the scale. Major tectonic units are labeled.

ABKT.BHZ 1994 54 11 54 mb= 5.3 Distance= 823 km Filtered 0.75-9.0 Hz

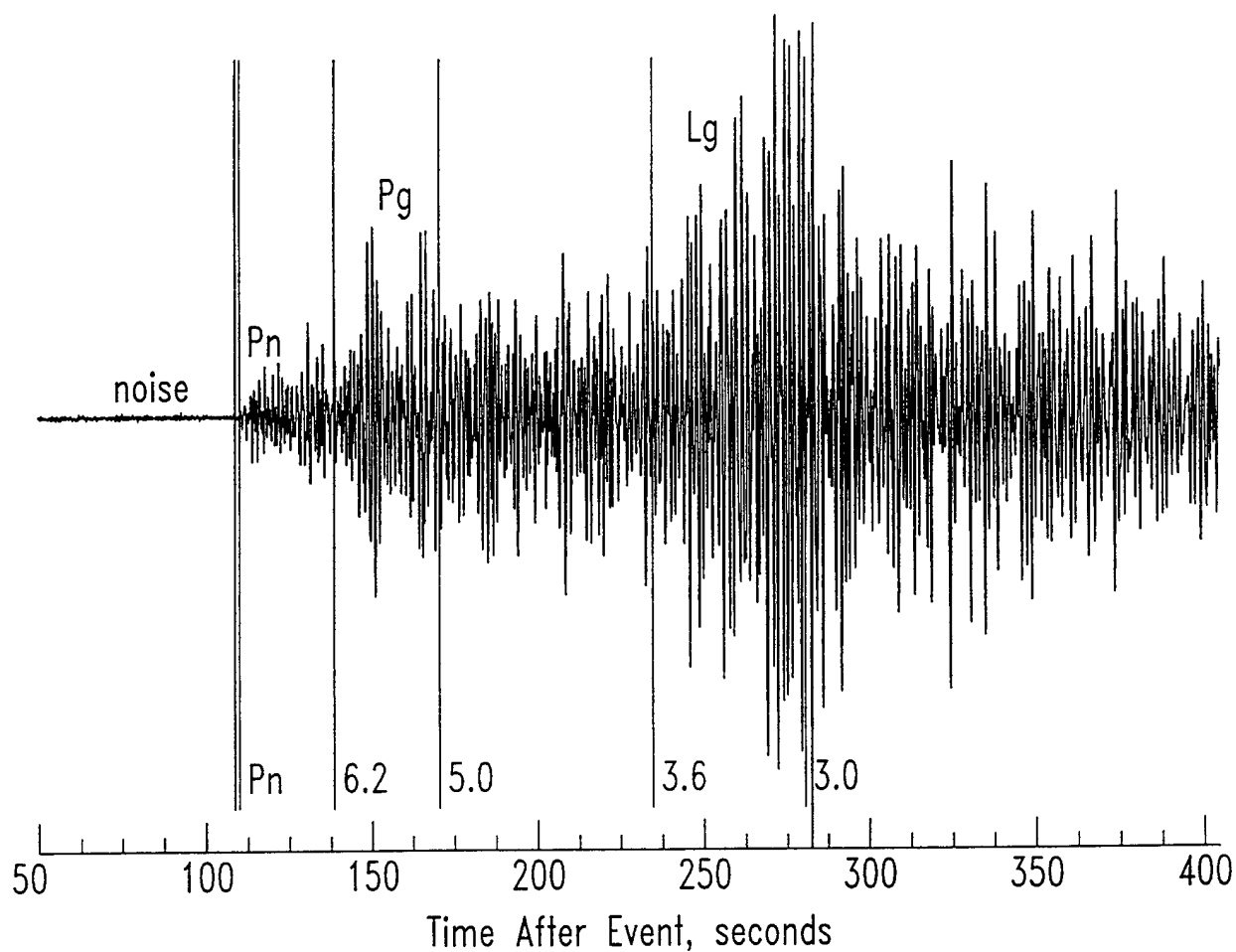


**Figure 2.** Recording of an eastern Iran event at ABKT showing the windowing of the noise, Pn, Pg, and Lg phases. The trace is pass band filtered (0.75-9.0 Hz).



Propagation of regional phases in this region is strongly influenced by the complex topographic and tectonic structure. High elevations of the Turkish-Iranian Plateau are associated with recent volcanic activity and low sub-Moho P-wave velocities (Hearn and Ni, 1994). Regions of low Pn velocities are strongly correlated with a zone of inefficient Sn propagation (Kadinsky-Cade et al., 1981; Rodgers et al., 1997). Low Q within the crust of the Iranian Plateau leads to inefficient Lg propagation (Nuttli, 1980; Wu et al., 1996). The topographic relief associated with the boundaries of the Turkish-Iranian Plateau has been shown to weaken and/or block propagation of the Lg phase (Kadinsky-Cade et al., 1981; Rodgers et al., 1997). Figure 3 illustrates the variability in Lg propagation for the region. Pg/Lg amplitude ratios were made as described below using the time domain rms amplitudes in four frequency bands. The Pg/Lg ratio for each path is plotted and color coded. Note that the Pn to pre-Pn amplitude ratio (signal-to-noise) cut-off is 2:1 and that many data for paths crossing the Iranian Plateau that survive this criterion for lower frequencies (0.75-1.5 Hz) are too noisy at high frequencies (6.0-9.0 Hz). This suggests that attenuation is higher in the Iranian lithosphere relative to the Kazahk Platform. For the lowest frequency band, 0.75-1.5 Hz, paths crossing the Iranian Plateau generally show weak Lg ( $Pg/Lg \geq 1.0$ ), whereas paths crossing the Kazahk Platform (with similar distances to ABKT) show strong Lg ( $Pg/Lg \leq 0.5$ ).

The complicated regional phase behavior of this region makes it well suited for evaluating regional phase measurement techniques because a wide range of Pg/Lg ratios is observed. However, for monitoring purposes azimuthal variations in regional phase amplitude ratios complicate the use of a single distance correction. Investigation of the azimuthal dependence of regional phase propagation at this station and distance corrections will be presented in a future study.

### Time Domain Measurements - Methodology

Time domain measurements of phase amplitudes were made by narrow band filtering the waveforms using a 4-pole, 2-pass Butterworth filter (bands: 0.75-1.5; 1.5-3.0; 3.0-6.0; 6.0-9.0 Hz). Pn, Pg and Lg phases were isolated as described above. For each windowed, de-measured phase,  $s(t)$ , we measured the: absolute mean (L1 norm):

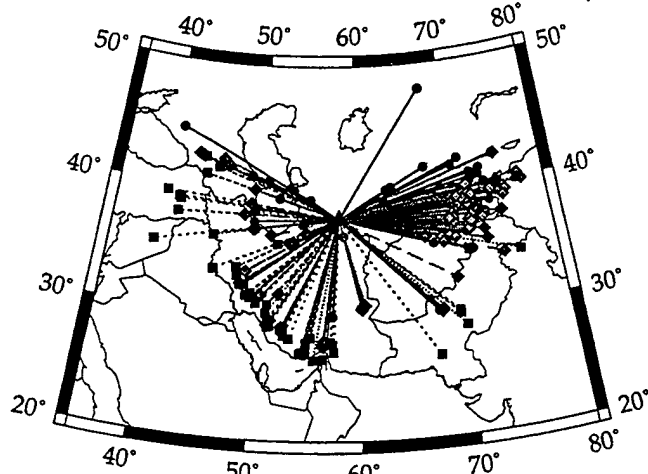
$$\text{abs. mean} = \overline{|s(t)|} ; \text{ where } |s(t)| = |s(t)| ; \quad (1)$$

rms (root-mean-square or L2 norm):

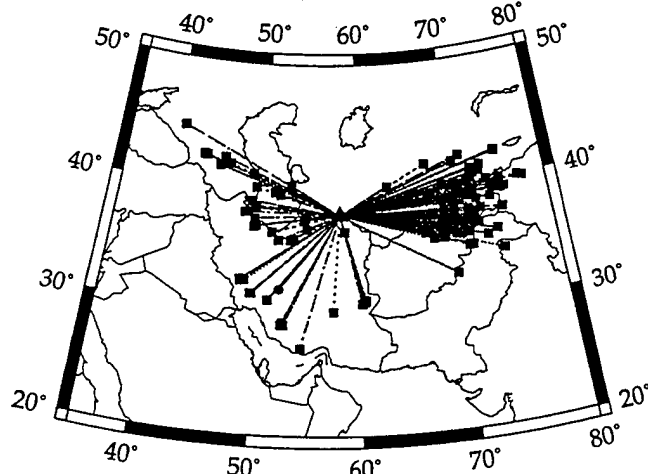
$$\text{rms} = \left[ \overline{s(t)^2} \right]^{1/2} ; \quad (2)$$

# ABKT $P_g/L_g$

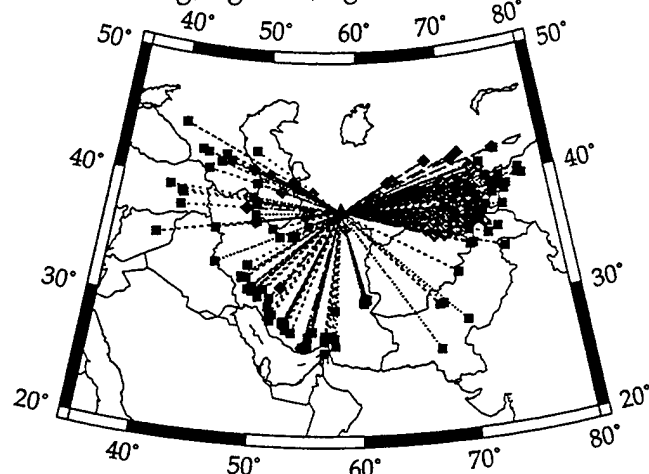
Amplitude Ratio  $\bullet$  —  $P_g/L_g < 0.5$ , Lg efficient  
 Time domain: Rms  $\diamond$  - - -  $0.5 \leq P_g/L_g \leq 1.0$ , Lg intermediate  
 Pn/noise  $> 2.0$   $\blacksquare$  .....  $P_g/L_g > 1.0$ , Lg weak



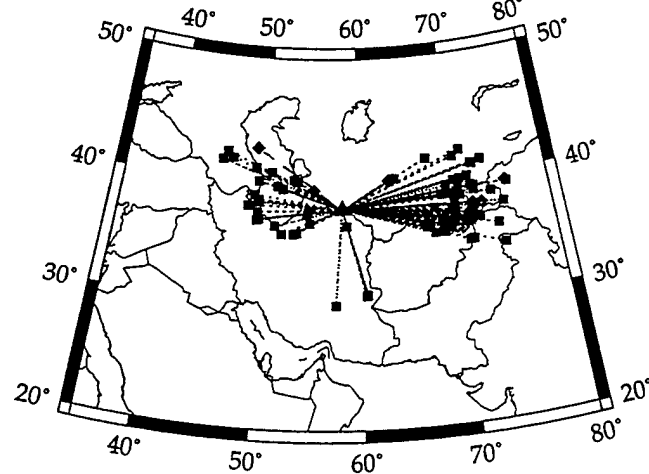
0.75-1.5 Hz



3.0-6.0 Hz



1.5-3.0 Hz



6.0-9.0 Hz

Figure 3. Map of Lg propagation efficiency for station ABKT.  $P_g/L_g$  ratios plotted along the path are color coded (key upper right).

envelope mean:

$$\text{env. mean} = \overline{e(t)} ; \text{ where } e(t) = \left[ s(t)^2 + H[s(t)]^2 \right]^{1/2} ; \quad (3)$$

and  $H[s(t)]$  is the Hilbert transform; the absolute maximum, abs. max. =  $\max[l(t)]$ ; and envelope maximum, env. max. =  $\max[e(t)]$ . The absolute mean, rms and envelope mean are measures of the average energy in the window, whereas the absolute maximum and envelope maximum are measures of the peak energy. Time domain measurements for each phase are made for each pass band separately.

## Time Domain Measurements - Results

The waveform data at ABKT were recorded as digital counts proportional to ground velocity. After deconvolution of the instrument response and integration the trace represents true ground displacement. Comparisons of the Pn/Lg amplitude ratios measured in the time domain from raw velocity and instrument deconvolved displacement seismograms are shown in Figure 4. Rms amplitudes were used and the ratio of Pn to the pre-Pn noise was required to be 2.0 or greater. The comparison is shown for the same four frequency bands as Figure 3. The individual  $\log_{10}[\text{Pn} / \text{Lg}]$  ratios are plotted as circles and are fit to a straight line. Also shown in each panel are the number of points, linear correlation, standard error about the best-fit straight line and the slope of the fit. The raw velocity and instrument deconvolved displacement give very similar Pn/Lg amplitude ratios. The slopes and linear correlations are all close to 1.0. As noted above, the number of data surviving the signal-to-noise criterion rapidly decreases as the frequency pass band is increased. Also note that the lower Pn/Lg ratios ( $\log_{10}[\text{Pn}/\text{Lg}] \leq 0.0$ ) are preferentially discarded due to the signal-to-noise criteria.

Comparison of the various time domain measurements for Pn/Lg and Pg/Lg are compiled in Tables 1 and 2, respectively. The various time domain measurements give fairly consistent results. The absolute and envelope measurements, both mean and maximum, are particularly strongly related. The rms (energy measure) and the absolute maximum (peak measure) are not correlated as well as the other pairs shown. The standard error generally increases and the linear correlation decreases as frequency increases.

## Frequency Domain Measurements - Methodology

# ABKT Pn/Lg

measure: rms , Pn/pre-Pn noise > 2.0

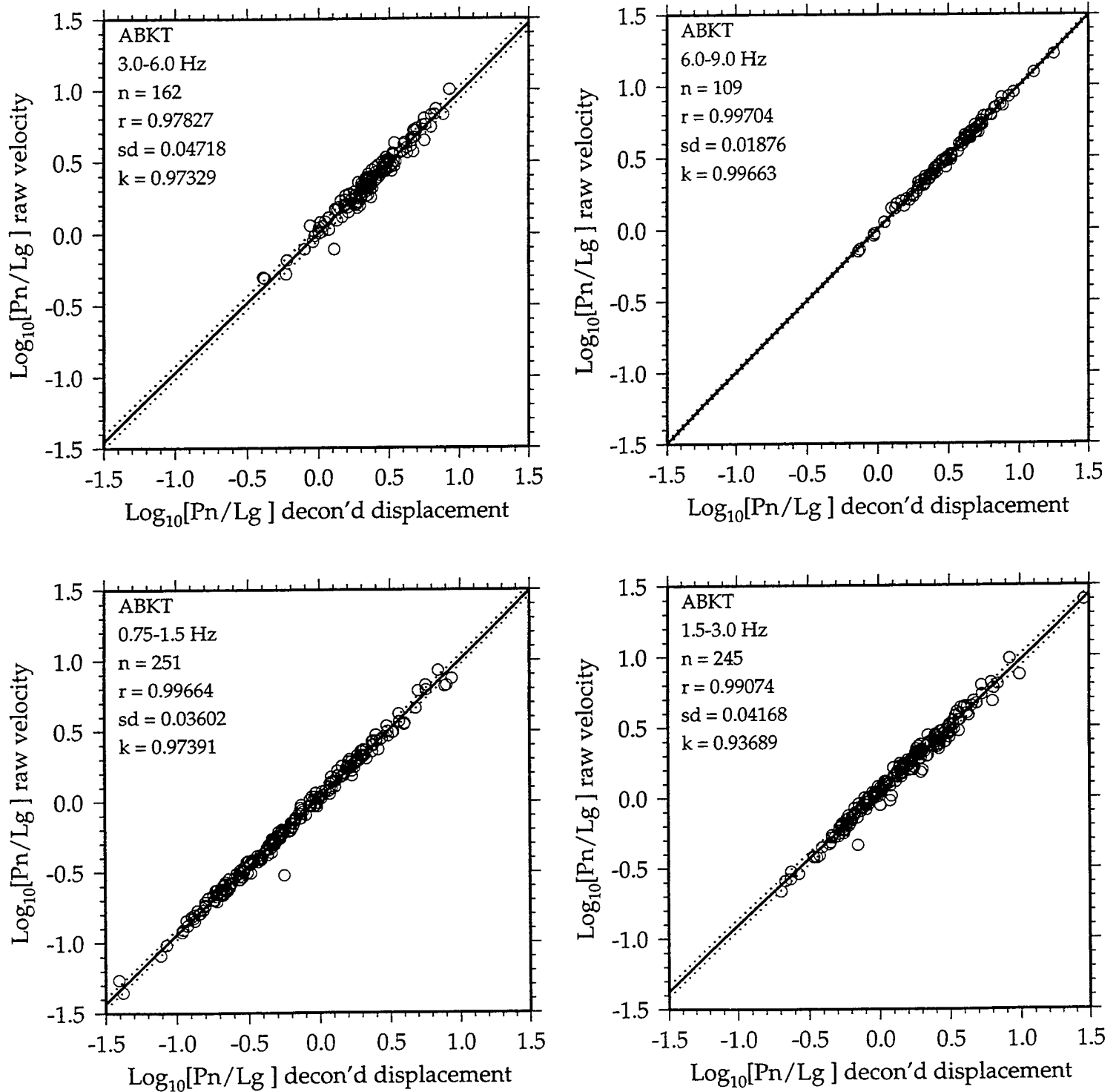


**Figure 4.** Comparison of Pn/Lg amplitude ratios (rms amplitude in the time-domain) for raw velocity and instrument deconvolved displacement for the four pass bands. The pre-Pn noise to Pn amplitude ratio was required to be greater than or equal to 2.0. The data (circles) were fit to the straight (solid) line.  $1-\sigma$  errors in the fit are shown as dotted lines. The pass band, number of data,  $n$ , linear correlation,  $r$ , standard error about the best-fitting straight line,  $sd$ , and the slope of the fit,  $k$ , are given.

**Table 1.**

**Pn/Lg Amplitude Ratios - Comparison**

Frequency band	6.0-9.0 Hz			
Measures	n	r	sd	k
raw vel. vs. deconv. dis.	109	0.997	0.019	0.997
abs. mean vs. rms	109	0.977	0.052	1.032
abs. mean vs. env. mean	109	1.000	0.002	1.001
rms vs. env. mean	109	0.977	0.049	0.926
abs. max. vs. env. max.	109	0.998	0.019	0.996
rms vs. abs. max.	109	0.910	0.127	1.150
rms vs. freq. log	102	0.717	0.222	0.823
rms vs. freq. lin.	119	0.789	0.204	0.990

Frequency band	3.0-6.0 Hz			
Measures	n	r	sd	k
raw vel. vs. deconv. dis.	162	0.978	0.047	0.973
abs. mean vs. rms	161	0.990	0.032	1.006
abs. mean vs. env. mean	161	1.000	0.002	0.999
rms vs. env. mean	161	0.990	0.031	0.974
abs. max. vs. env. max.	161	0.997	0.021	0.984
rms vs. abs. max.	161	0.931	0.095	1.060
rms vs. freq. log	164	0.889	0.101	0.864
rms vs. freq. lin.	182	0.955	0.065	0.927

Frequency band	1.5-3.0 Hz			
Measures	n	r	sd	k
raw vel. vs. deconv. dis.	245	0.991	0.042	0.937
abs. mean vs. rms	245	0.997	0.026	0.984
abs. mean vs. env. mean	245	1.000	0.001	1.000
rms vs. env. mean	245	0.997	0.026	1.010
abs. max. vs. env. max.	245	0.999	0.013	0.992
rms vs. abs. max.	245	0.967	0.081	0.955
rms vs. freq. log	251	0.953	0.091	0.890
rms vs. freq. lin.	254	0.979	0.065	0.984

Frequency band	0.75-1.5 Hz			
Measures	n	r	sd	k
raw vel. vs. deconv. dis.	251	0.997	0.036	0.974
abs. mean vs. rms	251	0.998	0.028	0.996
abs. mean vs. env. mean	251	1.000	0.001	1.000
rms vs. env. mean	251	0.998	0.028	1.001
abs. max. vs. env. max.	251	1.000	0.012	1.000
rms vs. abs. max.	251	0.985	0.079	1.009
rms vs. freq. log	256	0.984	0.080	0.991
rms vs. freq. lin.	254	0.992	0.056	0.997

**Table 2.**

**Pg/Lg Amplitude Ratios - Comparison**

Frequency band		6.0-9.0 Hz			
Measures	n	r	sd	k	
raw vel. vs. deconv. dis.	109	0.997	0.016	0.988	
abs. mean vs. rms	109	0.972	0.046	1.021	
abs. mean vs. env. mean	109	1.000	0.002	1.000	
rms vs. env. mean	109	0.971	0.044	0.923	
abs. max. vs. env. max.	109	0.997	0.020	0.989	
rms vs. abs. max.	109	0.875	0.120	1.127	
rms vs. freq. log	102	0.625	0.173	0.689	
rms vs. freq. lin.	119	0.714	0.171	0.888	

Frequency band		3.0-6.0 Hz			
Measures	n	r	sd	k	
raw vel. vs. deconv. dis.	162	0.971	0.038	0.975	
abs. mean vs. rms	161	0.982	0.030	1.035	
abs. mean vs. env. mean	161	1.000	0.002	0.999	
rms vs. env. mean	161	0.982	0.029	0.931	
abs. max. vs. env. max.	161	0.993	0.024	0.984	
rms vs. abs. max.	161	0.909	0.083	1.134	
rms vs. freq. log	164	0.832	0.088	0.810	
rms vs. freq. lin.	182	0.892	0.071	0.871	

Frequency band		1.5-3.0 Hz			
Measures	n	r	sd	k	
raw vel. vs. deconv. dis.	245	0.987	0.035	0.925	
abs. mean vs. rms	245	0.995	0.022	1.014	
abs. mean vs. env. mean	245	1.000	0.001	0.999	
rms vs. env. mean	245	0.995	0.022	0.977	
abs. max. vs. env. max.	245	0.999	0.013	0.988	
rms vs. abs. max.	245	0.952	0.075	1.019	
rms vs. freq. log	251	0.914	0.084	0.837	
rms vs. freq. lin.	254	0.956	0.065	0.941	

Frequency band		0.75-1.5 Hz			
Measures	n	r	sd	k	
raw vel. vs. deconv. dis.	251	0.994	0.029	0.977	
abs. mean vs. rms	251	0.996	0.026	0.995	
abs. mean vs. env. mean	251	1.000	0.001	1.000	
rms vs. env. mean	251	0.996	0.026	0.996	
abs. max. vs. env. max.	251	0.999	0.012	1.001	
rms vs. abs. max.	251	0.961	0.081	1.009	
rms vs. freq. log	256	0.968	0.073	1.007	
rms vs. freq. lin.	254	0.980	0.055	0.996	

Frequency domain measurements were made by windowing the noise and each phase as described above, de-meaning and tapering the trace, then computing the frequency spectrum for a broad frequency range (0.03-9.99 Hz) by fast-Fourier transform (fft). The frequency spectrum was re-sampled and stored. Then the  $\log_{10}$ -mean spectral amplitude was computed for the same frequency bands considered above (0.75-1.5; 1.5-3.0; 3.0-6.0; 6.0-9.0 Hz). Only frequencies within the pass band were used to compute the  $\log_{10}$ -mean spectral amplitude of each phase. An immediate advantage of frequency domain techniques is that the broadband spectra of each phase need only be calculated once and the operation of computing the log-mean spectral amplitude is fast.

### Comparing Time and Frequency Domain Measurements

Comparison of the time and frequency domain Pg/Lg phase amplitude ratios is shown in Figure 5. Statistics for comparison of time and frequency domain Pn/Lg and Pg/Lg amplitude ratios are compiled in Tables 1 and 2, respectively. Time domain measurements were made on instrument deconvolved displacement data using the rms measurement. For the lowest frequency band (0.75-1.5 Hz), the measurements compare quite favorably, although they are more scattered than most of the time domain comparisons. However, as the pass band increases the correlation decreases, the slope deviates from 1.0 and the data become more scattered. Scatter is partly due to signal-to-noise. We found that increasing the signal-to-noise criteria reduced the standard errors, but the linear correlation and slope were largely unaffected and the number of data were strongly reduced. Similar decreases in correlation and slope were found for Pn/Lg.

The trend of the slopes in Figure 5 indicates that the time domain measurements of Pg/Lg are consistently larger than the frequency domain measurements for the higher pass bands. Insight into possible causes of this disagreement can be seen by plotting the frequency spectra of the broadband and narrow band filtered data, shown in Figure 6. This is for the seismogram shown in Figure 2. The noise and Pn, Pg and Lg phases were windowed as described above. Then the broadband (0.5-9.99 Hz) and narrow band filtered (0.75-1.5, 1.5-3.0, 3.0-6.0 and 6.0-9.0 Hz, 2-, 4- and 8-pole, 2-pass Butterworth filter) spectra were computed by fft. Within the 0.75-1.5, 1.5-3.0 and 3.0-6.0 Hz pass bands the spectra of the filtered data compare quite well with the broadband spectra. However, significant energy from outside the pass band, particularly at frequencies below the pass band, contributes to the filtered spectra. The time domain filtering is equivalent to multiplication in the frequency domain of a symmetric

# ABKT Pg/Lg

chan: BHZ , Pn/pre-Pn noise > 2.0

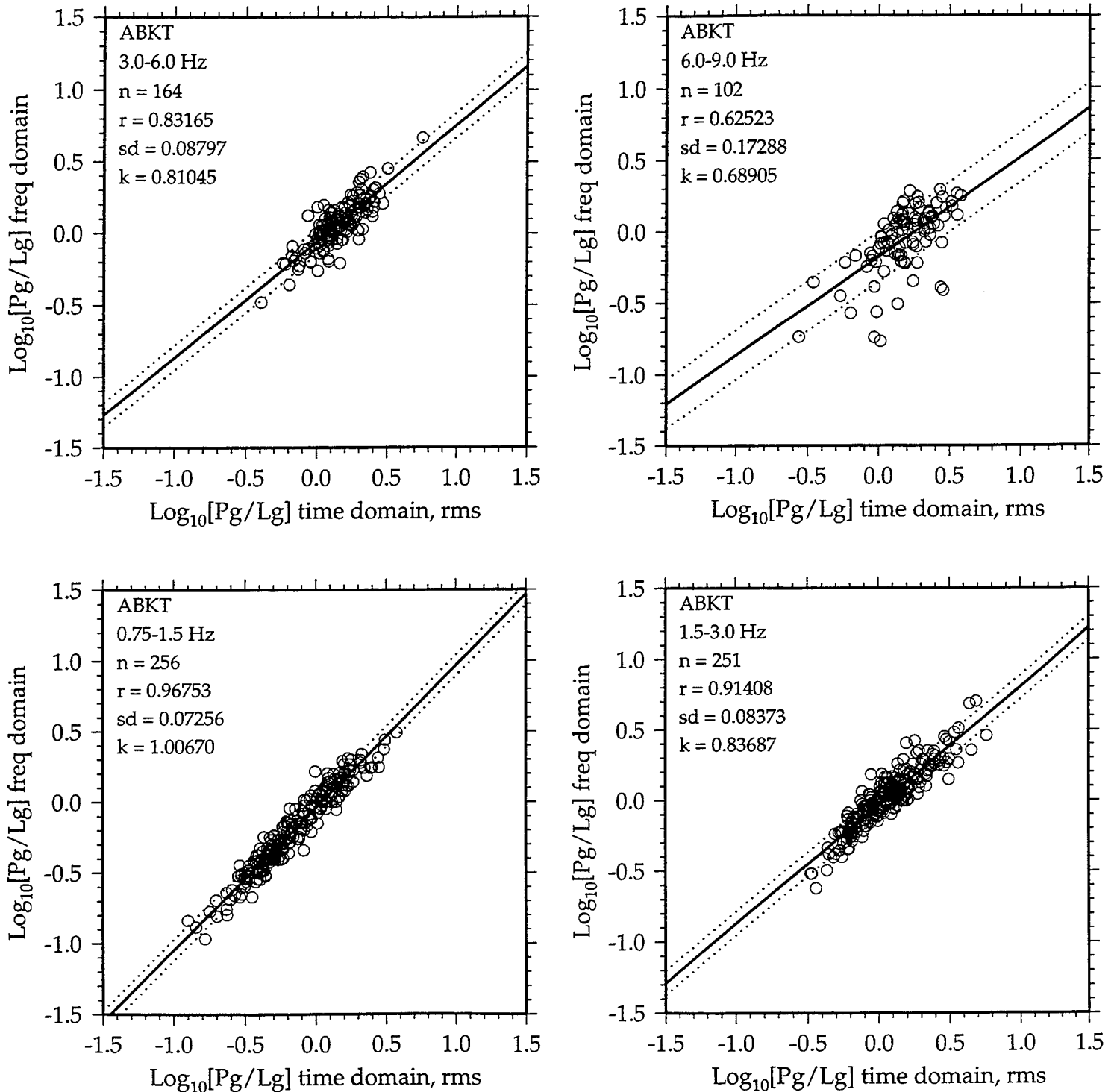


**Figure 5.** Comparison of Pg/Lg amplitude ratios measured in the time (instrument deconvolved displacement, rms) and frequency domains, similar to Figure 4. The pre-Pn noise to Pn amplitude ratio was required to be greater than or equal to 2.0.



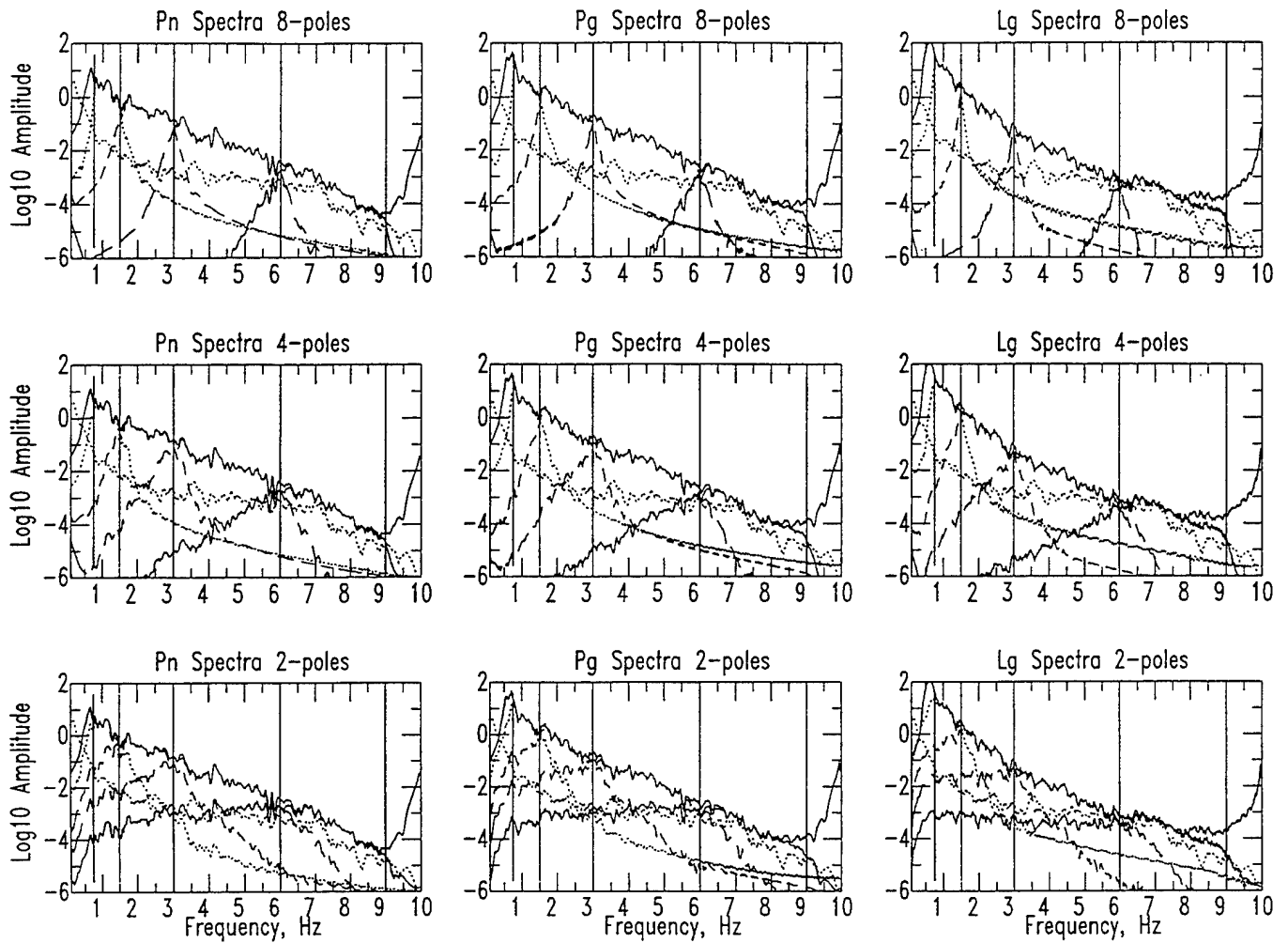


**Figure 6.** Comparison of Pn, Pg and Lg spectra for broadband (solid) and narrow band filtered data (dashed) for the waveform shown in Figure 2. The noise spectrum is shown as the dotted black line. Spectra are plotted as  $\log_{10}$  amplitude. Vertical lines indicate the filter pass band frequencies.

Butterworth filter with the regional phase spectrum, which drops off rapidly with increasing frequency. The resulting spectrum is skewed to lower frequencies. Increasing the number of poles strongly reduces the energy from outside the pass band, while maintaining excellent agreement to the broadband spectrum within the pass band. We found that the relationship of the time domain measurements to the frequency domain measurements was generally similar to that shown in Figure 5, regardless of how many poles were used for the time domain measurements. This suggests that energy from outside the pass band is not the primary cause of the disagreement between the time and frequency domain measurements.

For the highest frequency band (6.0-9.0 Hz), note that the broadband spectra in Figure 6 begin to increase around 9.0 Hz. This results from deconvolution of the instrument response. The anti-aliasing filter starts rolling off at around 6.0 Hz. When the observed spectra are divided by this response, the resulting spectra are greatly amplified. Clearly there are significant differences between the broadband and filtered spectra for this highest pass band. The noise spectrum is also shown in each panel of Figure 6 as the dotted black line. For the Lg phase, noise and signal spectra merge for the low end of this highest pass band. The signal-to-noise criteria is applied to the Pn and pre-Pn time windows. For the case shown, the Lg/pre-Pn amplitude ratio would probably fail to be greater than 2.0, although Pn and Pg would probably pass. Pn, Pg, Sn and Lg signal-to-noise ratio attributes for this station will be discussed further in a future paper.

We believe that the main cause of disagreement between the time and frequency domain measurements in Figure 5 is due to log averaging of the spectra. The spectra for all phases fall off very rapidly within the band 1.0-10 Hz. Averaging the  $\log_{10}$  of the spectrum does not weight the amplitudes associated with frequencies near the low end of the pass band as heavily as does linear averaging of the spectra. Time domain amplitude measurements weight each frequency equally and are thus biased toward the relatively larger amplitude energy at the low end of the pass band. To illustrate this point, we computed linear averages of the spectral amplitude of each phase and formed the amplitude ratios Pn/Lg and Pg/Lg. These measurements were well correlated with the time domain (rms) measurements and the slopes of the scatter plots were closer to 1.0. Results are compiled in Tables 1 and 2. Linear and log averaging of a spectrum should yield converging results as the pass band is narrowed. Remaining disagreement between the time and linearly averaged frequency domain measurements for the highest pass band is probably due to poor Lg signal-to-noise as described above.

## Discussion

In this study we present comparisons of regional phase amplitude ratio measurement techniques. Regional phase ratios ( $P_n/L_g$  and  $P_g/L_g$ ) for the area studied show large variation, and thus results for this region should be applicable to other regions. Various time domain measurements, particularly energy measures, agree very well with each other (linear correlations between 0.97-0.99). Absolute and envelope mean and maxima agree nearly perfectly. Energy and peak measures do not compare as favorably with each other, but they are still rather well correlated (linear correlations between 0.88-0.99). For some cases, peak measures in the time domain may discriminate better than energy measures. This could be due to the impulsive nature of P-waves from explosions. The population studied in this paper are all earthquakes, thus investigation of discriminant performance was not possible.

Time domain (rms) and frequency domain measurements compared favorably for the lowest frequency band, but the linear correlation decreased as the pass band increased. More importantly, however, is that the time domain  $P_n/L_g$  and  $P_g/L_g$  amplitude ratios were consistently higher than the log-averaged frequency domain ratios and that the disagreement increased as the pass band increased. A major disadvantage of time domain measurements is revealed in Figure 6. Time domain filtering does not offer much control over the frequencies which contribute to the measurement. Clearly significant energy from frequencies below the pass band contributes to the time domain measurements, particularly for the 2-pole, 2-pass filter. For the highest frequency band (6.0-9.0 Hz) significant differences between the broadband and filtered spectra (Figure 6) results from deconvolution of the instrument response. This probably contributes to the disagreement seen for this pass band in Figure 5 and Tables 1 and 2.

Linear averaging of the spectral amplitude brings the time and frequency domain measurements into much better agreement. Log-averaging provides a more robust estimate of the energy within a given pass band because the regional phase spectra vary by several orders of magnitude within the band 0.5-10.0 Hz. Time domain measurements weight all frequencies within the band equally and are thus biased by the large spectral amplitudes associated with the low end of the pass band. There is no easy way to make a time domain measurement that is not affected by this bias. Furthermore, because the broadband spectra need only be calculated and stored once, the frequency domain measurements are more efficient. Averages of the spectral amplitude within any band can be easily computed from the broadband spectra, instead of having to

read the data, filter and then compute the amplitude. Thus, we believe frequency domain measurements of regional phase amplitudes and amplitude ratios are superior to time domain measurements.

**Acknowledgements.** Raw waveform data were obtained from the Incorporated Research Institutions for Seismology-Data Management Center (IRIS-DMC). Parts of the analysis were done using the Datascope Seismic Data Application package obtained by from the University of Colorado, Joint Seismic Program Center and the Seismic Analysis Code (SAC2000) developed at Lawrence Livermore National Laboratory. This is Institute of Tectonics contribution #321 and this research was supported by Phillips Laboratory Contract F19628-95-K-0014.

## References

- Blandford, R. (1981). Seismic discrimination problems at regional distances, in *Identification of Seismic Sources-Earthquake or Explosion*, E. Husebye and S. Mykkeltveit (Editors), Reidel, Boston, 695-740.
- Hartse, H., S. Taylor, W. S. Phillips and G. Randall (1997). A preliminary study of regional seismic discrimination in central Asia with emphasis on western China, *Bull. Seism. Soc. Am.*, in press.
- Hearn, T. and J. Ni (1994). Pn velocities beneath continental collision zones: the Turkish-Iranian Plateau, *Geophys. J. Int.*, **117**, 273-283.
- Kadinsky-Cade, K., M. Barazangi, J. Oliver and B. Isacks (1981). Lateral variations of high-frequency seismic wave propagation at regional distances across the Turkish and Iranian Plateaus, *J. Geophys. Res.*, **86**, 9377-9396.
- Nuttli, O. (1980). The excitation and attenuation of seismic crustal phases in Iran, *Bull. Seism. Soc. Am.*, **70**, 469-485.
- Pomeroy, P., J. Best and T. McEvilly (1982). Test ban treaty verification with regional data - a review, *Bull. Seism. Soc. Am.*, **72**, S89-S129.
- Rodgers, A., J. Ni and T. Hearn (1997). Propagation characteristics of short-period Sn and Lg in the Middle East, *Bull. Seism. Soc. Am.*, in press.
- Taylor, S., N. Sherman and M. Denny (1989). Spectral discrimination between NTS explosions and western United States earthquakes at regional distances *Bull. Seism. Soc. Am.*, **78**, 1563-1579.

- Walter, W., K. Mayeda and H. Patton (1995). Phase and spectral ratio discrimination between NTS earthquakes and explosions. Part I: empirical observations, *Bull. Seism. Soc. Am.*, **85**, 1050-1067.
- Wu, J., J. Ni and T. Hearn (1996). Lg wave attenuation propagation characteristics in Iran, in *Monitoring a Comprehensive Test Ban Treaty*, NATO ASI Volume, Eds. E. Husebye and A. Dainty, 655-662, Kluwer Academic Publishers.
- Zhang, T. and T. Lay (1994). Analysis of short-period regional phase path effects associated with topography in Eurasia, *Bull. Seism. Soc. Am.*, **84**, 1665-1678.

**Correspondence:** Arthur Rodgers, Lawrence Livermore National Laboratory, L-202, P.O. Box 808, Livermore, CA 94551 USA; email: [rodgers@s156.es.llnl.gov](mailto:rodgers@s156.es.llnl.gov); phone: 510-423-4130; fax 510-423-1002.

### **Affiliations**

Lawrence Livermore National Laboratory, L-202, P.O. Box 808, Livermore, CA 94551 USA (A.J.R., W.R.W. and K.M.M.)

Earth Sciences Department and Institute of Tectonics, University of California, Earth and Marine Sciences Building, Santa Cruz, CA 95064 USA (T.L.)

## Appendix

### WMQ Discriminant Measures and Path Dependence

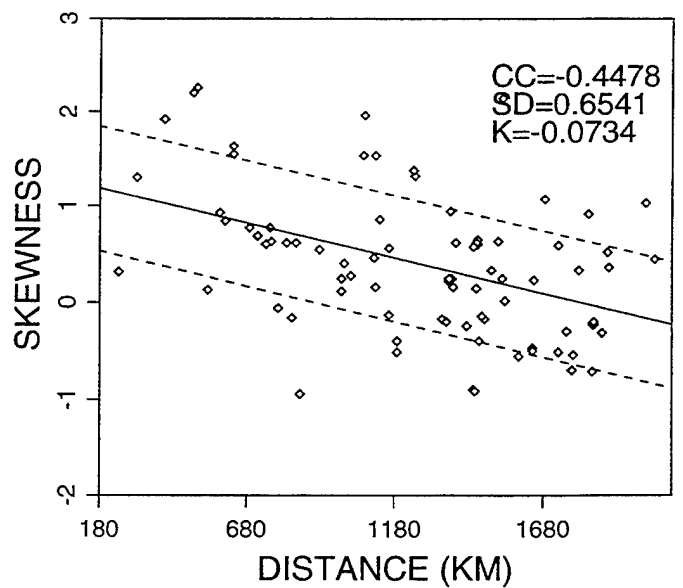
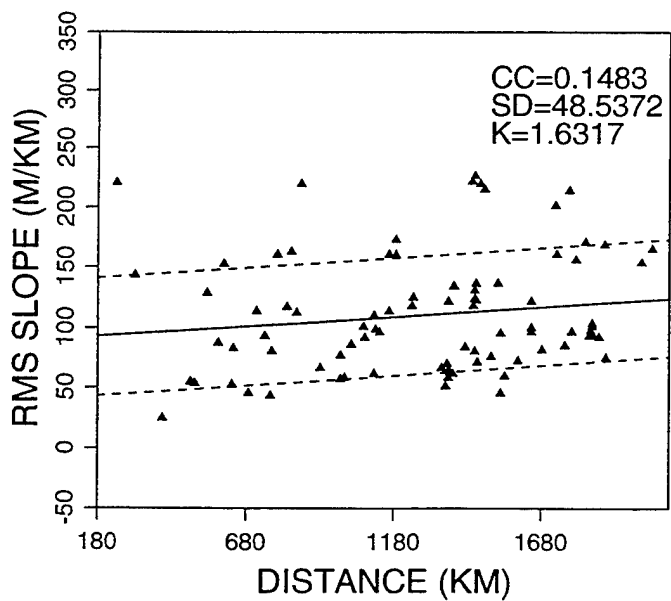
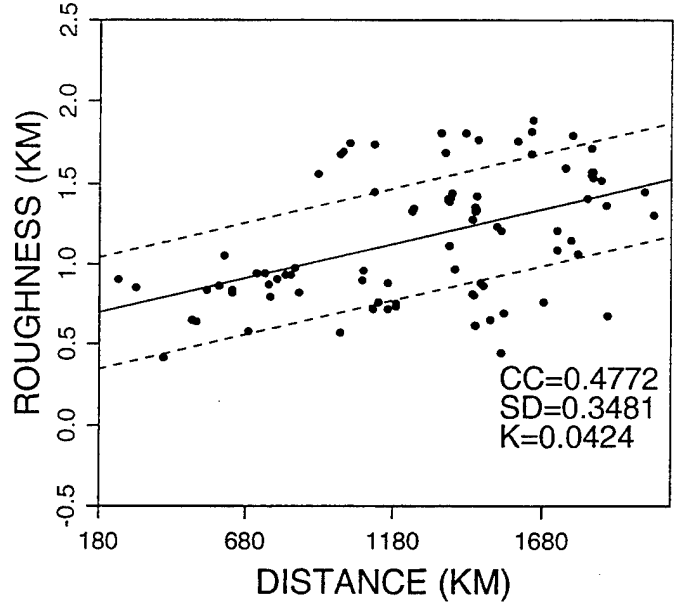
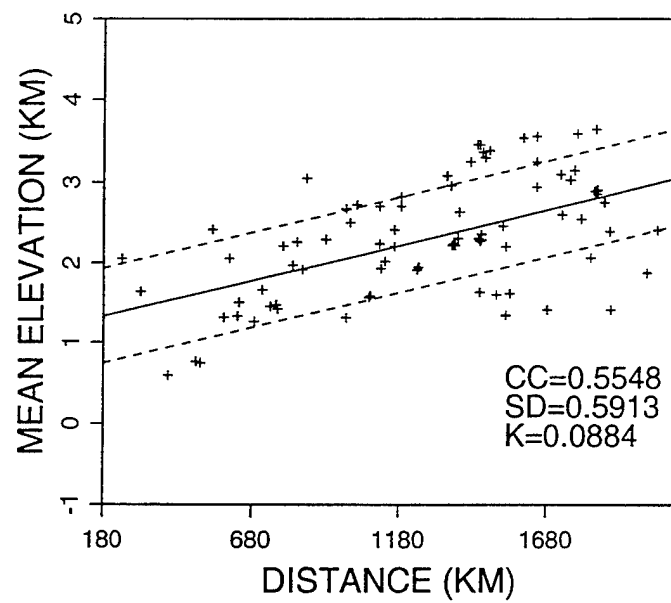


Figure A1a. Correlations between path properties for the WMQ observations. Relationships between path length (distance) and surface topography parameters.

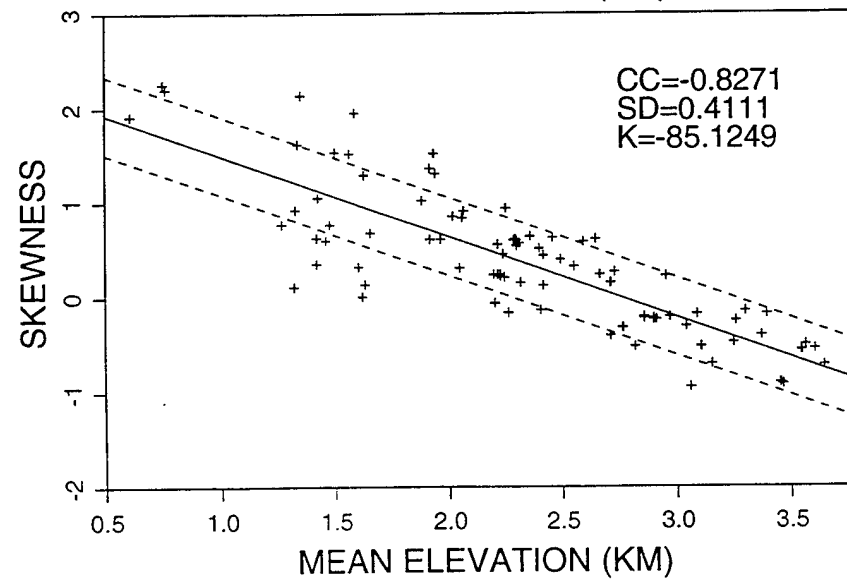
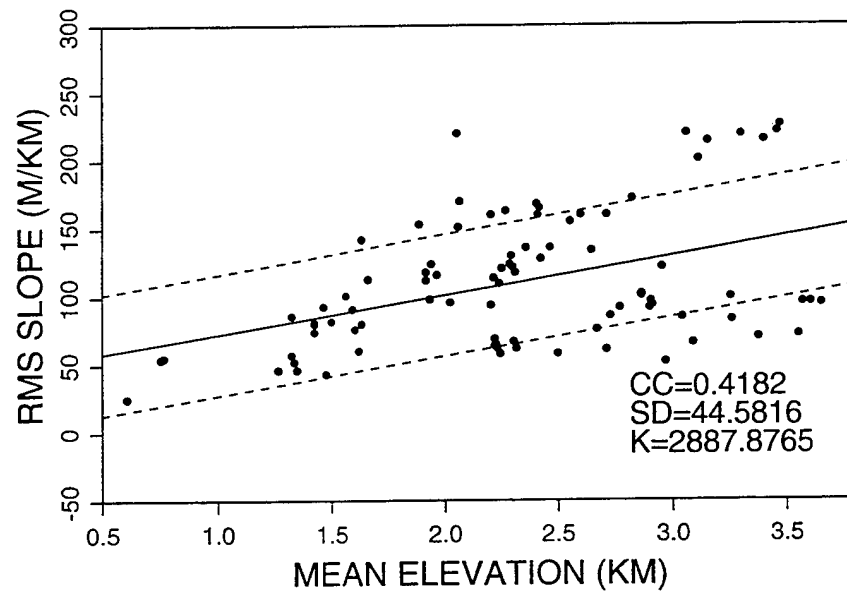
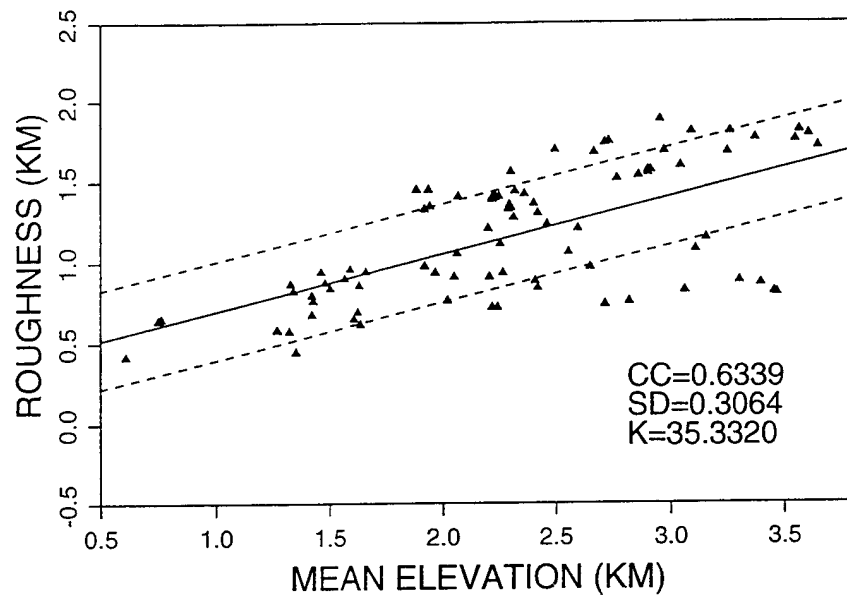


Figure A1b. Correlations between path properties for the WMQ observations. Relationships between mean path elevation and and other topographic parameters.



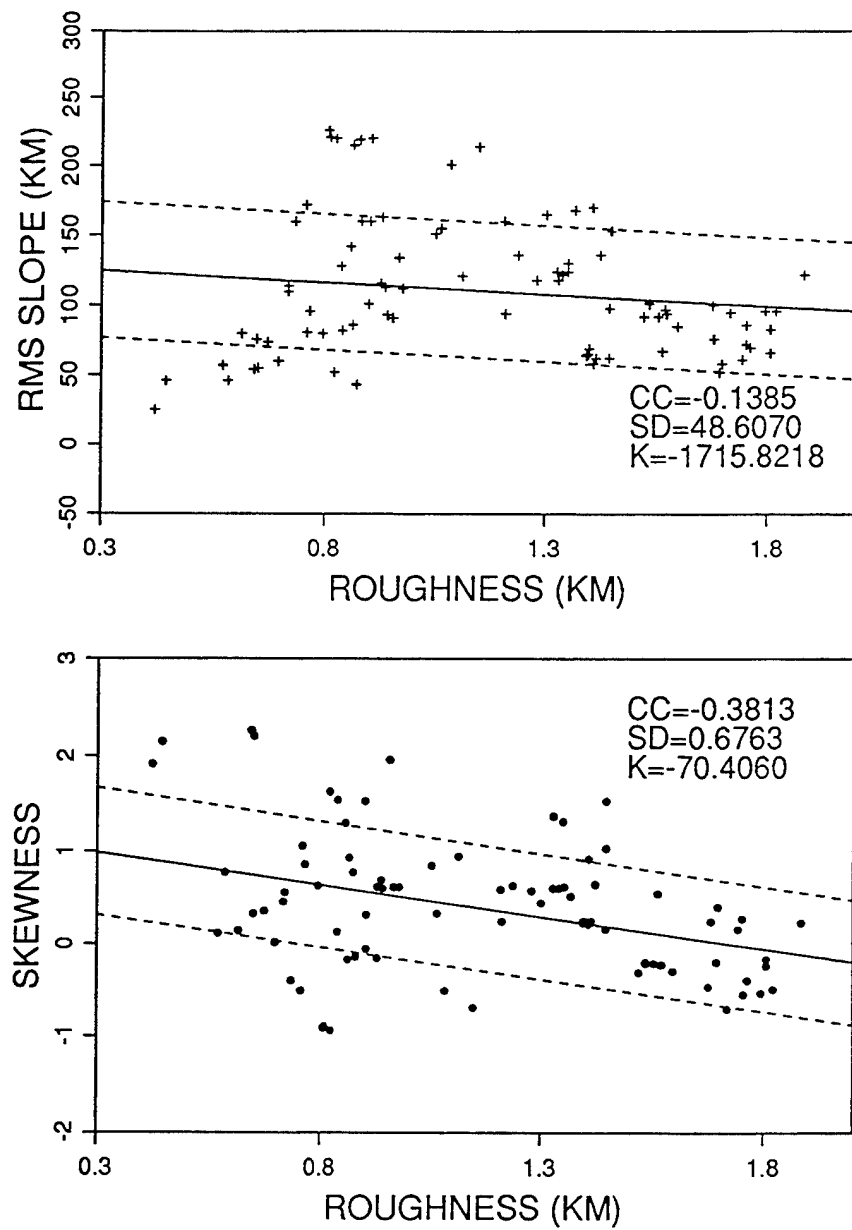


Figure A1c. Correlations between path properties for the WMQ observations. Relationships between mean path roughness and other topographic parameters.

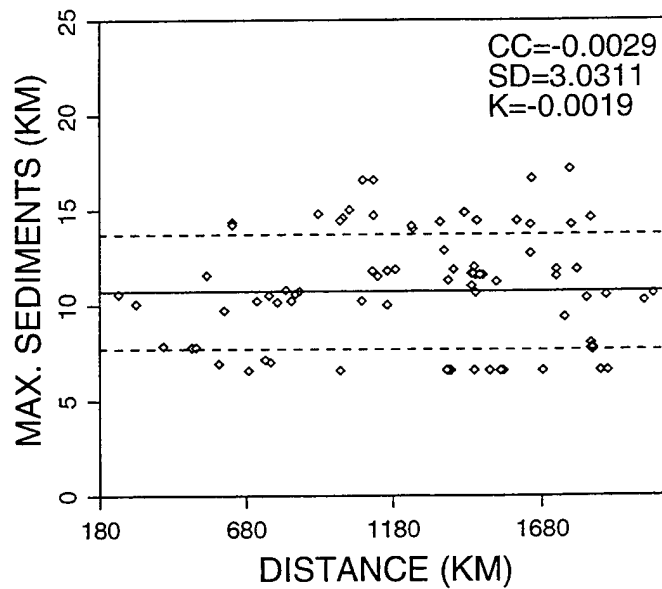
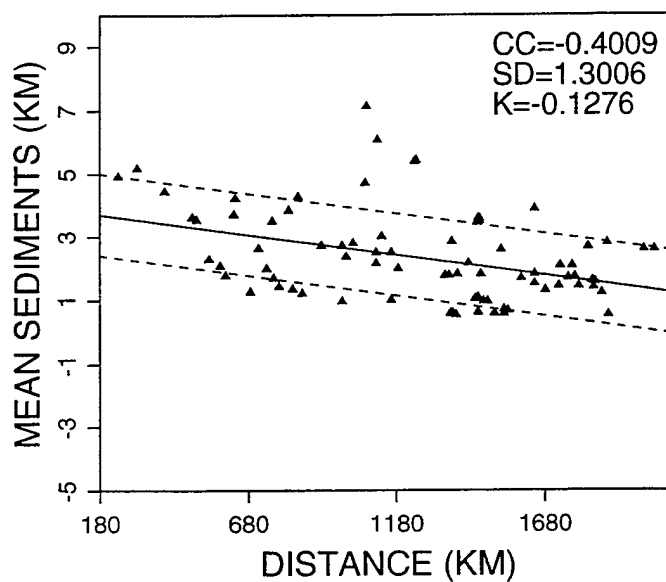
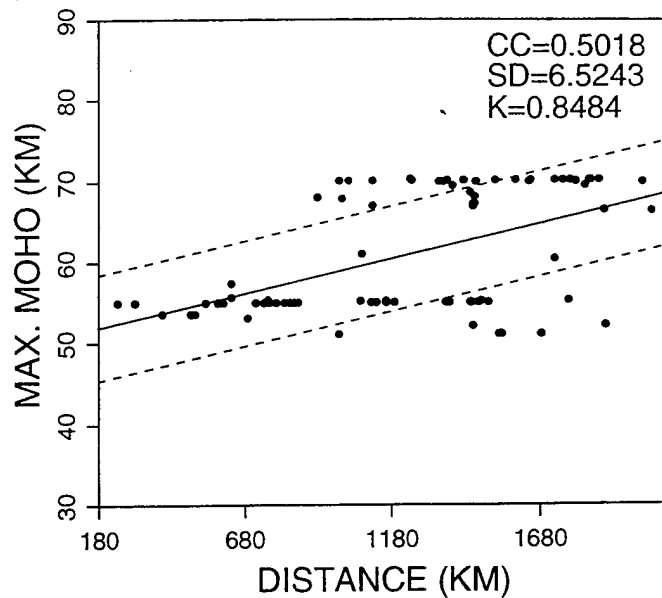
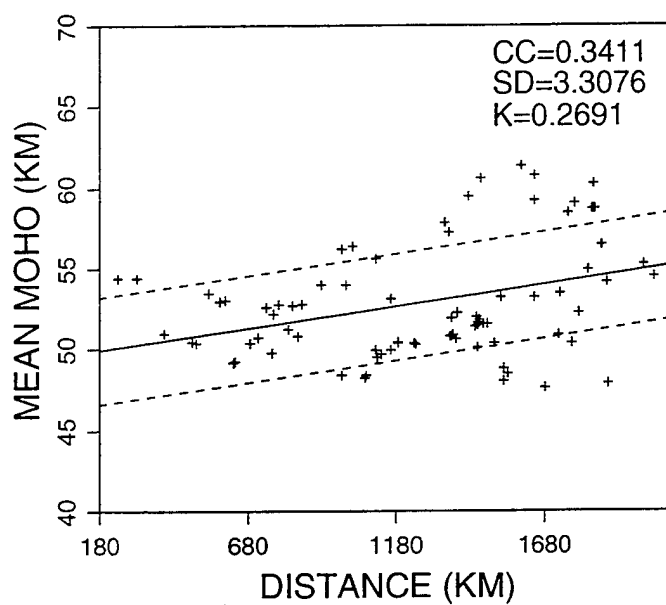


Figure A1d. Correlations between path properties for the WMQ observations. Relationships between path length (distance) and crustal waveguide parameters.

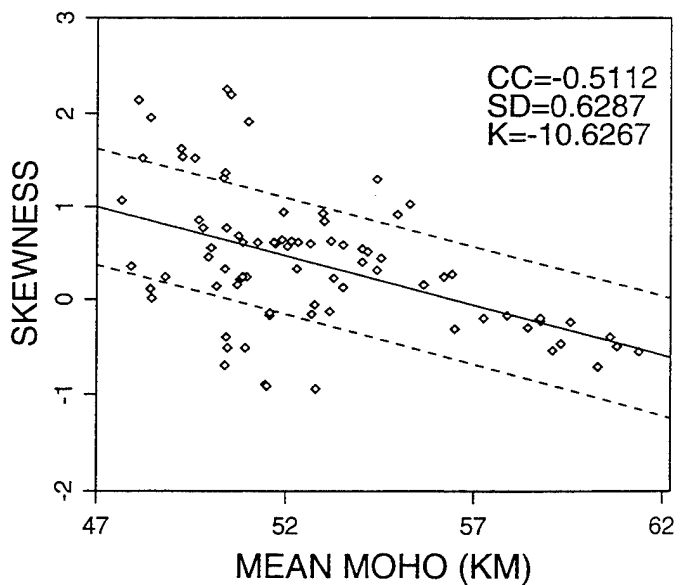
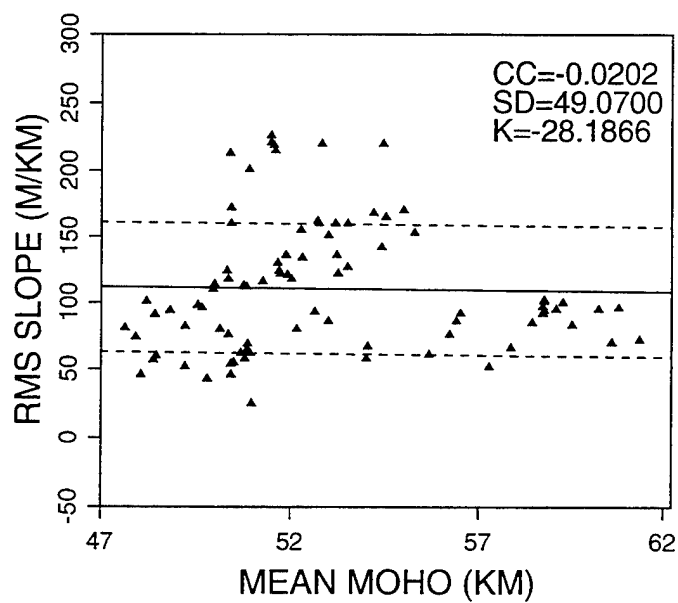
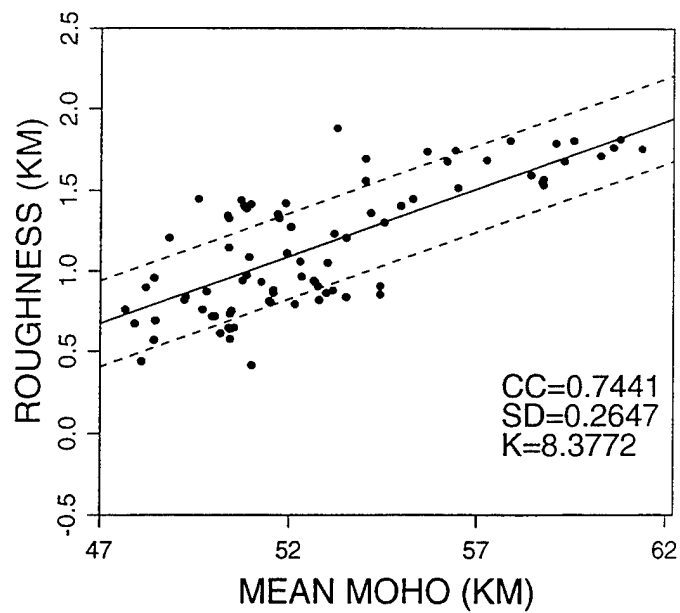
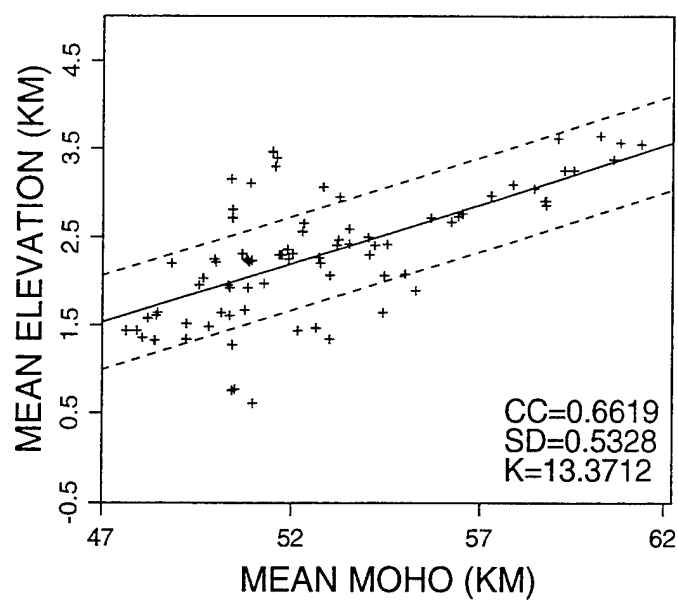


Figure A1e. Correlations between path properties for the WMQ observations. Relationships between mean Moho thickness and surface topography parameters.

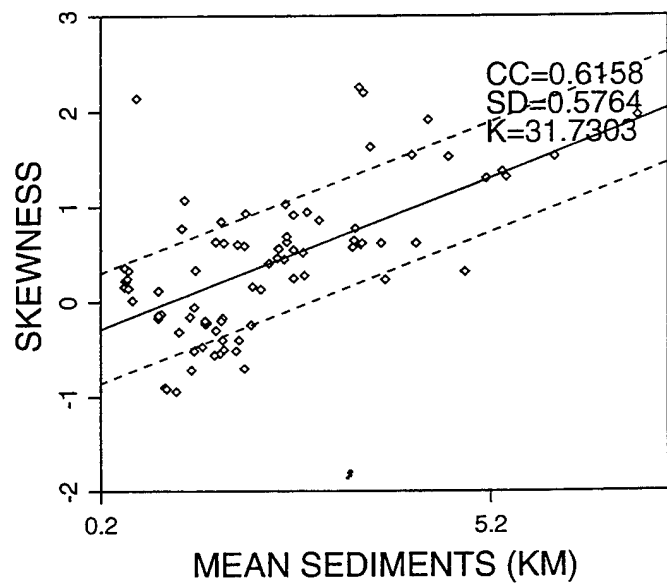
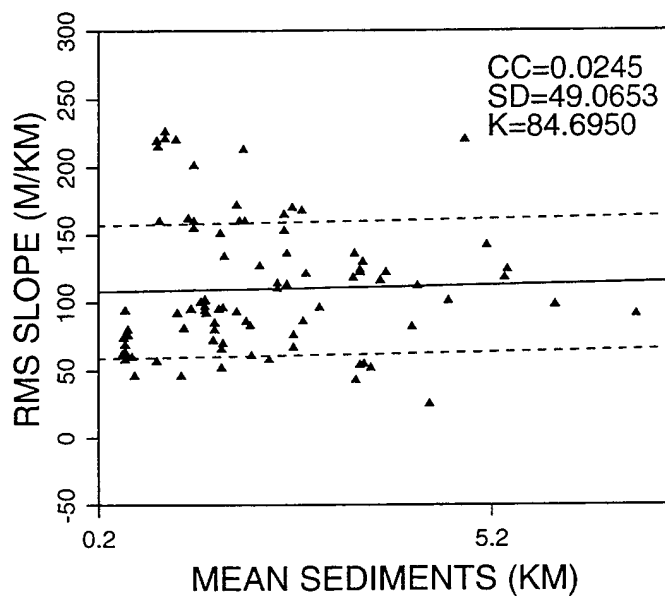
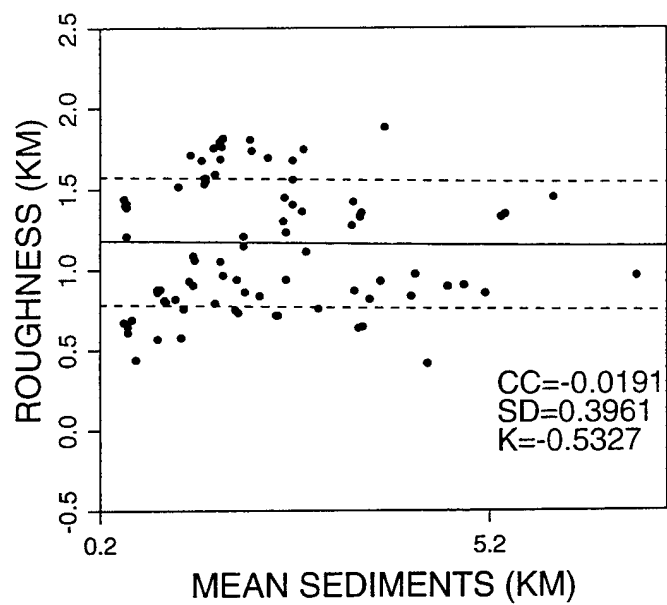
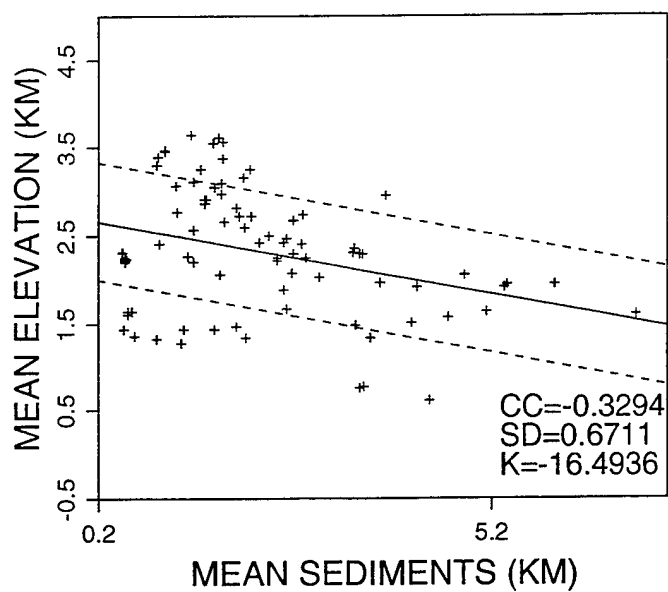


Figure A1f. Correlations between path properties for the WMQ observations. Relationships between mean sediment thickness and surface topography parameters.

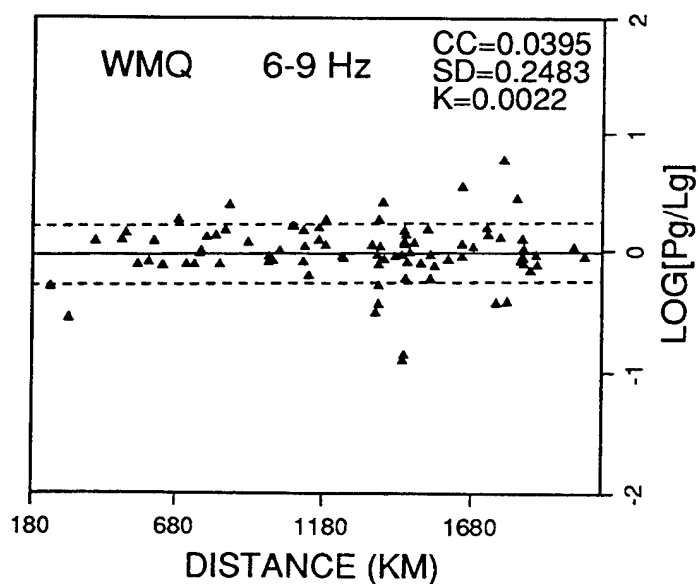
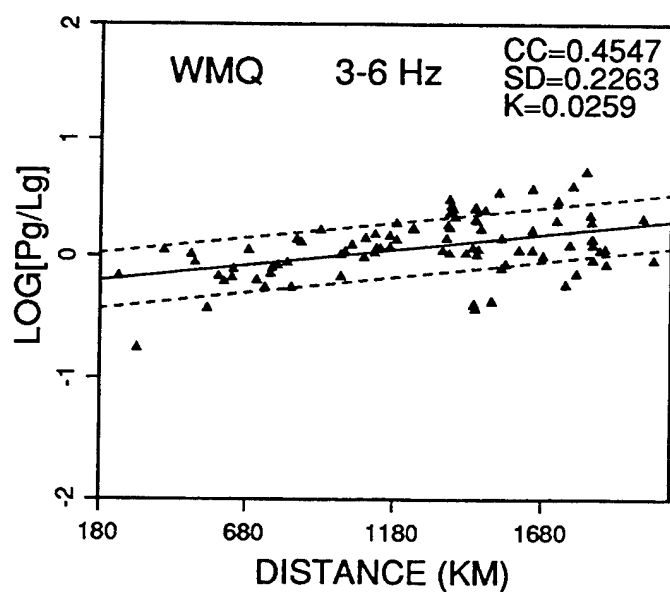
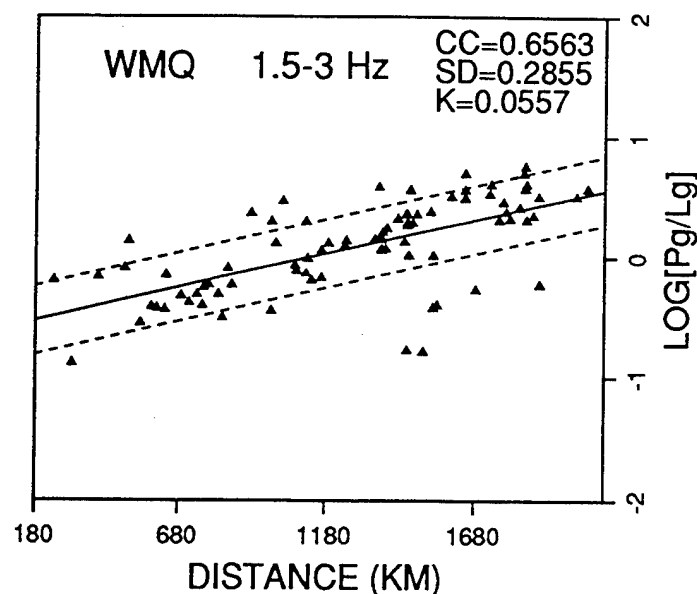
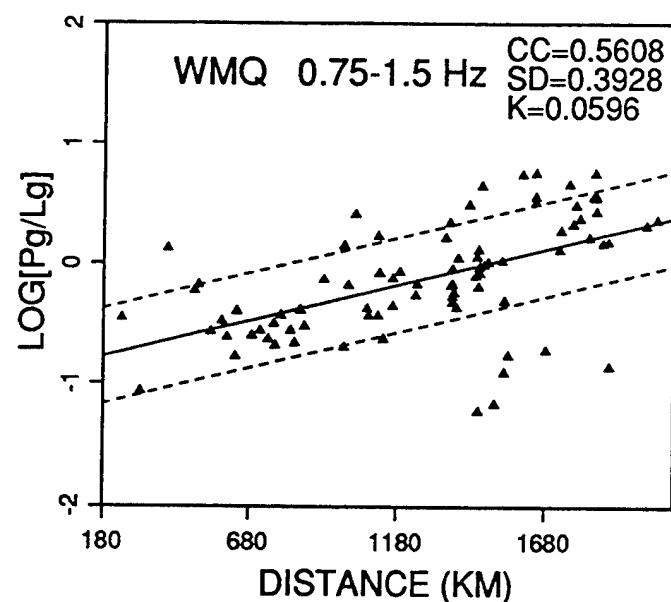


Figure A2a. Frequency dependent ratios of Pg/Lg phases recorded at WMQ plotted as a function of path length. CC denotes the linear correlation coefficient. SD denotes the standard deviation of the linear regression, with the dotted lines corresponding to  $\pm 1$  SD, and K denotes the slope of the regression.

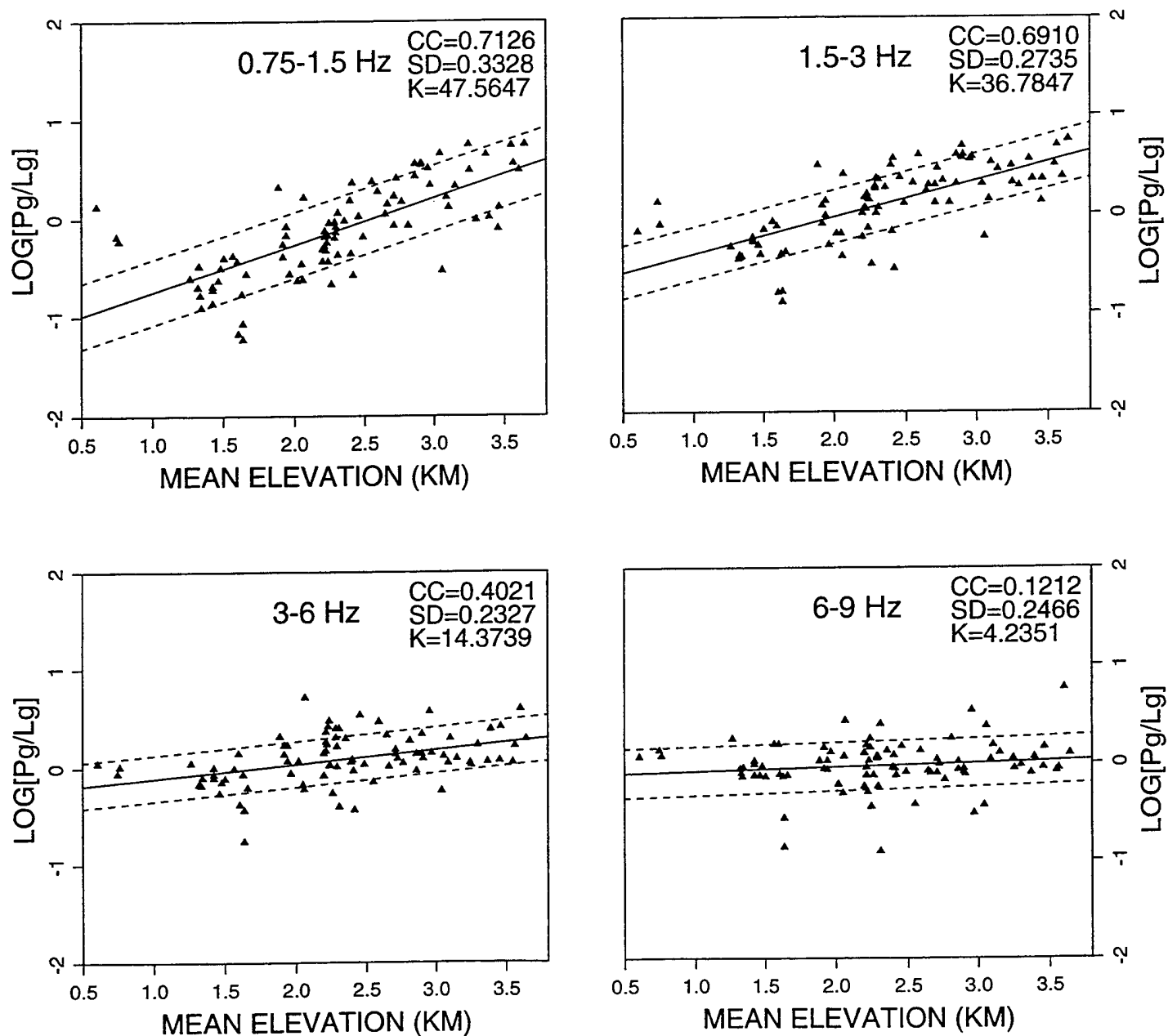


Figure A2b. Frequency dependent ratios of Pg/Lg phases recorded at WMQ plotted as a function of mean elevation of each path. CC denotes the linear correlation coefficient. SD denotes the standard deviation of the linear regression, with the dotted lines corresponding to  $\pm 1$  SD, and K denotes the slope of the regression.

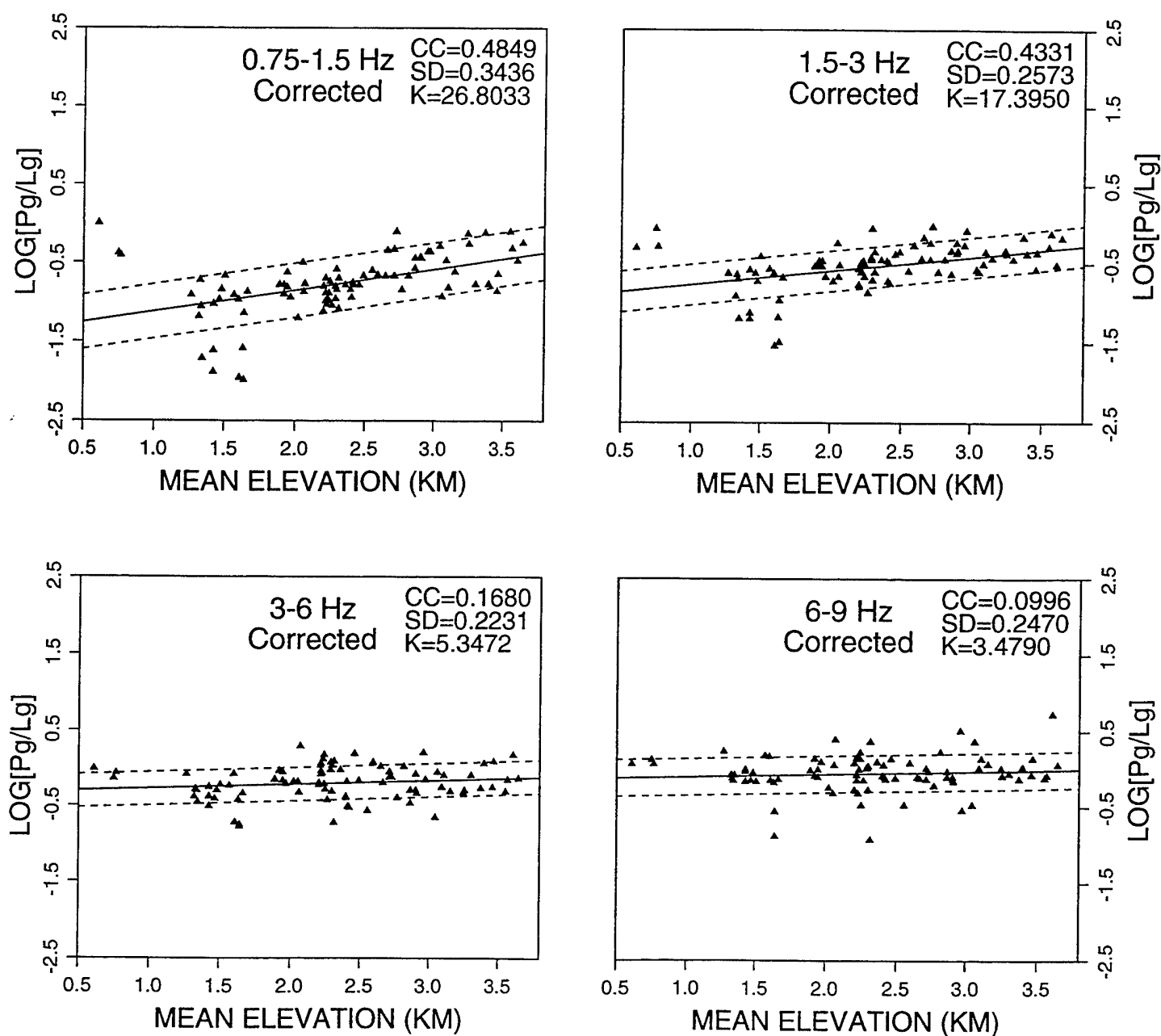


Figure A2c. Frequency dependent ratios of Pg/Lg phases recorded at WMQ plotted as a function of mean elevation of each path after correcting for the distance dependence in Figure A2a. CC denotes the linear correlation coefficient. SD denotes the standard deviation of the linear regression, with the dotted lines corresponding to  $\pm 1$  SD, and K denotes the slope of the regression.

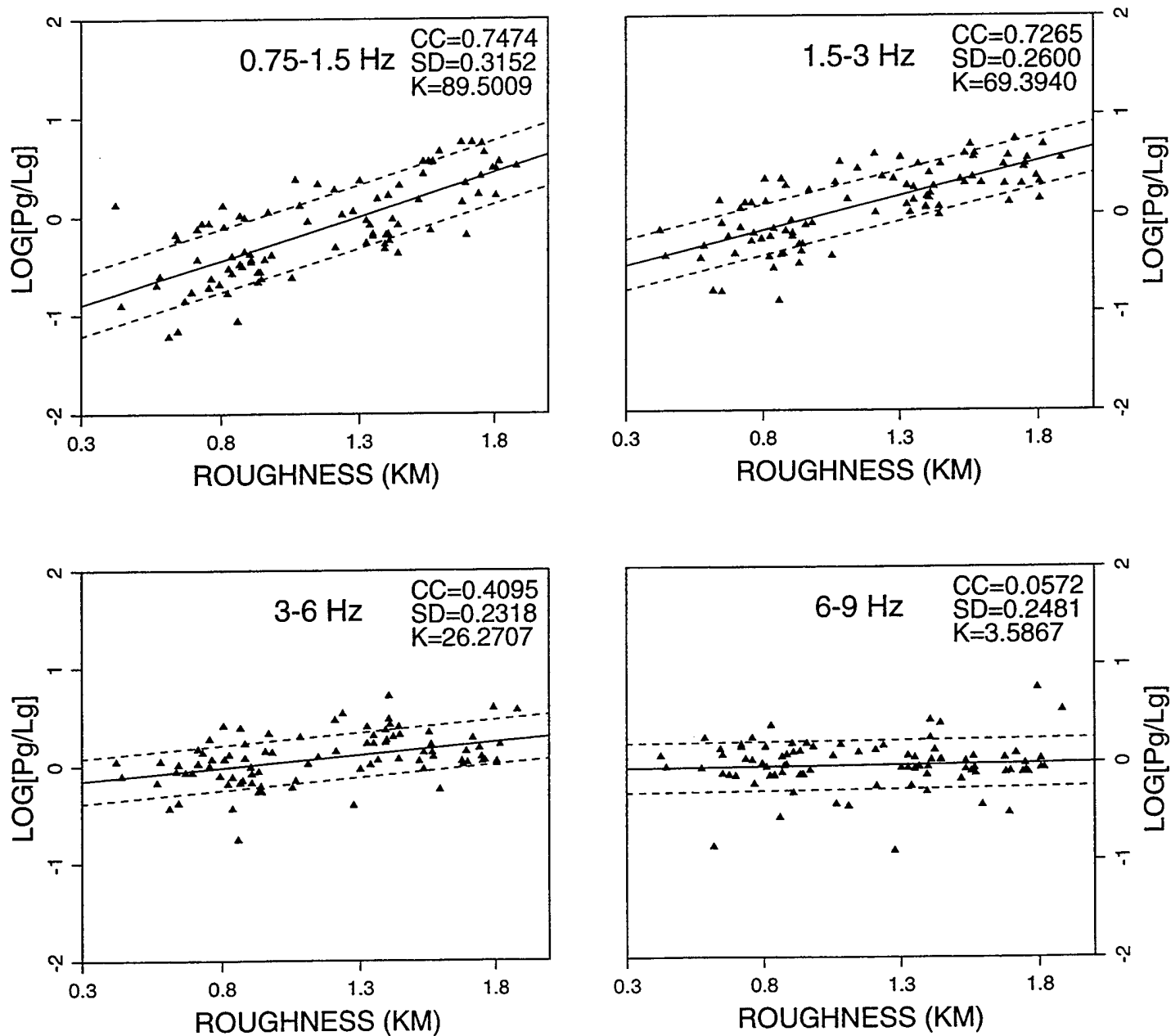


Figure A2d. Frequency dependent ratios of Pg/Lg phases recorded at WMQ plotted as a function of mean surface roughness of each path. CC denotes the linear correlation coefficient. SD denotes the standard deviation of the linear regression, with the dotted lines corresponding to  $\pm 1$  SD, and K denotes the slope of the regression.



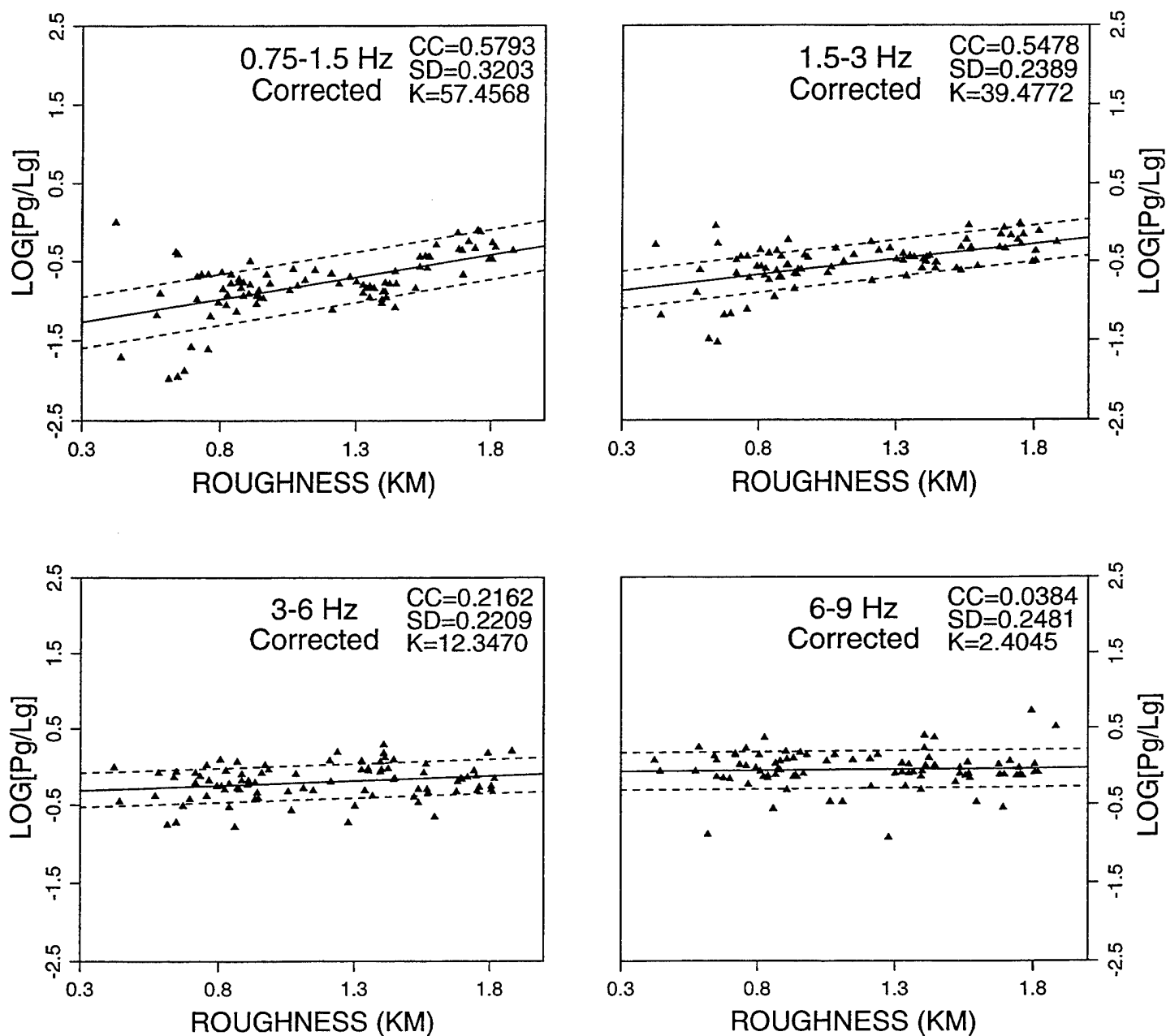


Figure A2e. Frequency dependent ratios of Pg/Lg phases recorded at WMQ plotted as a function of mean surface roughness of each path after correcting for the distance dependence in Figure A2a. CC denotes the linear correlation coefficient. SD denotes the standard deviation of the linear regression, with the dotted lines corresponding to  $\pm 1$  SD, and K denotes the slope of the regression.

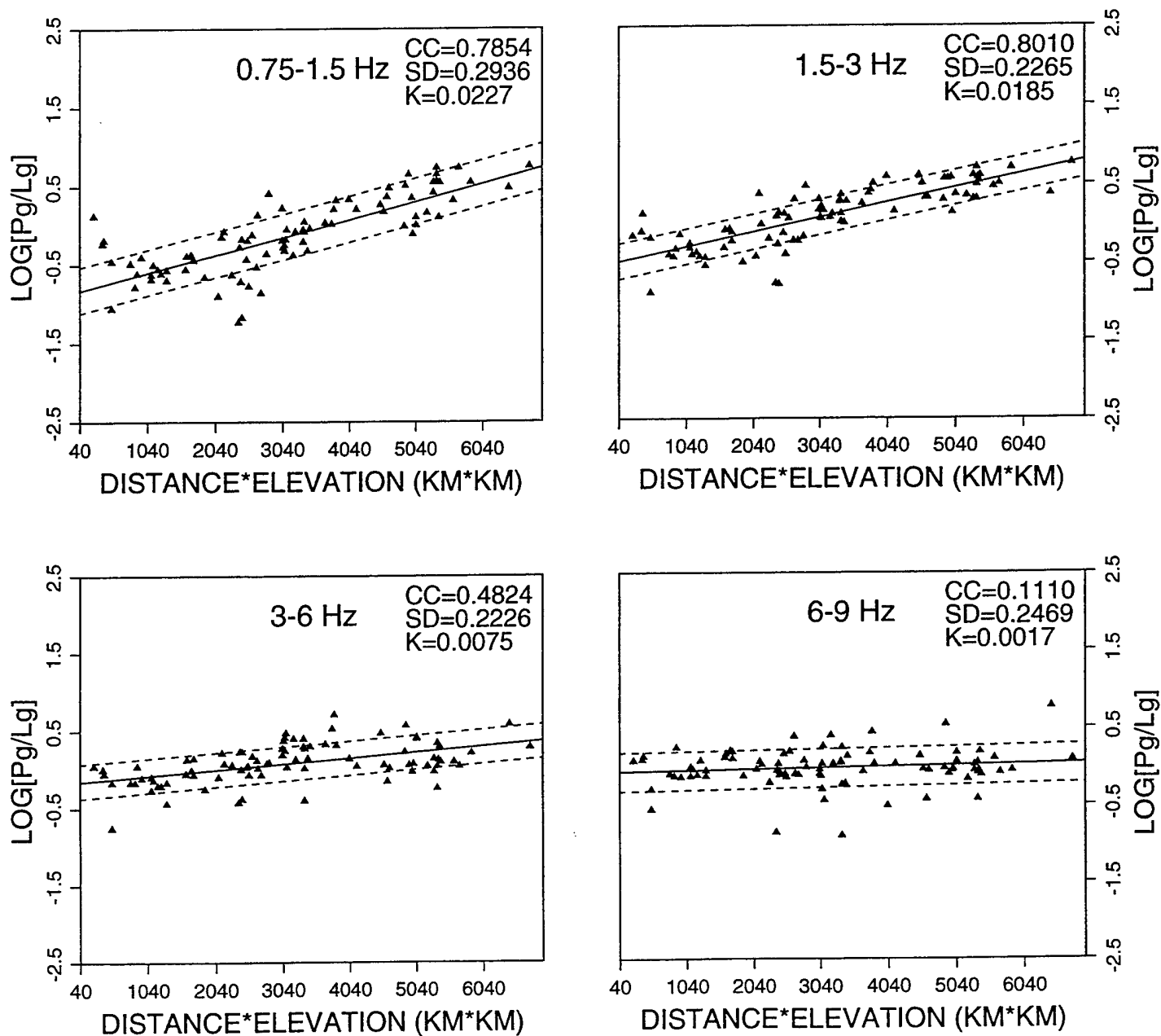


Figure A2f. Frequency dependent ratios of Pg/Lg phases recorded at WMQ plotted as a function of the product of path length times mean path elevation. CC denotes the linear correlation coefficient. SD denotes the standard deviation of the linear regression, with the dotted lines corresponding to  $\pm 1$  SD, and K denotes the slope of the regression.

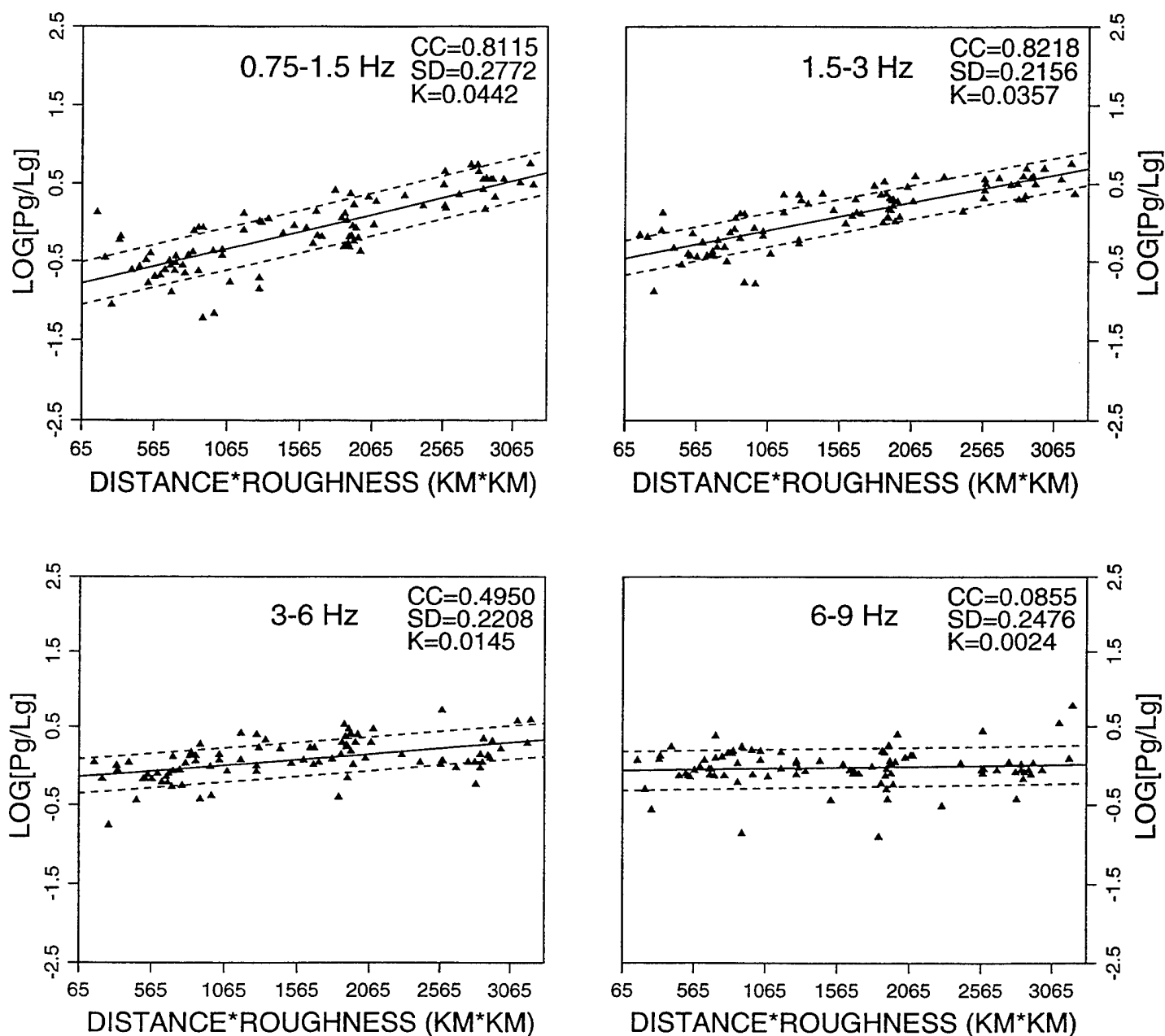


Figure A2g. Frequency dependent ratios of Pg/Lg phases recorded at WMQ plotted as a function of the product of path length times mean surface roughness. CC denotes the linear correlation coefficient. SD denotes the standard deviation of the linear regression, with the dotted lines corresponding to  $\pm 1$  SD, and K denotes the slope of the regression.

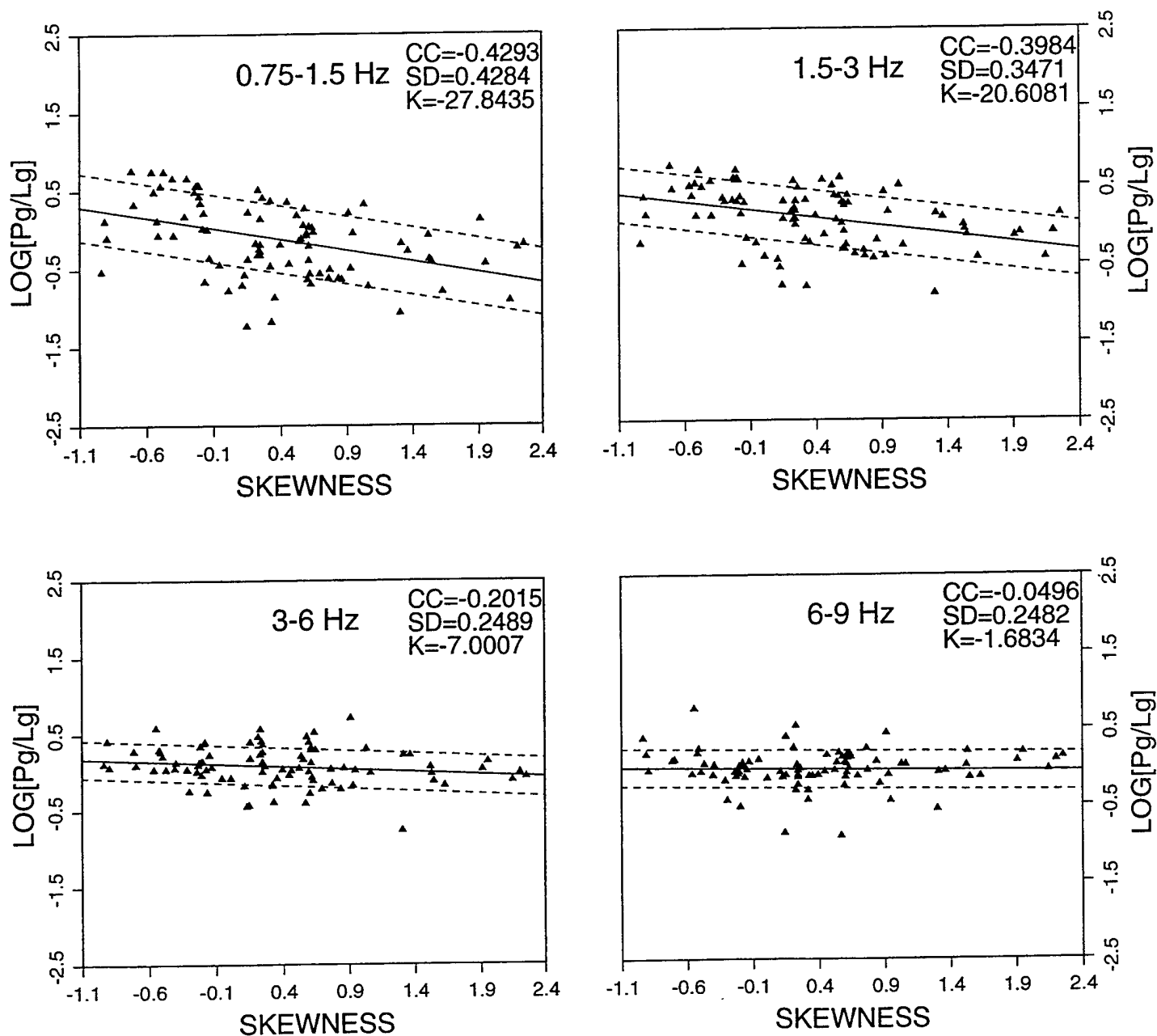


Figure A2h. Frequency dependent ratios of Pg/Lg phases recorded at WMQ plotted as a function of mean surface skewness of each path. CC denotes the linear correlation coefficient. SD denotes the standard deviation of the linear regression, with the dotted lines corresponding to  $\pm 1$  SD, and K denotes the slope of the regression.

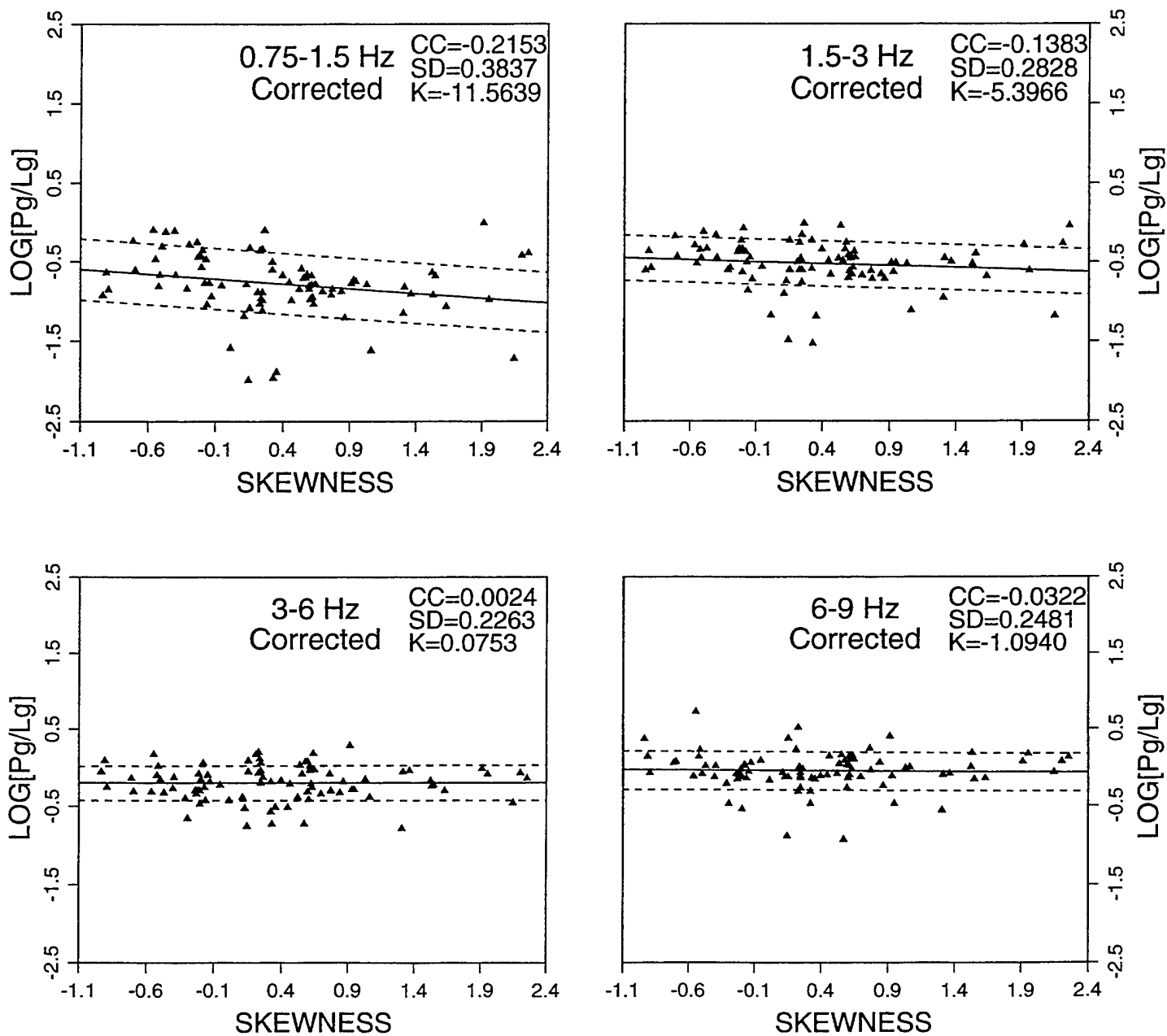


Figure A2i. Frequency dependent ratios of Pg/Lg phases recorded at WMQ plotted as a function of mean surface skewness of each path after correcting for the distance dependence in Figure A2a. CC denotes the linear correlation coefficient. SD denotes the standard deviation of the linear regression, with the dotted lines corresponding to  $\pm 1$  SD, and K denotes the slope of the regression.

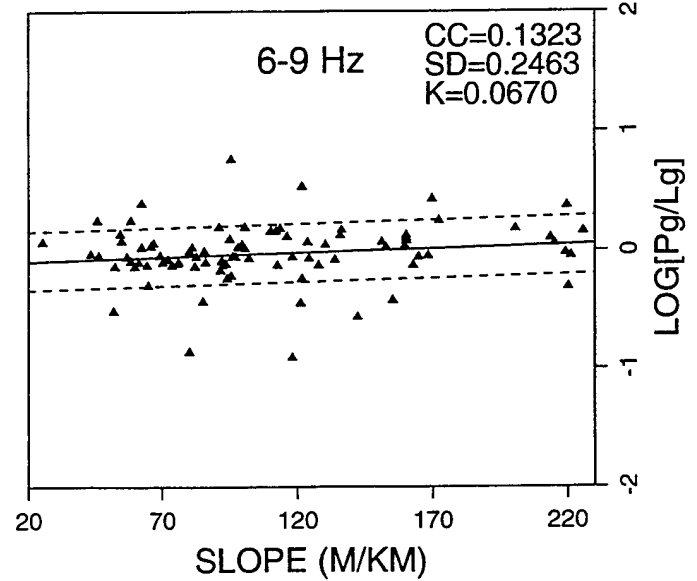
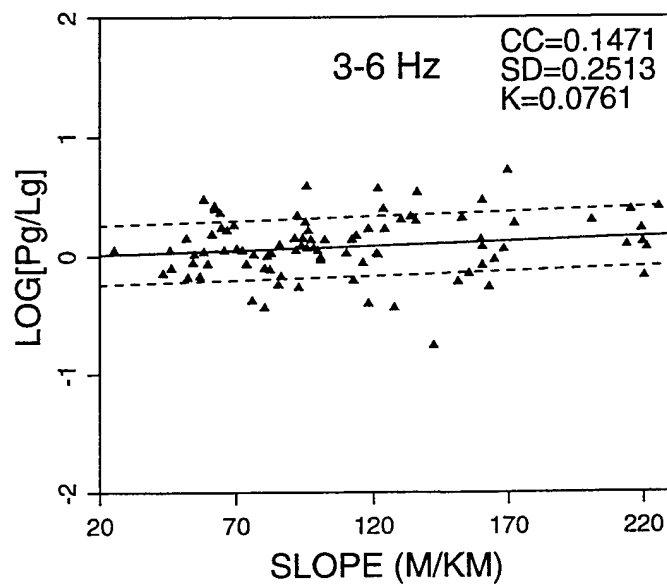
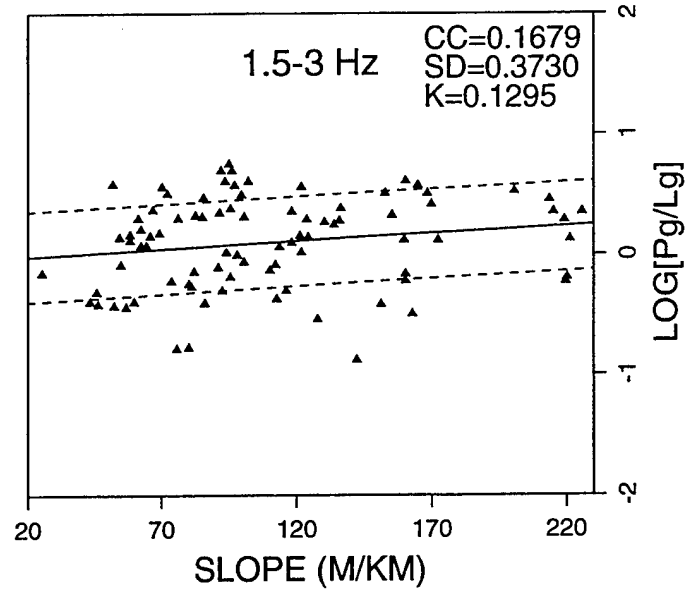
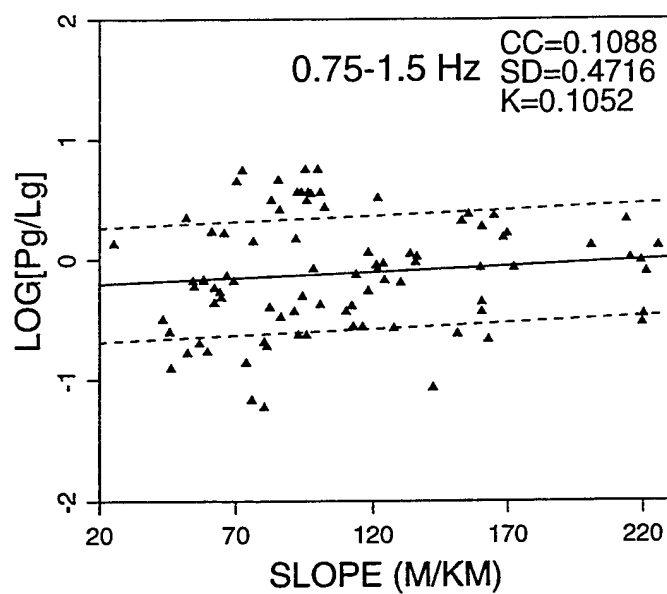


Figure A2j. Frequency dependent ratios of Pg/Lg phases recorded at WMQ plotted as a function of mean surface slope of each path. CC denotes the linear correlation coefficient. SD denotes the standard deviation of the linear regression, with the dotted lines corresponding to  $\pm 1$  SD, and K denotes the slope of the regression.

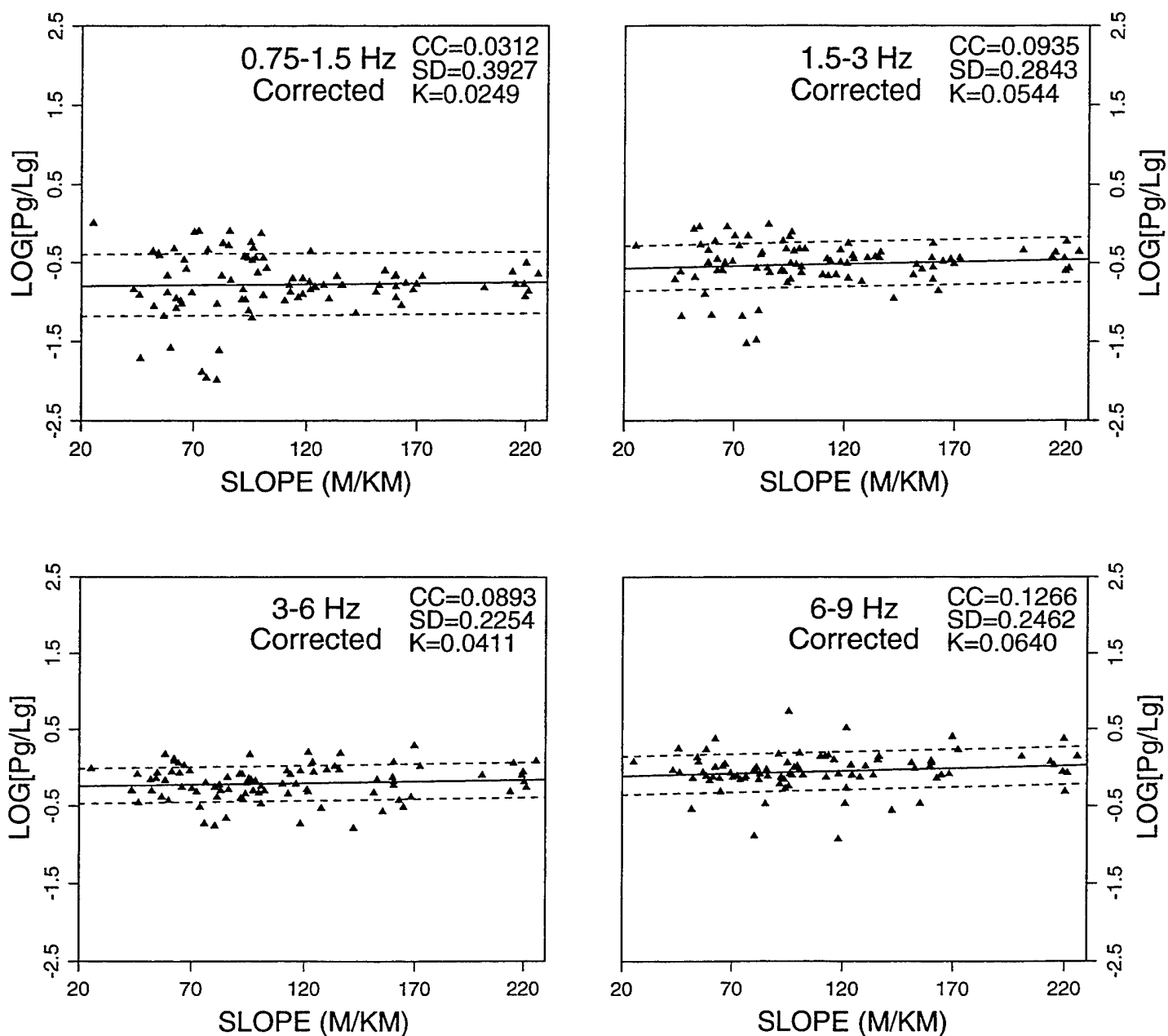


Figure A2k. Frequency dependent ratios of Pg/Lg phases recorded at WMQ plotted as a function of mean surface slope of each path after correcting for the distance dependence in Figure A2a. CC denotes the linear correlation coefficient. SD denotes the standard deviation of the linear regression, with the dotted lines corresponding to  $\pm 1$  SD, and K denotes the slope of the regression.

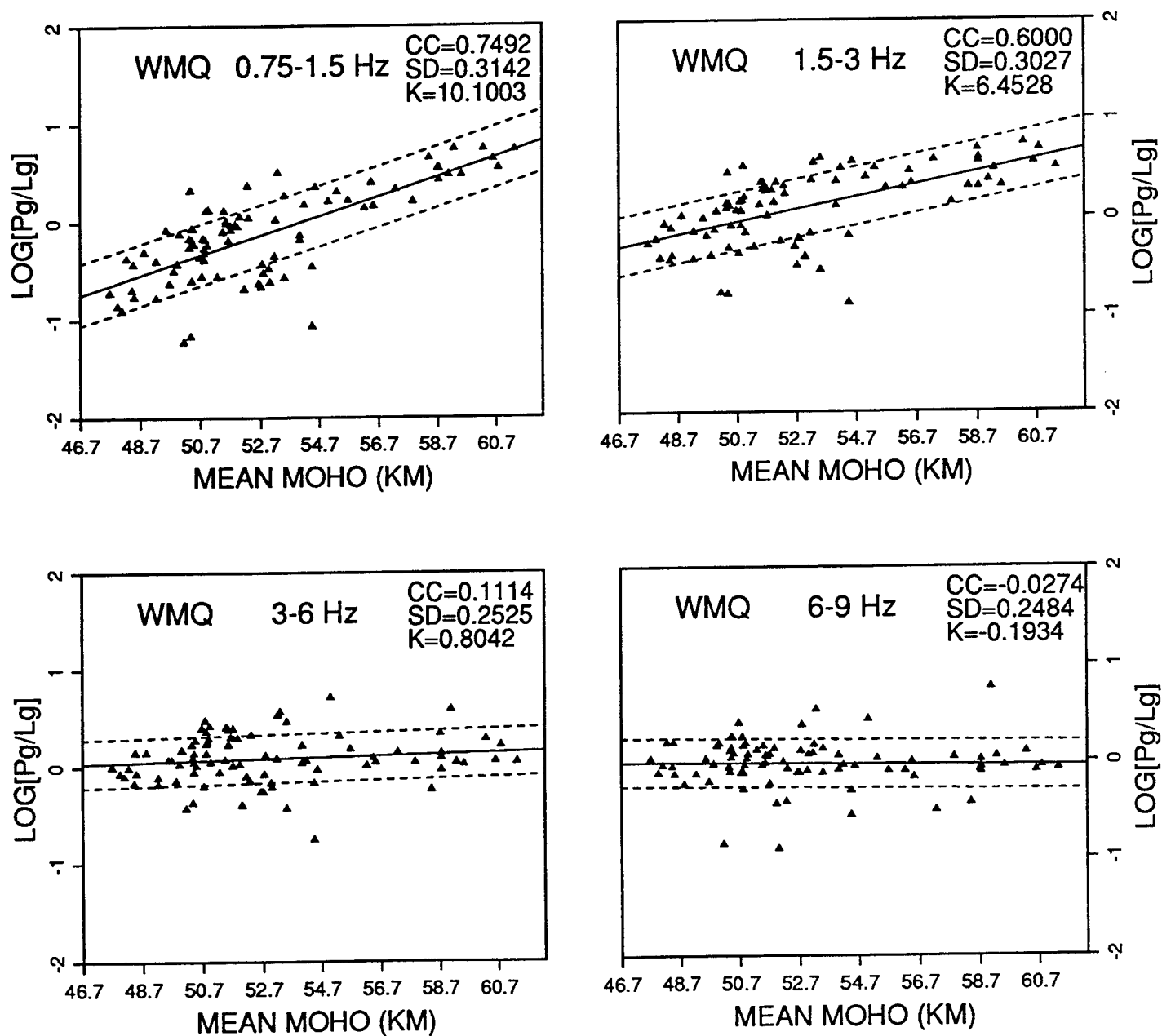


Figure A21. Frequency dependent ratios of Pg/Lg phases recorded at WMQ plotted as a function of mean crustal thickness of each path. CC denotes the linear correlation coefficient. SD denotes the standard deviation of the linear regression, with the dotted lines corresponding to  $\pm 1$  SD, and K denotes the slope of the regression.



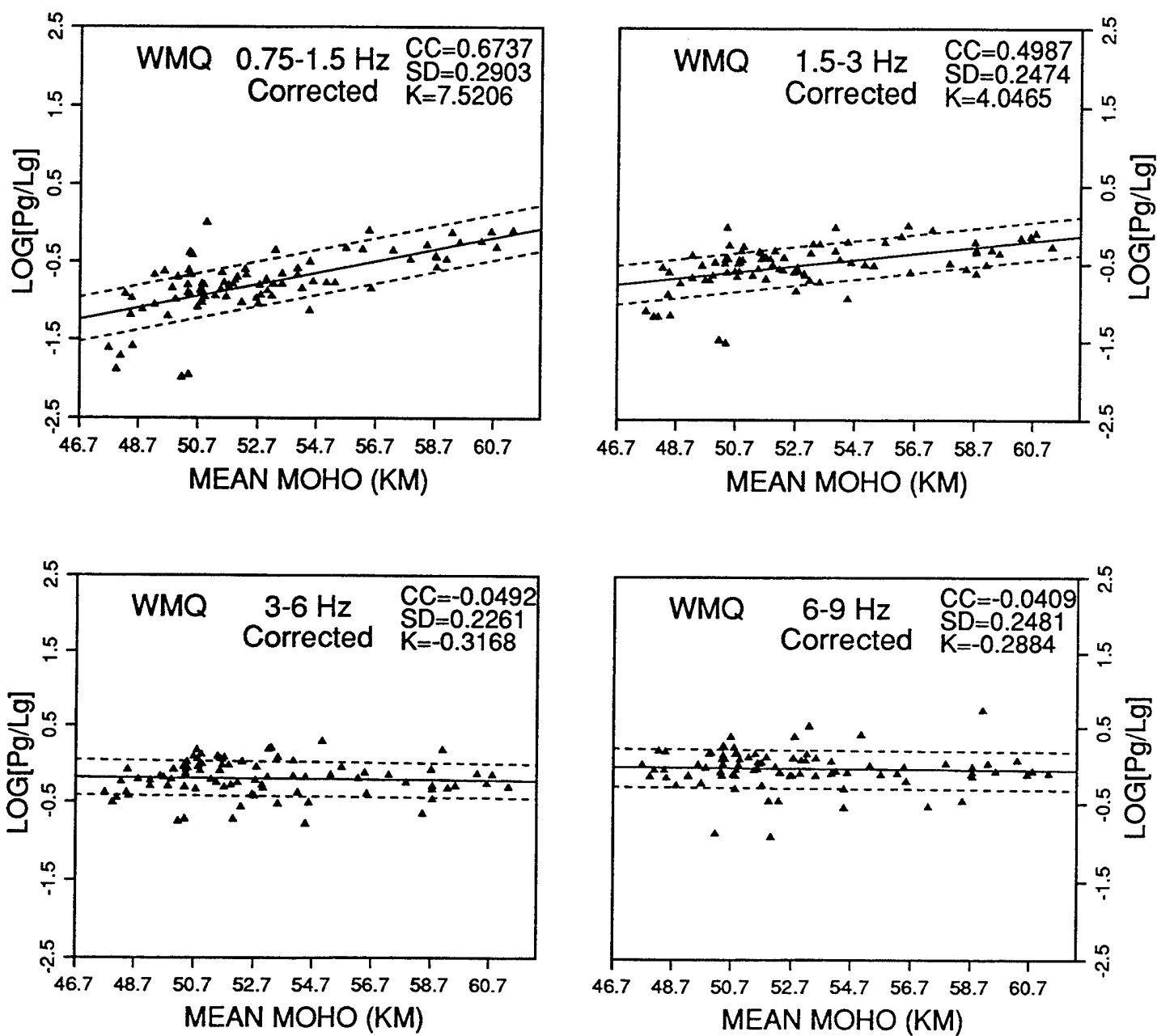


Figure A2m. Frequency dependent ratios of Pg/Lg phases recorded at WMQ plotted as a function of mean crustal thickness of each path after correcting for the distance dependence in Figure A2a. CC denotes the linear correlation coefficient. SD denotes the standard deviation of the linear regression, with the dotted lines corresponding to  $\pm 1$  SD, and K denotes the slope of the regression.

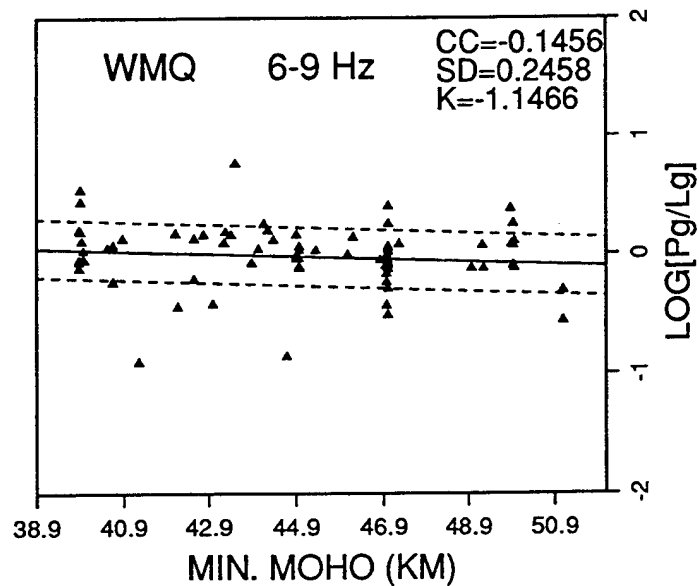
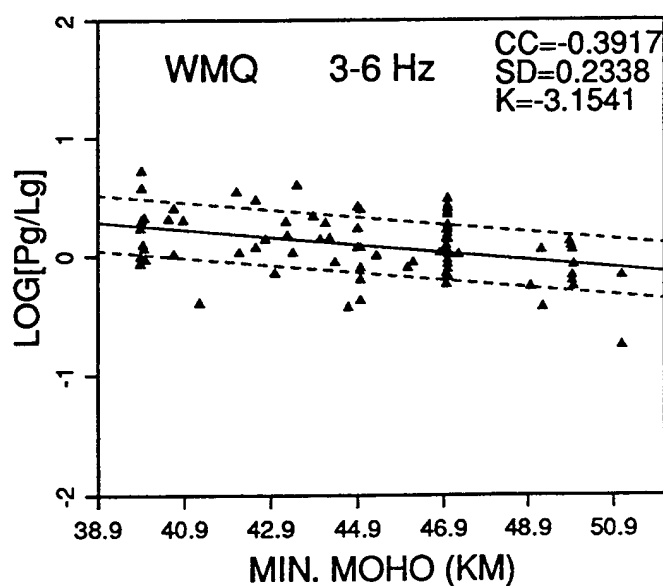
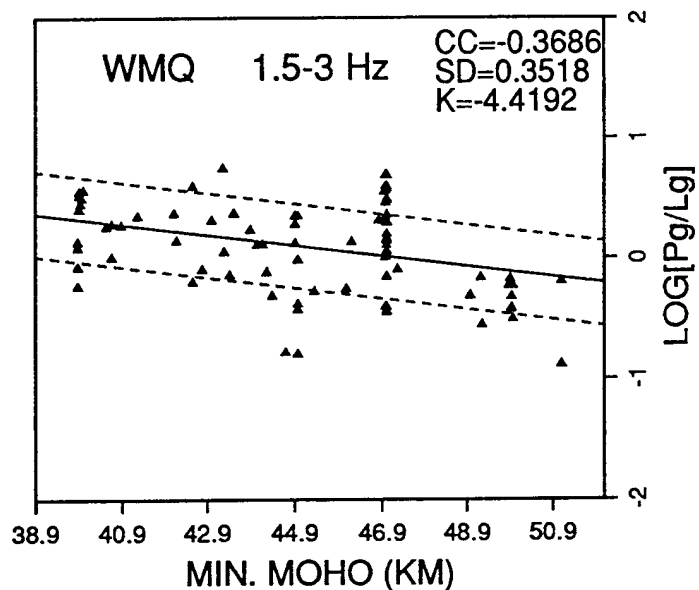
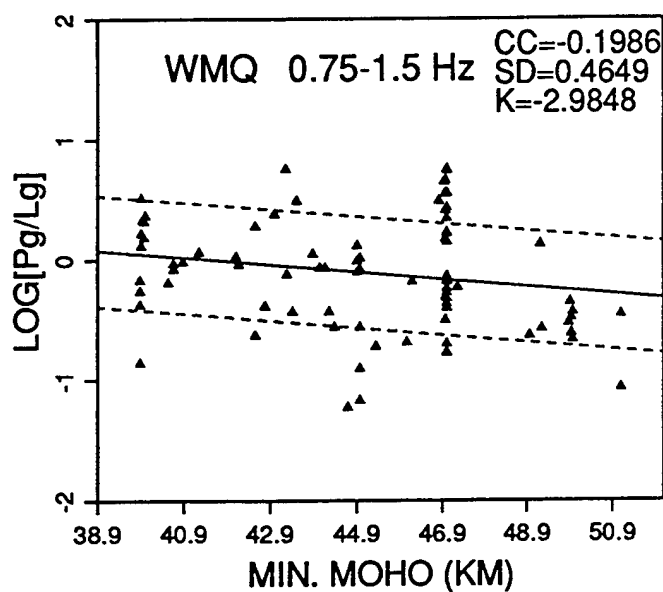


Figure A2n. Frequency dependent ratios of Pg/Lg phases recorded at WMQ plotted as a function of minimum crustal thickness on each path. CC denotes the linear correlation coefficient. SD denotes the standard deviation of the linear regression, with the dotted lines corresponding to  $\pm 1$  SD, and K denotes the slope of the regression.

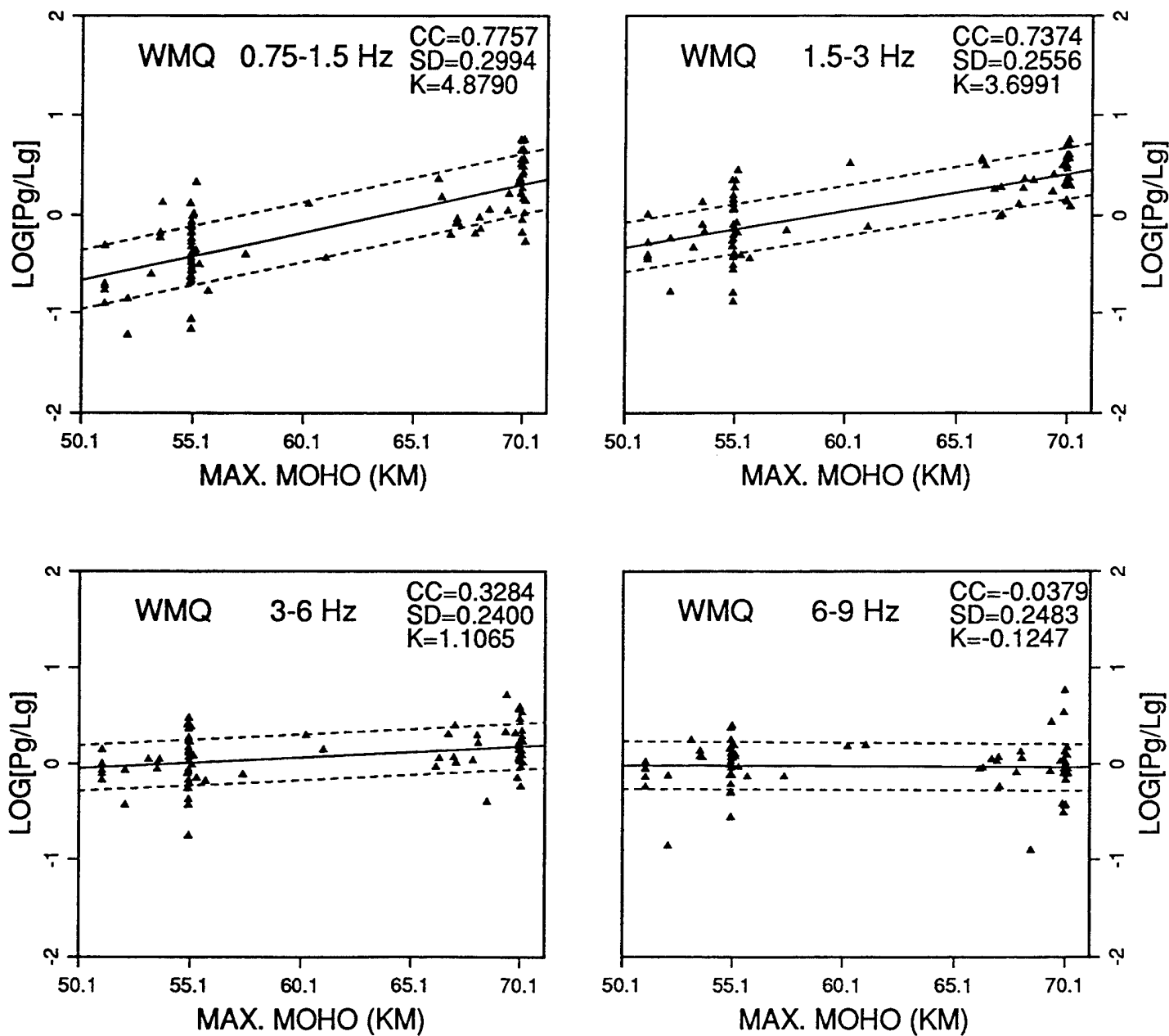


Figure A2o. Frequency dependent ratios of Pg/Lg phases recorded at WMQ plotted as a function of maximum crustal thickness on each path. CC denotes the linear correlation coefficient. SD denotes the standard deviation of the linear regression, with the dotted lines corresponding to  $\pm 1$  SD, and K denotes the slope of the regression.

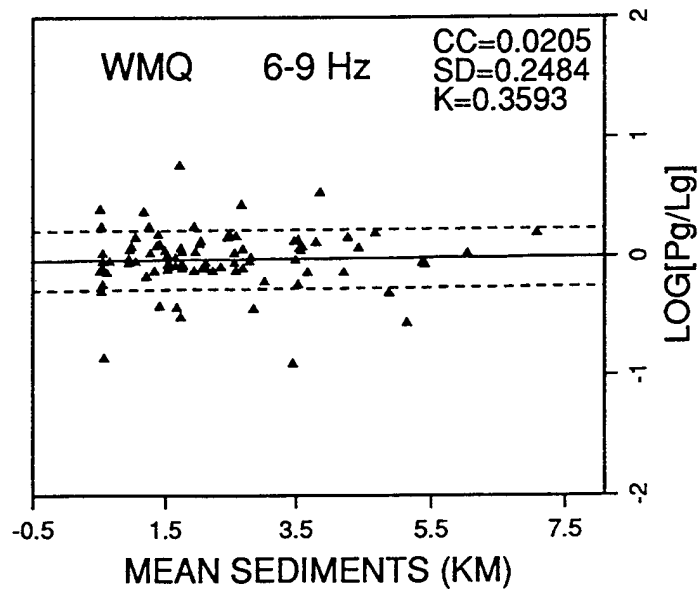
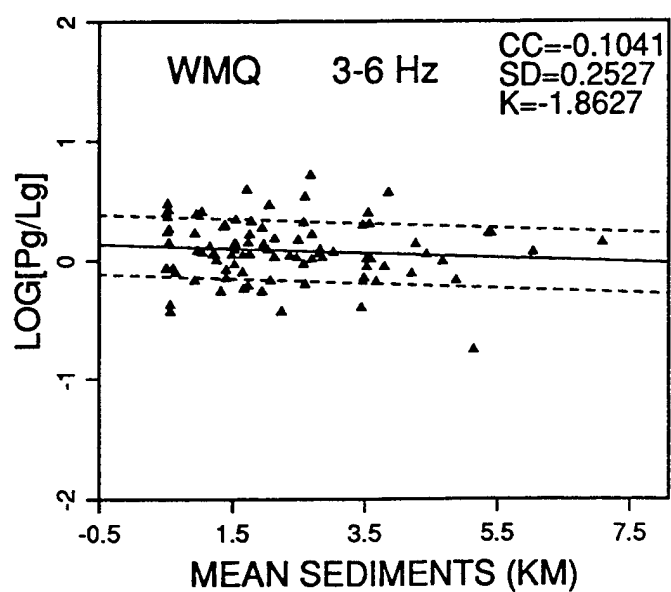
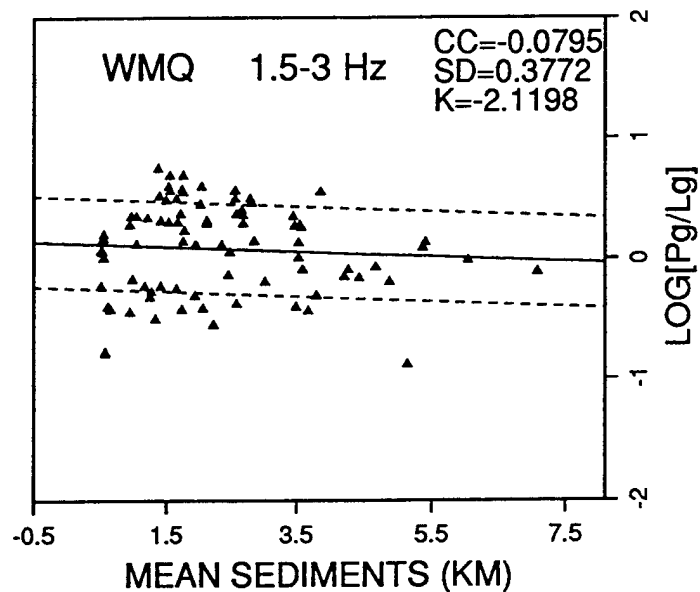
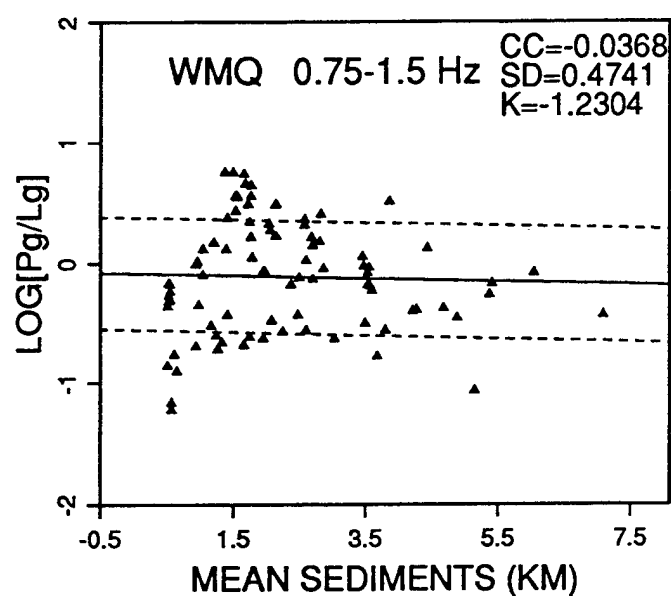


Figure A2p. Frequency dependent ratios of Pg/Lg phases recorded at WMQ plotted as a function of mean sediment thickness of each path. CC denotes the linear correlation coefficient. SD denotes the standard deviation of the linear regression, with the dotted lines corresponding to  $\pm 1$  SD, and K denotes the slope of the regression.

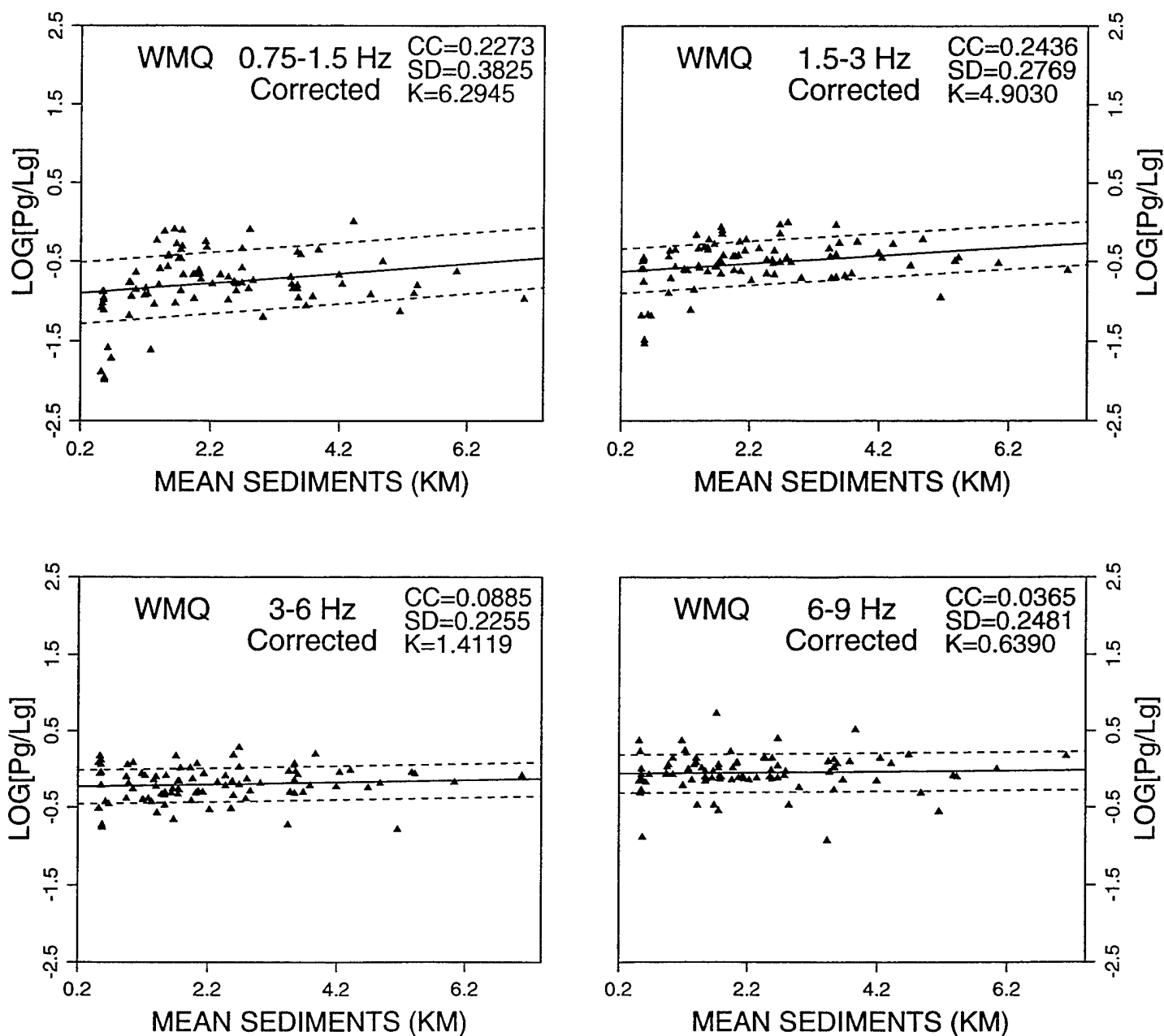


Figure A2q. Frequency dependent ratios of Pg/Lg phases recorded at WMQ plotted as a function of mean sediment thickness of each path after correcting for the distance dependence in Figure A2a. CC denotes the linear correlation coefficient. SD denotes the standard deviation of the linear regression, with the dotted lines corresponding to  $\pm 1$  SD, and K denotes the slope of the regression.

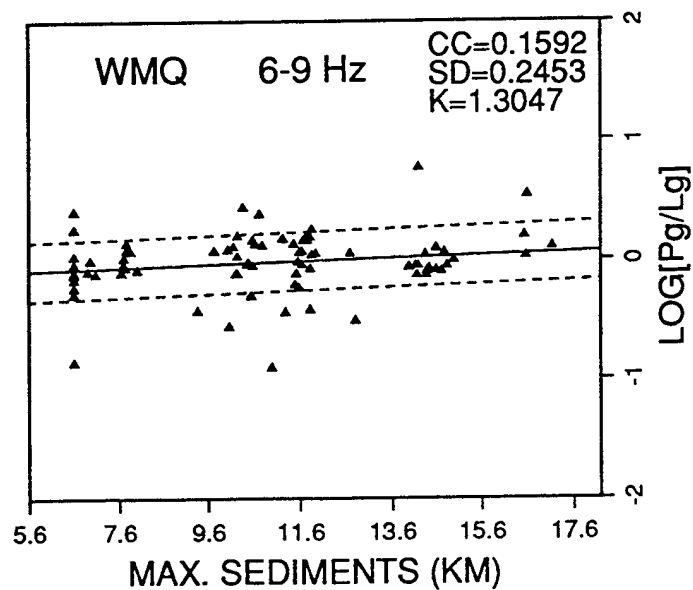
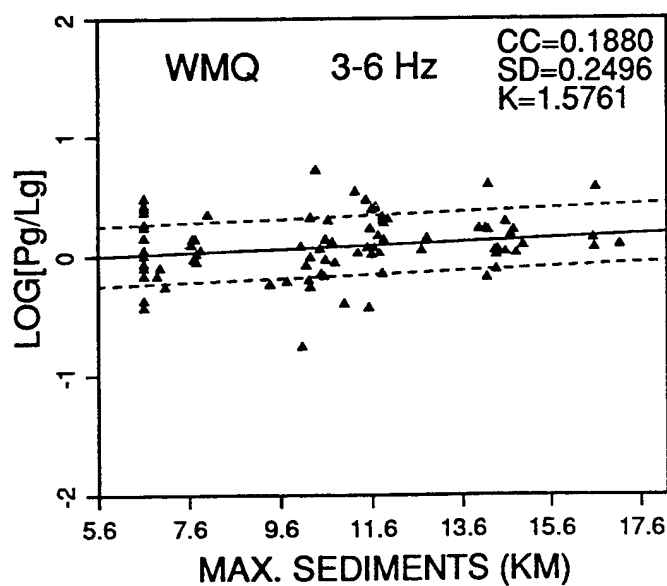
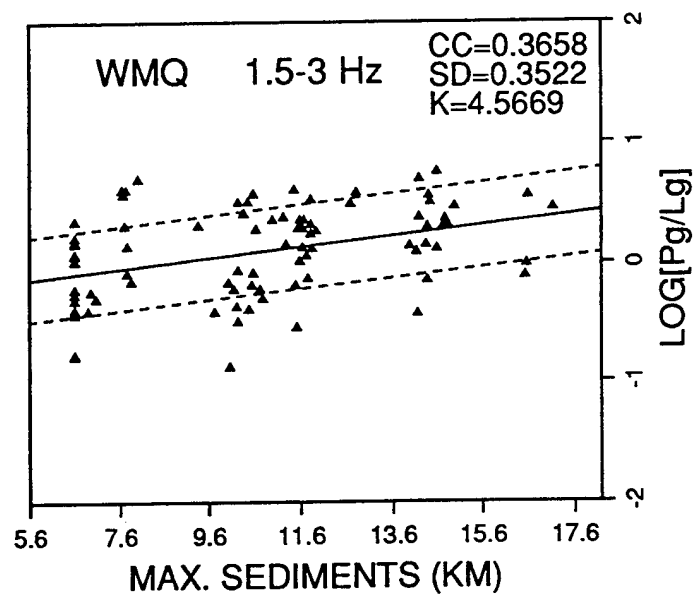
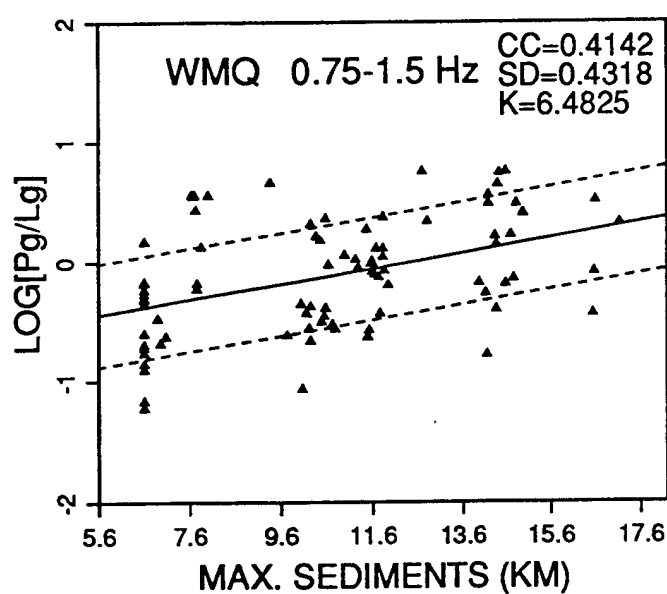


Figure A2r. Frequency dependent ratios of Pg/Lg phases recorded at WMQ plotted as a function of maximum sediment thickness on each path. CC denotes the linear correlation coefficient. SD denotes the standard deviation of the linear regression, with the dotted lines corresponding to  $\pm 1$  SD, and K denotes the slope of the regression.

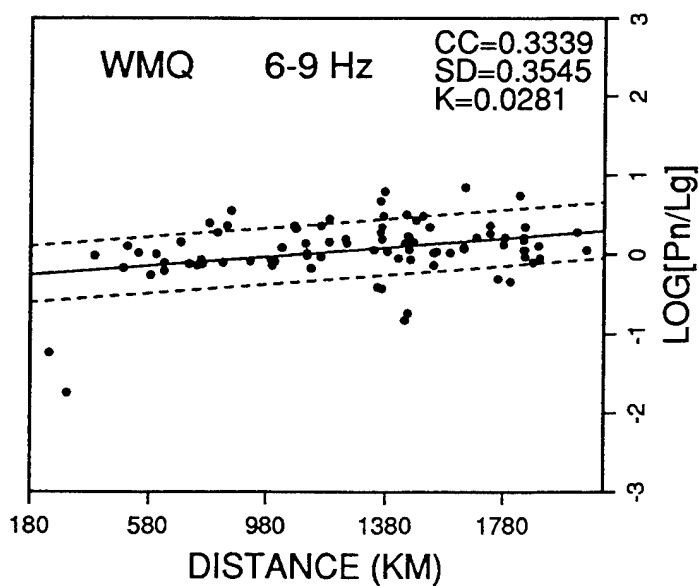
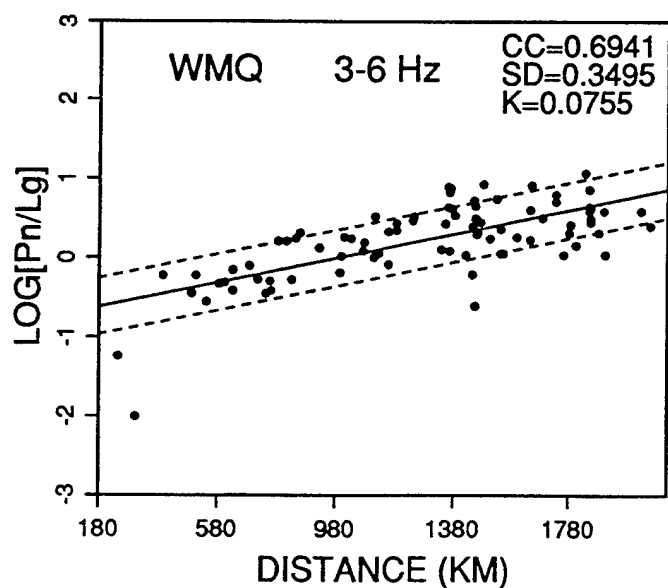
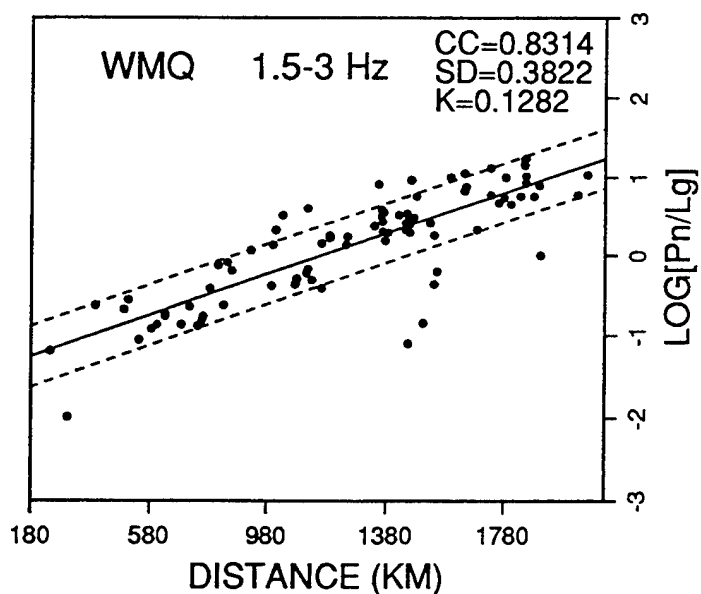
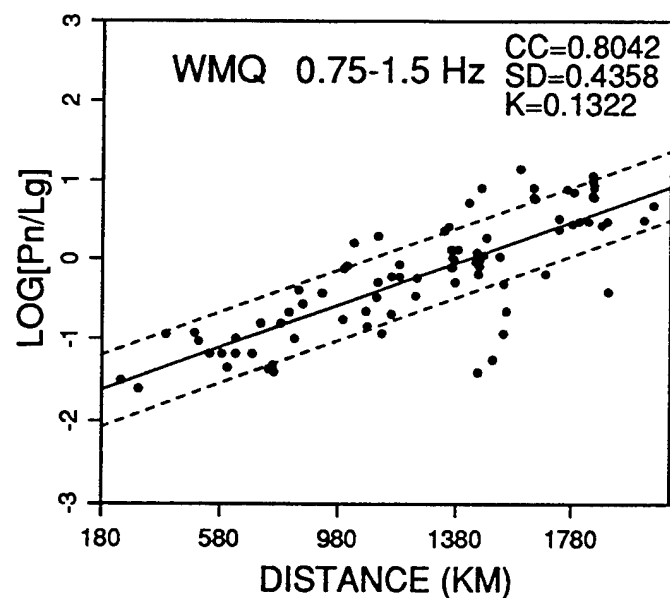


Figure A3a. Frequency dependent ratios of Pn/Lg phases recorded at WMQ plotted as a function of path length. CC denotes the linear correlation coefficient. SD denotes the standard deviation of the linear regression, with the dotted lines corresponding to  $\pm 1$  SD, and K denotes the slope of the regression.

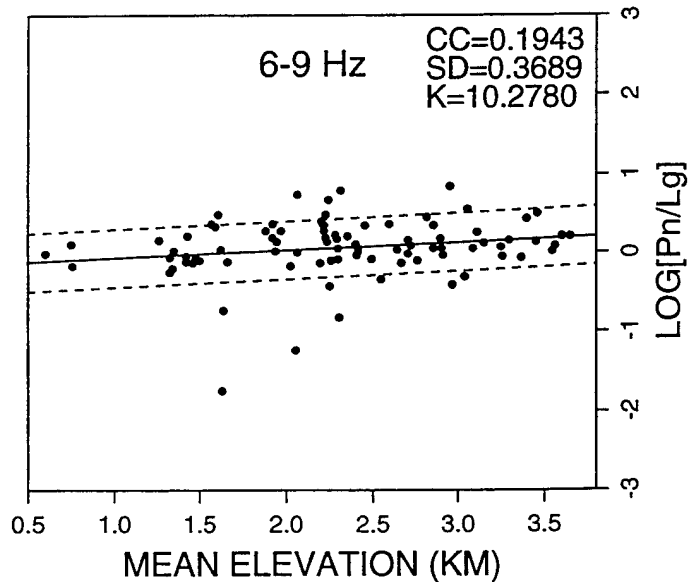
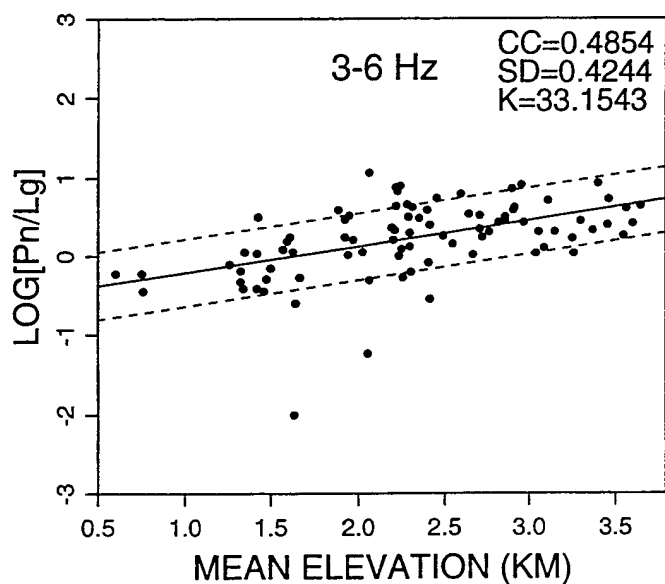
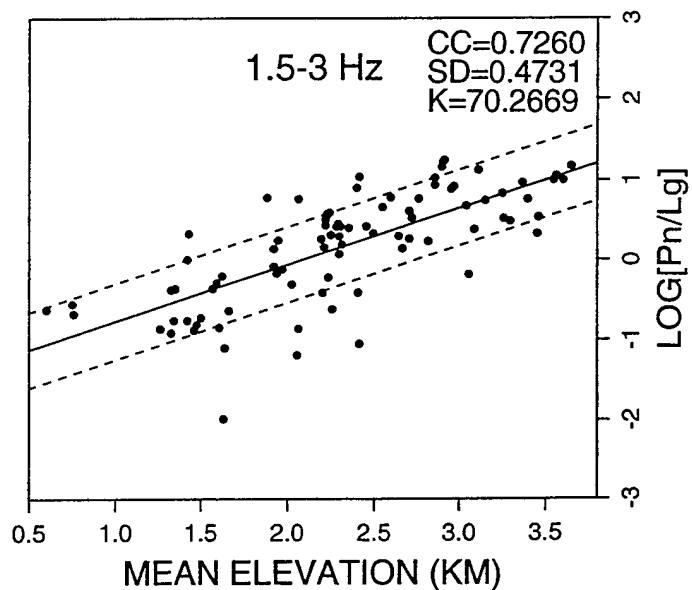
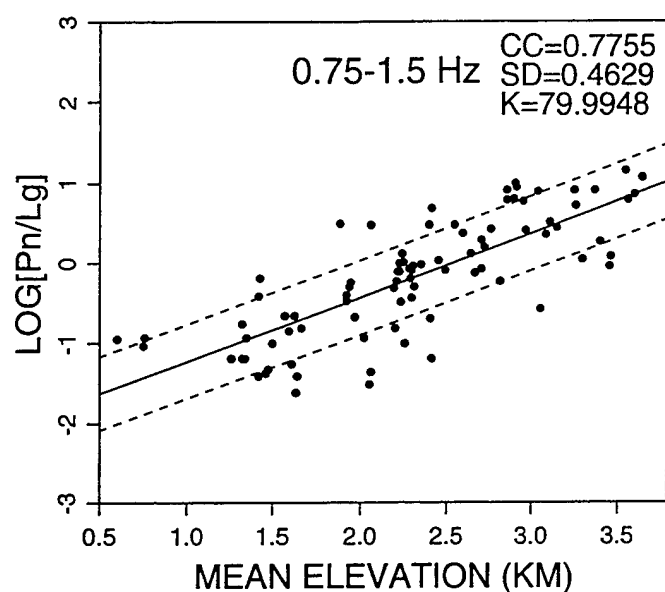


Figure A3b. Frequency dependent ratios of Pn/Lg phases recorded at WMQ plotted as a function of mean elevation of each path. CC denotes the linear correlation coefficient. SD denotes the standard deviation of the linear regression, with the dotted lines corresponding to  $\pm 1$  SD, and K denotes the slope of the regression.



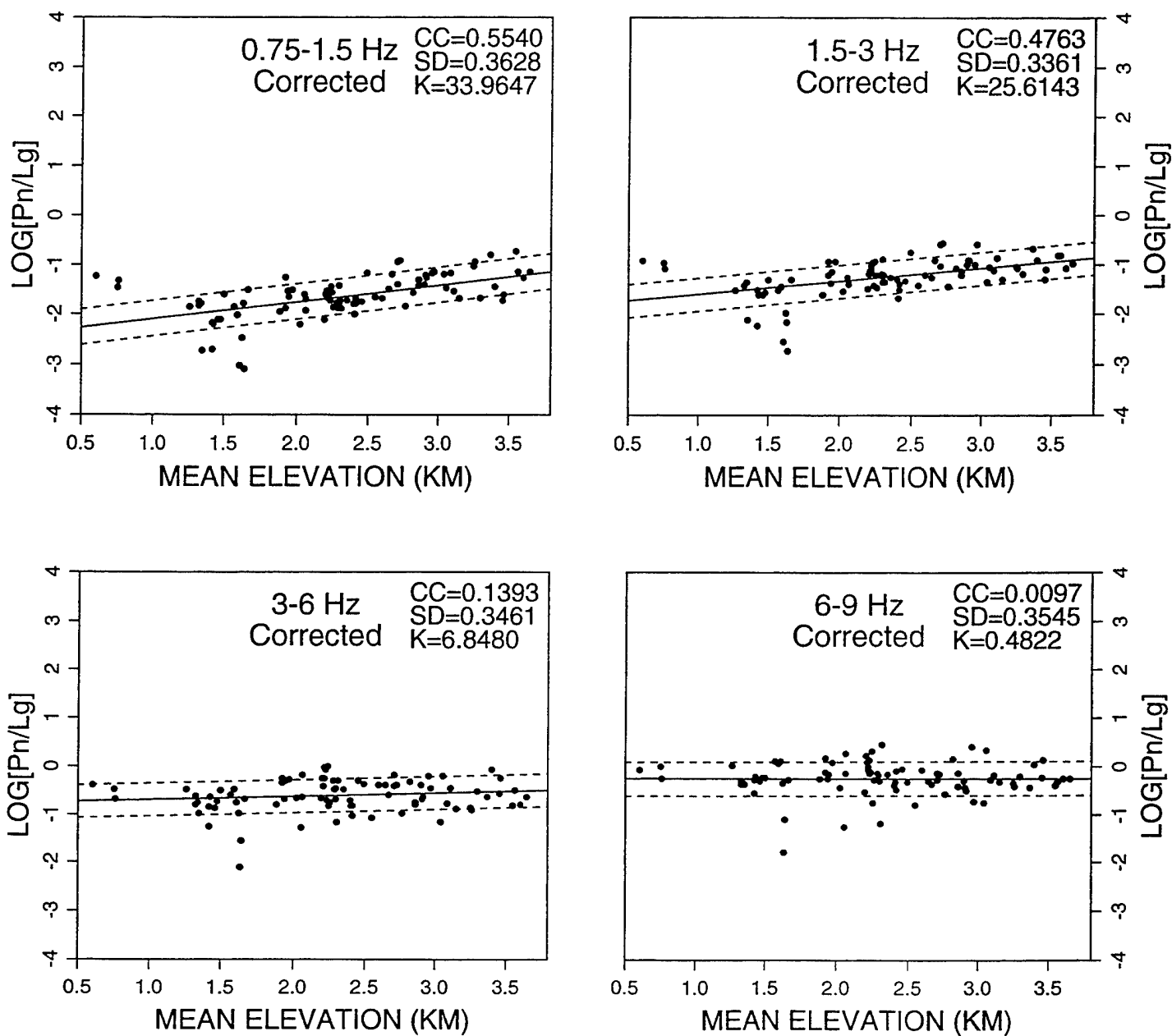


Figure A3c. Frequency dependent ratios of Pn/Lg phases recorded at WMQ plotted as a function of mean elevation of each path as shown in Figure A3a. CC denotes the linear correlation coefficient. SD denotes the standard deviation of the linear regression, with the dotted lines corresponding to  $\pm 1$  SD, and K denotes the slope of the regression.

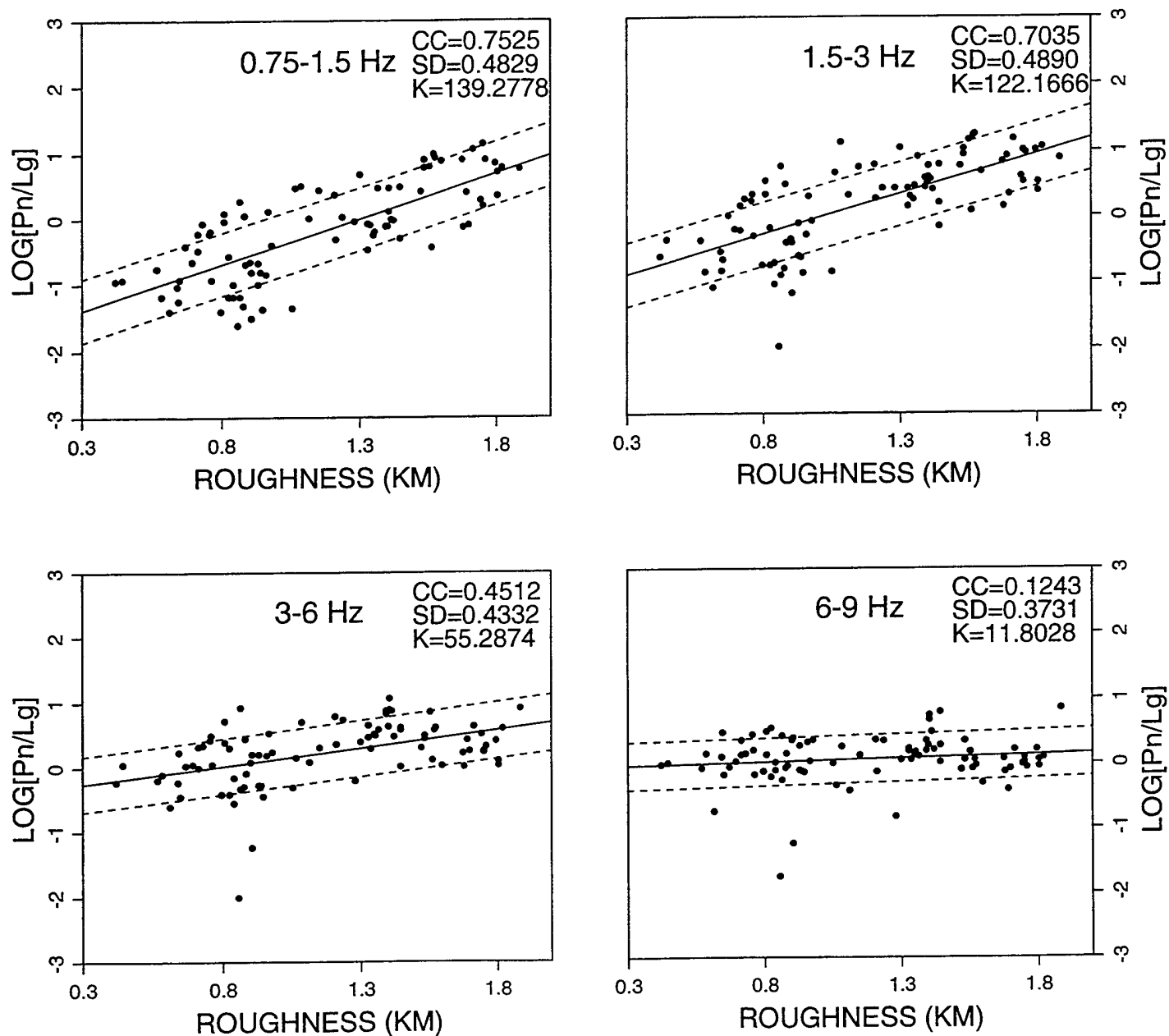


Figure A3d. Frequency dependent ratios of Pn/Lg phases recorded at WMQ plotted as a function of mean surface roughness of each path. CC denotes the linear correlation coefficient. SD denotes the standard deviation of the linear regression, with the dotted lines corresponding to  $\pm 1$  SD, and K denotes the slope of the regression.

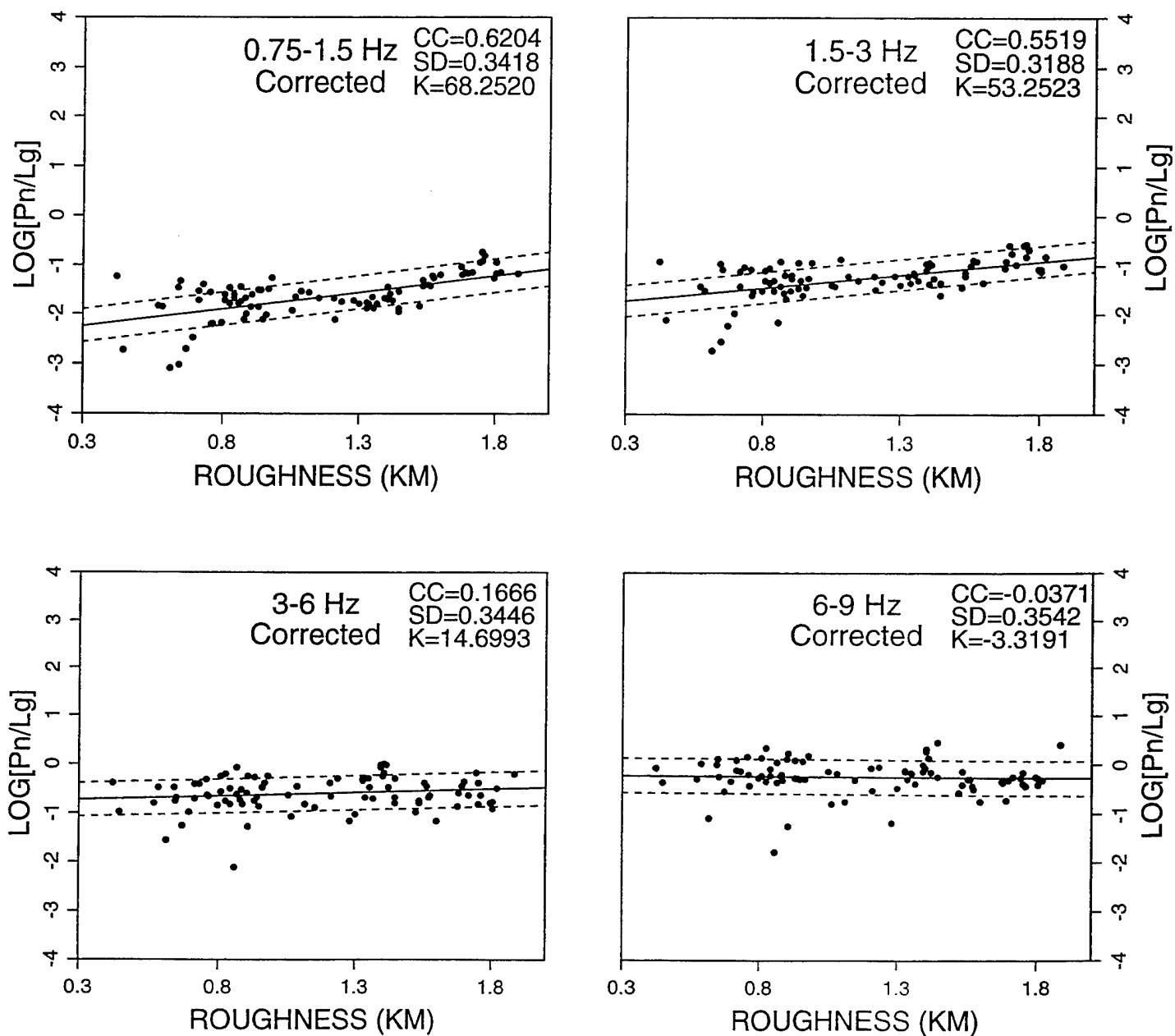


Figure A3e. Frequency dependent ratios of Pn/Lg phases recorded at WMQ plotted as a function of mean surface roughness of each path after correcting for the distance dependence in Figure A3a. CC denotes the linear correlation coefficient. SD denotes the standard deviation of the linear regression, with the dotted lines corresponding to  $\pm 1$  SD, and K denotes the slope of the regression.

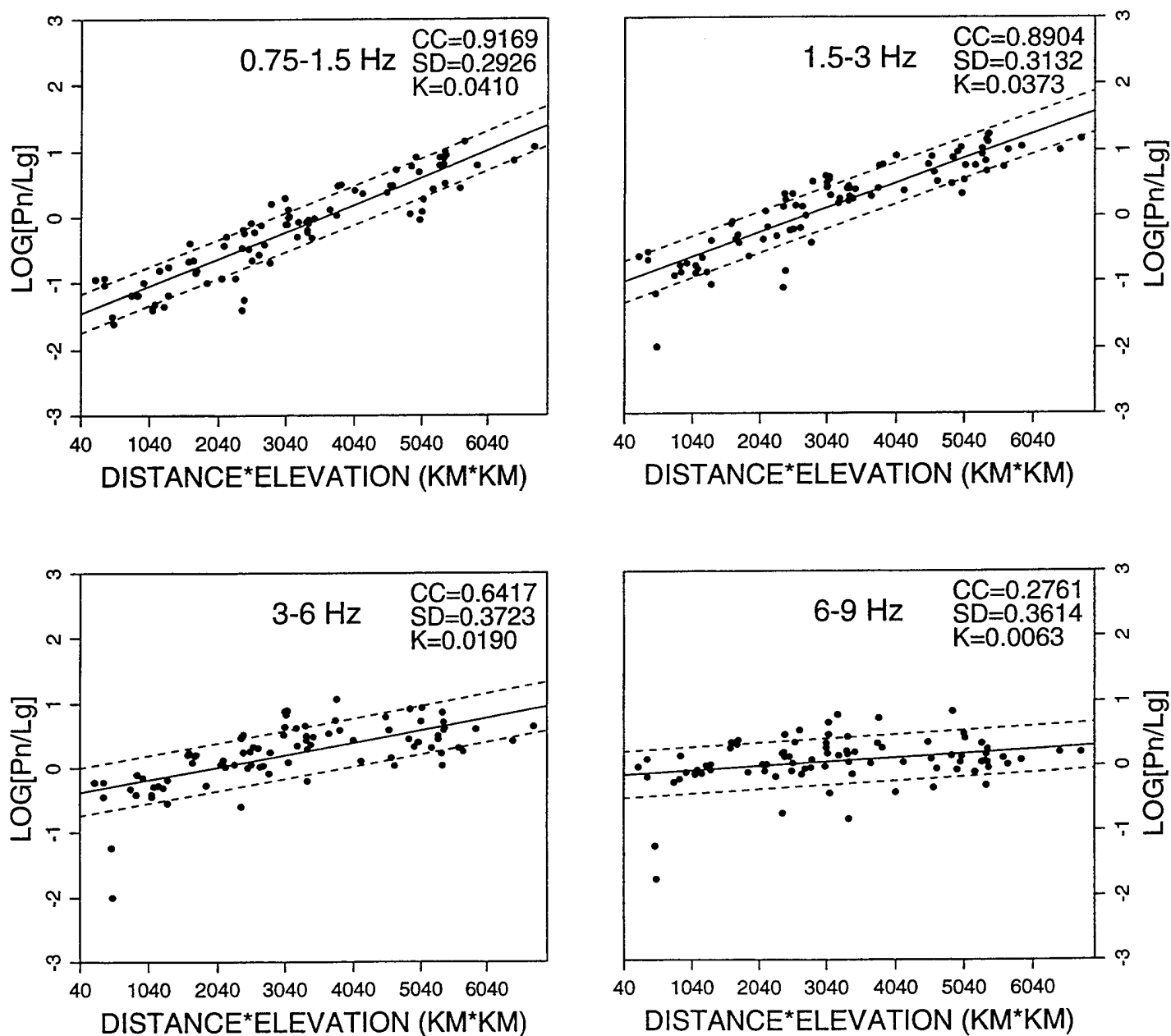


Figure A3f. Frequency dependent ratios of Pn/Lg phases recorded at WMQ plotted as a function of the product of path length times mean path elevation. CC denotes the linear correlation coefficient. SD denotes the standard deviation of the linear regression, with the dotted lines corresponding to  $\pm 1$  SD, and K denotes the slope of the regression.

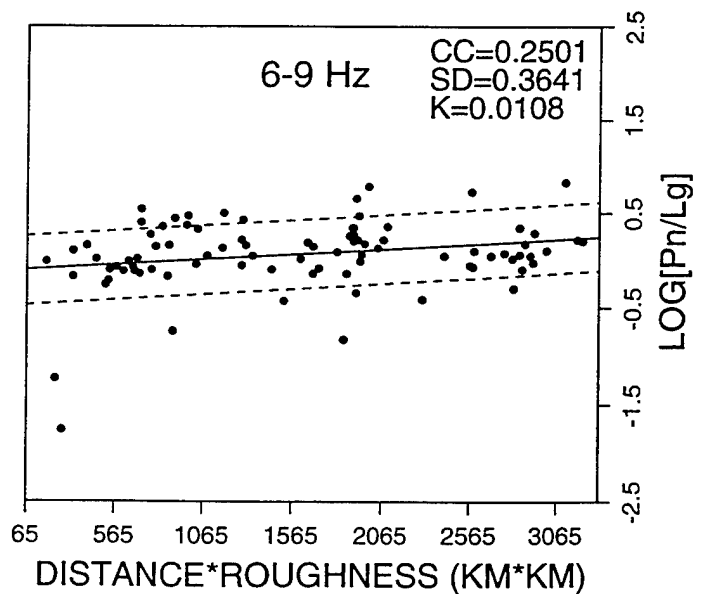
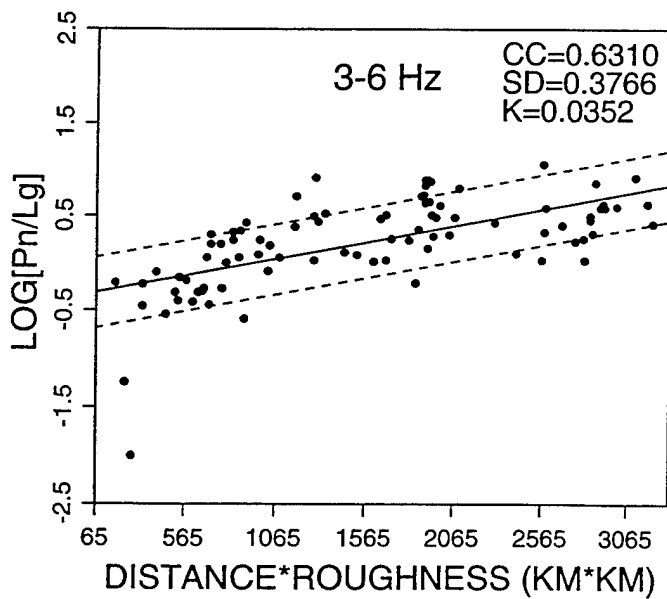
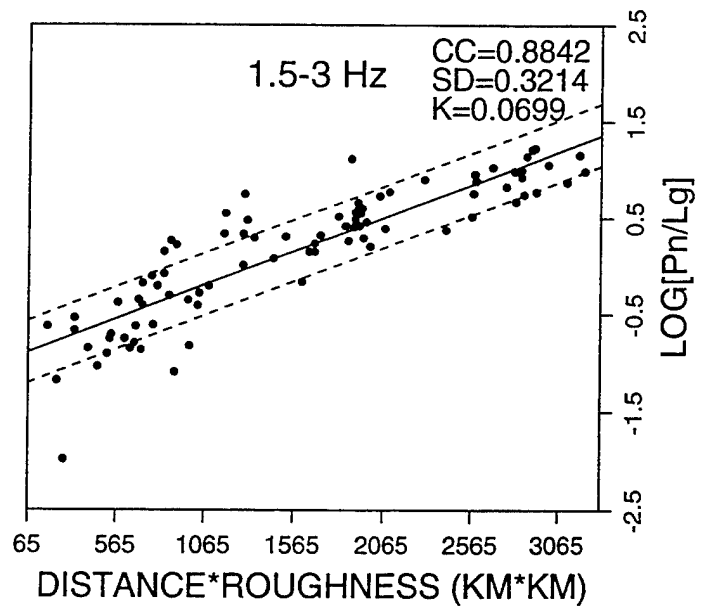
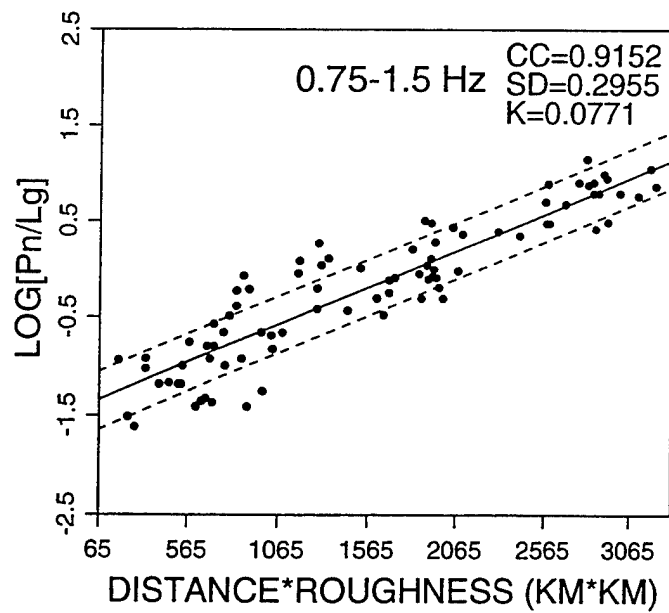


Figure A3g. Frequency dependent ratios of Pn/Lg phases recorded at WMQ plotted as a function of the product of path length times mean surface roughness. CC denotes the linear correlation coefficient. SD denotes the standard deviation of the linear regression, with the dotted lines corresponding to  $\pm 1$  SD, and K denotes the slope of the regression.

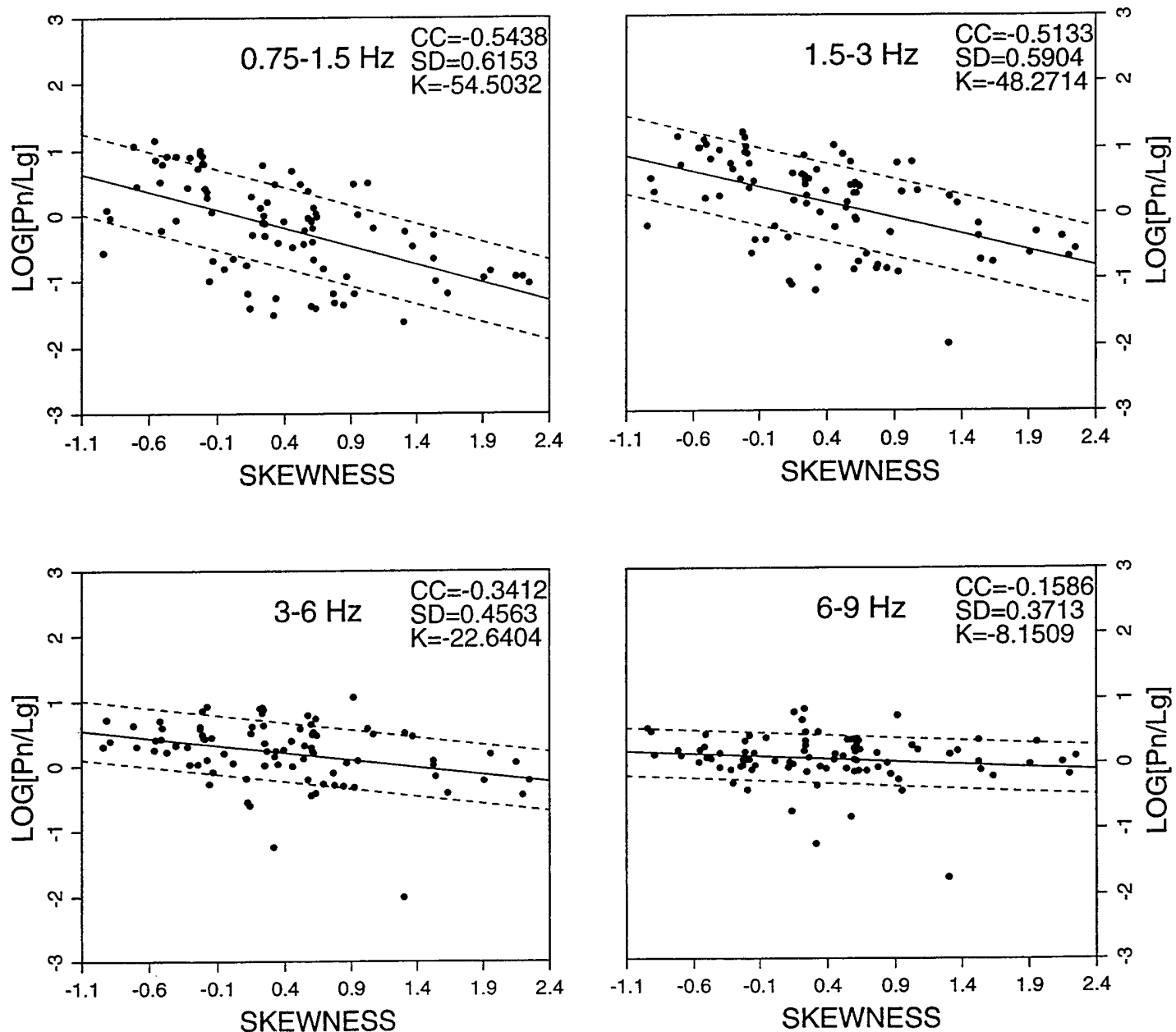


Figure A3h. Frequency dependent ratios of Pn/Lg phases recorded at WMQ plotted as a function of mean surface skewness of each path. CC denotes the linear correlation coefficient. SD denotes the standard deviation of the linear regression, with the dotted lines corresponding to  $\pm 1$  SD, and K denotes the slope of the regression.

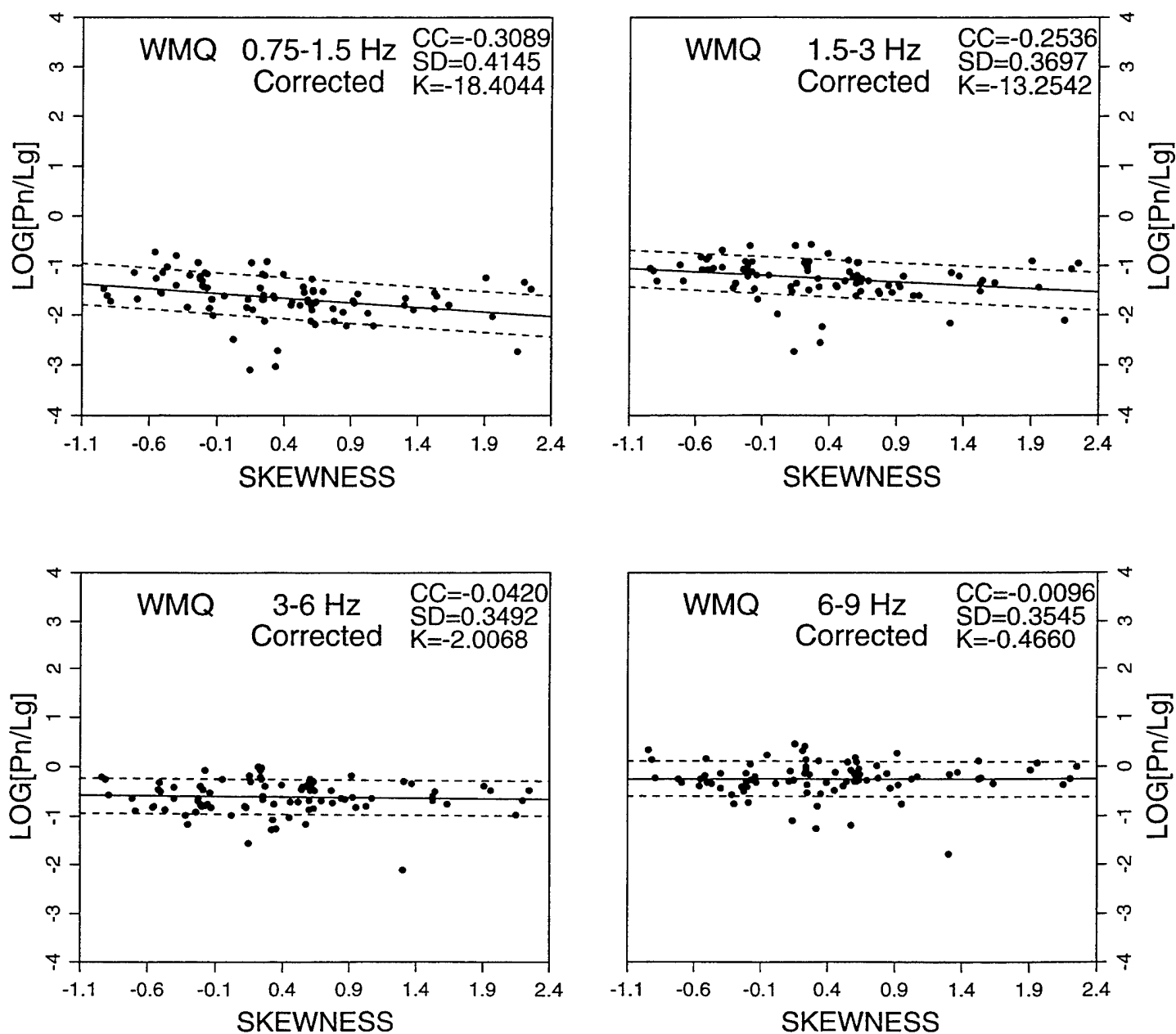


Figure A3i. Frequency dependent ratios of Pn/Lg phases recorded at WMQ plotted as a function of mean surface skewness of each path after correcting for the distance dependence in Figure A3a. CC denotes the linear correlation coefficient. SD denotes the standard deviation of the linear regression, with the dotted lines corresponding to  $\pm 1$  SD, and K denotes the slope of the regression.

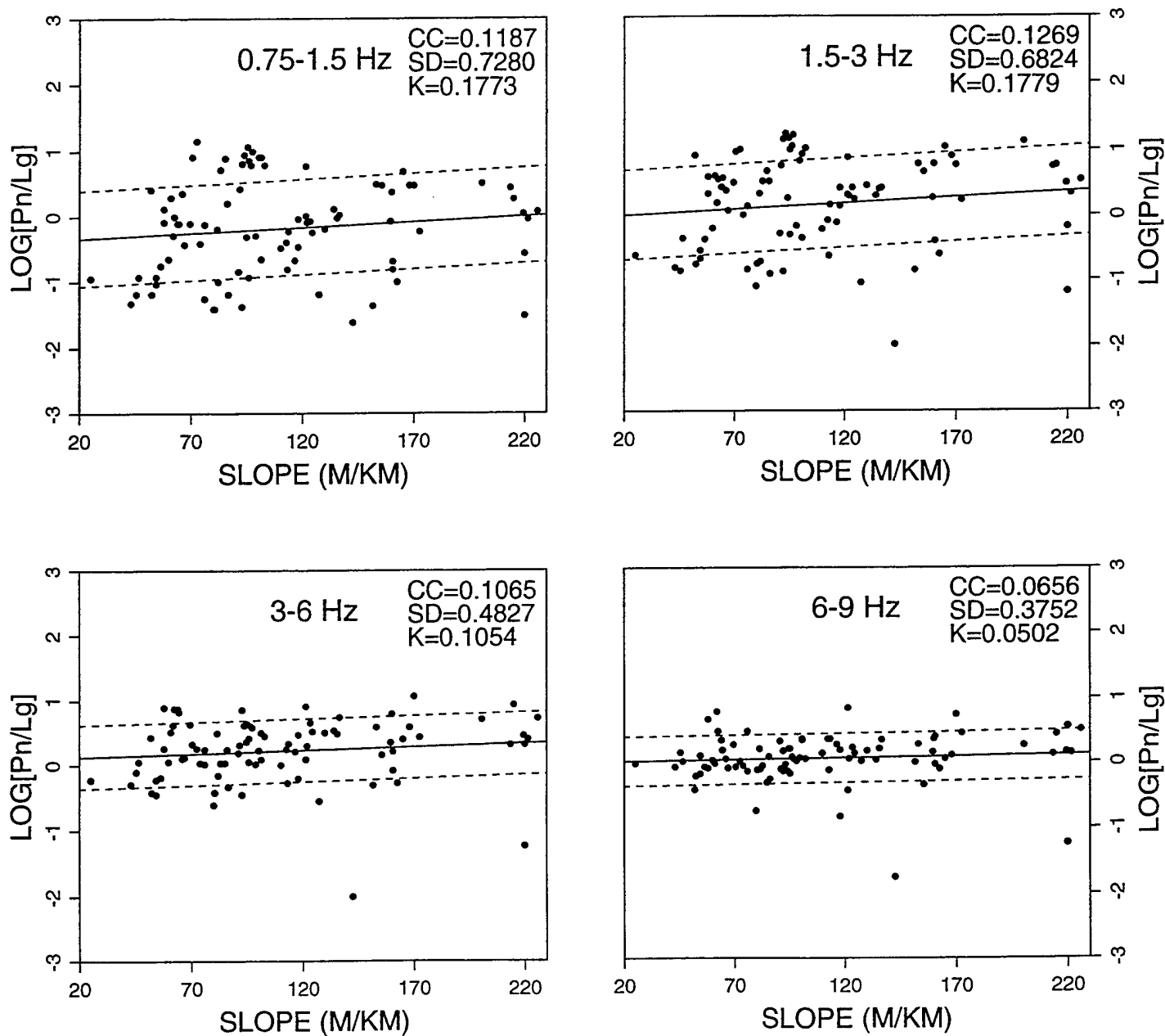


Figure A3j. Frequency dependent ratios of Pn/Lg phases recorded at WMQ plotted as a function of mean surface slope of each path. CC denotes the linear correlation coefficient. SD denotes the standard deviation of the linear regression, with the dotted lines corresponding to  $\pm 1$  SD, and K denotes the slope of the regression.



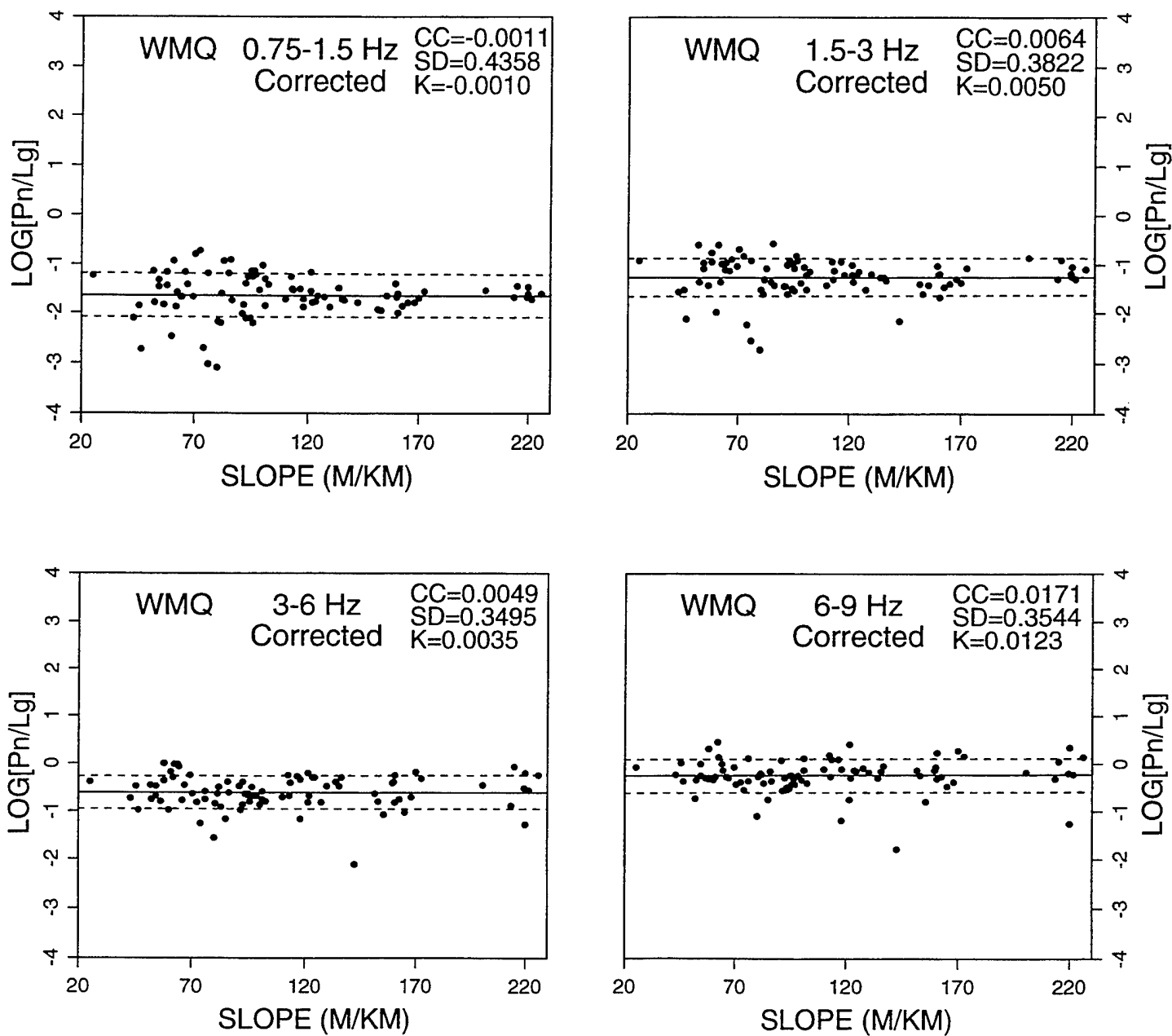


Figure A3k. Frequency dependent ratios of Pn/Lg phases recorded at WMQ plotted as a function of mean surface slope of each path after correcting for the distance dependence in Figure A3a. CC denotes the linear correlation coefficient. SD denotes the standard deviation of the linear regression, with the dotted lines corresponding to  $\pm 1$  SD, and K denotes the slope of the regression.

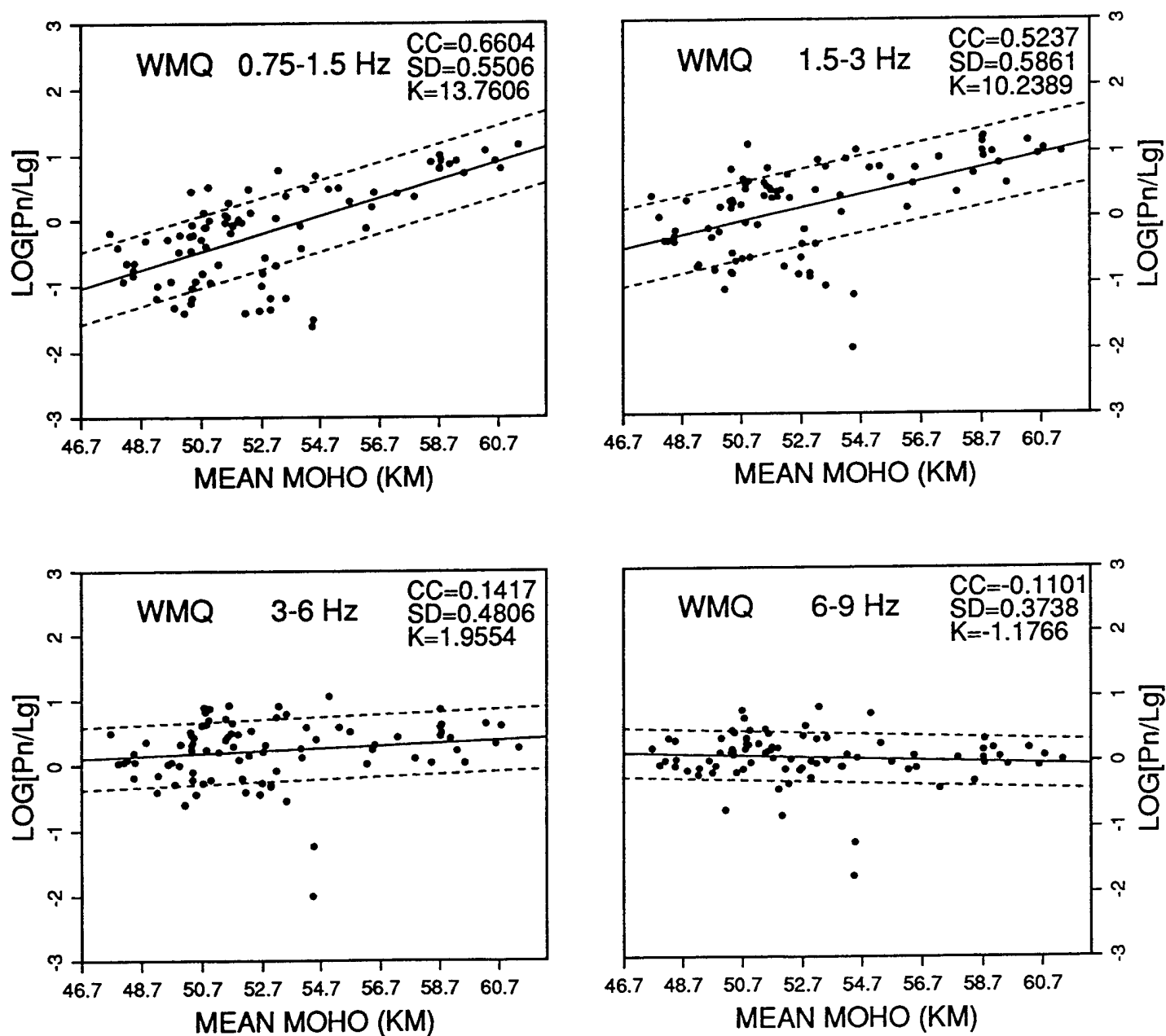


Figure A31. Frequency dependent ratios of Pn/Lg phases recorded at WMQ plotted as a function of mean crustal thickness of each path. CC denotes the linear correlation coefficient. SD denotes the standard deviation of the linear regression, with the dotted lines corresponding to  $\pm 1$  SD, and K denotes the slope of the regression.

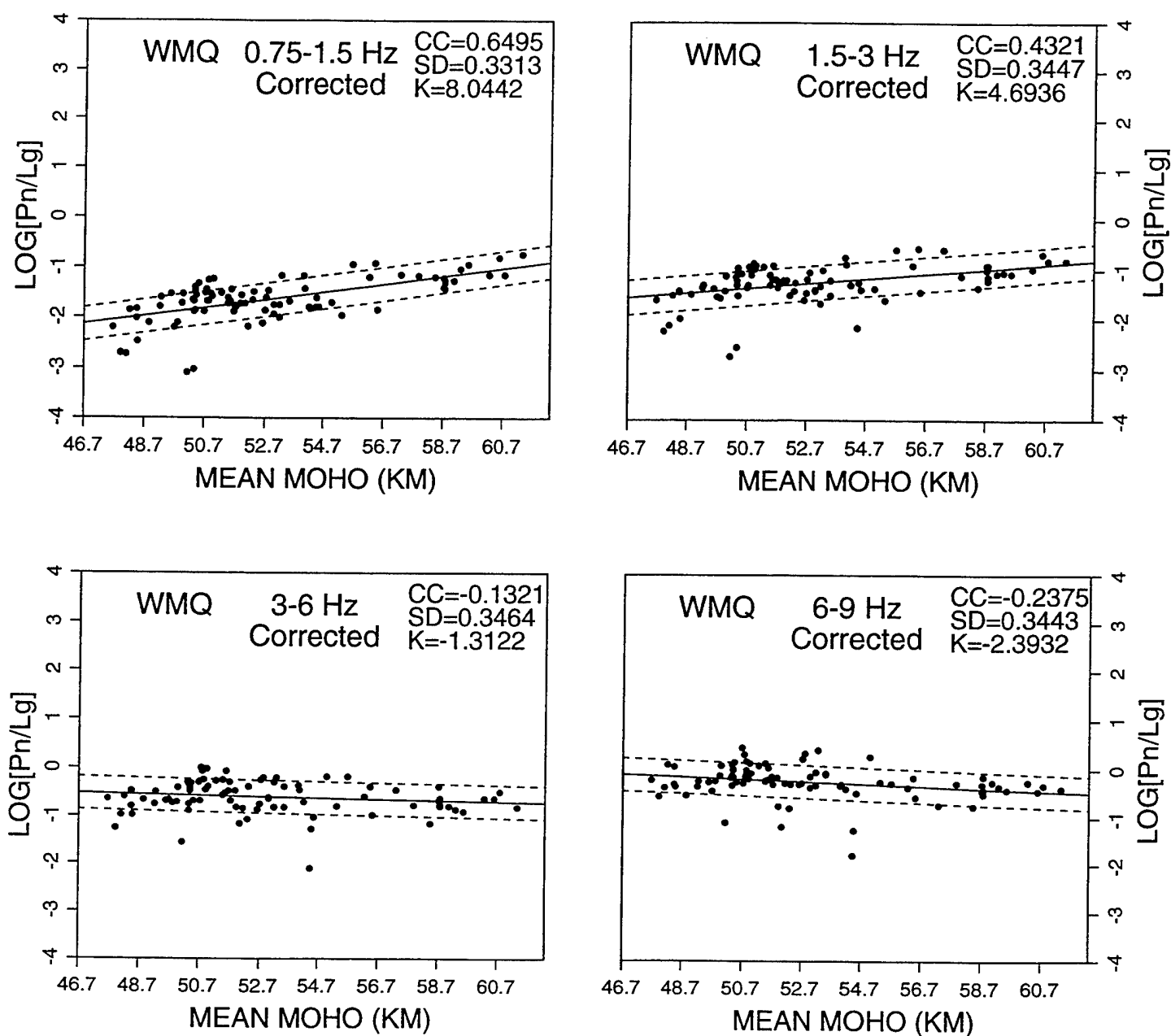


Figure A3m. Frequency dependent ratios of Pn/Lg phases recorded at WMQ plotted as a function of mean crustal thickness of each path after correcting for the distance dependence in Figure A3a. CC denotes the linear correlation coefficient. SD denotes the standard deviation of the linear regression, with the dotted lines corresponding to  $\pm 1$  SD, and K denotes the slope of the regression.

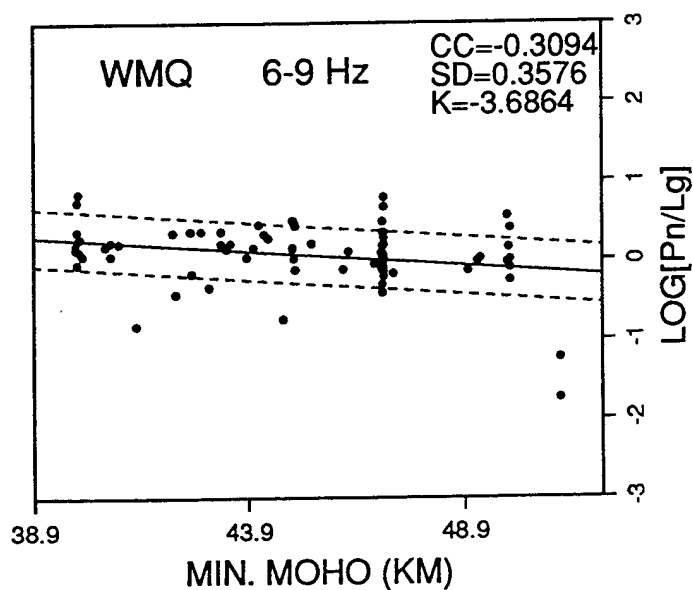
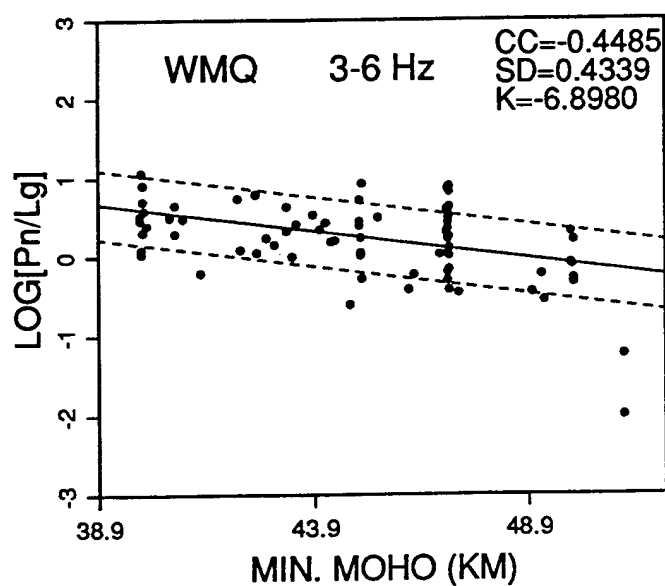
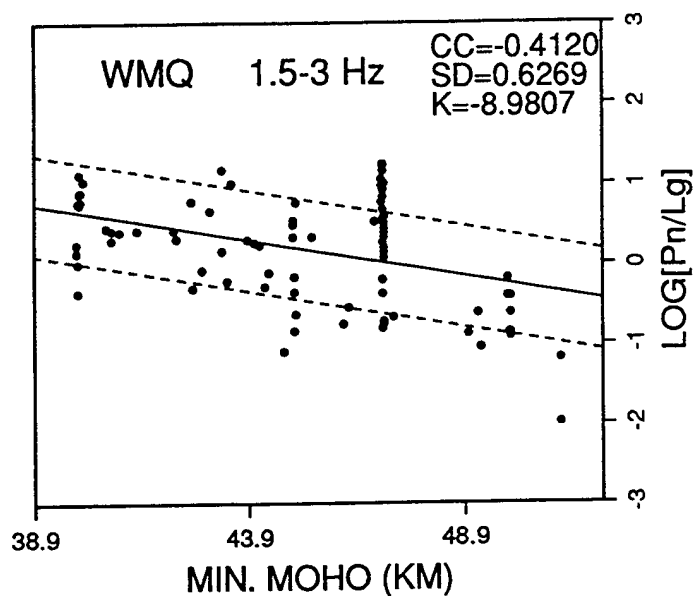
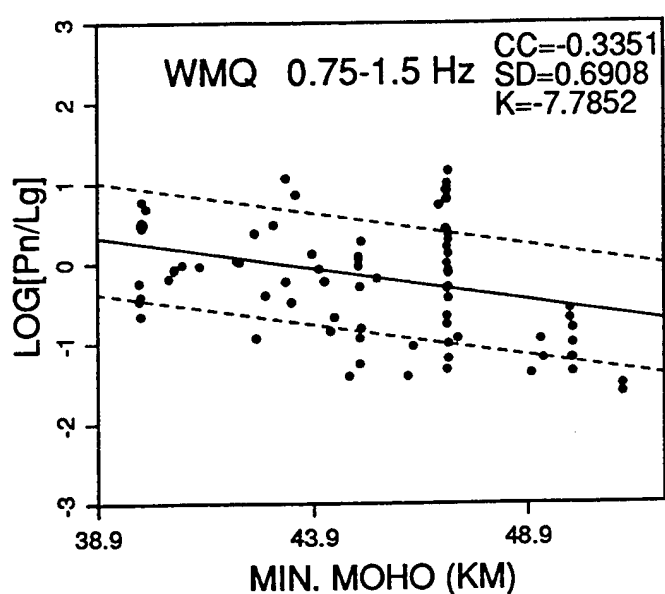


Figure A3n. Frequency dependent ratios of Pn/Lg phases recorded at WMQ plotted as a function of minimum crustal thickness on each path. CC denotes the linear correlation coefficient. SD denotes the standard deviation of the linear regression, with the dotted lines corresponding to  $\pm 1$  SD, and K denotes the slope of the regression.

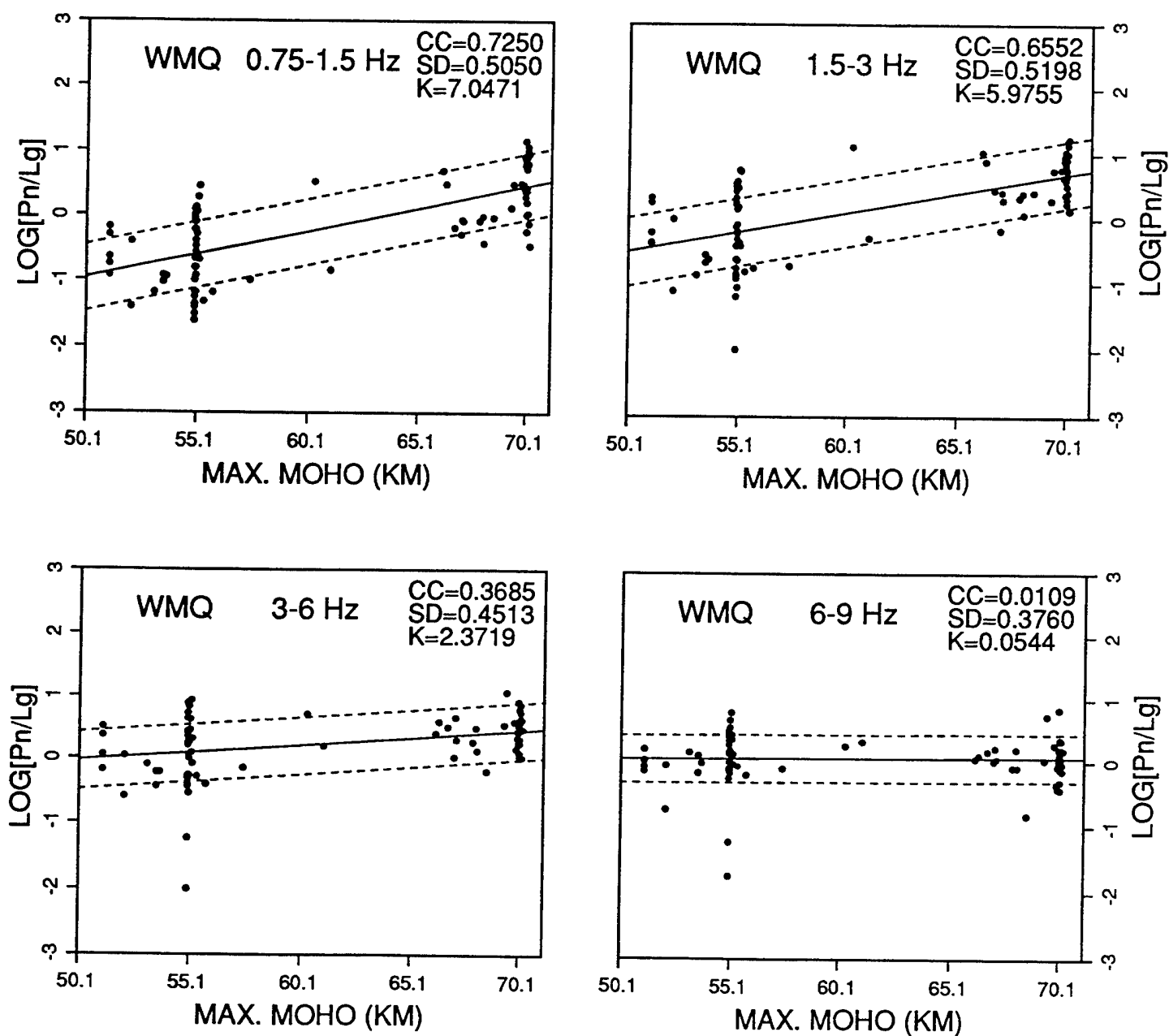


Figure A3o. Frequency dependent ratios of Pn/Lg phases recorded at WMQ plotted as a function of maximum crustal thickness on each path. CC denotes the linear correlation coefficient. SD denotes the standard deviation of the linear regression, with the dotted lines corresponding to  $\pm 1$  SD, and K denotes the slope of the regression.

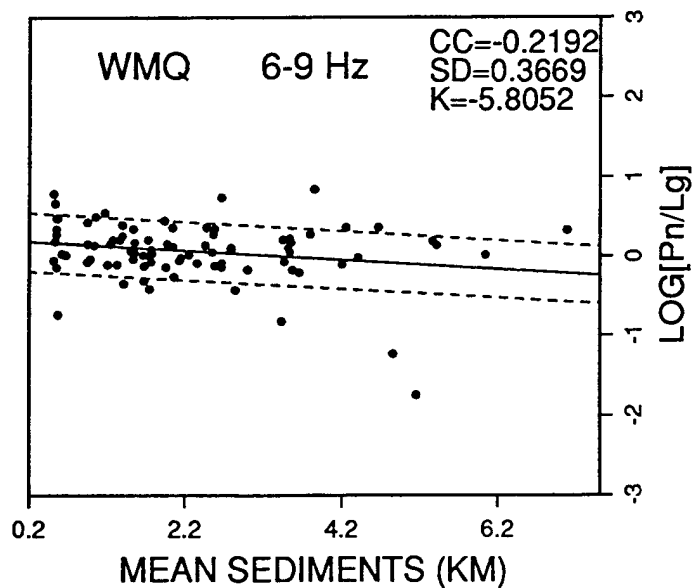
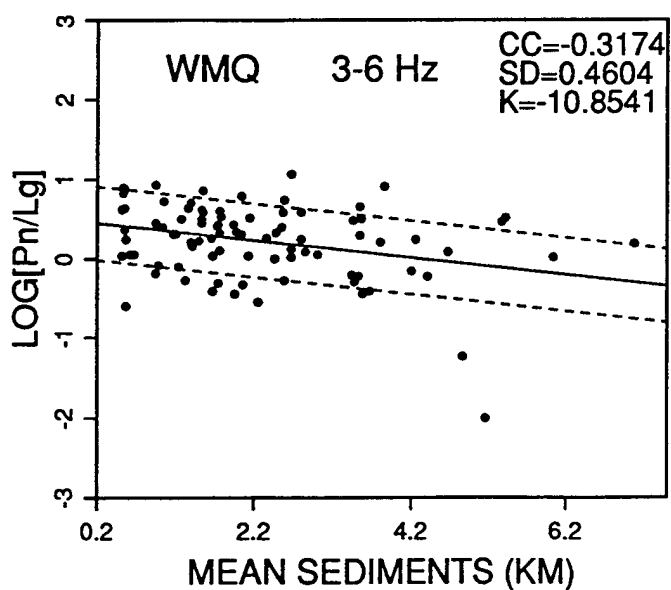
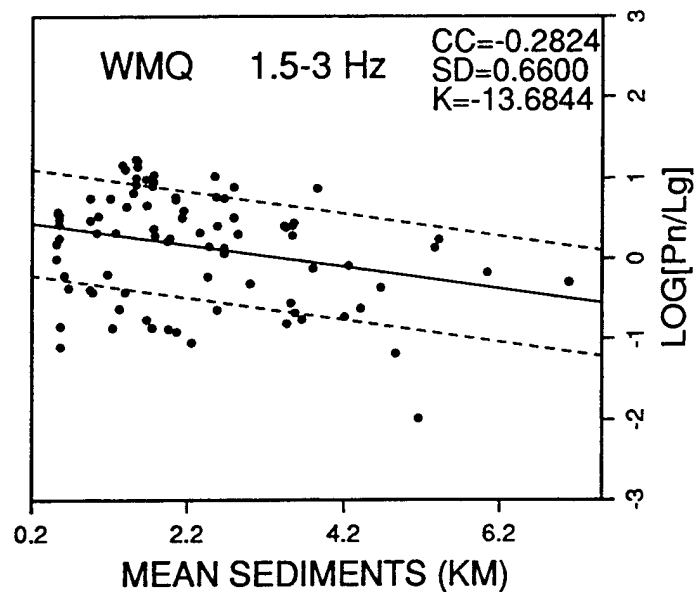
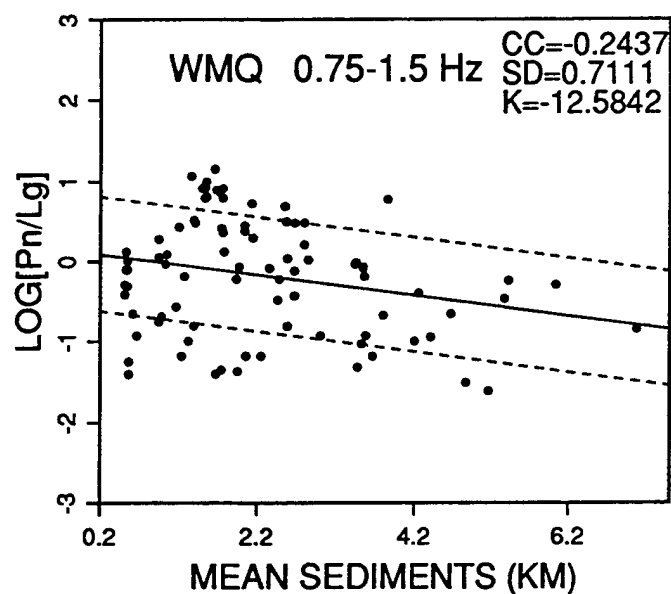


Figure A3p. Frequency dependent ratios of Pn/Lg phases recorded at WMQ plotted as a function of mean sediment thickness of each path. CC denotes the linear correlation coefficient. SD denotes the standard deviation of the linear regression, with the dotted lines corresponding to  $\pm 1$  SD, and K denotes the slope of the regression.

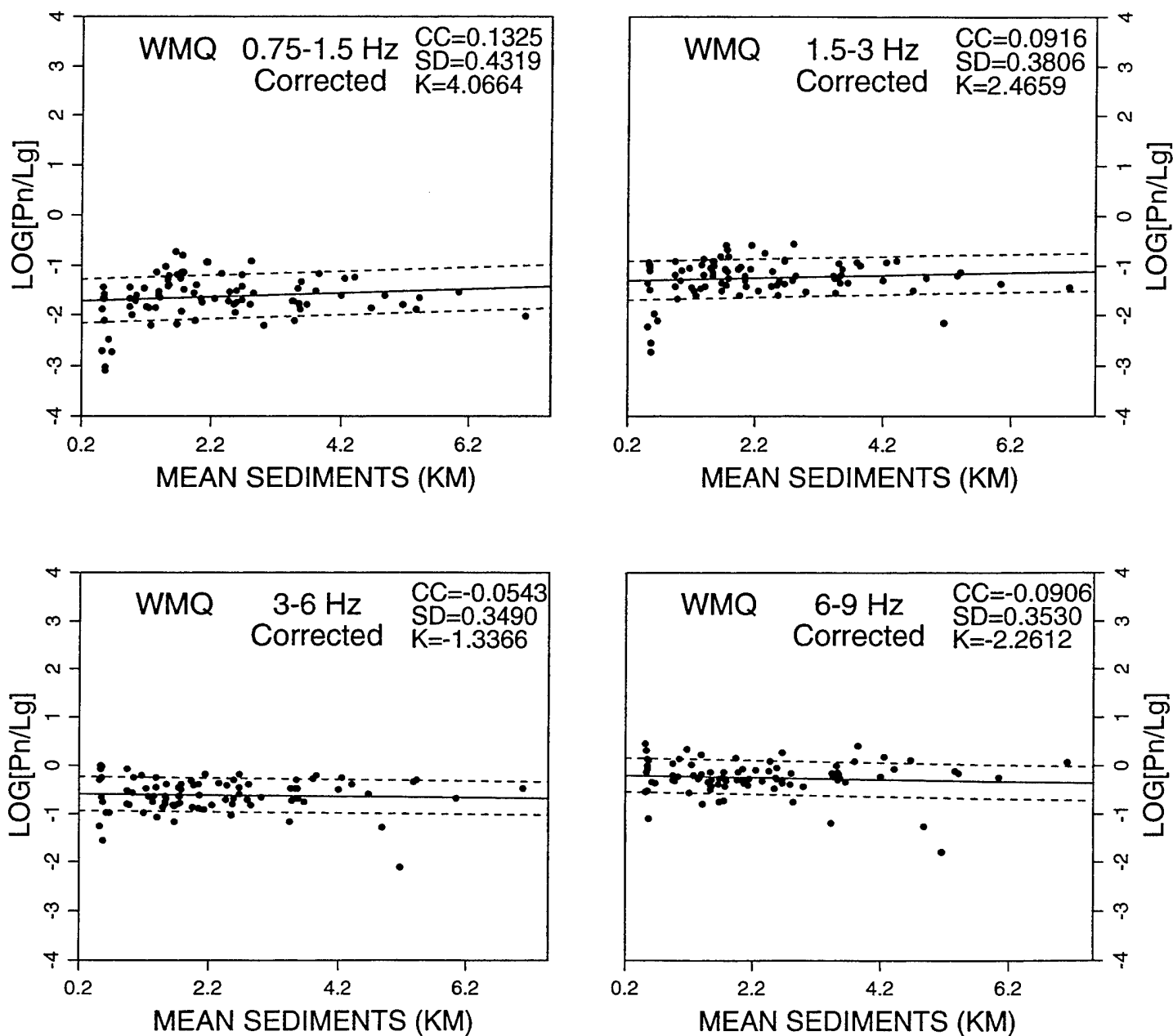


Figure A3q. Frequency dependent ratios of Pn/Lg phases recorded at WMQ plotted as a function of mean sediment thickness of each path after correcting for the distance dependence in Figure A3a. CC denotes the linear correlation coefficient. SD denotes the standard deviation of the linear regression, with the dotted lines corresponding to  $\pm 1$  SD, and K denotes the slope of the regression.

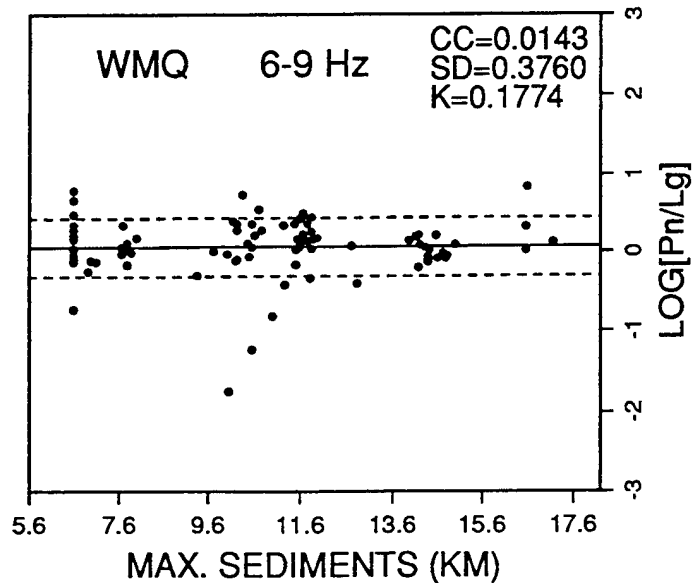
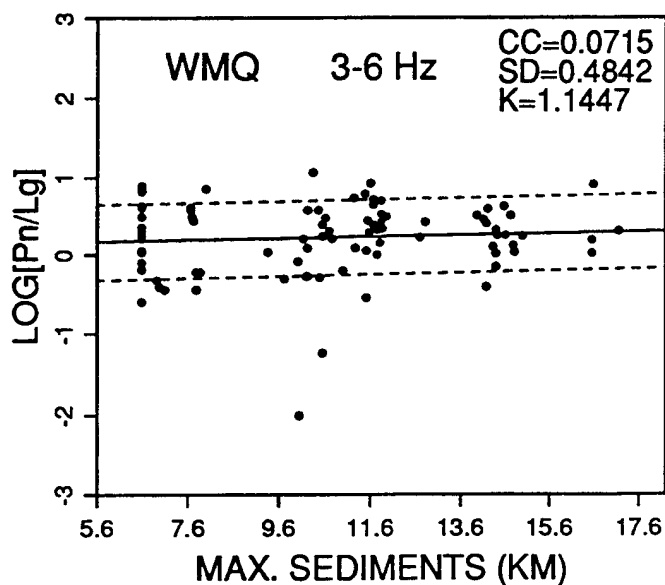
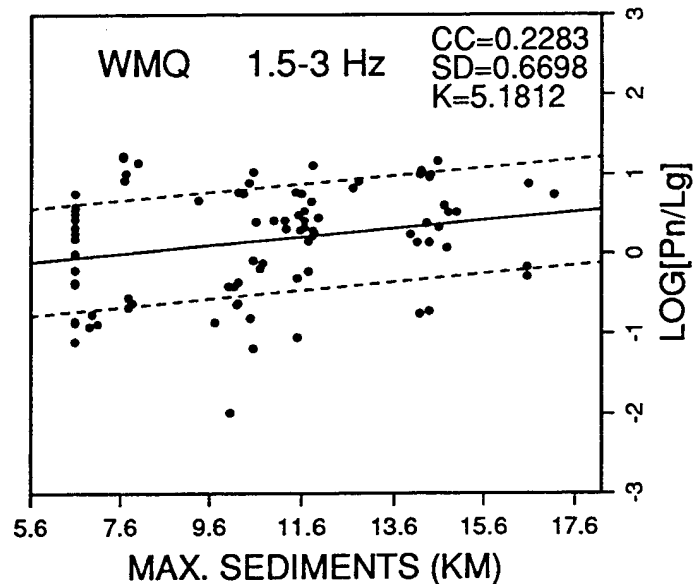
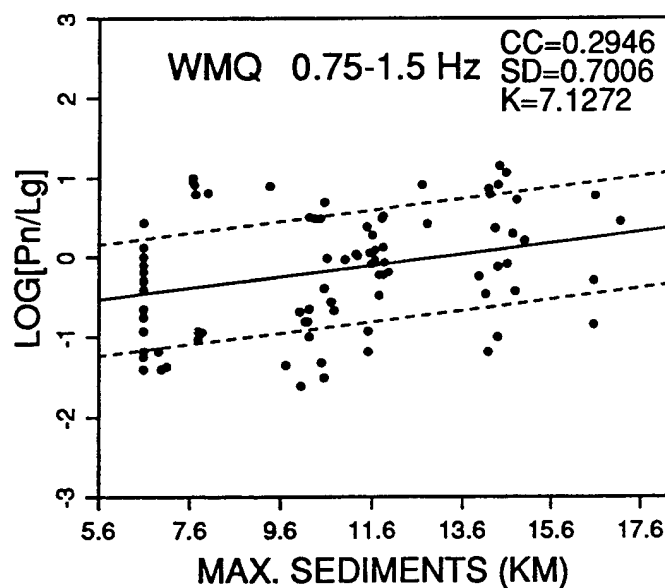


Figure A3r. Frequency dependent ratios of Pn/Lg phases recorded at WMQ plotted as a function of maximum sediment thickness on each path. CC denotes the linear correlation coefficient. SD denotes the standard deviation of the linear regression, with the dotted lines corresponding to  $\pm 1$  SD, and K denotes the slope of the regression.



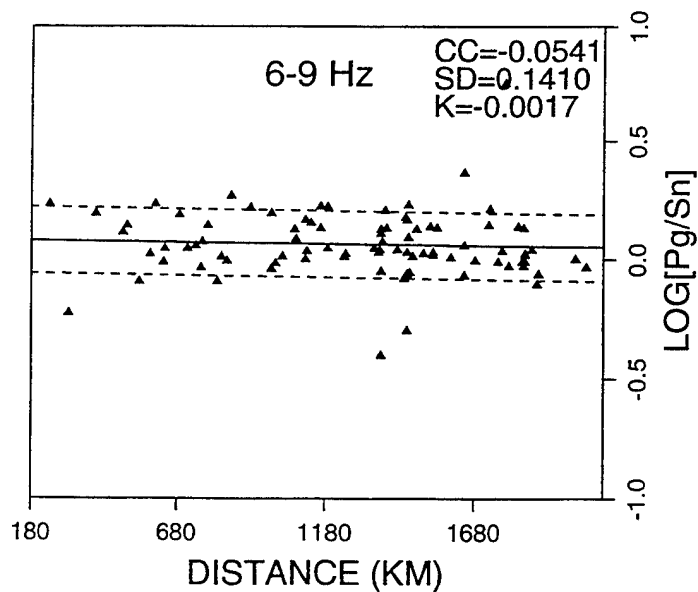
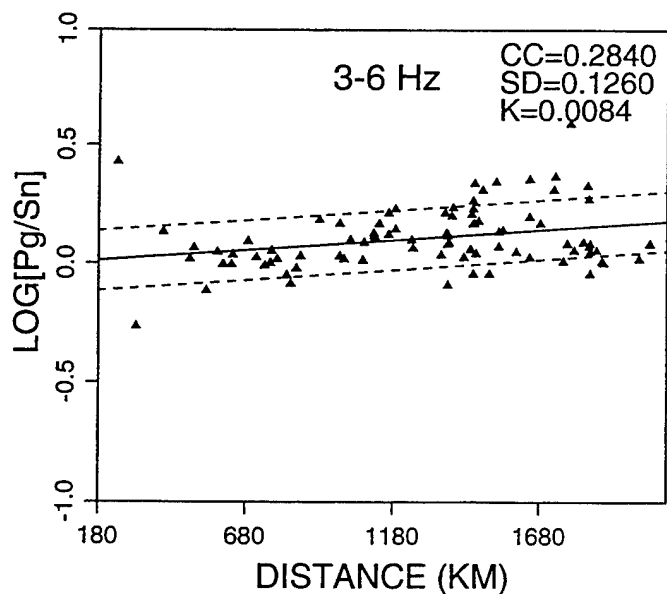
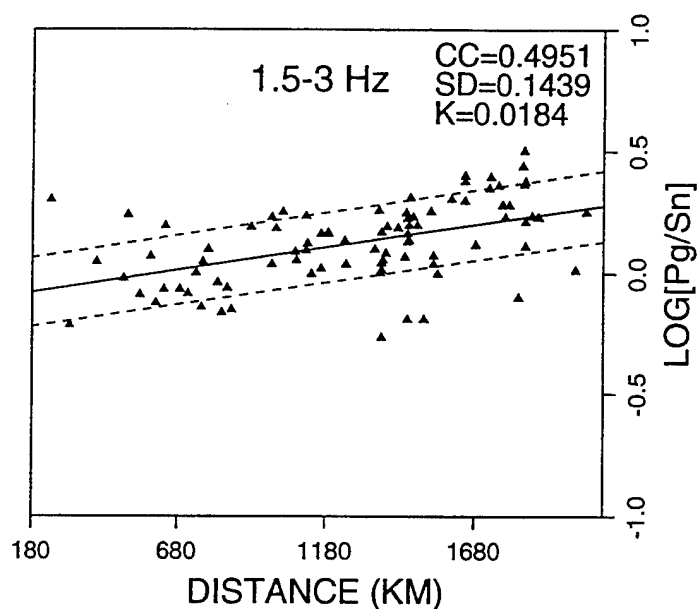
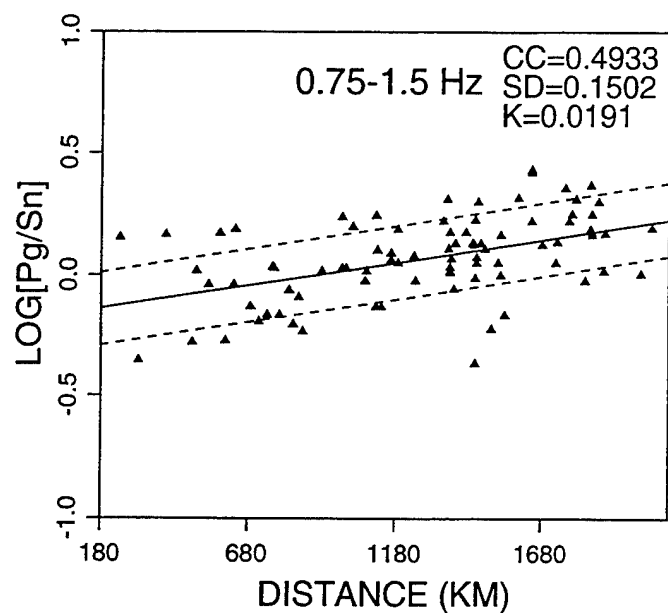


Figure A4a. Frequency dependent ratios of Pg/Sn phases recorded at WMQ plotted as a function of path length. CC denotes the linear correlation coefficient. SD denotes the standard deviation of the linear regression, with the dotted lines corresponding to  $\pm 1$  SD, and K denotes the slope of the regression.

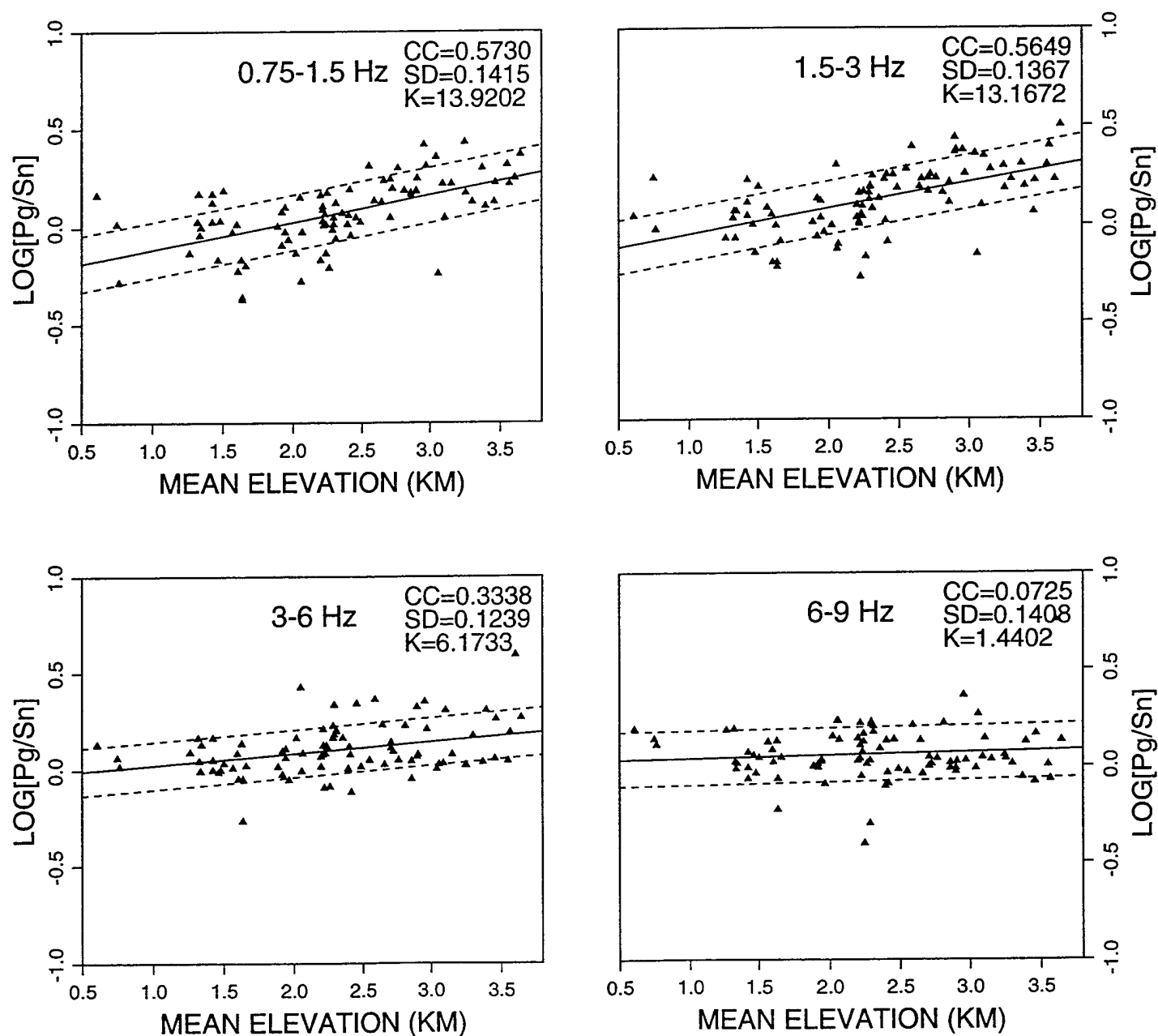


Figure A4b. Frequency dependent ratios of Pg/Sn phases recorded at WMQ plotted as a function of mean elevation of each path. CC denotes the linear correlation coefficient. SD denotes the standard deviation of the linear regression, with the dotted lines corresponding to  $\pm 1$  SD, and K denotes the slope of the regression.

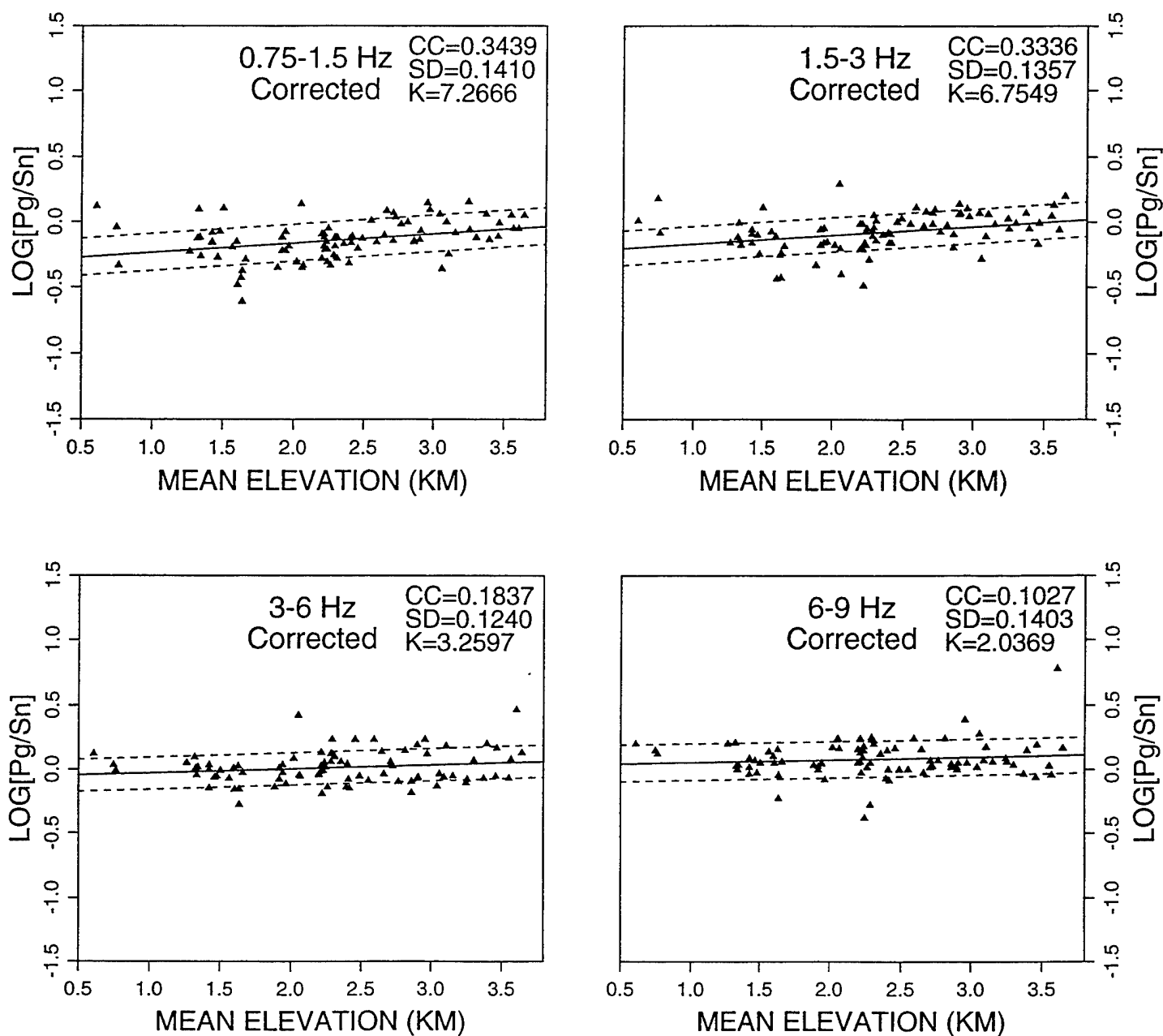


Figure A4c. Frequency dependent ratios of Pg/Sn phases recorded at WMQ plotted as a function of mean elevation of each path after correcting for the distance dependence in Figure A4a. CC denotes the linear correlation coefficient. SD denotes the standard deviation of the linear regression, with the dotted lines corresponding to  $\pm 1$  SD, and K denotes the slope of the regression.

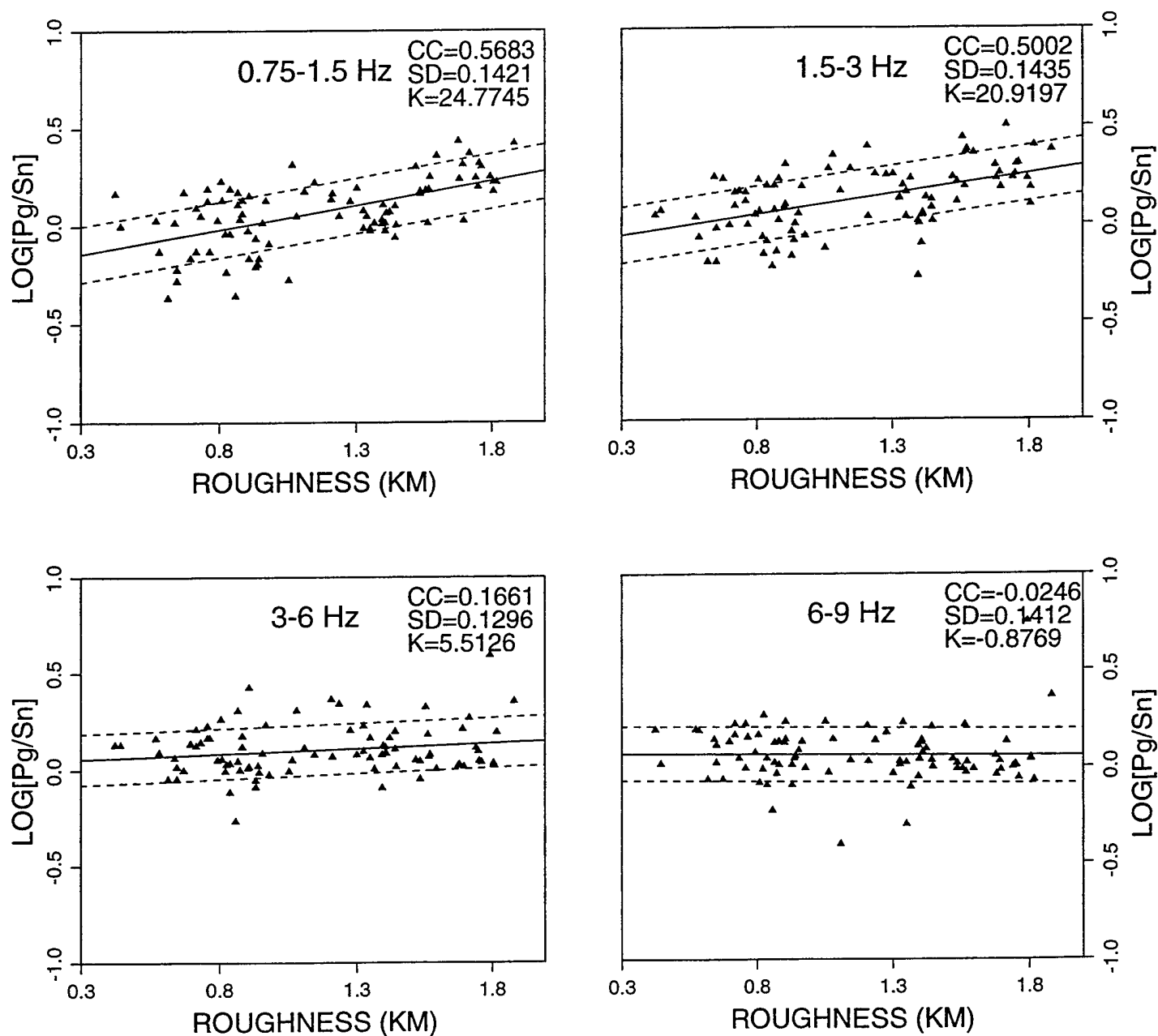


Figure A4d. Frequency dependent ratios of Pg/Sn phases recorded at WMQ plotted as a function of mean surface roughness of each path. CC denotes the linear correlation coefficient. SD denotes the standard deviation of the linear regression, with the dotted lines corresponding to  $\pm 1$  SD, and K denotes the slope of the regression.

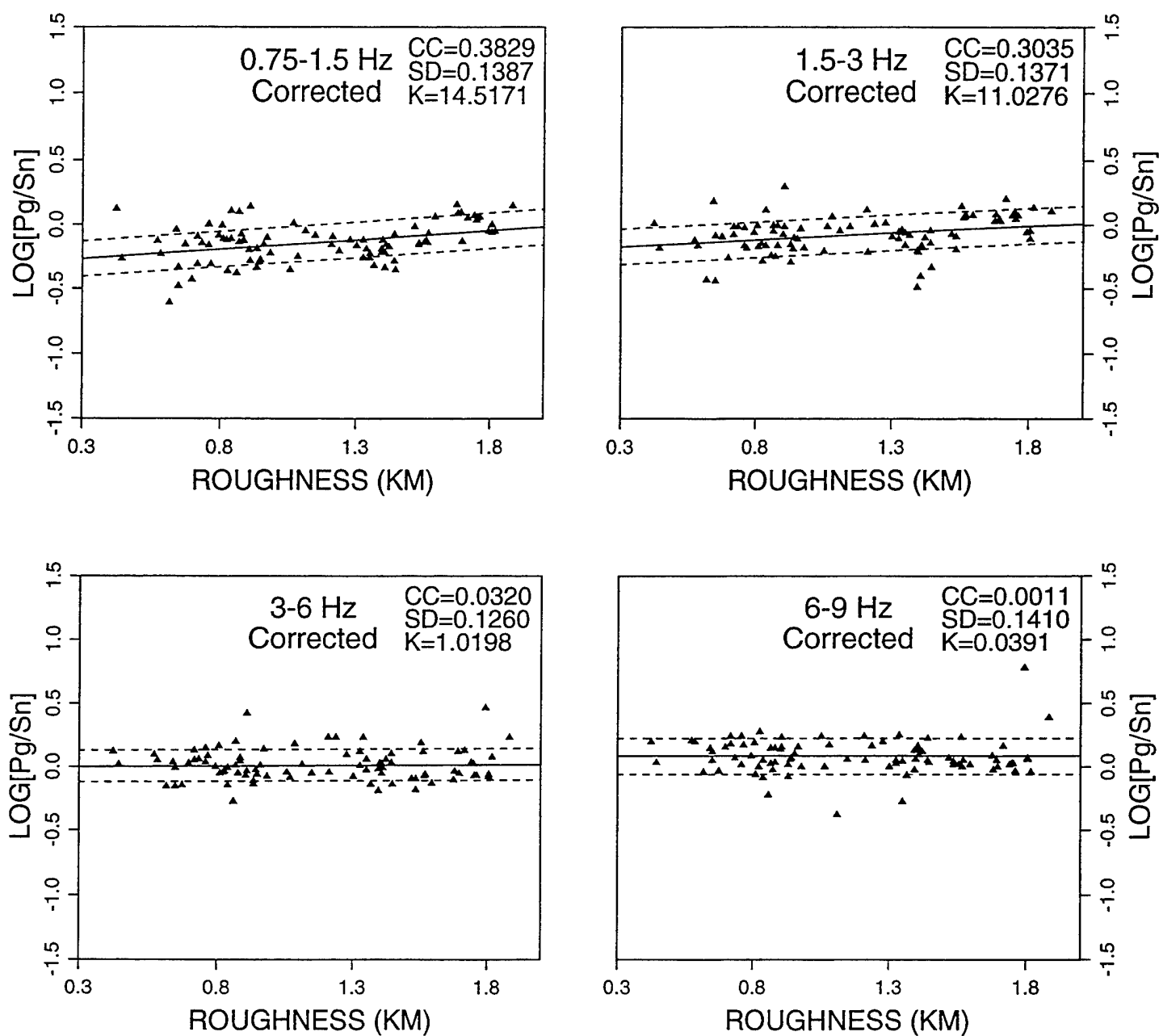


Figure A4e. Frequency dependent ratios of Pg/Sn phases recorded at WMQ plotted as a function of mean surface roughness of each path after correcting for the distance dependence in Figure A4a. CC denotes the linear correlation coefficient. SD denotes the standard deviation of the linear regression, with the dotted lines corresponding to  $\pm 1$  SD, and K denotes the slope of the regression.

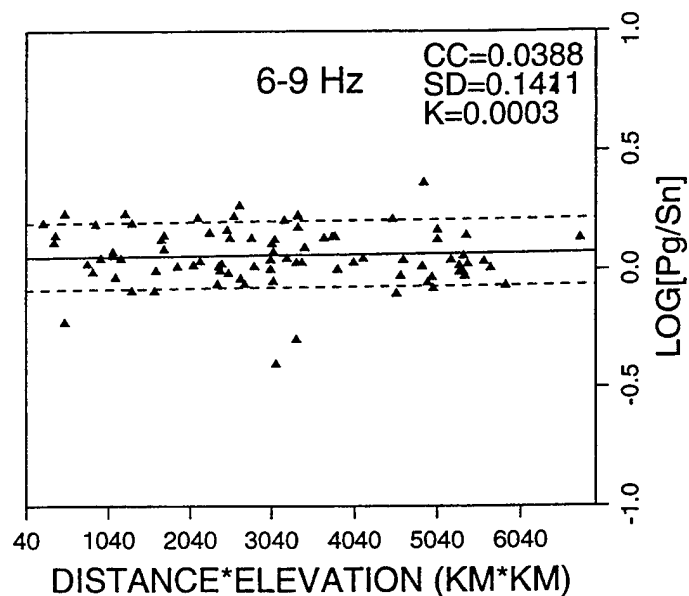
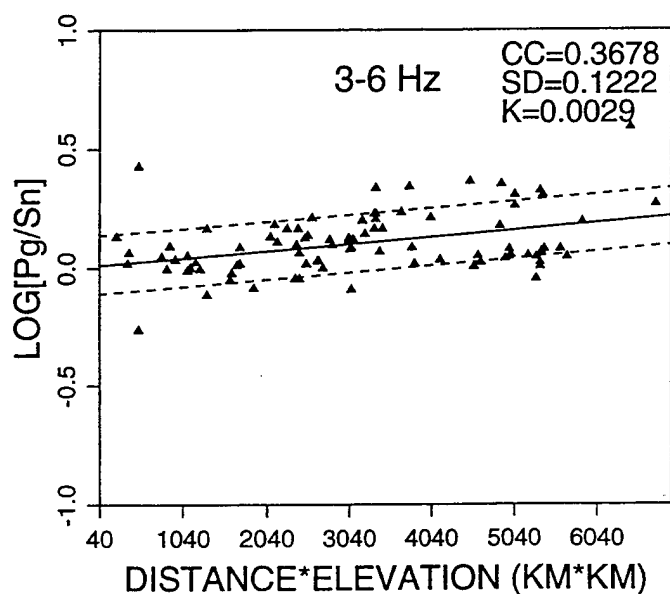
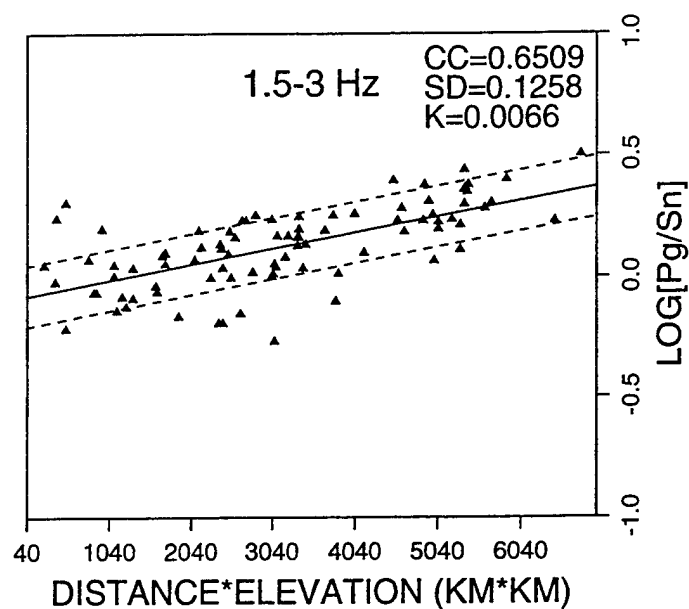
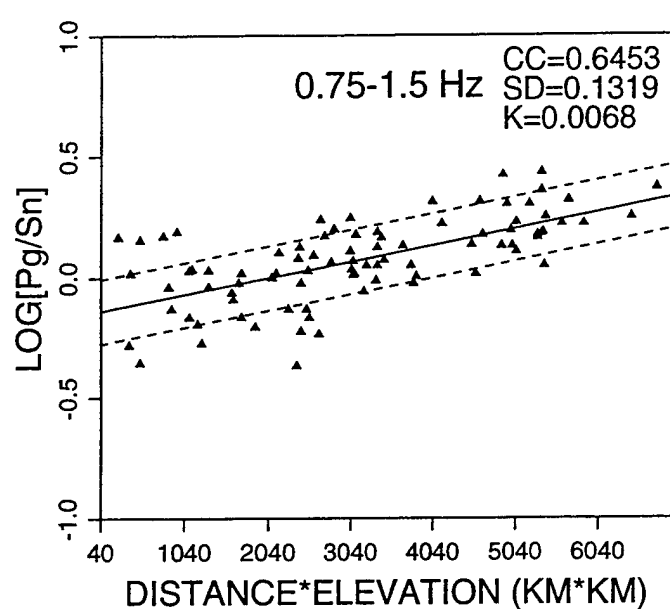


Figure A4f. Frequency dependent ratios of Pg/Sn phases recorded at WMQ plotted as a function of the product of path length times mean path elevation. CC denotes the linear correlation coefficient. SD denotes the standard deviation of the linear regression, with the dotted lines corresponding to  $\pm 1$  SD, and K denotes the slope of the regression.

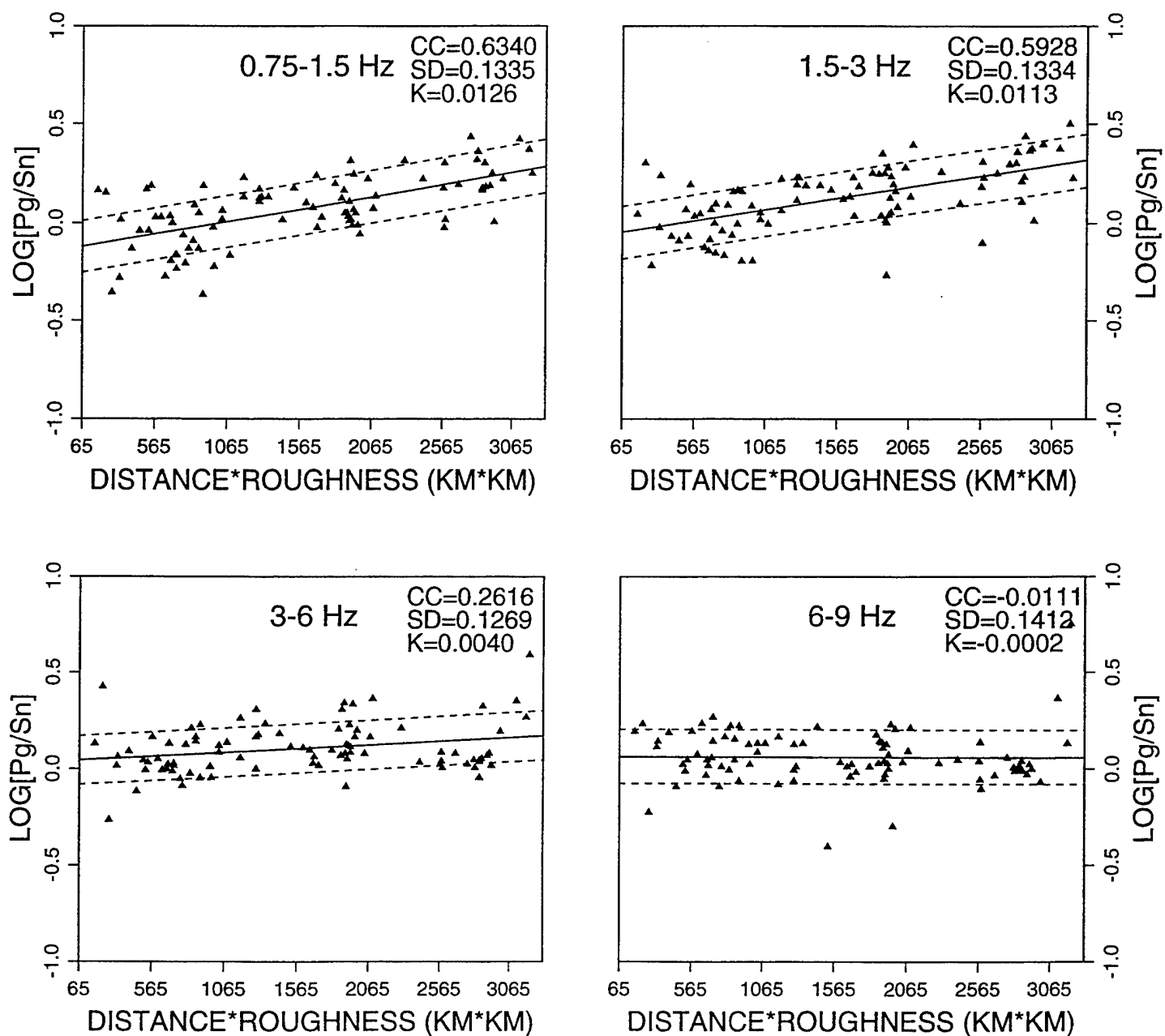


Figure A4g. Frequency dependent ratios of Pg/Sn phases recorded at WMQ plotted as a function of the product of path length times mean surface roughness. CC denotes the linear correlation coefficient. SD denotes the standard deviation of the linear regression, with the dotted lines corresponding to  $\pm 1$  SD, and K denotes the slope of the regression.

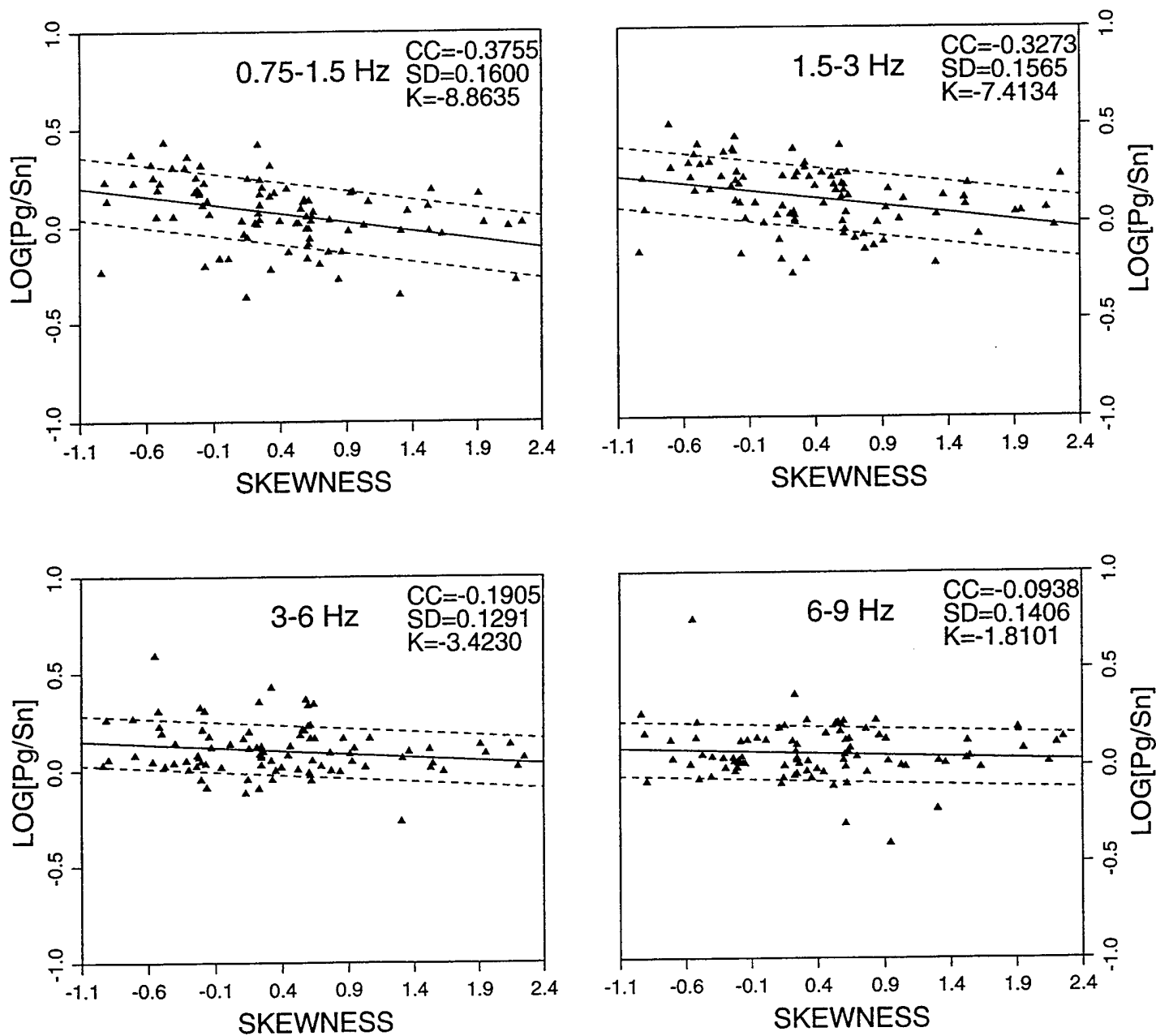


Figure A4h. Frequency dependent ratios of Pg/Sn phases recorded at WMQ plotted as a function of mean surface skewness of each path. CC denotes the linear correlation coefficient. SD denotes the standard deviation of the linear regression, with the dotted lines corresponding to  $\pm 1 \text{ SD}$ , and K denotes the slope of the regression.



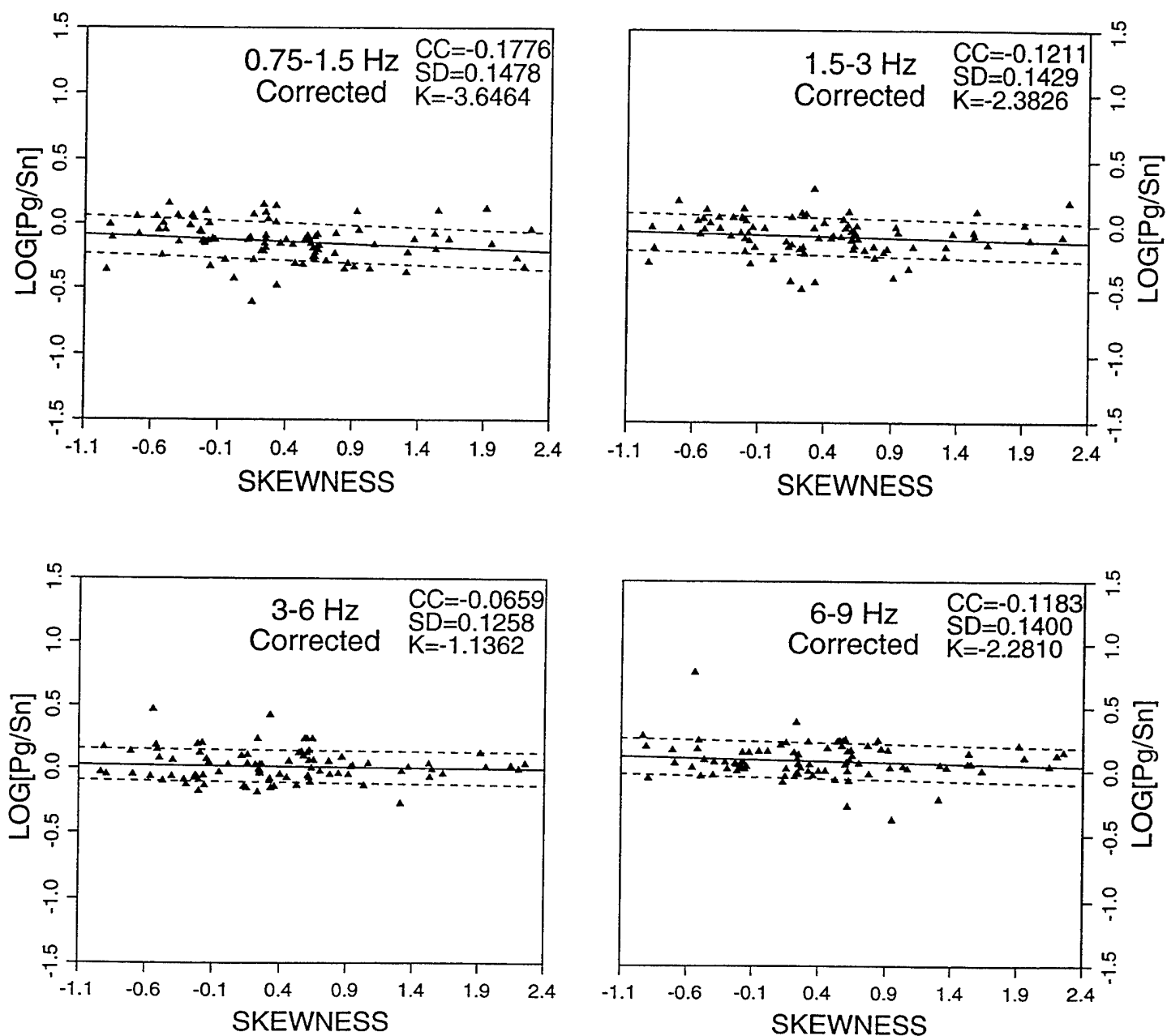


Figure A4i. Frequency dependent ratios of Pg/Sn phases recorded at WMQ plotted as a function of mean surface skewness of each path after correcting for the distance dependence in Figure A4a. CC denotes the linear correlation coefficient. SD denotes the standard deviation of the linear regression, with the dotted lines corresponding to  $\pm 1$  SD, and K denotes the slope of the regression.

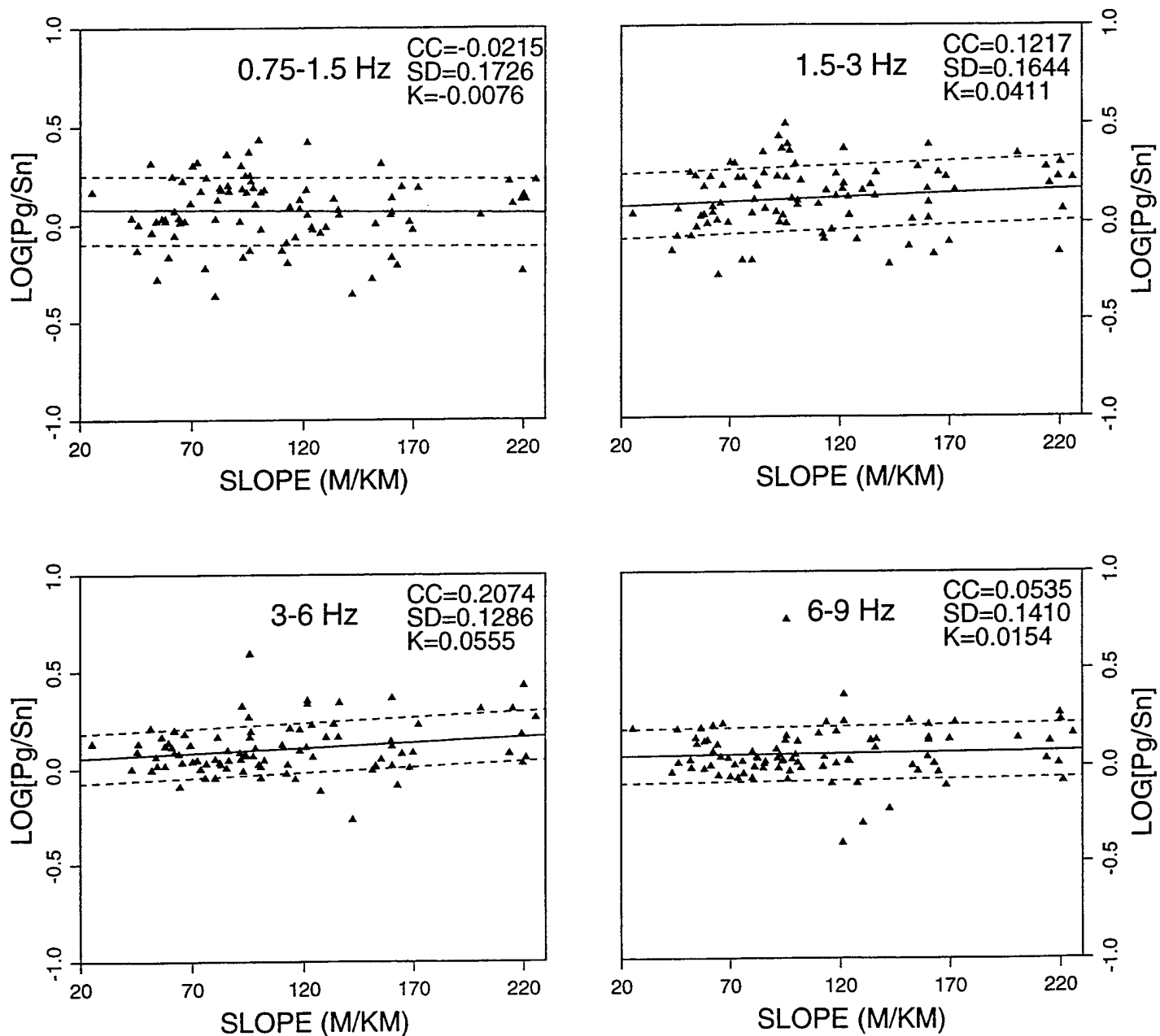


Figure A4j. Frequency dependent ratios of Pg/Sn phases recorded at WMQ plotted as a function of mean surface slope of each path. CC denotes the linear correlation coefficient. SD denotes the standard deviation of the linear regression, with the dotted lines corresponding to  $\pm 1$  SD, and K denotes the slope of the regression.

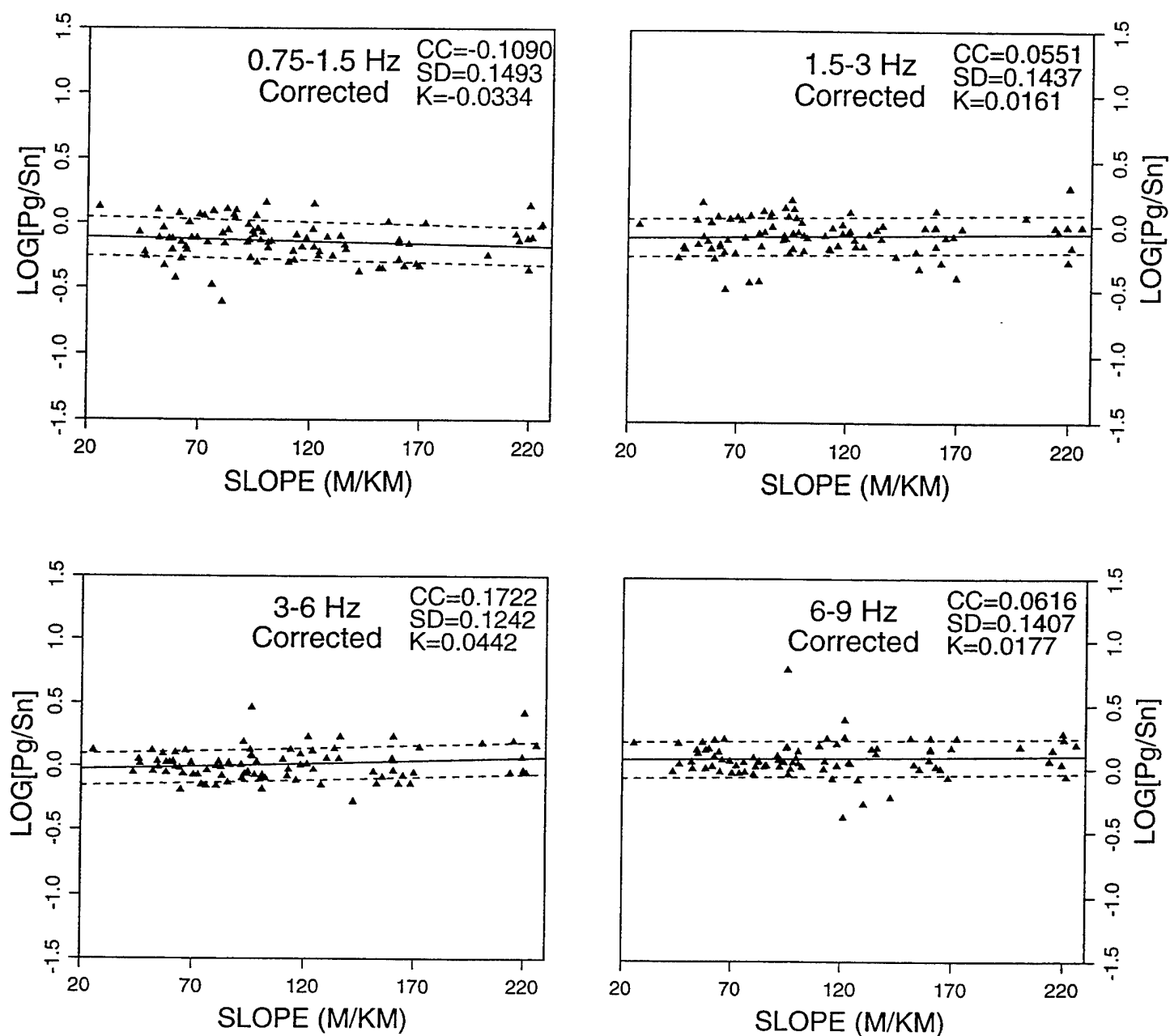


Figure A4k. Frequency dependent ratios of Pg/Sn phases recorded at WMQ plotted as a function of mean surface slope of each path after correcting for the distance dependence in Figure A4a. CC denotes the linear correlation coefficient. SD denotes the standard deviation of the linear regression, with the dotted lines corresponding to  $\pm 1$  SD, and K denotes the slope of the regression.

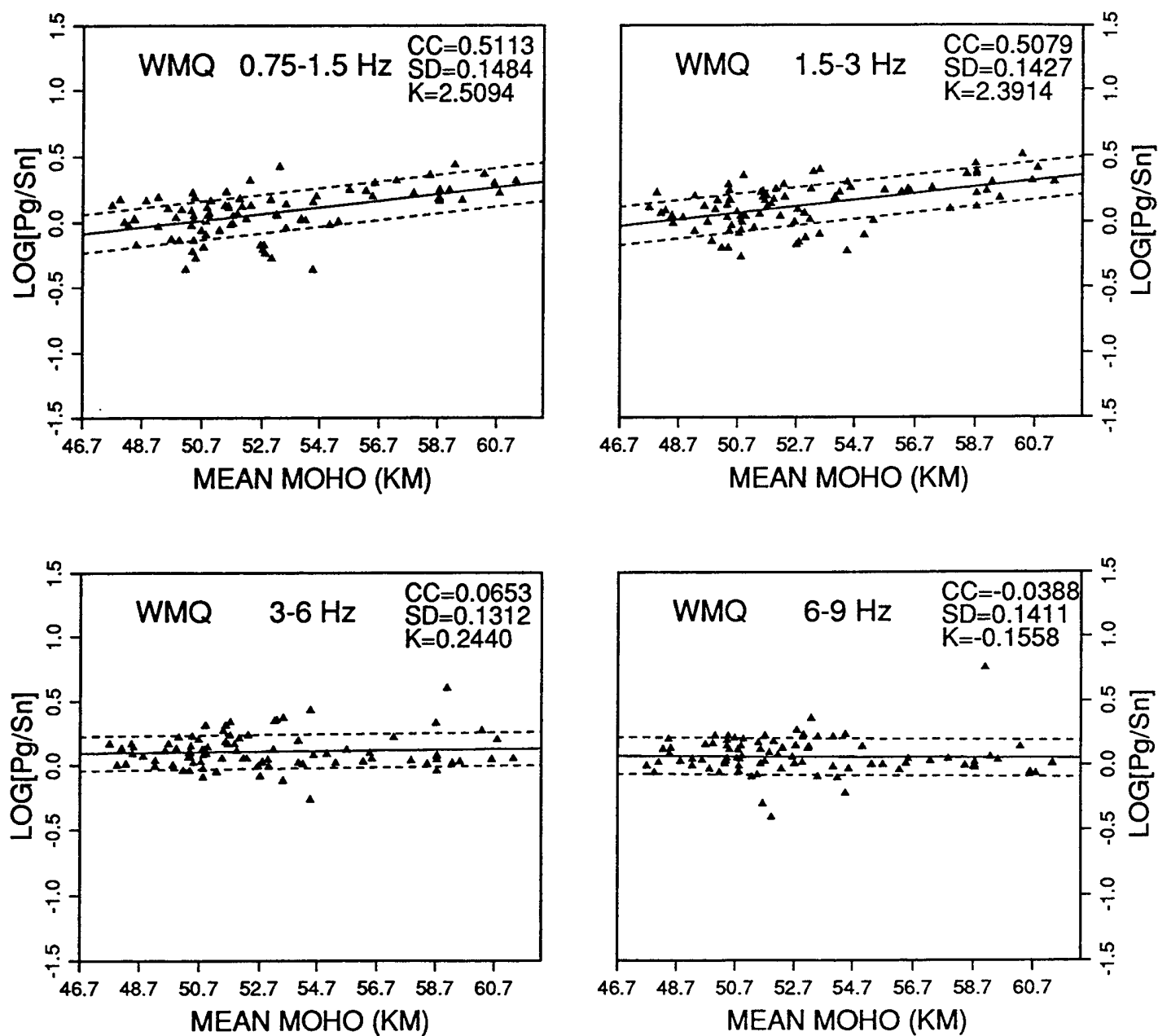


Figure A41. Frequency dependent ratios of Pg/Sn phases recorded at WMQ plotted as a function of mean crustal thickness of each path. CC denotes the linear correlation coefficient. SD denotes the standard deviation of the linear regression, with the dotted lines corresponding to  $\pm 1$  SD, and K denotes the slope of the regression.

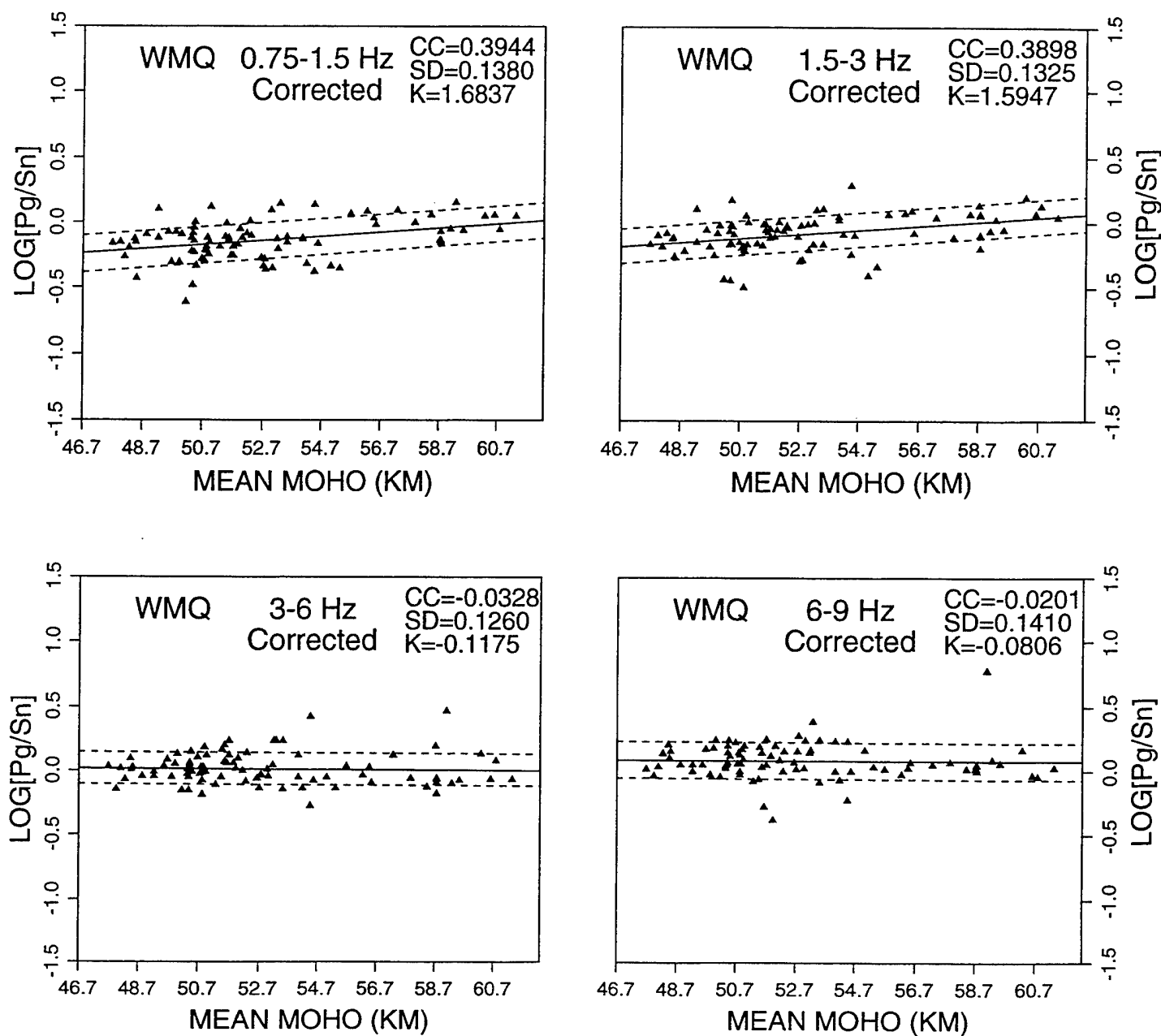


Figure A4m. Frequency dependent ratios of Pg/Sn phases recorded at WMQ plotted as a function of mean crustal thickness of each path after correcting for the distance dependence in Figure A4a. CC denotes the linear correlation coefficient. SD denotes the standard deviation of the linear regression, with the dotted lines corresponding to  $\pm 1$  SD, and K denotes the slope of the regression.

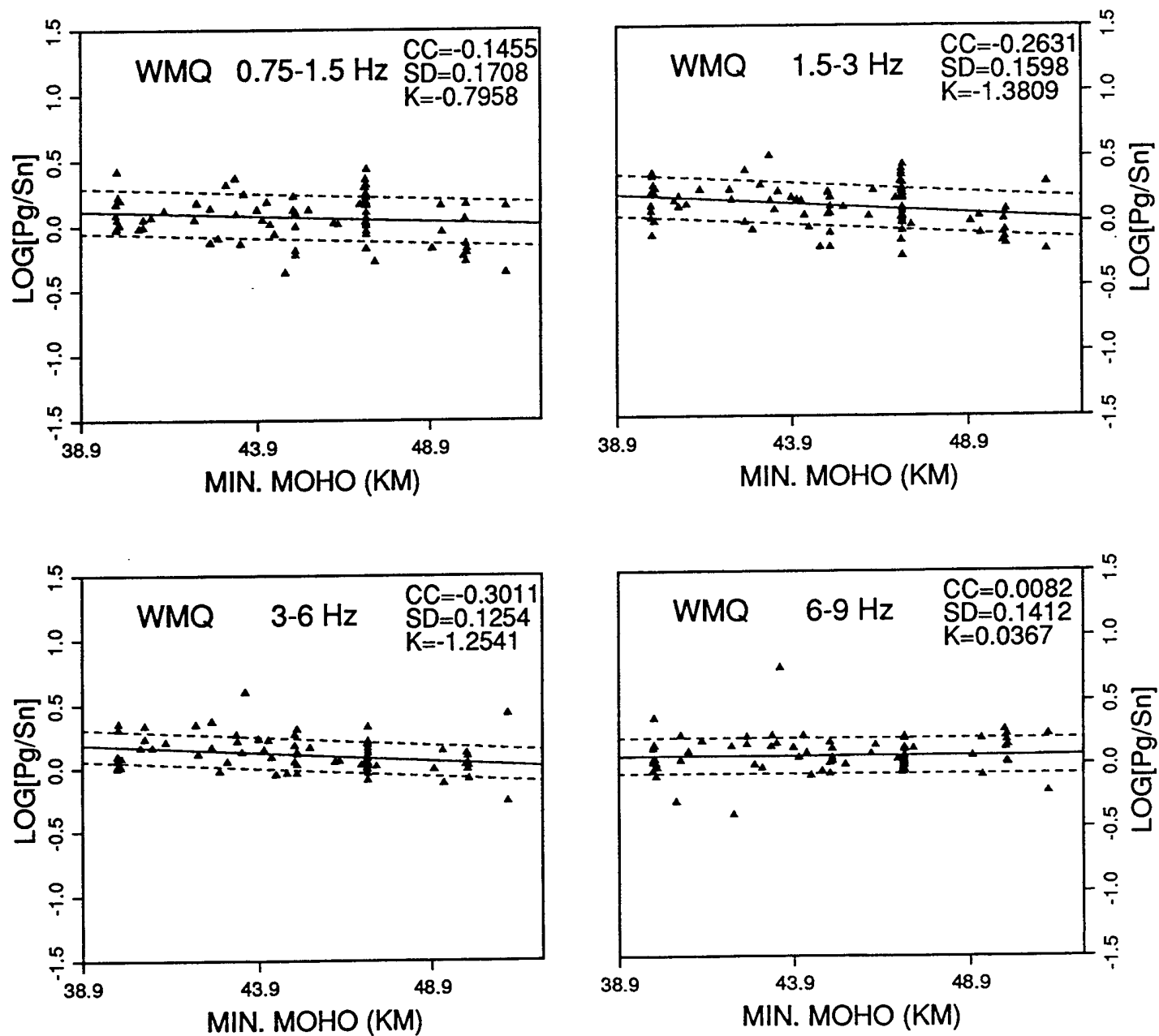


Figure A4n. Frequency dependent ratios of Pg/Sn phases recorded at WMQ plotted as a function of minimum crustal thickness on each path. CC denotes the linear correlation coefficient. SD denotes the standard deviation of the linear regression, with the dotted lines corresponding to  $\pm 1$  SD, and K denotes the slope of the regression.

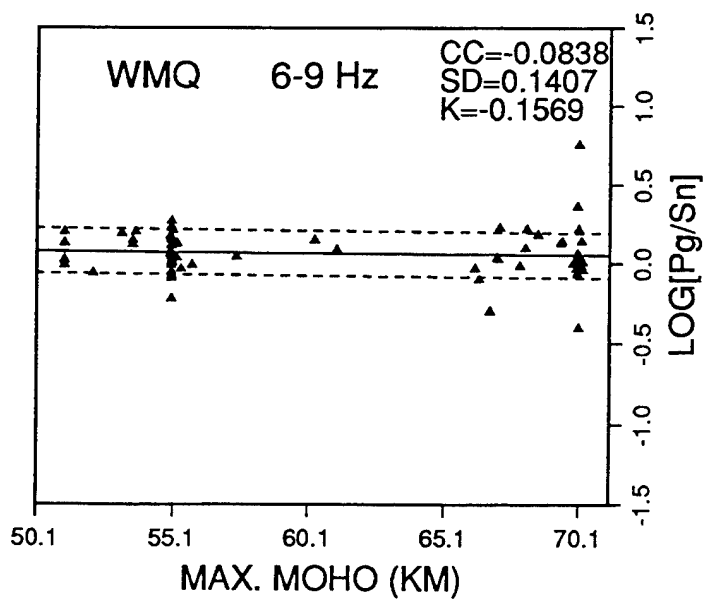
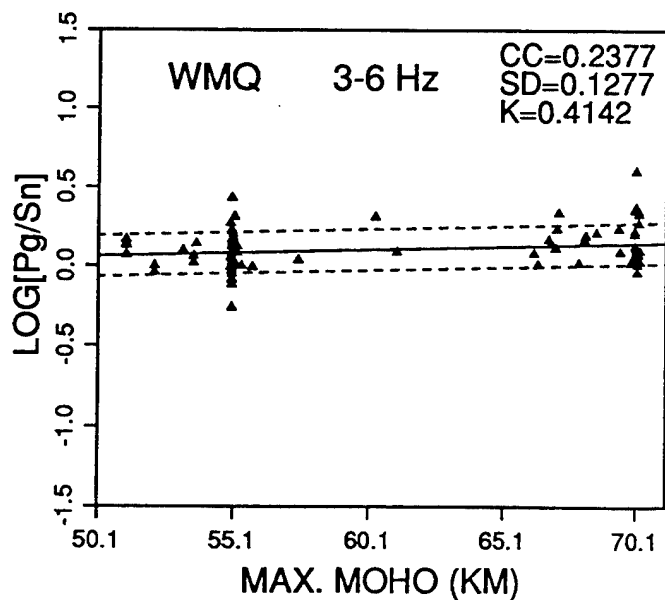
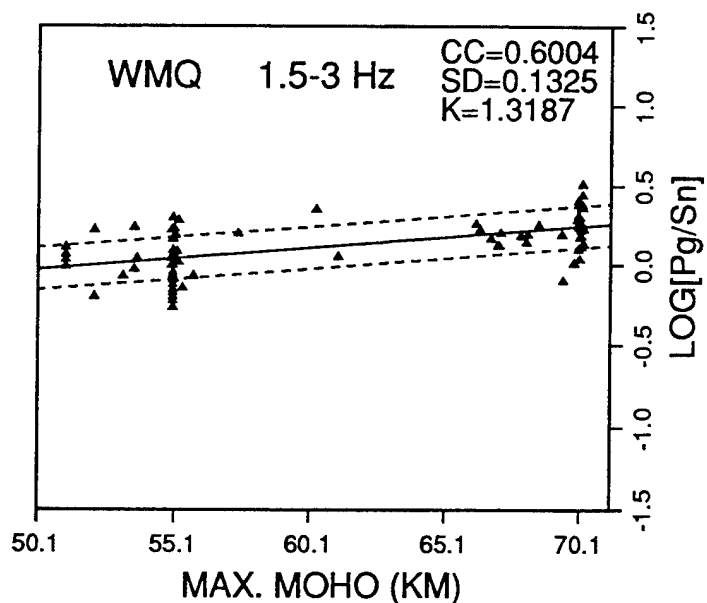
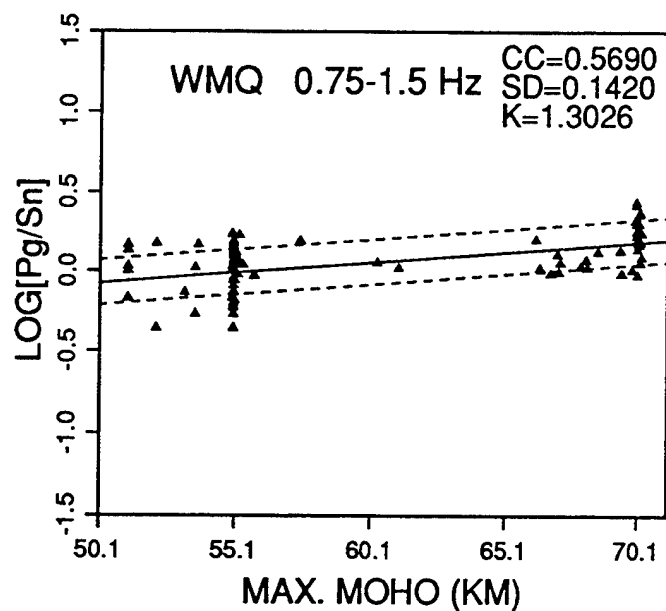


Figure A4o. Frequency dependent ratios of Pg/Sn phases recorded at WMQ plotted as a function of maximum crustal thickness on each path. CC denotes the linear correlation coefficient. SD denotes the standard deviation of the linear regression, with the dotted lines corresponding to  $\pm 1$  SD, and K denotes the slope of the regression.

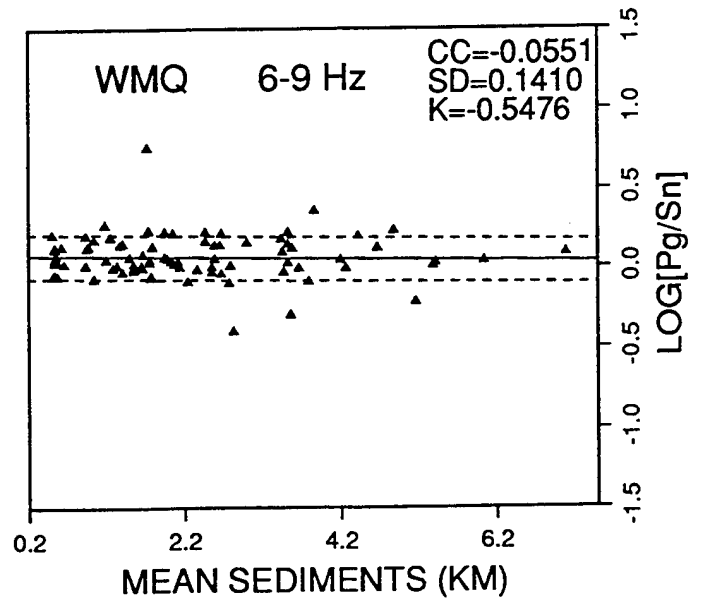
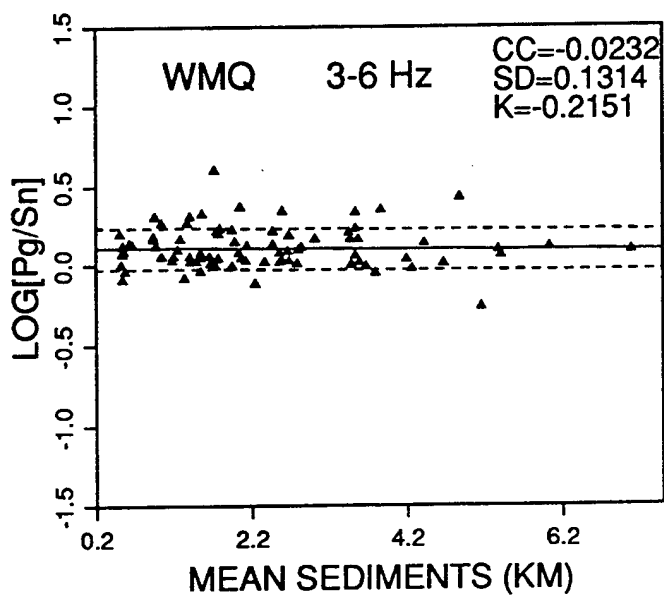
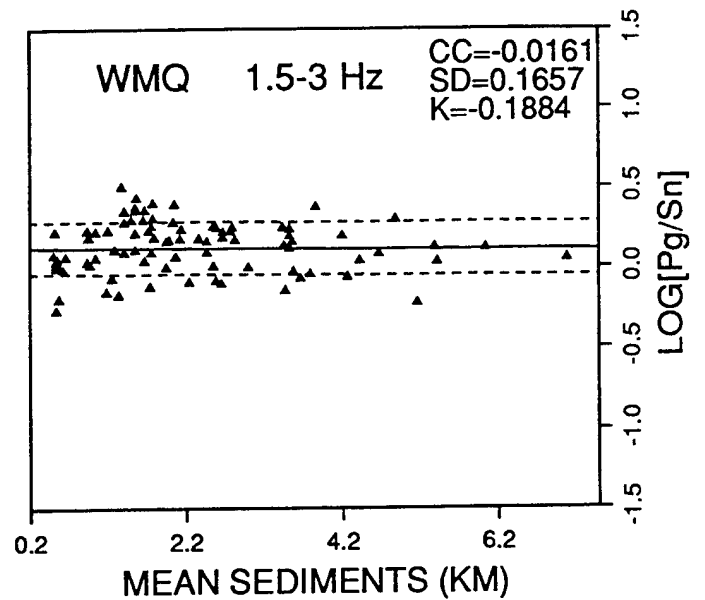
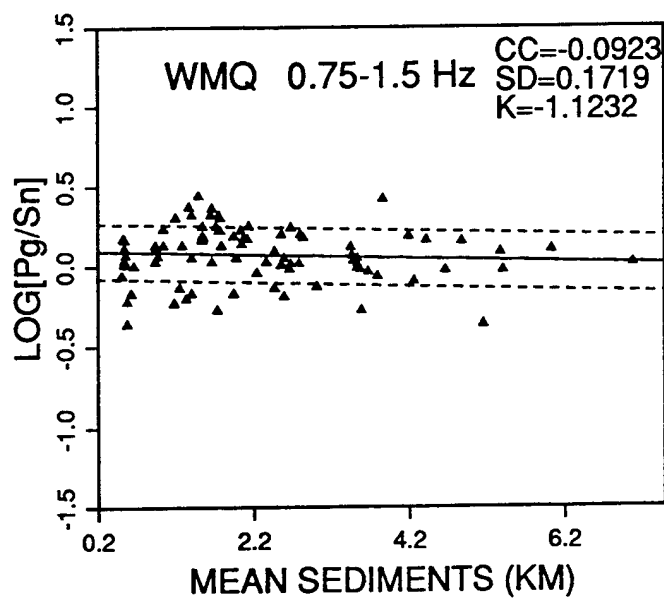


Figure A4p. Frequency dependent ratios of Pg/Sn phases recorded at WMQ plotted as a function of mean sediment thickness of each path. CC denotes the linear correlation coefficient. SD denotes the standard deviation of the linear regression, with the dotted lines corresponding to  $\pm 1$  SD, and K denotes the slope of the regression.



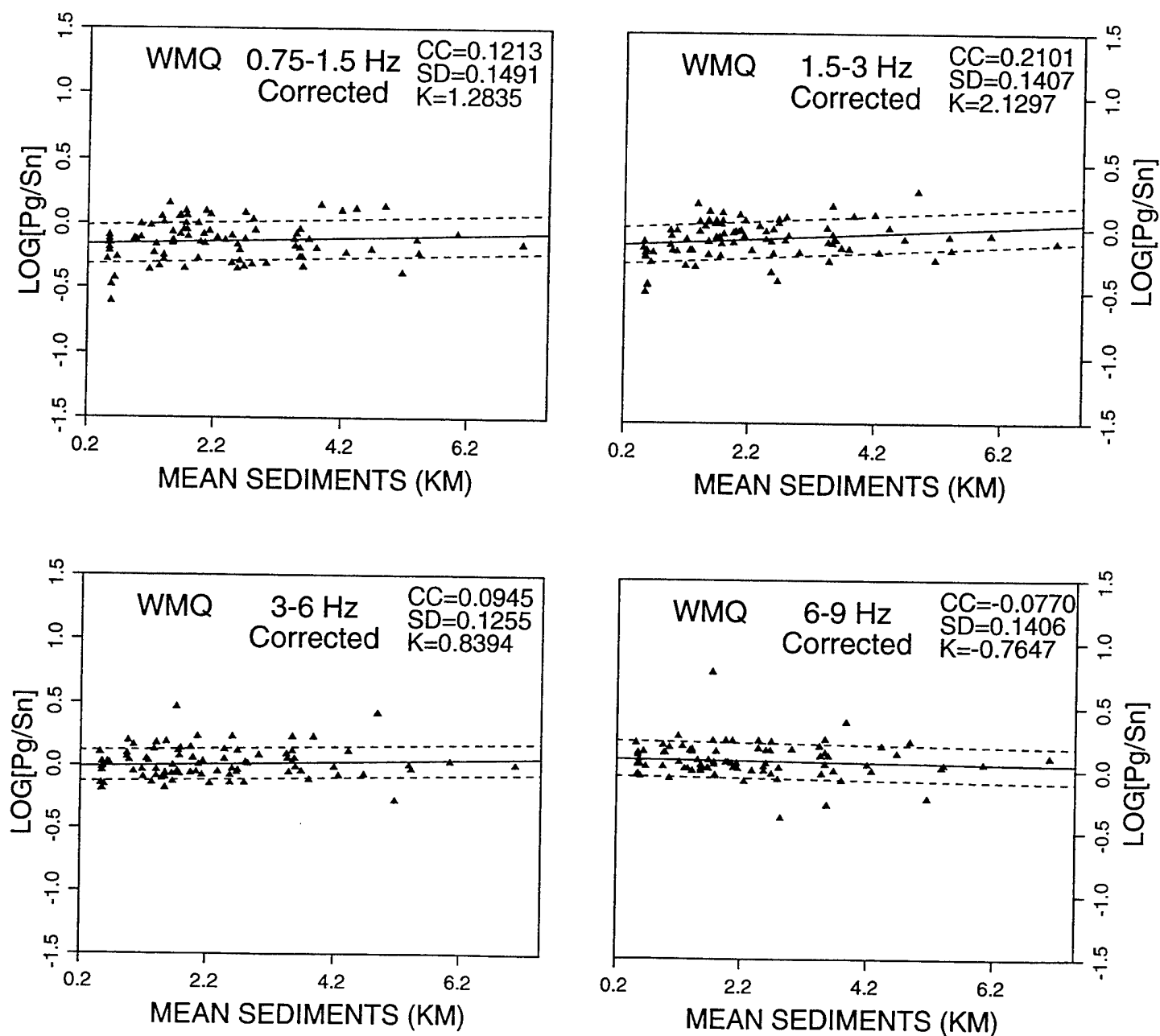


Figure A4q. Frequency dependent ratios of Pg/Sn phases recorded at WMQ plotted as a function of mean sediment thickness of each path after correcting for the distance dependence in Figure A4a. CC denotes the linear correlation coefficient. SD denotes the standard deviation of the linear regression, with the dotted lines corresponding to  $\pm 1$  SD, and K denotes the slope of the regression.

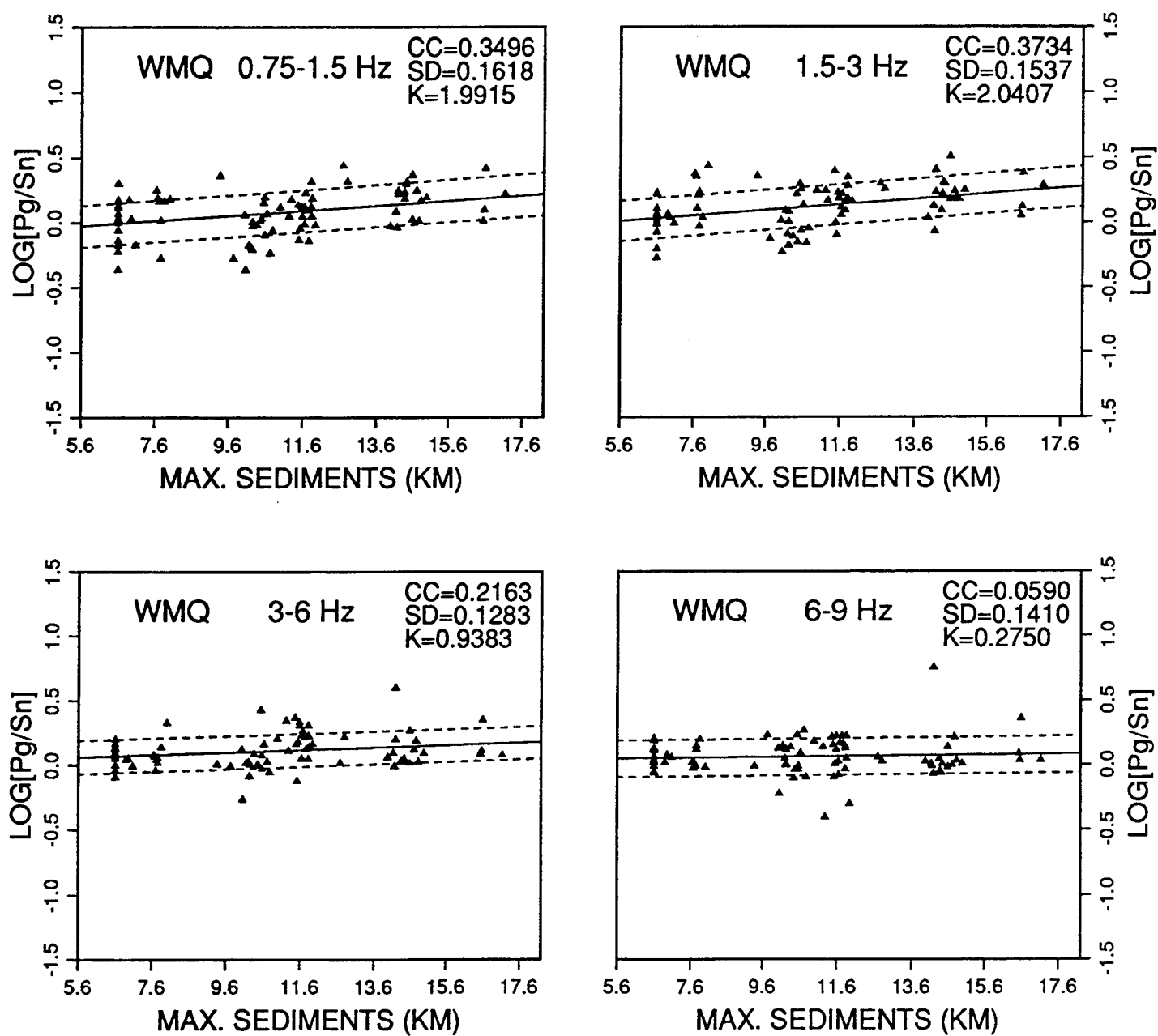


Figure A4r. Frequency dependent ratios of Pg/Sn phases recorded at WMQ plotted as a function of maximum sediment thickness on each path. CC denotes the linear correlation coefficient. SD denotes the standard deviation of the linear regression, with the dotted lines corresponding to  $\pm 1$  SD, and K denotes the slope of the regression.

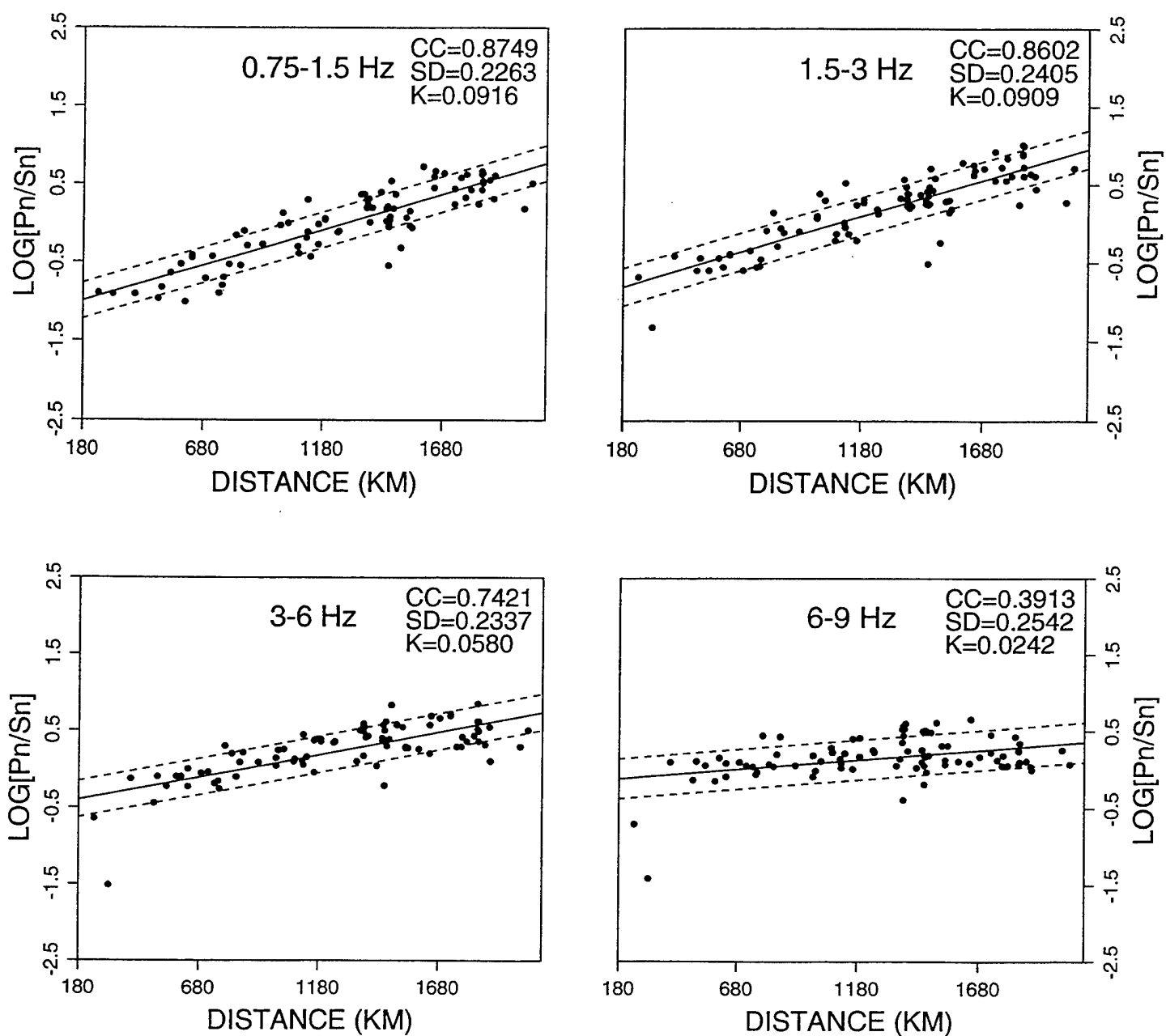


Figure A5a. Frequency dependent ratios of Pn/Sn phases recorded at WMQ plotted as a function of path length. CC denotes the linear correlation coefficient. SD denotes the standard deviation of the linear regression, with the dotted lines corresponding to  $\pm 1$  SD, and K denotes the slope of the regression.

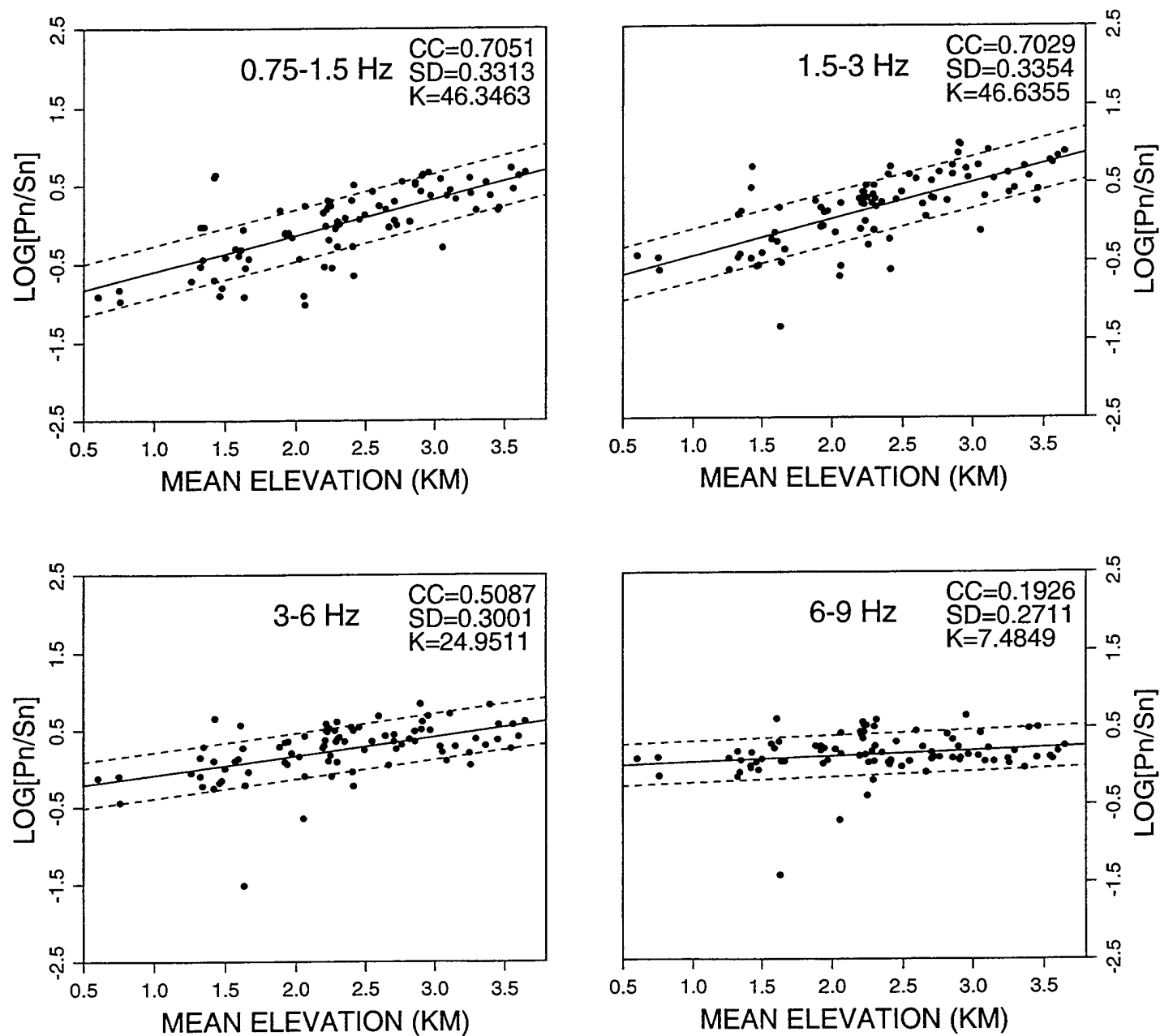


Figure A5b. Frequency dependent ratios of Pn/Sn phases recorded at WMQ plotted as a function of mean elevation of each path. CC denotes the linear correlation coefficient. SD denotes the standard deviation of the linear regression, with the dotted lines corresponding to  $\pm 1$  SD, and K denotes the slope of the regression.

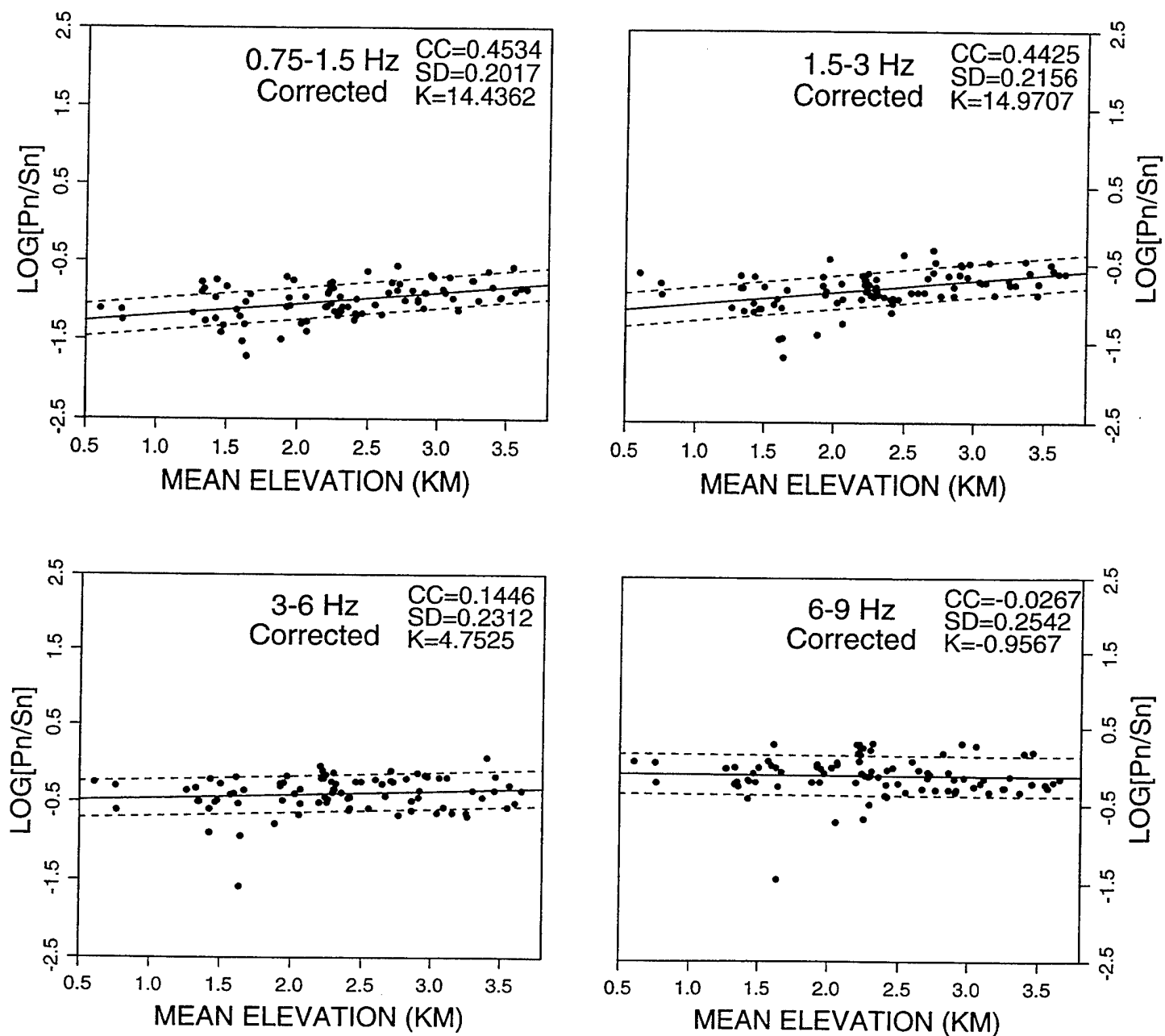


Figure A5c. Frequency dependent ratios of Pn/Sn phases recorded at WMQ plotted as a function of mean elevation of each path after correcting for the distance dependence in Figure A5a. CC denotes the linear correlation coefficient. SD denotes the standard deviation of the linear regression, with the dotted lines corresponding to  $\pm 1$  SD, and K denotes the slope of the regression.

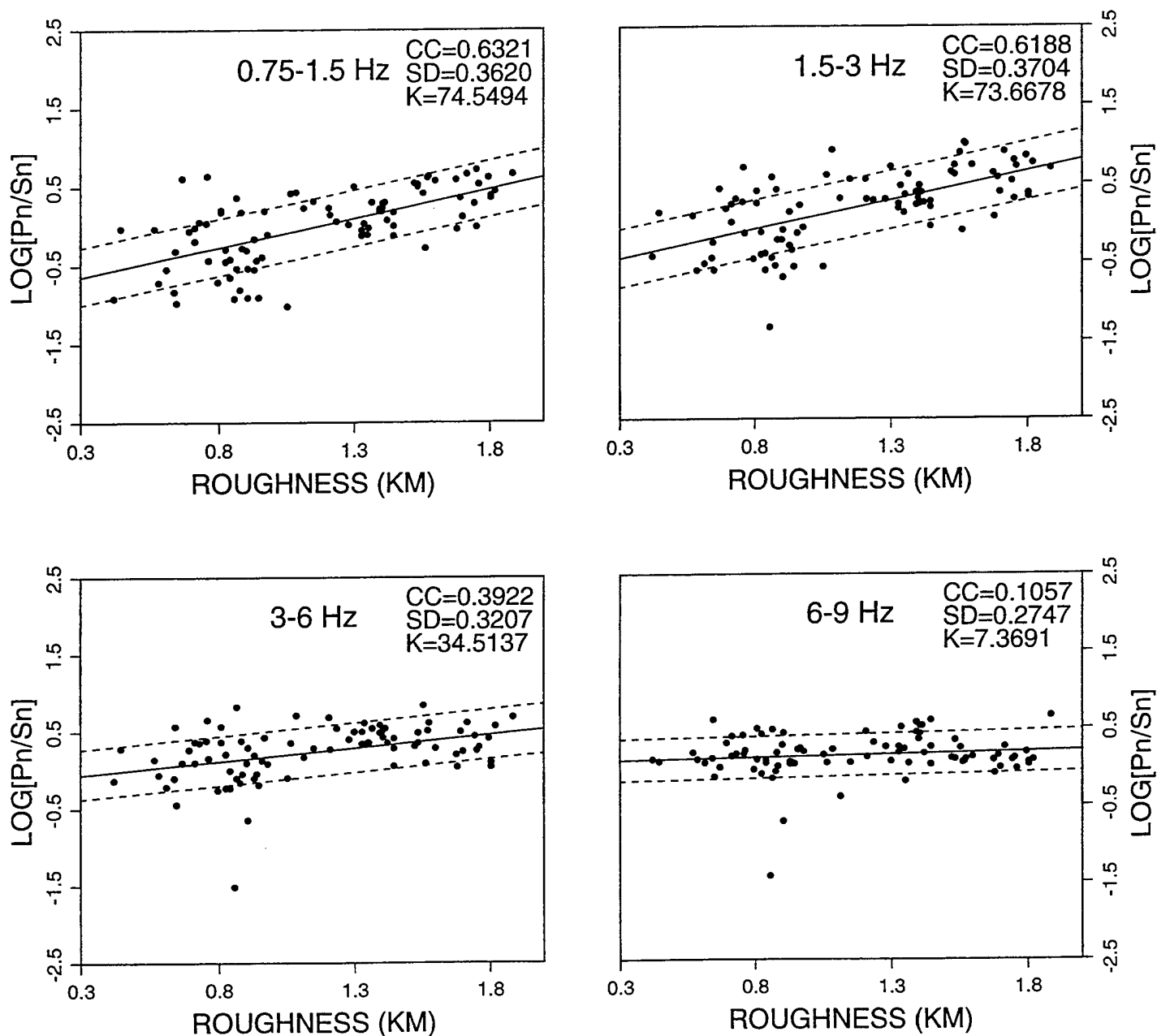


Figure A5d. Frequency dependent ratios of Pn/Sn phases recorded at WMQ plotted as a function of mean surface roughness of each path. CC denotes the linear correlation coefficient. SD denotes the standard deviation of the linear regression, with the dotted lines corresponding to  $\pm 1$  SD, and K denotes the slope of the regression.

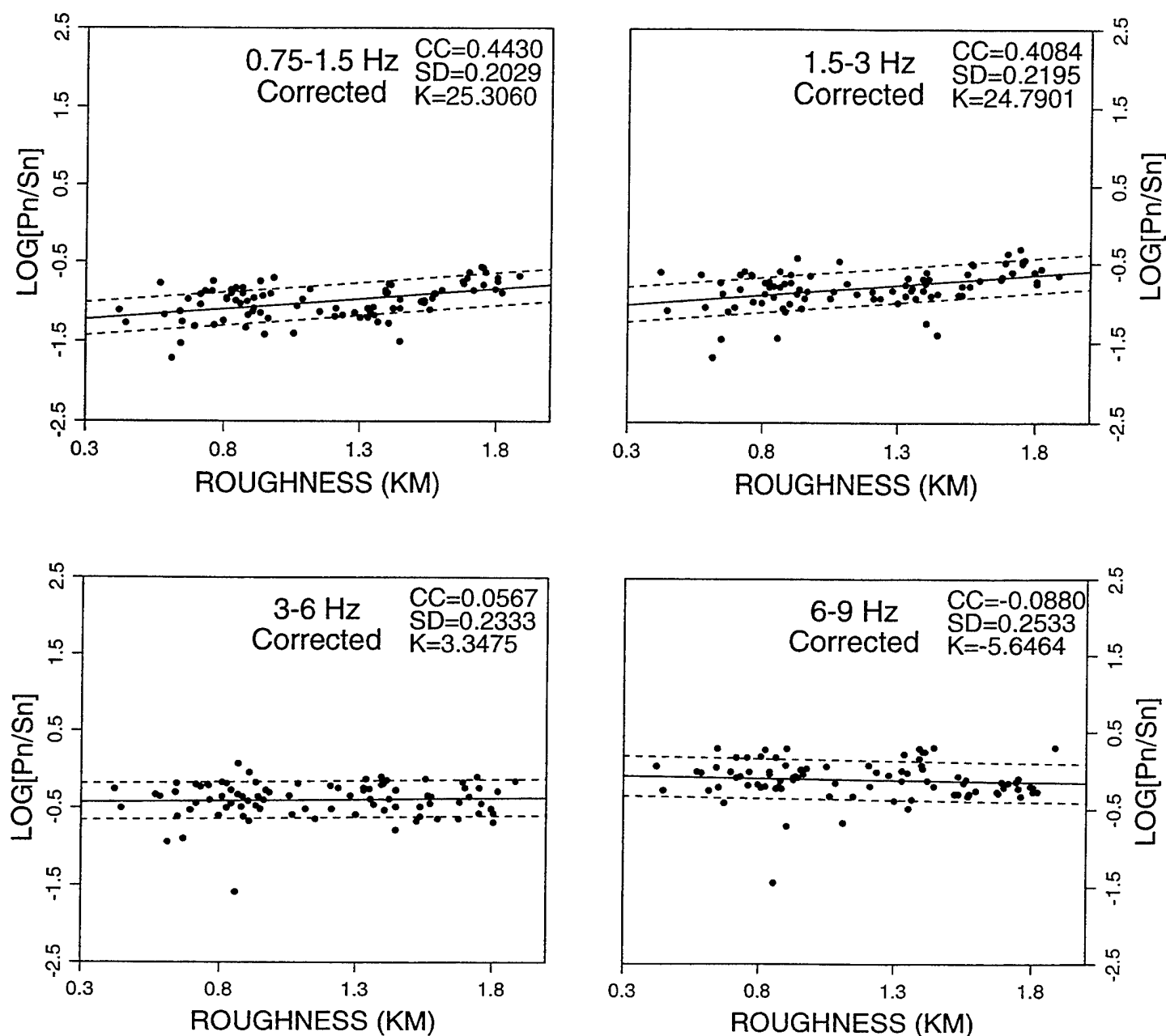


Figure A5e. Frequency dependent ratios of Pn/Sn phases recorded at WMQ plotted as a function of mean surface roughness of each path after correcting for the distance dependence in Figure A5a. CC denotes the linear correlation coefficient. SD denotes the standard deviation of the linear regression, with the dotted lines corresponding to  $\pm 1$  SD, and K denotes the slope of the regression.

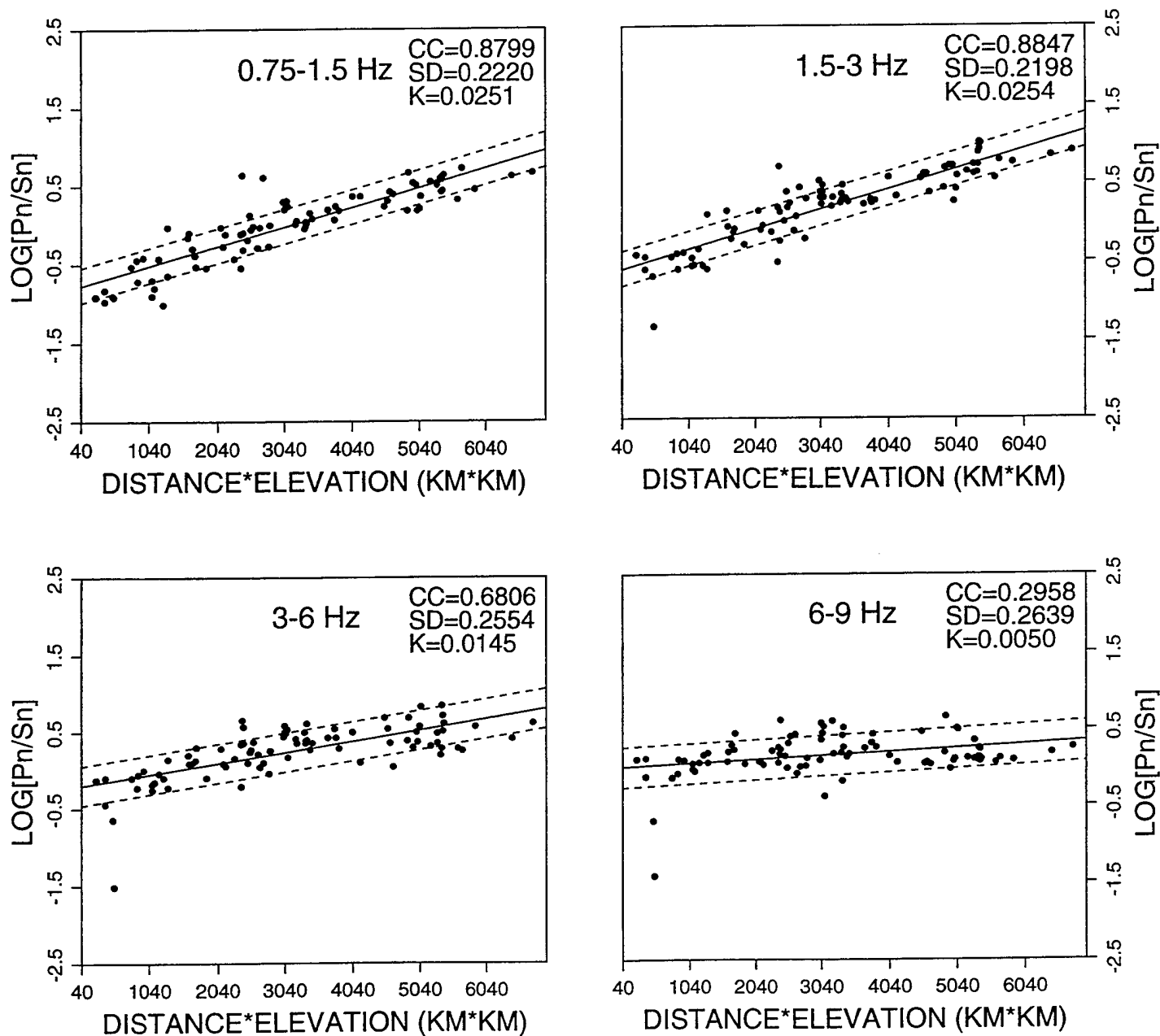


Figure A5f. Frequency dependent ratios of Pn/Sn phases recorded at WMQ plotted as a function of the product of path length times mean path elevation. CC denotes the linear correlation coefficient. SD denotes the standard deviation of the linear regression, with the dotted lines corresponding to  $\pm 1$  SD, and K denotes the slope of the regression.



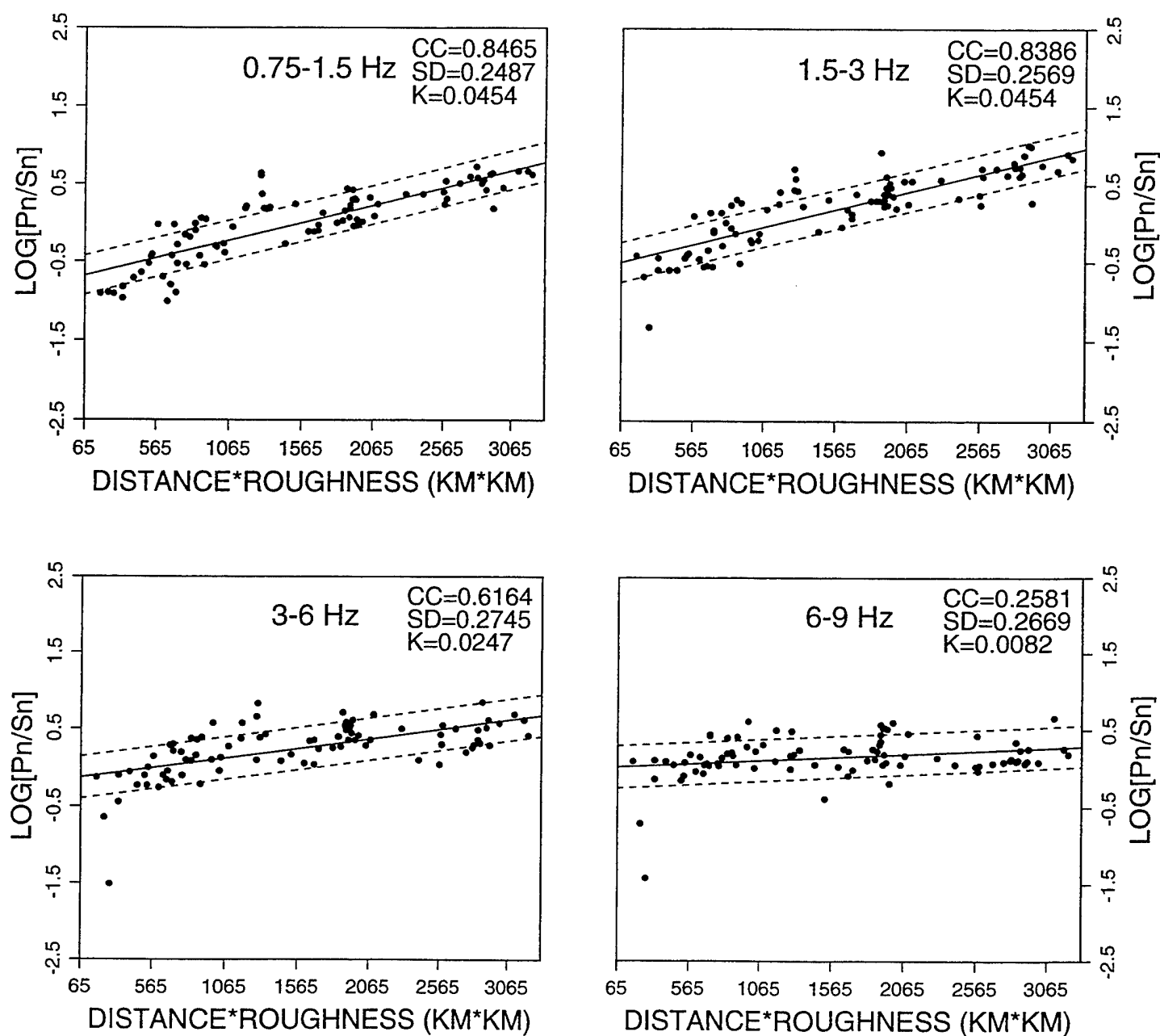


Figure A5g. Frequency dependent ratios of Pn/Sn phases recorded at WMQ plotted as a function of the product of path length times mean surface roughness. CC denotes the linear correlation coefficient. SD denotes the standard deviation of the linear regression, with the dotted lines corresponding to  $\pm 1$  SD, and K denotes the slope of the regression.

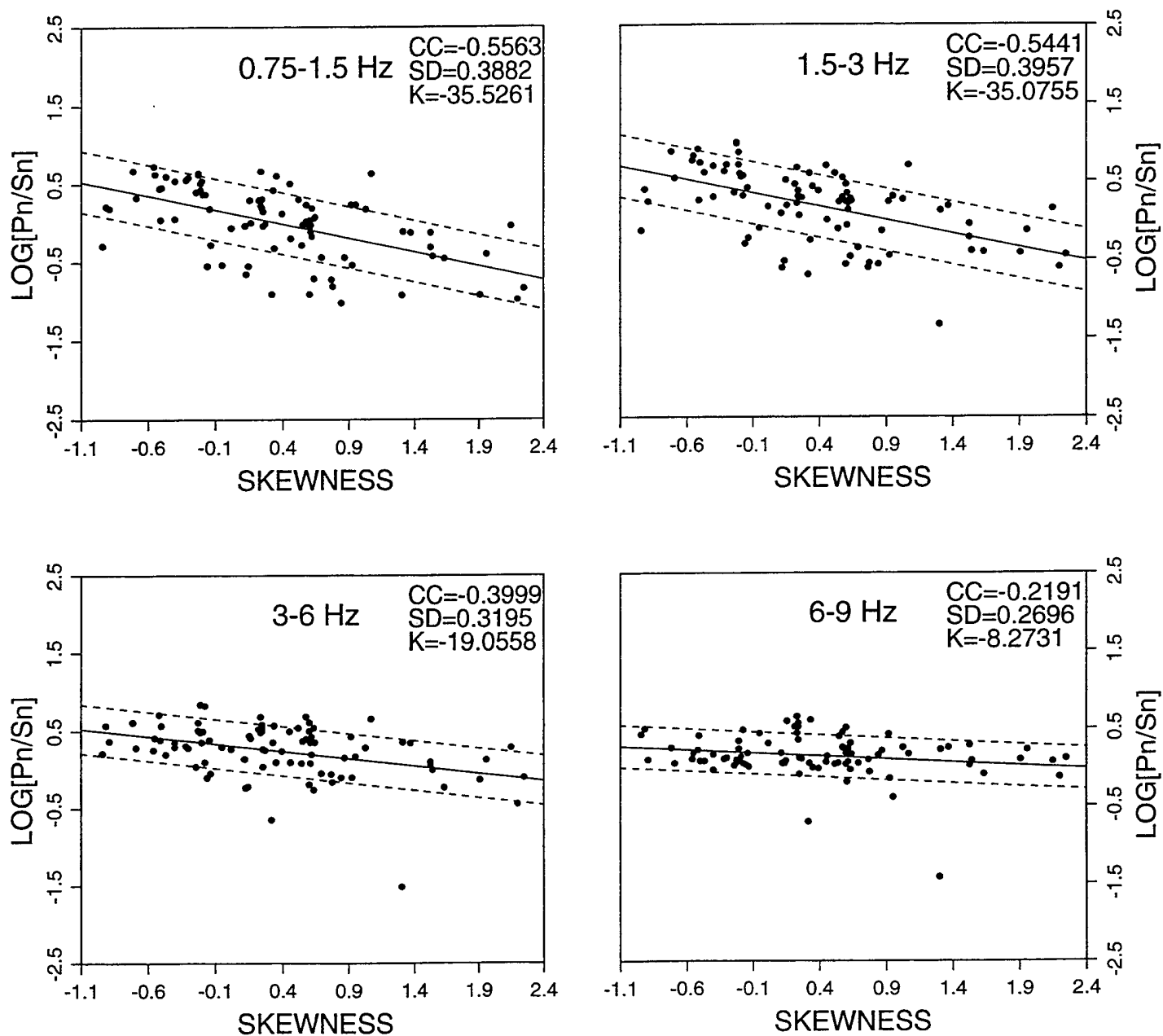


Figure A5h. Frequency dependent ratios of Pn/Sn phases recorded at WMQ plotted as a function of mean surface skewness of each path. CC denotes the linear correlation coefficient. SD denotes the standard deviation of the linear regression, with the dotted lines corresponding to  $\pm 1$  SD, and K denotes the slope of the regression.

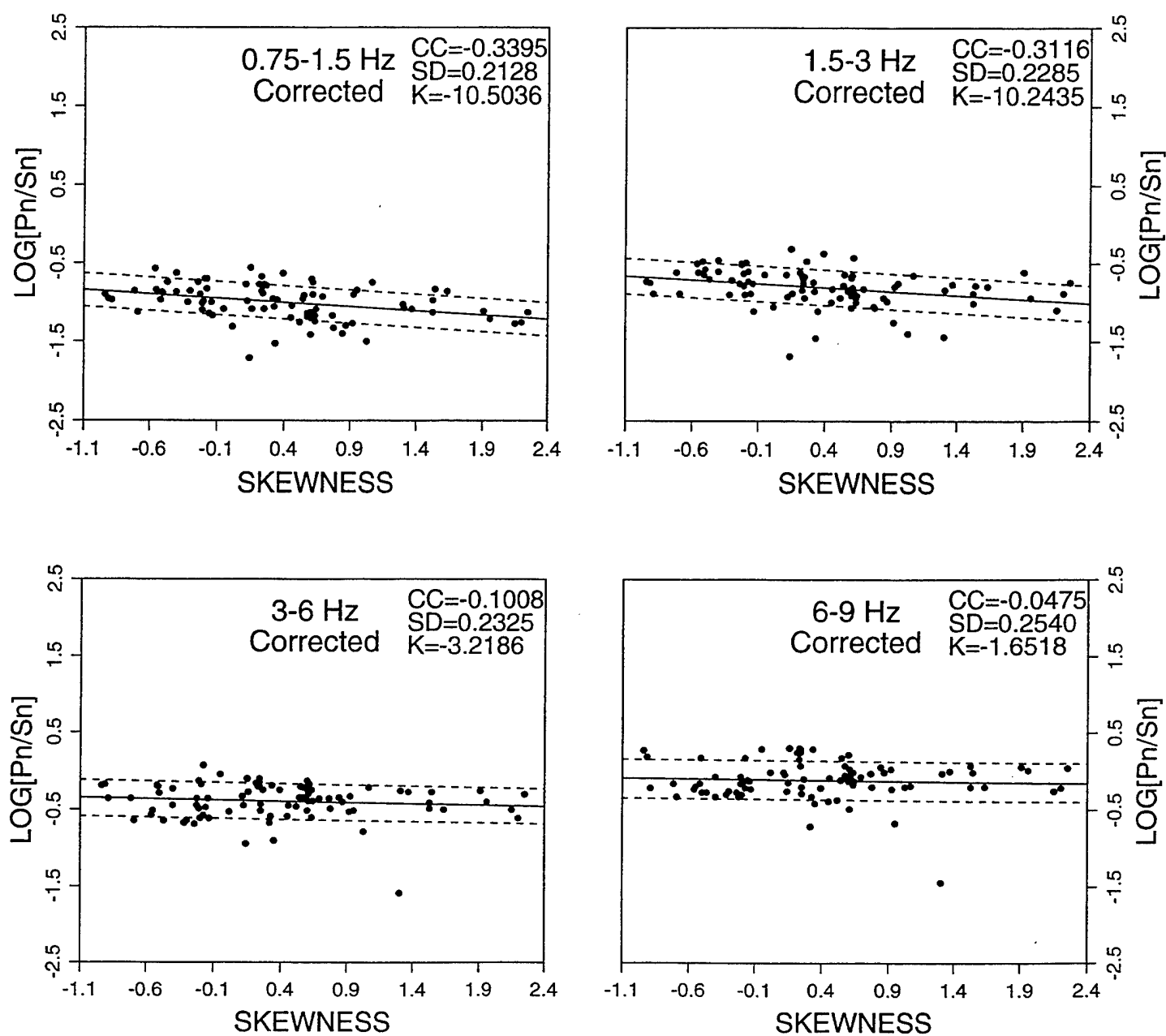


Figure A5i. Frequency dependent ratios of Pn/Sn phases recorded at WMQ plotted as a function of mean surface skewness of each path after correcting for the distance dependence in Figure A5a. CC denotes the linear correlation coefficient. SD denotes the standard deviation of the linear regression, with the dotted lines corresponding to  $\pm 1$  SD, and K denotes the slope of the regression.

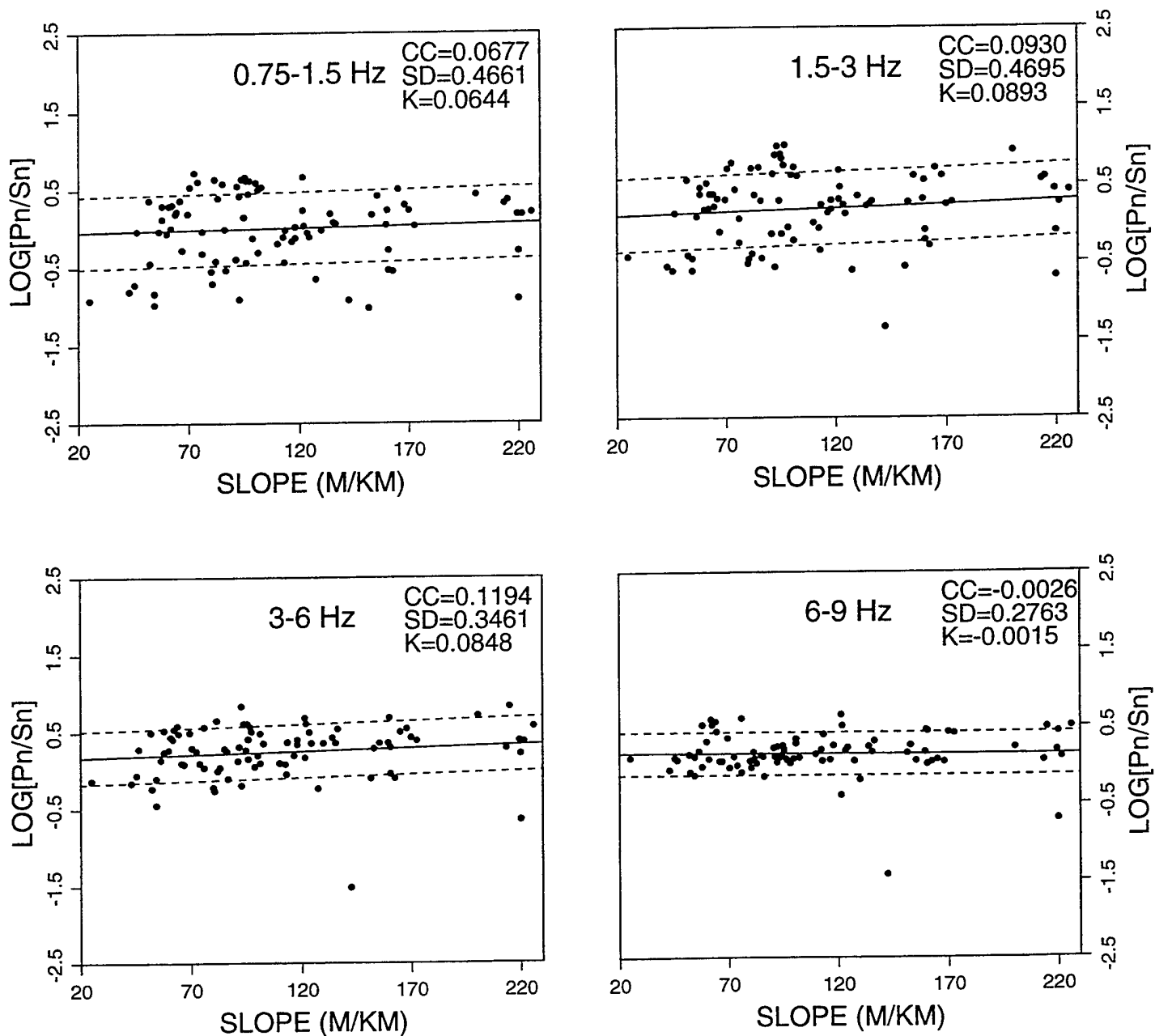


Figure A5j. Frequency dependent ratios of Pn/Sn phases recorded at WMQ plotted as a function of mean surface slope of each path. CC denotes the linear correlation coefficient. SD denotes the standard deviation of the linear regression, with the dotted lines corresponding to  $\pm 1$  SD, and K denotes the slope of the regression.

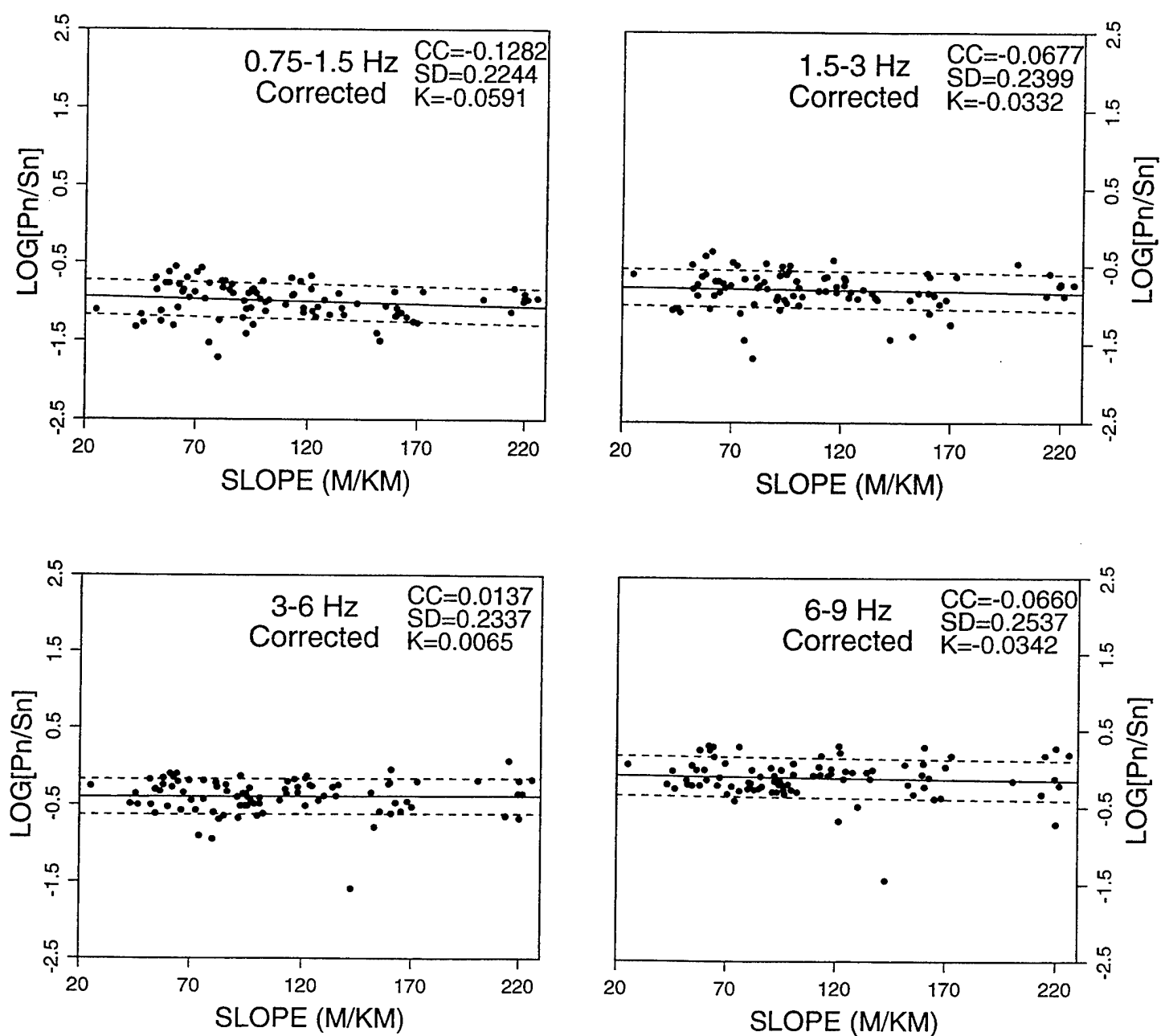


Figure A5k. Frequency dependent ratios of Pn/Sn phases recorded at WMQ plotted as a function of mean surface slope of each path after correcting for the distance dependence in Figure A5a. CC denotes the linear correlation coefficient. SD denotes the standard deviation of the linear regression, with the dotted lines corresponding to  $\pm 1$  SD, and K denotes the slope of the regression.

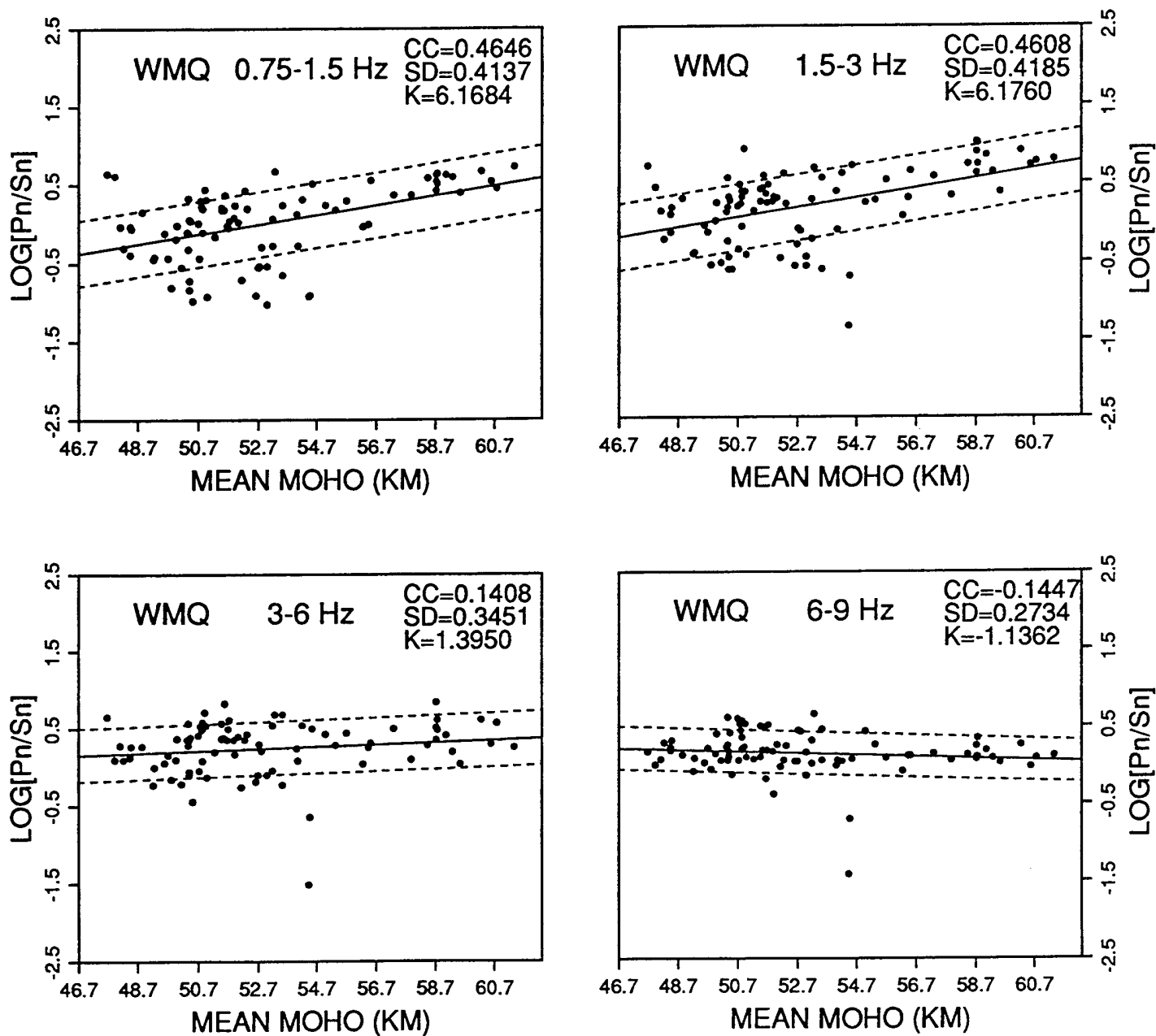


Figure A51. Frequency dependent ratios of Pn/Sn phases recorded at WMQ plotted as a function of mean crustal thickness of each path. CC denotes the linear correlation coefficient. SD denotes the standard deviation of the linear regression, with the dotted lines corresponding to  $\pm 1$  SD, and K denotes the slope of the regression.

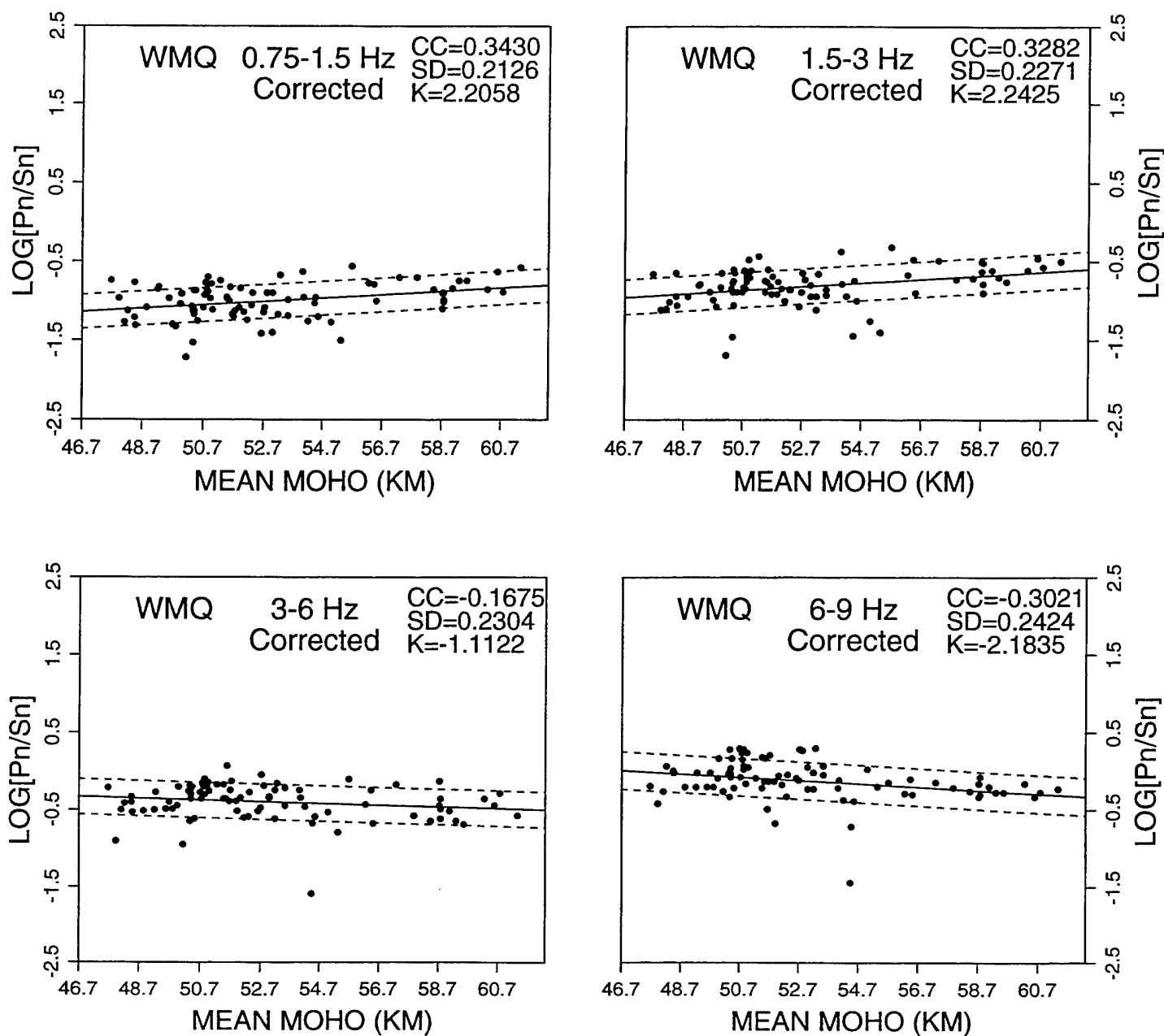


Figure A5m. Frequency dependent ratios of Pn/Sn phases recorded at WMQ plotted as a function of mean crustal thickness of each path after correcting for the distance dependence in Figure A5a. CC denotes the linear correlation coefficient. SD denotes the standard deviation of the linear regression, with the dotted lines corresponding to  $\pm 1$  SD, and K denotes the slope of the regression.

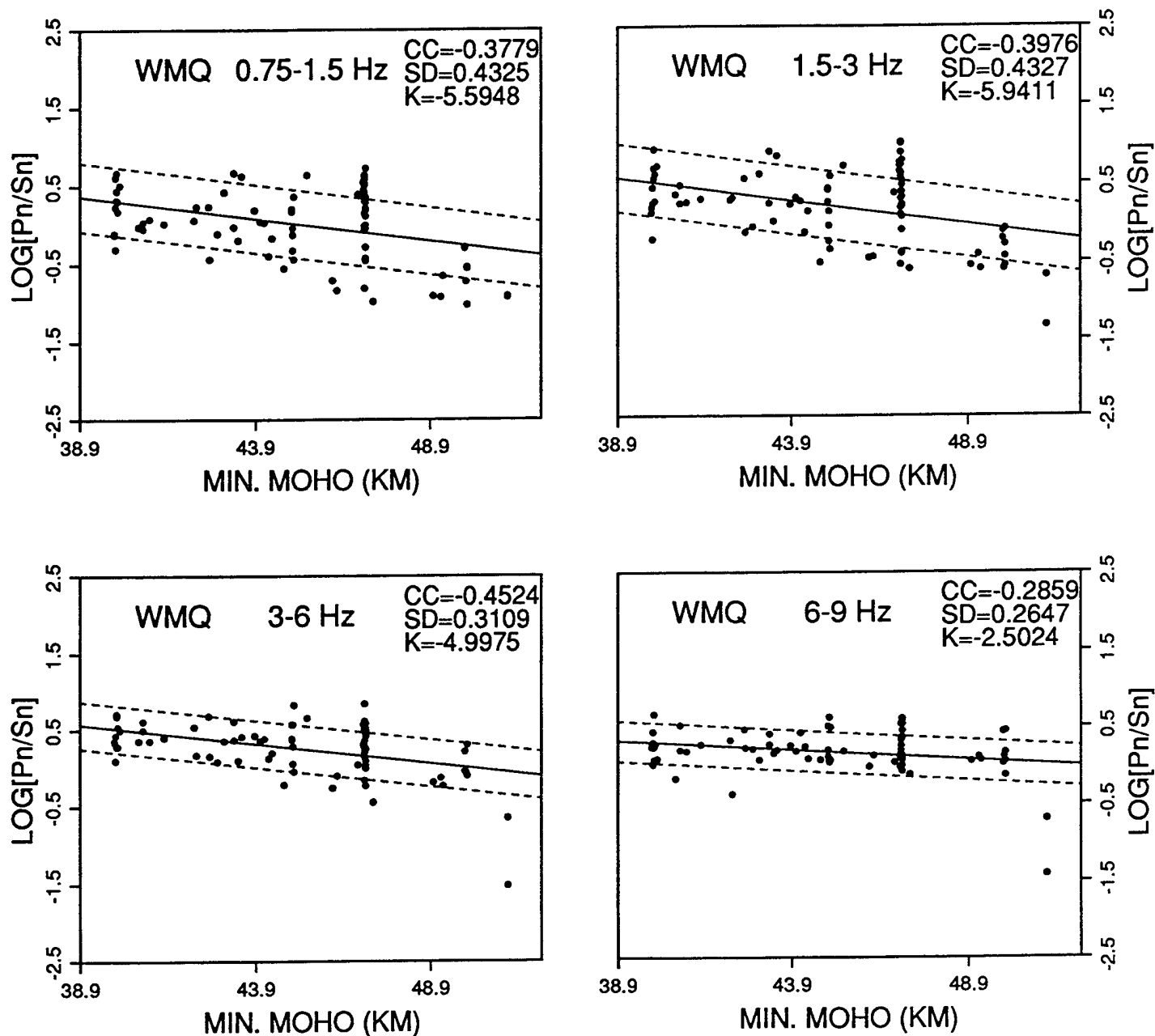


Figure A5n. Frequency dependent ratios of Pn/Sn phases recorded at WMQ plotted as a function of minimum crustal thickness on each path. CC denotes the linear correlation coefficient. SD denotes the standard deviation of the linear regression, with the dotted lines corresponding to  $\pm 1$  SD, and K denotes the slope of the regression.



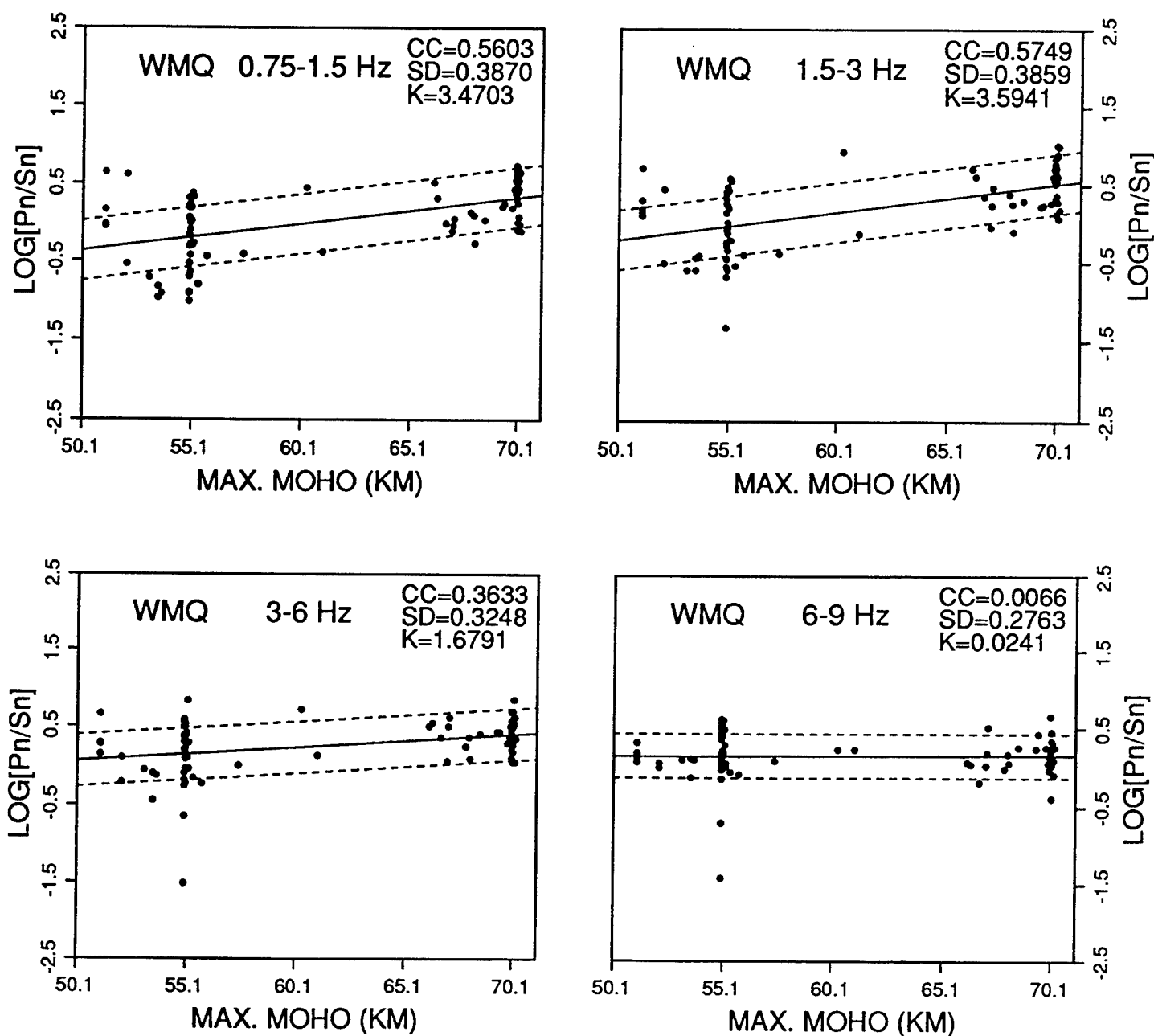


Figure A5o. Frequency dependent ratios of Pn/Sn phases recorded at WMQ plotted as a function of maximum crustal thickness on each path. CC denotes the linear correlation coefficient. SD denotes the standard deviation of the linear regression, with the dotted lines corresponding to  $\pm 1$  SD, and K denotes the slope of the regression.

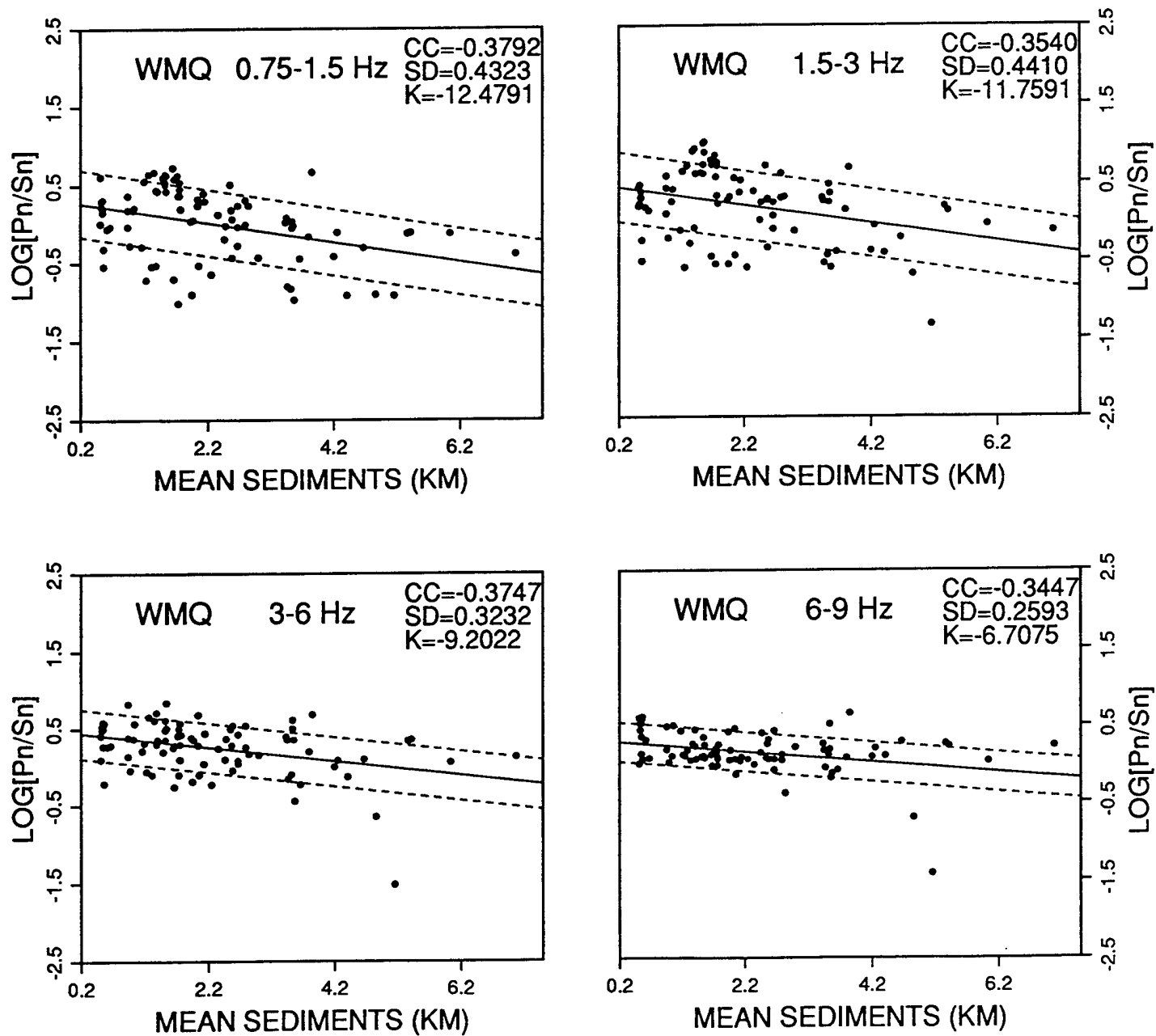


Figure A5p. Frequency dependent ratios of Pn/Sn phases recorded at WMQ plotted as a function of mean sediment thickness of each path. CC denotes the linear correlation coefficient. SD denotes the standard deviation of the linear regression, with the dotted lines corresponding to  $\pm 1$  SD, and K denotes the slope of the regression.

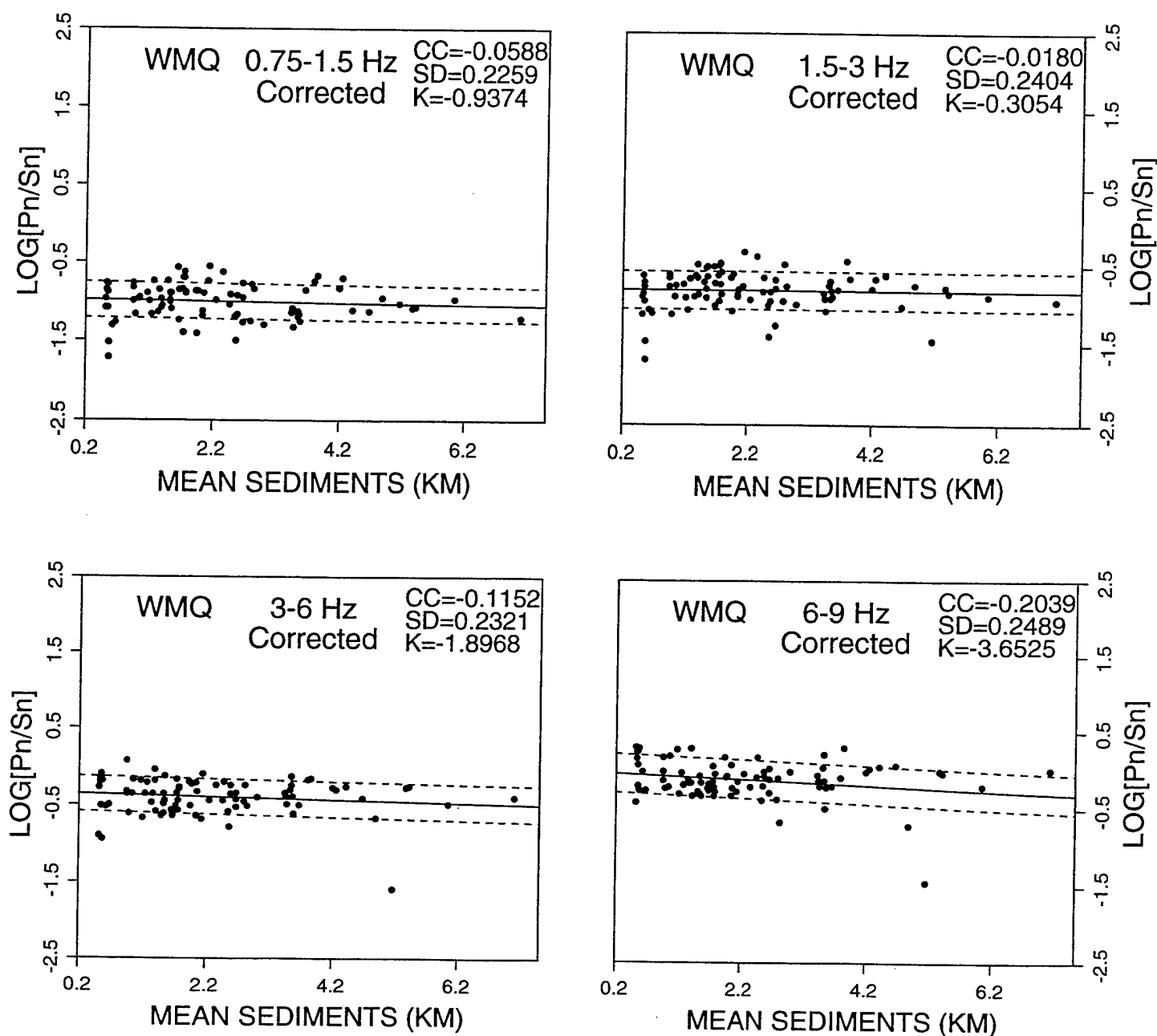


Figure A5q. Frequency dependent ratios of Pn/Sn phases recorded at WMQ plotted as a function of mean sediment thickness of each path after correcting for the distance dependence in Figure A5a. CC denotes the linear correlation coefficient. SD denotes the standard deviation of the linear regression, with the dotted lines corresponding to  $\pm 1$  SD, and K denotes the slope of the regression.

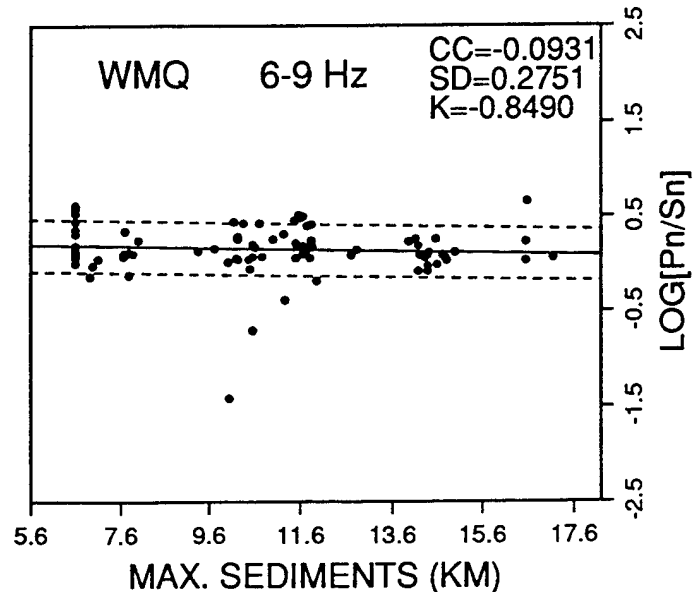
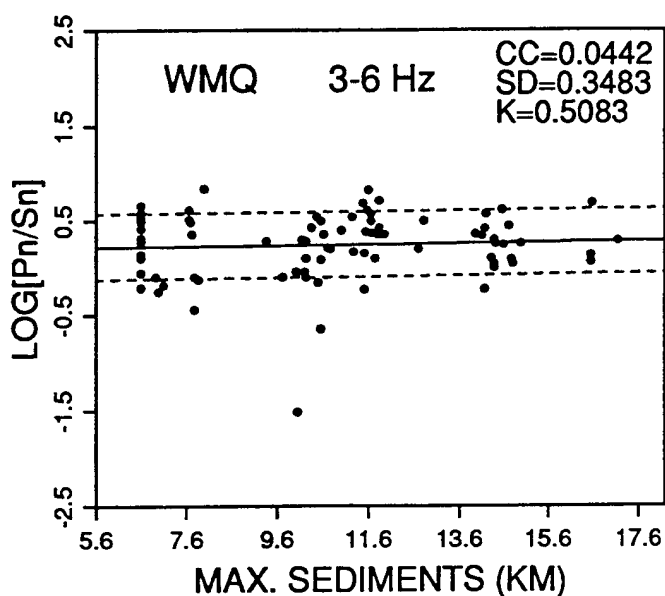
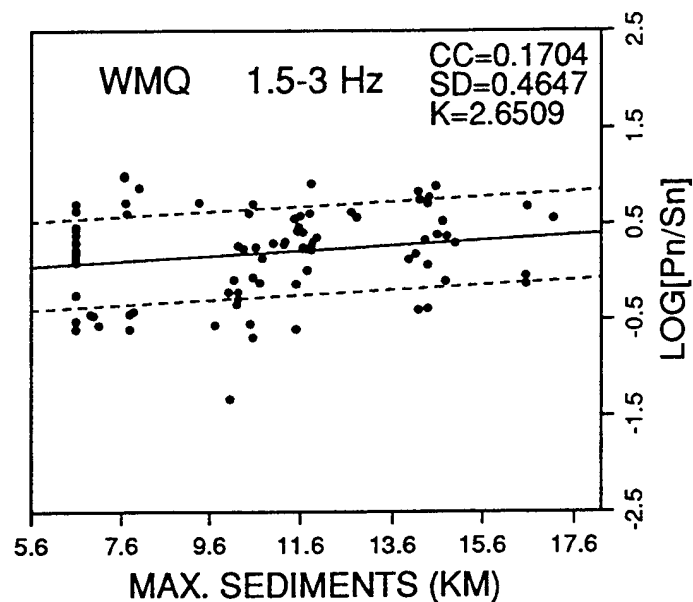
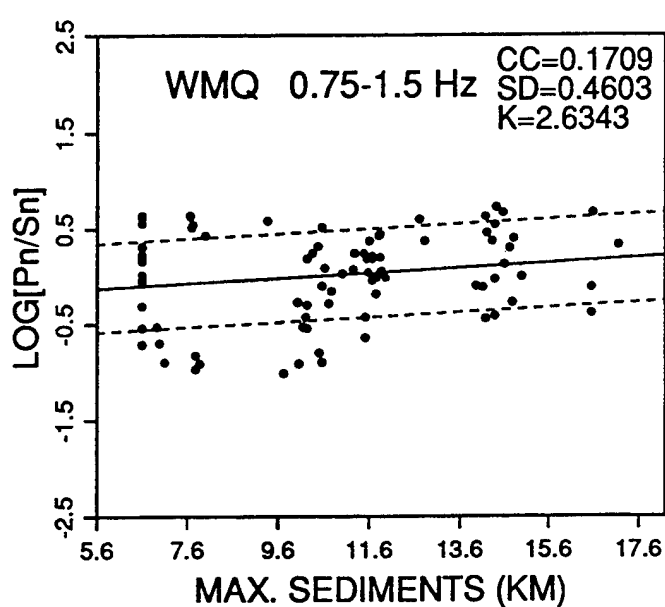


Figure A5r. Frequency dependent ratios of Pn/Sn phases recorded at WMQ plotted as a function of maximum sediment thickness on each path. CC denotes the linear correlation coefficient. SD denotes the standard deviation of the linear regression, with the dotted lines corresponding to  $\pm 1$  SD, and K denotes the slope of the regression.

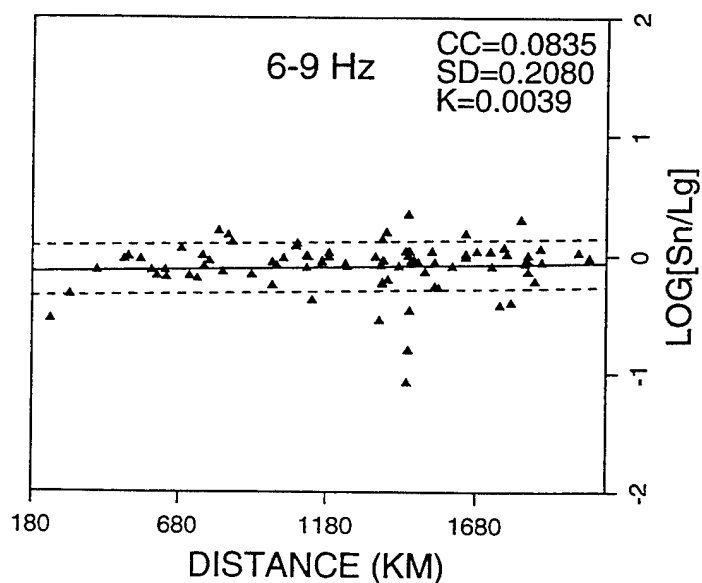
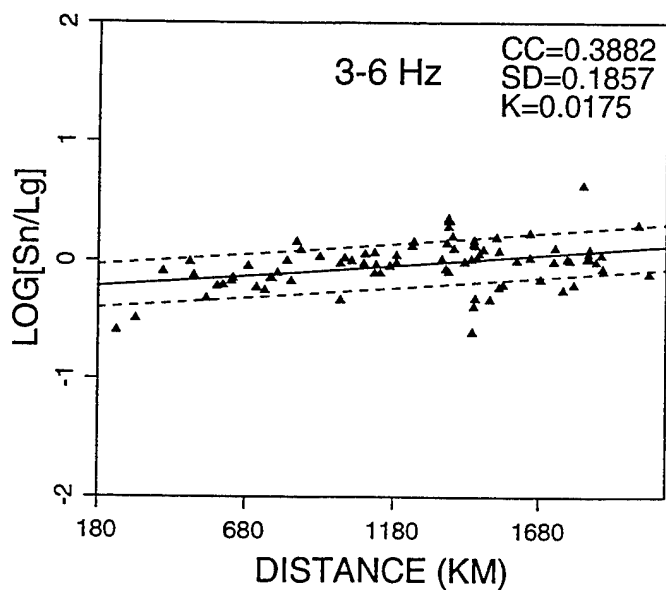
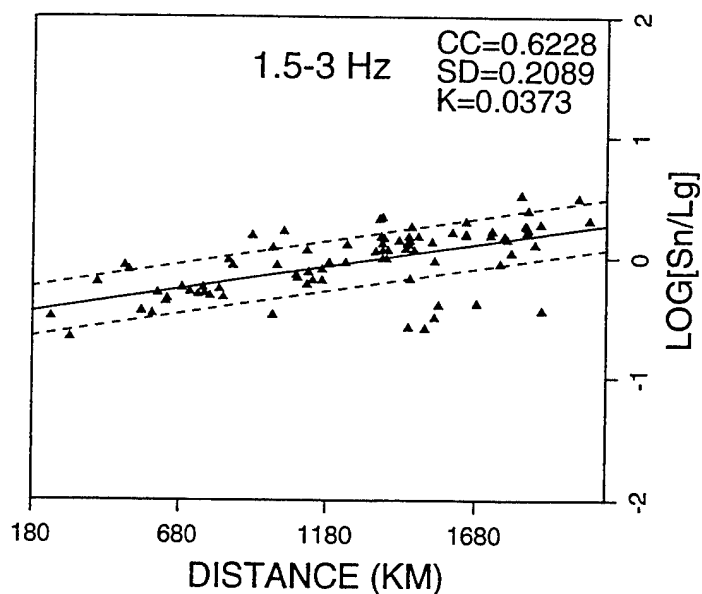
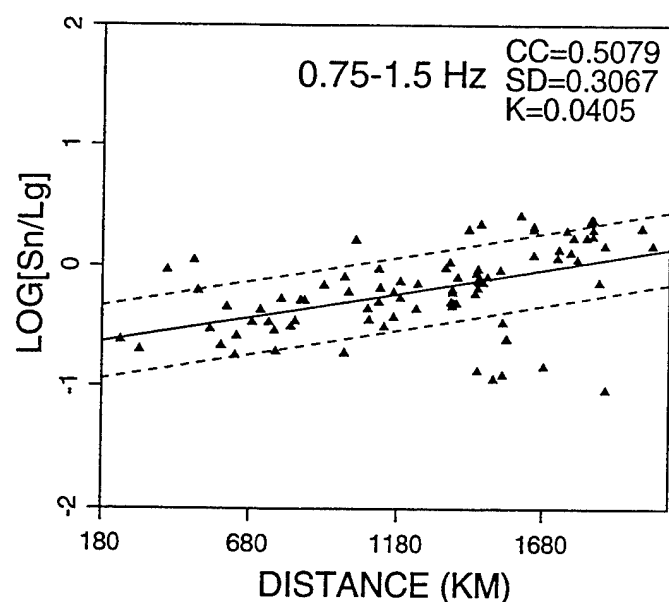


Figure A6a. Frequency dependent ratios of Sn/Lg phases recorded at WMQ plotted as a function of path length. CC denotes the linear correlation coefficient. SD denotes the standard deviation of the linear regression, with the dotted lines corresponding to  $\pm 1$  SD, and K denotes the slope of the regression.

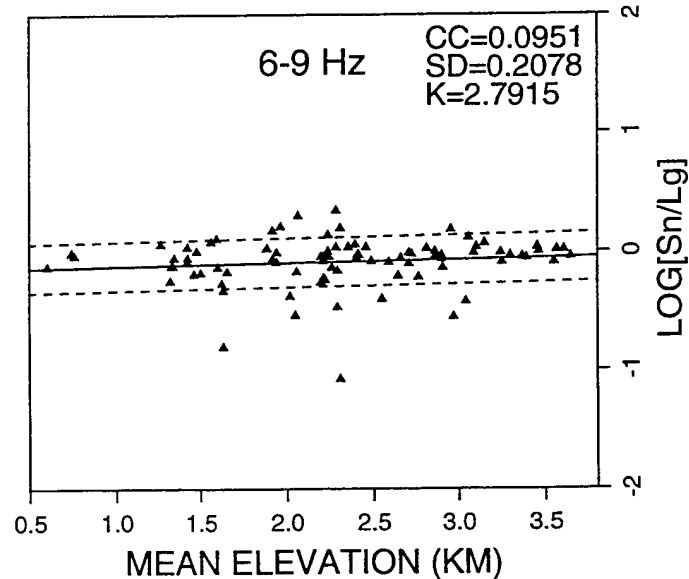
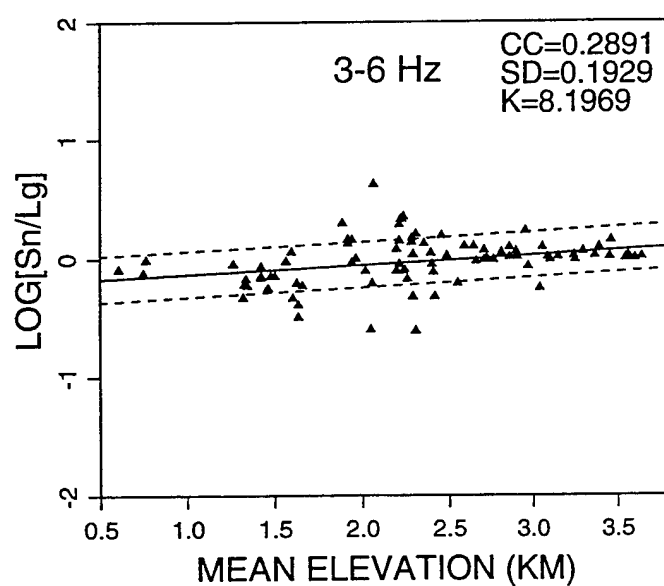
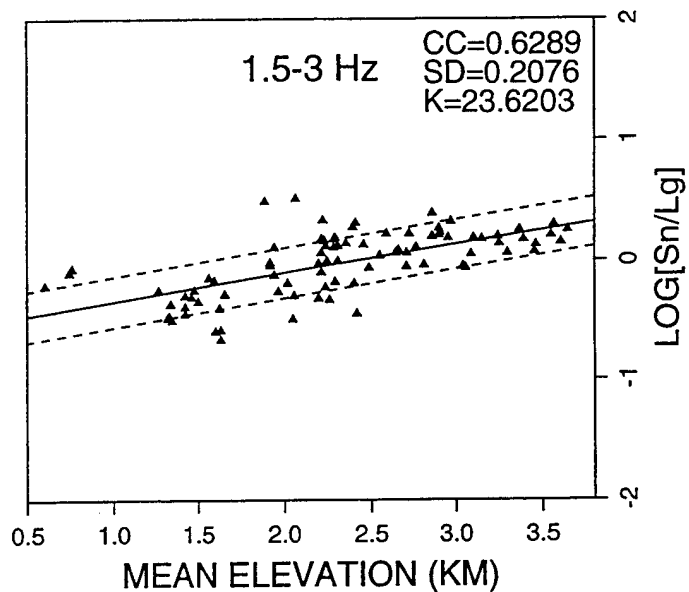
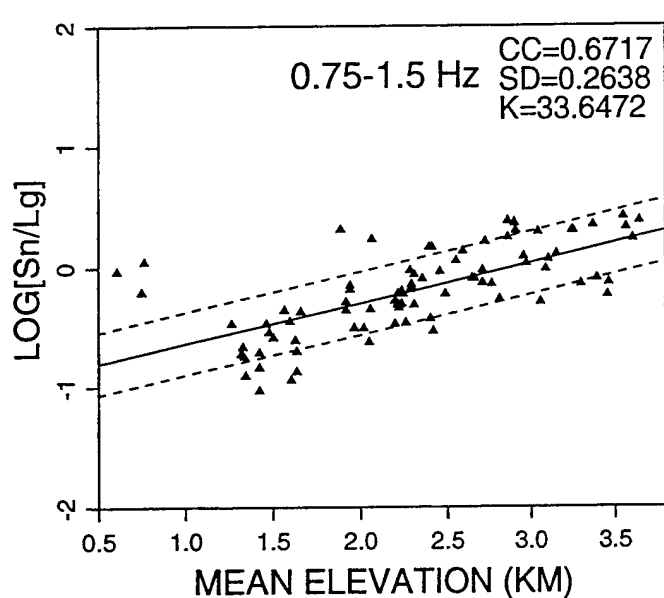


Figure A6b. Frequency dependent ratios of Sn/Lg phases recorded at WMQ plotted as a function of mean elevation of each path. CC denotes the linear correlation coefficient. SD denotes the standard deviation of the linear regression, with the dotted lines corresponding to  $\pm 1$  SD, and K denotes the slope of the regression.

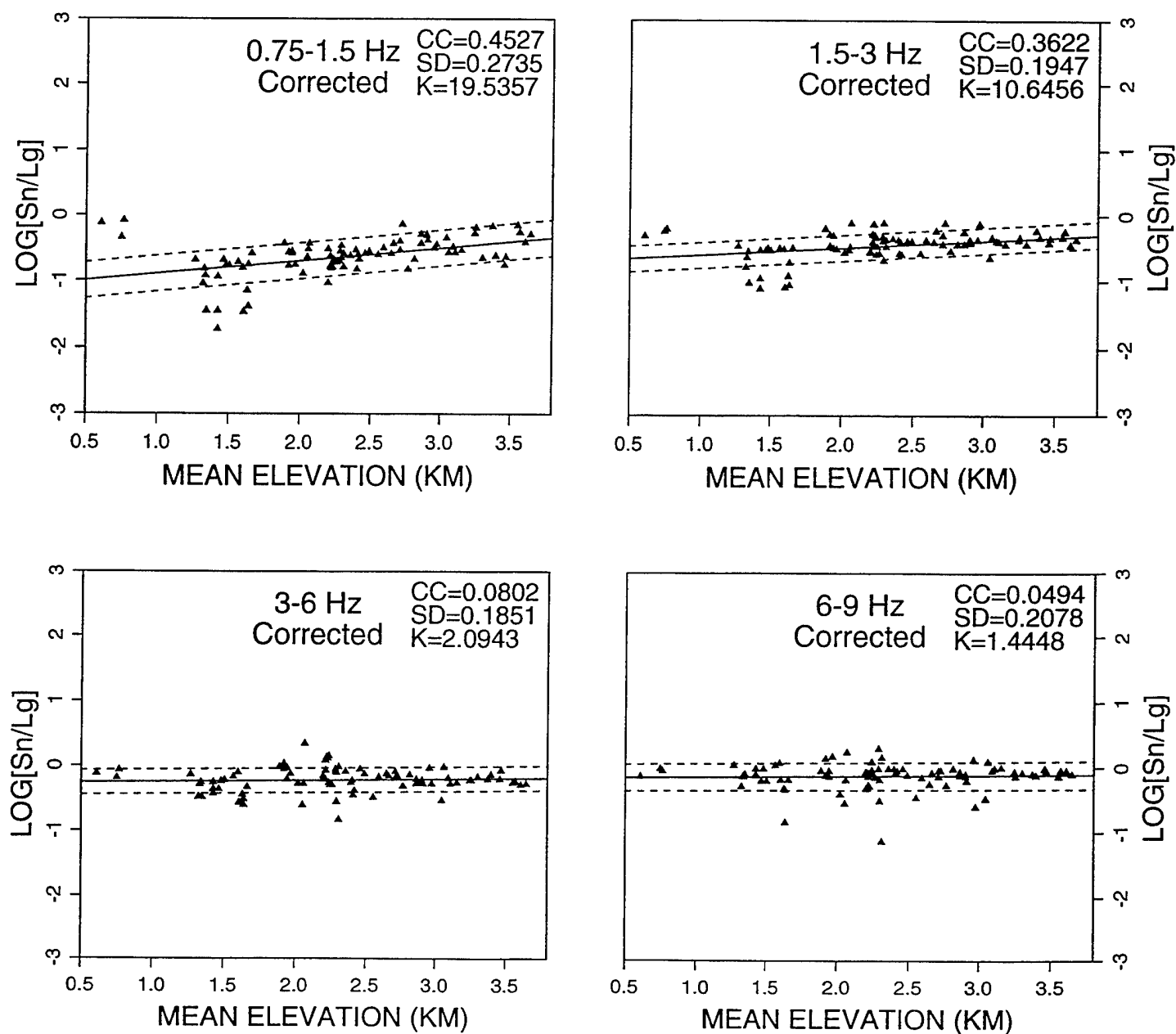


Figure A6c. Frequency dependent ratios of Sn/Lg phases recorded at WMQ plotted as a function of mean elevation of each path after correcting for the distance dependence in Figure A6a. CC denotes the linear correlation coefficient. SD denotes the standard deviation of the linear regression, with the dotted lines corresponding to  $\pm 1$  SD, and K denotes the slope of the regression.

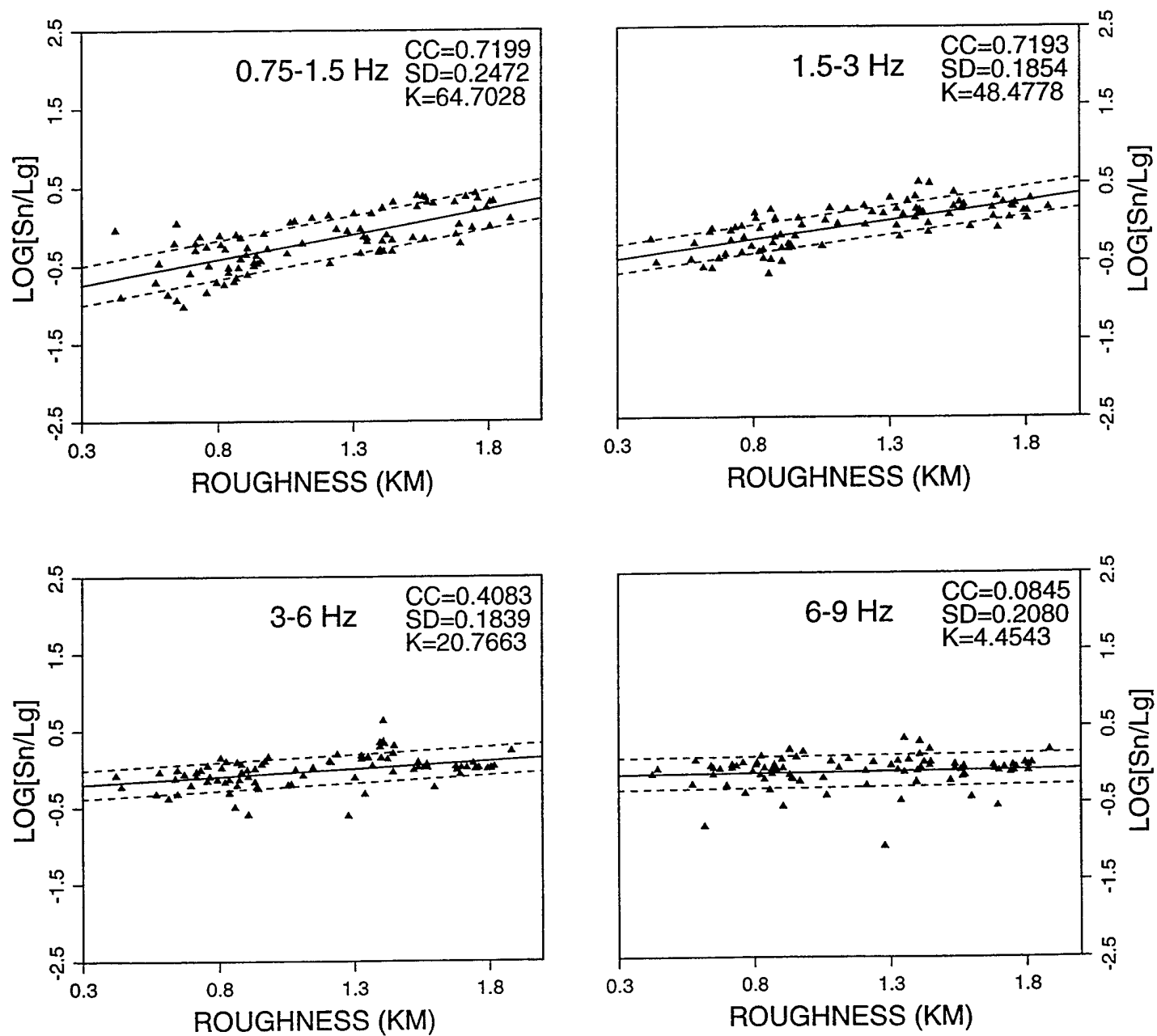


Figure A6d. Frequency dependent ratios of Sn/Lg phases recorded at WMQ plotted as a function of mean surface roughness of each path. CC denotes the linear correlation coefficient. SD denotes the standard deviation of the linear regression, with the dotted lines corresponding to  $\pm 1$  SD, and K denotes the slope of the regression.



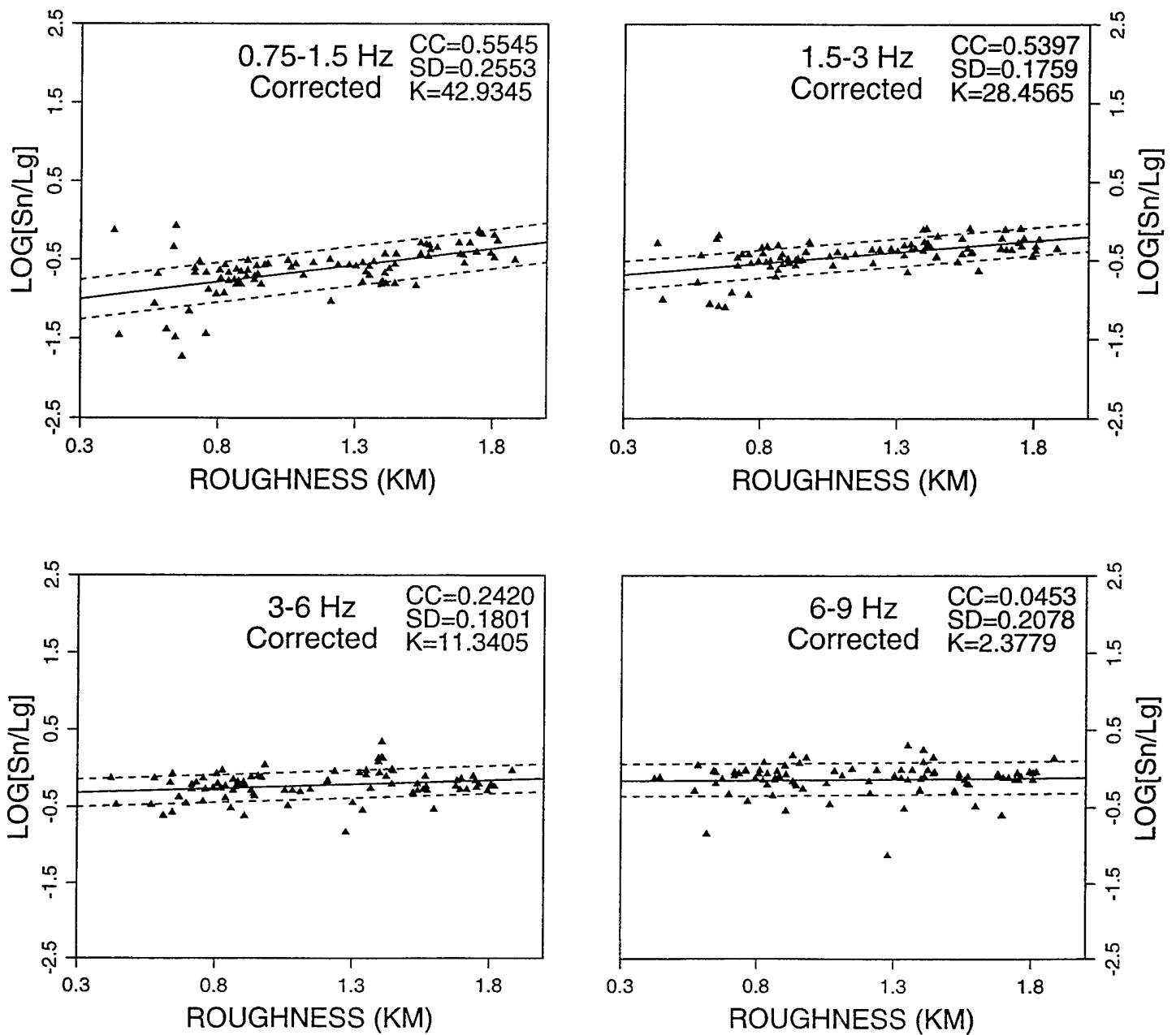


Figure A6e. Frequency dependent ratios of Sn/Lg phases recorded at WMQ plotted as a function of mean surface roughness of each path after correcting for the distance dependence in Figure A6a. CC denotes the linear correlation coefficient. SD denotes the standard deviation of the linear regression, with the dotted lines corresponding to  $\pm 1$  SD, and K denotes the slope of the regression.

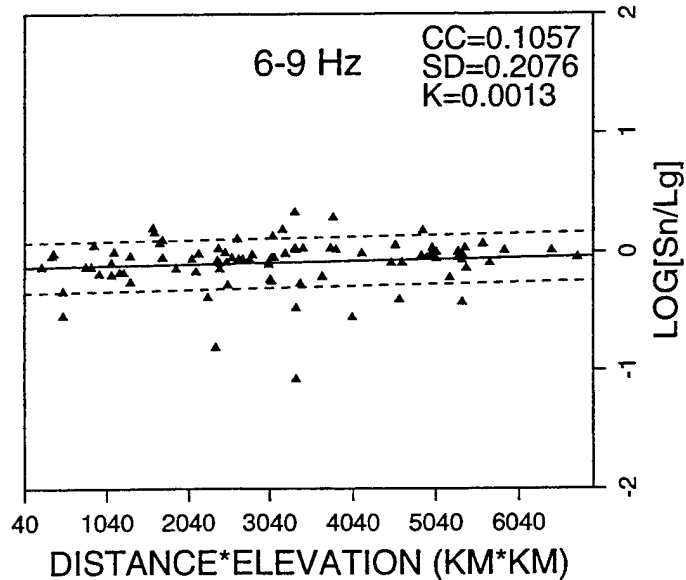
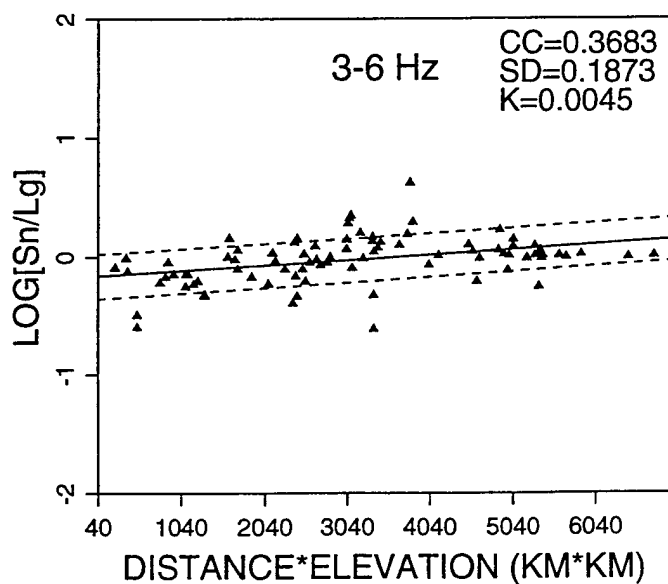
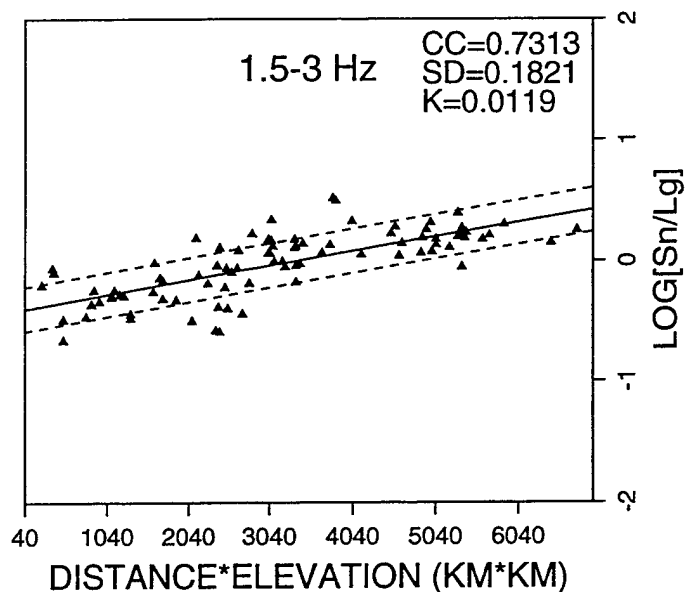
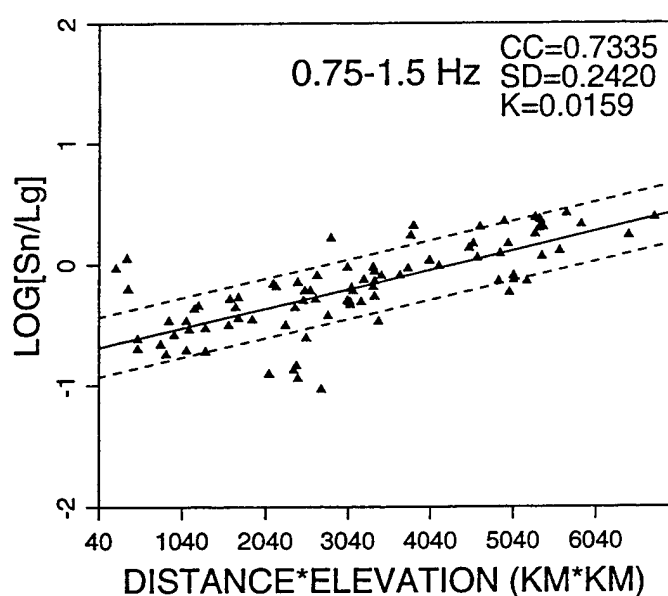


Figure A6f. Frequency dependent ratios of Sn/Lg phases recorded at WMQ plotted as a function of the product of path length times mean path elevation. CC denotes the linear correlation coefficient. SD denotes the standard deviation of the linear regression, with the dotted lines corresponding to  $\pm 1$  SD, and K denotes the slope of the regression.

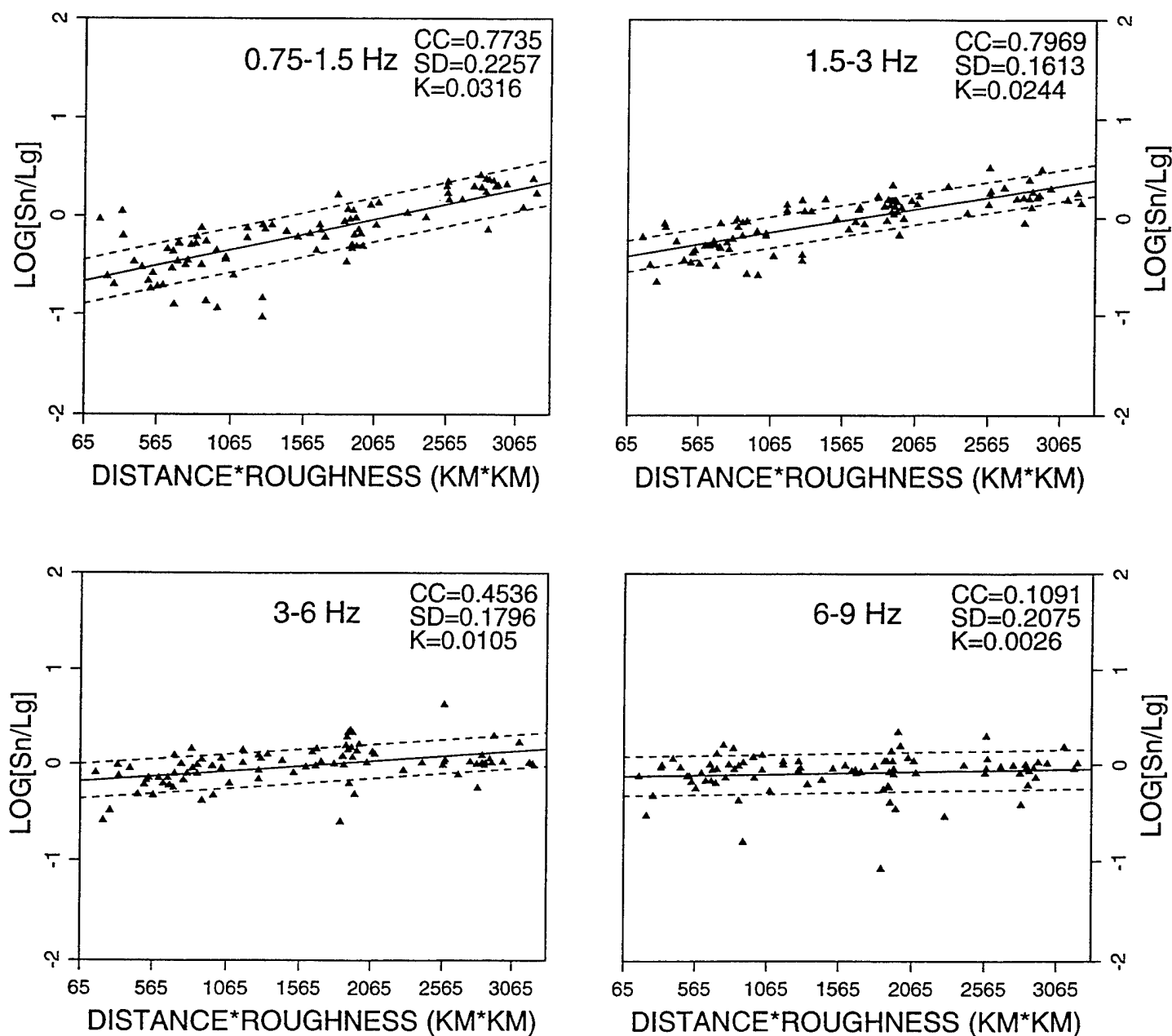


Figure A6g. Frequency dependent ratios of Sn/Lg phases recorded at WMQ plotted as a function of the product of path length times mean surface roughness. CC denotes the linear correlation coefficient. SD denotes the standard deviation of the linear regression, with the dotted lines corresponding to  $\pm 1$  SD, and K denotes the slope of the regression.

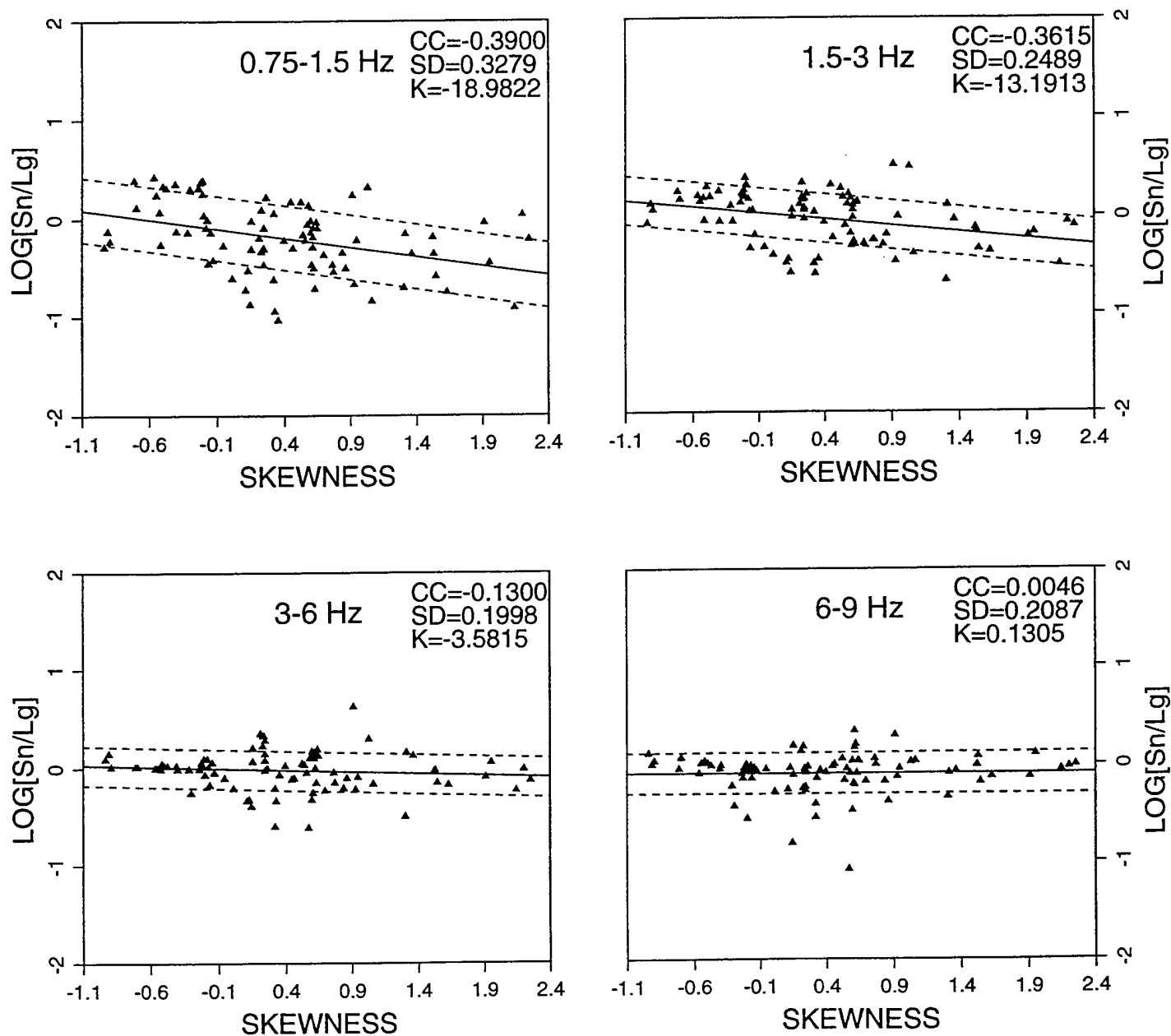


Figure A6h. Frequency dependent ratios of Sn/Lg phases recorded at WMQ plotted as a function of mean surface skewness of each path. CC denotes the linear correlation coefficient. SD denotes the standard deviation of the linear regression, with the dotted lines corresponding to  $\pm 1$  SD, and K denotes the slope of the regression.

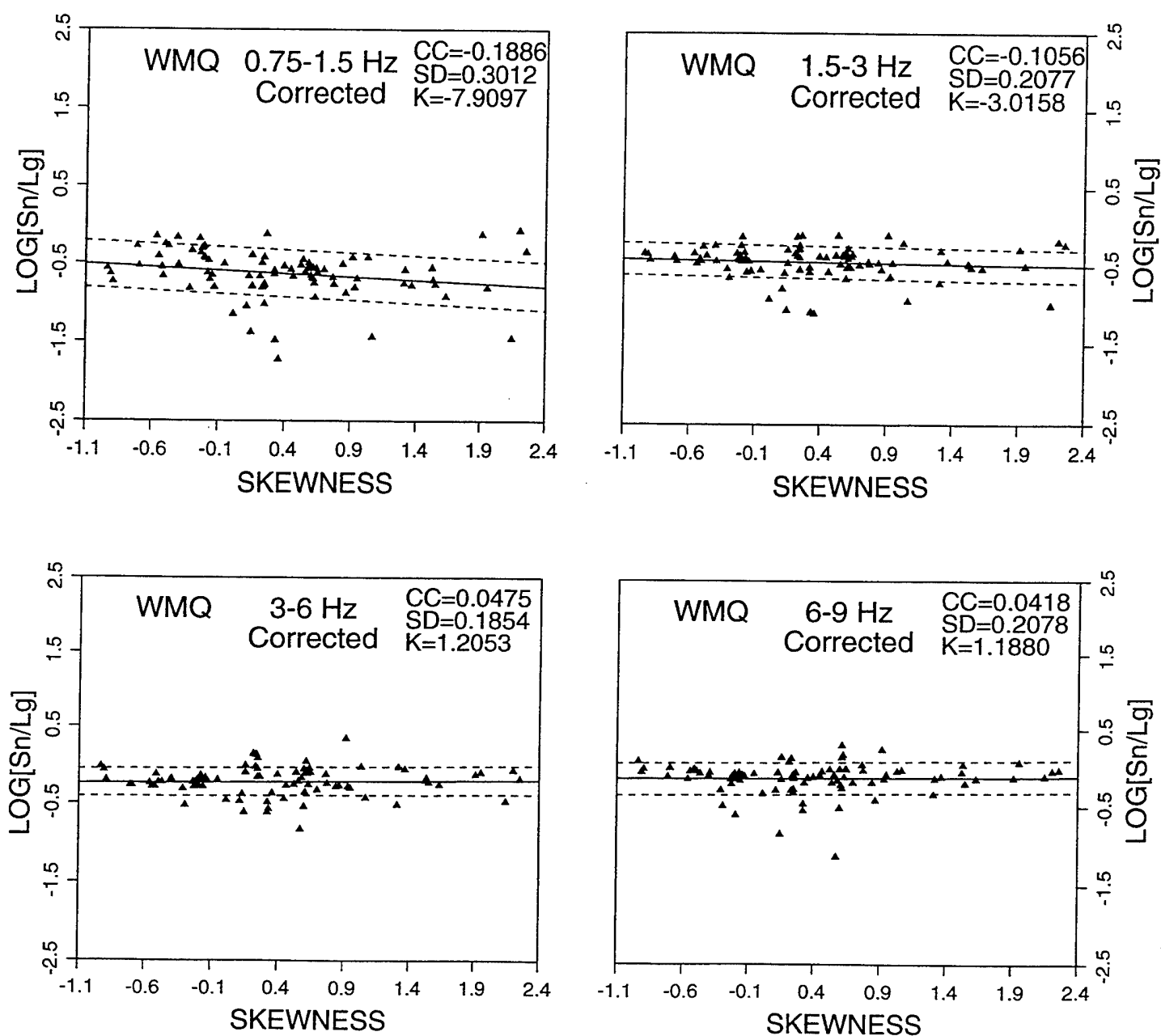


Figure A6i. Frequency dependent ratios of Sn/Lg phases recorded at WMQ plotted as a function of mean surface skewness of each path after correcting for the distance dependence in Figure A6a. CC denotes the linear correlation coefficient. SD denotes the standard deviation of the linear regression, with the dotted lines corresponding to  $\pm 1$  SD, and K denotes the slope of the regression.

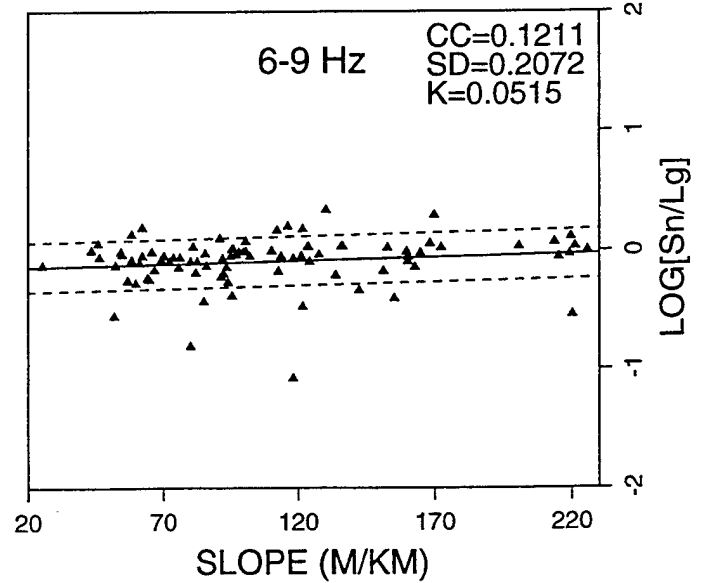
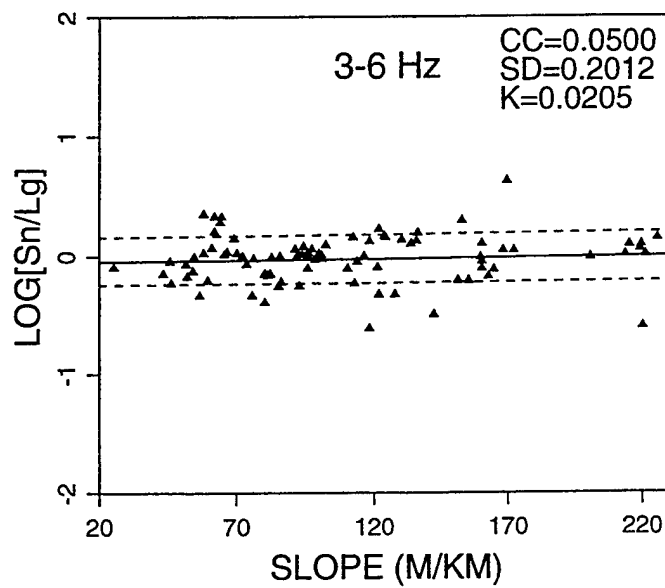
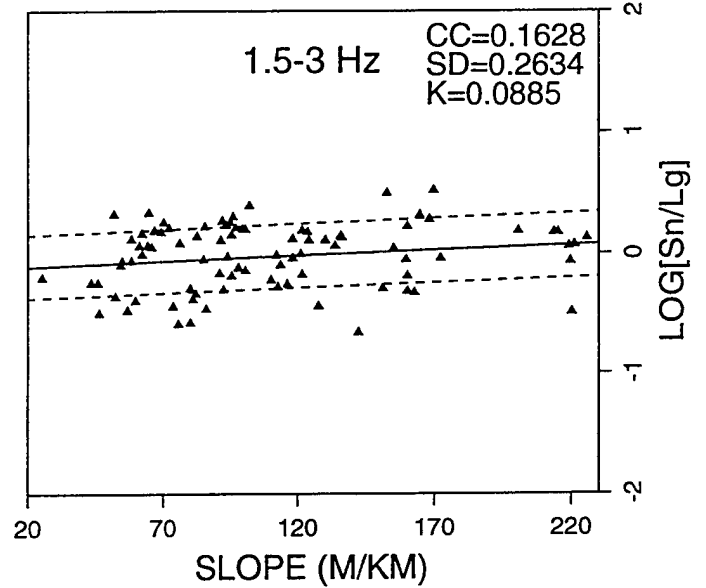
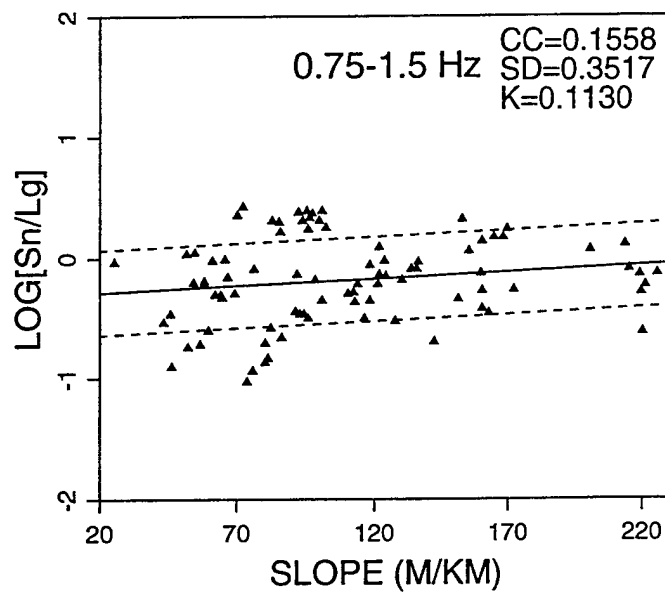


Figure A6j. Frequency dependent ratios of Sn/Lg phases recorded at WMQ plotted as a function of mean surface slope of each path. CC denotes the linear correlation coefficient. SD denotes the standard deviation of the linear regression, with the dotted lines corresponding to  $\pm 1$  SD, and K denotes the slope of the regression.

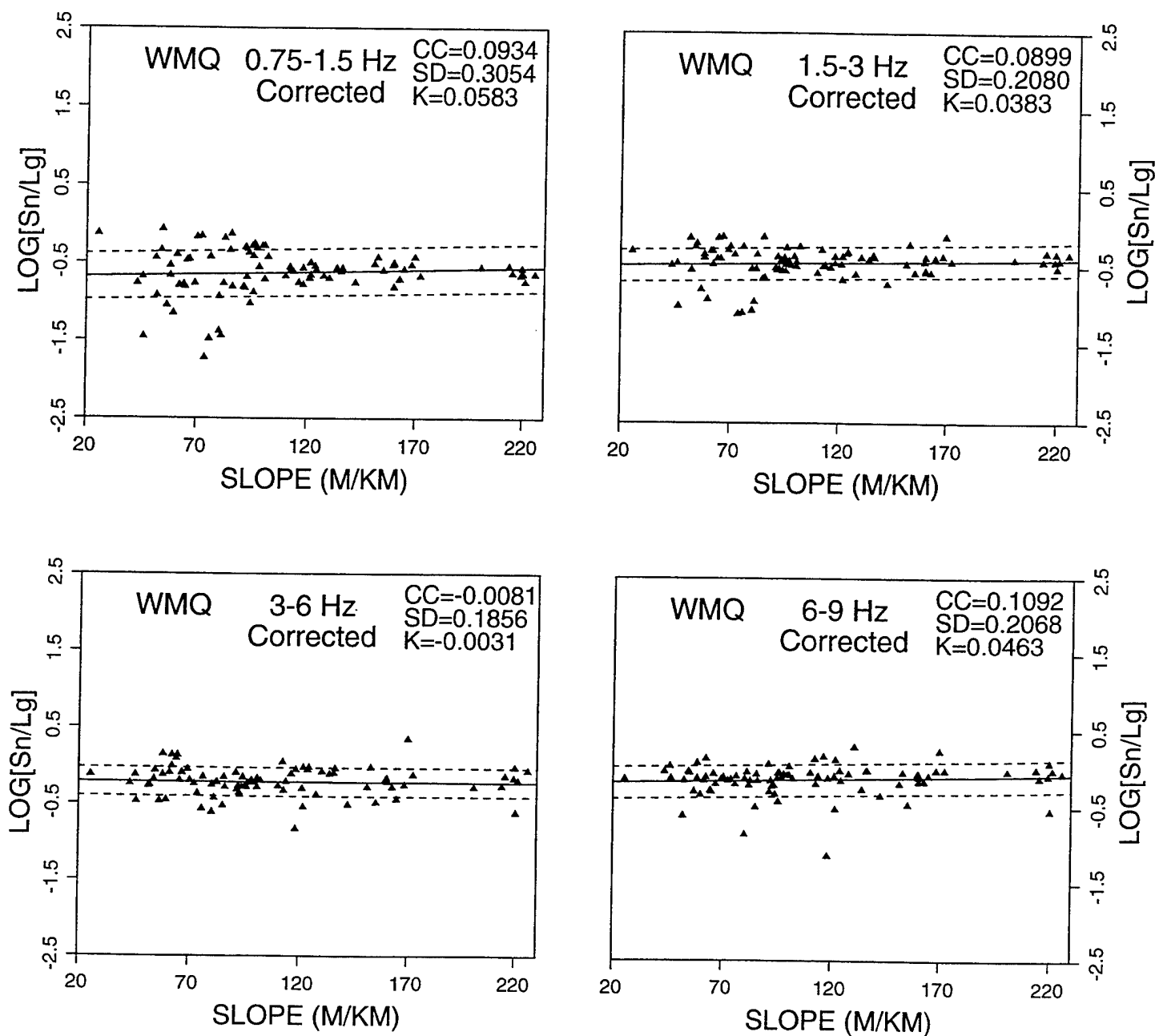


Figure A6k. Frequency dependent ratios of Sn/Lg phases recorded at WMQ plotted as a function of mean surface slope of each path after correcting for the distance dependence in Figure A6a. CC denotes the linear correlation coefficient. SD denotes the standard deviation of the linear regression, with the dotted lines corresponding to  $\pm 1$  SD, and K denotes the slope of the regression.